UNIVERSITÉ DU LUXEMBOURG

PhD-FSTM-2024-113
The Faculty of Science, Technology and Medicine

DISSERTATION

Defence held on 06/12/2024 in Belvaux - Sanem

to obtain the degree of

DOCTEUR DE L'UNIVERSITÉ DU LUXEMBOURG

EN *PHYSIQUE*

by

José Enrique MARTÍNEZ MEDINA
Born on 31 January 1992 in Tenancingo, Estado de México (Mexico)

MICROSTRUCTURE AND ELECTRICAL TRANSPORT PROPERTIES OF METALLIC CLUSTER-ASSEMBLED FILMS

Dissertation defence committee

Dr Emanuele Barborini, dissertation supervisor
Luxembourg Institute of Science and Technology

Dr Carlo Spartaco Casari
Professor, Politecnico di Milano

Dr Susanne Siebentritt, Chairman
Professor, Université du Luxembourg

Dr Yury Kolenko
International Iberian Nanotechnology Laboratory

Dr Paolo Milani, Vice Chairman
Professor, Università degli Studi di Milano

Affidavit

I hereby confirm that the Ph.D. thesis entitled “Microstructure and electrical transport properties of metallic cluster-assembled films” has been written independently and without any other sources than cited.

Luxemboug,_____

ACKNOWLEDGEMENTS

I would like to express my deepest gratitude to my supervisor, Dr. Emanuele Barborini, who gave me the opportunity to work on the CLASMARTS project. He has been an outstanding supervisor, always sharing his knowledge and experience. His unwavering support and insightful critiques throughout my research journey have been invaluable. Thank you for being an exceptional mentor; words cannot adequately convey my deep gratitude for his guidance and support over these years.

I am also deeply thankful to the members of my thesis supervision committee, Prof. Dr. Susanne Siebentritt and Prof. Dr. Paolo Milani, for their invaluable contributions and the suggestions they provided during each CET meeting. I would also like to extend my sincere gratitude to Prof. Dr. Carlo Spartaco Casari and Dr. Yury Kolenko for agreeing to be part of my dissertation defense committee and reviewing this thesis.

I want to thank Fonds National de la Recherche (FNR) for funding my PhD which is part of the CLASMARTS project, under the 2019 CORE program (C19/MS/13685974). Special thanks to Mathieu Gerard, Noureddine Bousri, Olivier Bouton and Nicolas Cremonesi for designing and assembling SCBD prototype at MRT department of LIST, which enabled the starting of my PhD research. Special thanks to Dr. Jérôme Polesel and Dr. Stéphanie Girod, for discussions and all their support in setting up and fabricating the interdigitated electrodes, a critical part of my work.

I am grateful to Dr. Adrian-Marie Philippe and Dr. Patrick Grysan for their invaluable assistance and expertise in TEM and AFM for characterizing my samples. Their contributions led to significant results and insights that greatly enhanced this work. I also like to thank Dr. Christèle Vergne and Dr. Jérôme Guillot for their expertise and support on XPS characterization.

I also want to extend my heartfelt thanks to all the friends I made in Luxembourg during this journey. Your friendship, support, and the unforgettable moments we've shared have greatly enriched my life. Whether in times of challenge or celebration, your presence has made this journey even more meaningful. A special thanks to the “Borondo guys”: Aleja, Mary and Daniel, for making the last three summers unforgettable with our trips and festivals.

I would like to extend my deepest gratitude to my parents Margarita and Antonio, for their unconditional love and unwavering support throughout this journey. Their constant encouragement and guidance have been a constant source of strength and inspiration. Thank you for always being there for me.

TABLE OF CONTENTS

LIST OF TABLES

LIST OF FIGURES

LIST OF SYMBOLS AND ACRONYMS

α	Roughness exponent
β	Resistivity exponent
ρ	Resistivity
AFM	Atomic Force Microscopy
EFIE	Electric-field-induced evaporation
EFISD	Electric field induced surface diffusion
EDS	Energy dispersive X-ray spectroscopy
FN	Fowler Nordheim
G	Conductance
GUI	Graphical user interface
IDE	Interdigitated Electrode
I-V	Current-Voltage
K_n	Knudsen number
LECBD	Low energy cluster beam deposition
MIM	Metal-insulator-metal
NP	Nanoparticle
PMCS	Pulsed microplasma cluster source
QCM	Quartz crystal microbalance

S	Supersaturation
SCBD	Supersonic cluster beam deposition
SEM	Scanning electron microscopy
TEM	Transmission electron microscopy
UHV	Ultra-high vacuum
V_t	Transition voltage

ABSTRACT

Nanostructured cluster-assembled metallic films have unique properties that can deviate remarkably from their atom-assembled counterparts, making them auspicious materials for a wide range of applications in different fields, including but not limited to chemoresistive gas sensing, electrochemical devices (lithium-ion batteries, fuel cells), memristive electronic devices. In all these cases, the understanding of the electrical transport properties of the films and the link with their micro- and nanostructure is of fundamental importance. In this context, I present a comparative study of the electrical conduction properties in cluster-assembled nanostructured Sn, Pt, Ni and W films produced by Supersonic Cluster Beam Deposition (SCBD), investigated in-situ during film growth, spanning from insulating phase to percolation and three-dimensional growth beyond percolation. Ex-situ morphological characterization provided information about the evolution of the nanoparticle morphology, microscale growth and oxidation after exposure to air. The investigated materials include very low and very high melting point metals, as well as less prone and more prone to oxidation ones.

My research highlights nanoparticle size and coalescence's critical role in the electrical conduction behavior at the percolation for the investigated cluster-assembled films. Specifically, I have observed that for Sn films, the deposition rate interferes with coalescence dynamics at the early stages of the growth. Lower deposition rates favor the coalescence of primeval size particles, resulting in enlarged islands and denser films. This, in turn, shifts the percolation threshold to a higher thickness with an abrupt onset of conductance. Conversely, higher deposition rates promote an advanced formation of percolation paths, with the growth of smaller islands and more porous structures, leading to an earlier percolation threshold with a more gradual transition from insulating to conducting phase. This behavior contrasts with Pt, Ni and W films, where coalescence plays a much less significant role at percolation, and particles with a smaller size are efficiently formed well-connected paths, achieving percolation at reduced thicknesses.

Following the percolation phase, electrical conduction stabilizes, and film resistivity sets at values 2-3 orders of magnitude larger than bulk one for both materials, allegedly

due to the nanogranular nature of cluster-assembled films. In this three-dimensional growth beyond percolation, resistivity shows an increasing trend with thickness, a feature ascribable to the decrease of the density of interconnections between particles in the topmost layer during film growth, as expected in ballistic growth. Understanding the impact of nanoparticle size and coalescence and its implications on the electrical transport of nanostructured metallic films is essential for tailoring the properties and optimizing their performance in different applications.

Additionally, below the percolation threshold, cluster-assembled metallic films exhibit nonlinear current-voltage (I-V) characteristics, indicating that quantum tunneling is the primary charge transport mechanism across nanoscale gaps. This consistent behavior across all studied materials highlights a common conduction mechanism in this regime. However, Fowler-Nordheim tunnelling currents were only observed in Sn films, highlighting the microstructural differences resulting from coalescence in comparison with the high melting point studied materials.

Preliminary results demonstrate the effectiveness of combining two metals (Sn and Pt) for chemoresistive gas sensing applications. Additionally, according to the scientific literature, distinct mechanisms of non-linear electrical conduction and conductance switching, relevant to neuromorphic applications, were observed in Sn films near the percolation threshold, Ni and Pt films beyond the percolation threshold, and WO_x films.

The research conducted in this PhD thesis is part of the CLASMARTS project, funded by the Luxembourg National Research Fund (FNR) under the 2019 CORE program (C19/MS/13685974), led by Principal Investigator E. Barborini, and carried out at the Luxembourg Institute of Science and Technology (LIST). During the first year of the CLASMARTS project (and of this PhD work), a SCBD prototype system was designed and constructed with the support of the prototype team of LIST. I specifically looked after the prototype parts dedicated to in-situ electrical conduction measurements, as elaborated in Chapter 3.

I. FUNDAMENTALS

CHAPTER 1. INTRODUCTION

1.1 Electrical conduction in metallic thin films

Electrical transport in metallic thin films is primarily governed by the motion of electrons under an applied electric field. In bulk metals, this process is well described by the Drude model, where conduction electrons move freely, interrupted occasionally by scattering events with impurities and lattice vibrations (phonons) [1–3]. However, as thin films decrease in thickness, especially nanogranular ones, microstructural factors such as grain boundaries, grain size, and surface roughness significantly influence electron transport, resulting in behavior that deviates from bulk material predictions.

The first significant refinement came with the Fuchs-Sondheimer (FS) model, developed to address the impact of surface scattering in thin films. This model considers that as film thickness decreases, the likelihood of electron scattering at surfaces increases, especially when the thickness approaches or is smaller than the electron mean free path [4–6]. The FS model modifies the bulk resistivity by incorporating a specularity parameter p, which describes the nature of electron reflections at the surface—specular or diffuse. The model's equation is given by:

$$\rho = \rho_0 \left[1 + \frac{3}{8}\frac{l}{t}(1-p)\right] \tag{1.1}$$

where ρ_0 is the bulk resistivity, l is the electron mean free path, t is the thickness, and p ranges from 0 (diffuse scattering) to 1 (specular scattering).

Namba’s contributions complement the FS model by introducing a correction for surface roughness, which further increases scattering as surface roughness increases [6,7]. Namba's work demonstrates that in films with significant roughness, electron scattering is even more pronounced, leading to further increases in resistivity. The impact of both roughness and thickness on resistivity is thus critical for understanding the electrical behavior of nanogranular thin films.

Later, the Mayadas-Shatzkes (MS) model extended the theory to include grain boundary scattering, particularly in polycrystalline and nanogranular films. In nanogranular films, where the grain size approaches the electron mean free path, grain boundaries act as potential barriers to electron flow, leading to increased resistivity. The MS model describes how electrons are either scattered or reflected at grain boundaries, depending on the grain boundary reflectivity parameter, R [1,8]. This model is especially relevant for thin films where the grain structure plays a more dominant role than in thicker films.

In nanogranular thin films, additional conduction mechanisms, such as quantum tunnelling between grains, become significant. As metallic grains in these films may not be fully connected, electron transport depends on tunnelling through barriers, adding complexity to the conduction mechanism.

Percolation theory offers another framework for understanding electron transport in nanogranular films. Below a critical threshold of metallic content, the system behaves as an insulator due to isolated grains. However, when the metallic content surpasses this threshold, continuous conductive paths form, and the film transitions to a conductor. This transition is critical for describing the behavior of nanogranular thin films, where conduction depends heavily on the formation of percolation networks. This will be further discussed in Section 6.1.

Cluster-assembled films represent a particularly interesting case of nanogranular materials for studying electrical transport. These films are characterized by high porosity and a large number of grain boundaries, which significantly impact their electrical properties [9–11]. One of the most effective methods for producing

nanogranular cluster-assembled films is cluster assembly, where atomic clusters are deposited with low kinetic energy per atom, preserving their individuality.

The unique structural and electrical properties of cluster metallic thin films make them suitable for a wide range of advanced technological applications, opening up possibilities in fields such as electronics, sensors, catalysis, and energy storage, as will be discussed next.

1.2 Applications of Nanogranular Films

The morphology of nanogranular films plays a crucial role in shaping their electrical transport properties, enhancing their versatility for diverse applications such as catalysis, sensing, energy storage, and memristive devices. The granular microstructure, characterized by distinct grain boundaries and interfaces, directly impacts charge transport, offering tunable properties that are often superior to those of non-granular materials. This allows nanogranular films to exhibit unique behaviors, such as enhanced surface area and tailored conductivity, making them particularly advantageous for specialized technological applications.

One of the primary advantages of nanogranular films is their high surface area-to-volume ratio. This structural feature enhances interactions at the material's surface, making them highly effective in catalysis and sensing applications. For instance, in catalysis, the high surface area allows for more active sites, improving the efficiency of chemical reactions. The ability to control particle size and composition in nanogranular films allows for the fine-tuning of catalytic performance of these films. Studies show that this flexibility is crucial for applications in chemical conversion and environmental remediation [12,13]. In sensing applications, nanogranular films are highly sensitive to environmental changes, such as gas presence or chemical shifts, because their nanoscale structure promotes better interaction with analytes [14] .

In energy storage, the microstructure of nanogranular films plays a pivotal role. The granularity shortens the diffusion paths for ions and electrons, facilitating faster charge transfer and enhancing energy storage capabilities [15]. Nanostructured materials have been integrated into batteries and supercapacitors, offering improved cycling

performance and energy densities. Additionally, the films provide structural flexibility, which contributes to better mechanical stability during the expansion and contraction cycles typical in devices like lithium-ion batteries.

Furthermore, recent advancements in memristive applications also benefit from the microstructure of nanogranular films. The unique microstructure of these films results in non-ohmic electrical transport properties with a complex switching behavior, making them ideal candidates for memristors and neuromorphic computing devices [9,10].

1.3 Objectives of the thesis

Despite the promising applications, several challenges persist in the synthesis and integration of nanogranular films. Controlling the microstructure at the nanoscale is inherently difficult, and minor variations can significantly impact performance. Additionally, a comprehensive understanding of the mechanisms governing electrical transport in correlation with the microstructure in these films is necessary to optimize their functionality.

Nanostructured cluster-assembled metallic films have unique properties that can deviate remarkably from their atom-assembled counterparts, making them auspicious materials for a wide range of applications where microstructure and electrical transport are important (as reviewed in previous section). Through a proper experimental setup, the correlation between microstructure and electrical transport properties can be investigated during the film growth. In this context, Barborini et al. [11] reported a clear correlation between microstructure and electrical transport properties in cluster-assembled films of Fe, Pd, Nb, W, and Mo. More recently, Borghi et al. [10] extended this investigation to cluster-assembled Au films, providing further insights into how the microstructural features of these materials influence their conductive behaviour.

This thesis aims to conduct a comparative study of the electrical conduction properties of cluster-assembled metallic films (Sn, Ni, Pt, and W) produced by Supersonic Cluster Beam Deposition (SCBD). The electrical properties are investigated in-situ during film growth, spanning from the insulating phase to percolation and subsequent

three-dimensional growth. Ex-situ morphological characterization is employed to provided insights into the evolution of nanoparticle morphology, sub-monolayer aggregation mechanisms and microscale growth, in correlation with the electrical properties.

Furthermore, in addition to the promising applications mentioned in the previous section, the selected materials represent a range of low-to high-melting-point metals in which the aggregation mechanism in the sub-monolayer and 3D growth can differ, thus affecting their electrical properties.

Additionally, from an applicative perspective in chemiresistive gas sensing, this study will also explore the experimental production of bimetallic Sn-Pt clusters and their film assemblies.

The thesis is structured as follows, in Chapter 1, I introduce the overall motivation and objectives of the research. Chapter 2 provides the scientific background, covering the fundamental concepts of clusters, their formation mechanisms, and nanogranular films by low-energy cluster beam deposition (LECBD). In Chapter 3, I describe the design of the SCBD system I used throughout this work, including the main components, sample holder, and the protocols I followed for the deposition process. As well as the characteristics of the cluster source employed in this study.

Chapter 4 details the setup and techniques used for in-situ electrical measurements during deposition of the cluster-assembled films, as well as the techniques employed for sample characterization in both sub-monolayer and thin-film regimes. Chapter 5 presents the morphological characterization results, starting with isolated particles and progressing to the sub-monolayer 2D regime, which was analyzed using TEM. The chapter also explores aggregation mechanisms for both low- and high-melting-point materials, as well as the transition to the 3D growth regime, characterized using AFM. This chapter concludes with an analysis of oxidation mechanisms affecting isolated particles and oxidation analysis of cluster-assembled films.

In Chapter 6, I present the in-situ electrical transport analysis, in correlation with the morphological properties studied in Chapter 5, covering the transition from insulating

to the percolation regime, and to the 3D regime. I also analyzed how particle coalescence influence the onset of conductance in low melting point materials. Additionally, I analyze the electrical behavior near the percolation threshold through I-V characteristics, providing more insight into how these systems behave as they approach this critical point.

In Chapter 7, I discuss preliminary results on the production and characterization of bimetallic Sn-Pt clusters, as well as the gas-sensing behavior of Sn-Pt cluster-assembled films. Additionally, preliminary results on memristive properties of films near percolation, beyond percolation and metal oxide films will be presented.

Finally, Chapter 8 summarizes the results of the doctoral dissertation and discusses perspectives for future research.

CHAPTER 2. SYNTHESIS AND DEPOSITION OF ATOMIC CLUSTERS BY GAS PHASE METHODS

2.1 Atomic clusters

Atomic clusters and nanoparticles represent a bridge between atoms and bulk materials, exhibiting unique properties that differ from both due to their high surface-to-volume ratios, and distinct electronic structures [16–18]. As illustrated in Figure 2.1 (a), while atomic clusters generally consist of a small number of atoms (up to a few nanometers), and nanoparticles range from a few to hundreds of nanometers, both terms are often used interchangeably in the literature, depending on the context. In this thesis, the terms "cluster" and "nanoparticle" will be used synonymously to simplify discussions unless specific differences are critical to the topic.

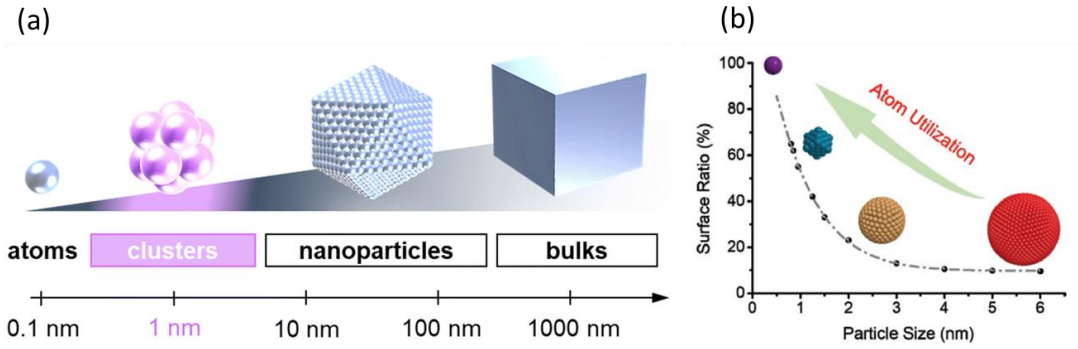

Figure 2.1. Size dependent properties of atomic clusters. (a) Categorization of materials based on the size scale. Taken from [18]. (b) Relationship between particle size and surface atom utilization. Smaller clusters exhibit a higher surface-to-volume ratio, enhancing their catalytic and reactive properties. Taken from [19].

The high surface atom exposure, as shown in Figure 2.1 (b), is a defining feature of atomic clusters. Smaller clusters have a significantly higher surface atom ratio, enhancing their reactivity and catalytic activity [19,20]. This trend of surface-to-volume ratio decreasing with increasing particle size underlines the importance of controlling nanoparticle size for various applications, such as catalysis and sensors [21].

The synthesis of clusters can be achieved using several methods; among these, advances in gas-phase techniques provide precise control over the size, structure, and composition of clusters, enabling the fine-tuning of these characteristics [22]. While atomic clusters can be studied as isolated systems, their integration into cluster-assembled films has emerged as a significant area of research [23]. These films formed by the soft assembly of clusters, preserve many of the size-dependent properties of individual clusters, allowing for the creation of nanogranular materials with distinctive electrical properties, as discussed in CHAPTER 1.

How to produce atomic clusters and then cluster-assembled films by soft assembly will be discussed in the subsequent sections.

2.2 Mechanism of nanoparticle formation

The gas-phase aggregation technique is one of the primary physical methods for synthesizing nanoparticles, particularly in the context of research and development where precision in particle size and composition is crucial. Among the different methodologies available for nanoparticle production, the gas aggregation source (GAS) has garnered significant attention due to its solvent-free nature and ability to generate high-purity nanoparticles without the need for post-synthesis purification.

A critical aspect governing nanoparticle formation in this process is supersaturation, as this creates the necessary conditions for homogeneous nucleation, where small clusters of atoms or molecules form spontaneously in the gas phase. Supersaturation is defined as the ratio of the actual vapor pressure of the evaporated material to its equilibrium vapor pressure at a given temperature. It acts as the driving force for nucleation and the subsequent condensation of nanoparticles (Figure 2.2). When the system is in equilibrium (i.e., supersaturation ratio $S = 1$), the gas-phase atoms remain in a steady state with no tendency to nucleate. However, when $S > 1$, the system becomes supersaturated, leading to favorable conditions for nucleation and nanoparticle growth. The degree of supersaturation affects not only the rate of nucleation but also the size and uniformity of the nanoparticles.

A sufficiently high supersaturation ($S \gg 1$) is required to ensure rapid nucleation and efficient growth of nanoparticles. Additionally, the presence of a buffer gas, such as argon, helps to regulate the energy dissipation within the system, facilitating controlled particle growth and preventing uncontrolled aggregation. The following sections will detail the key steps involved in the nanoparticle formation process in GAS.

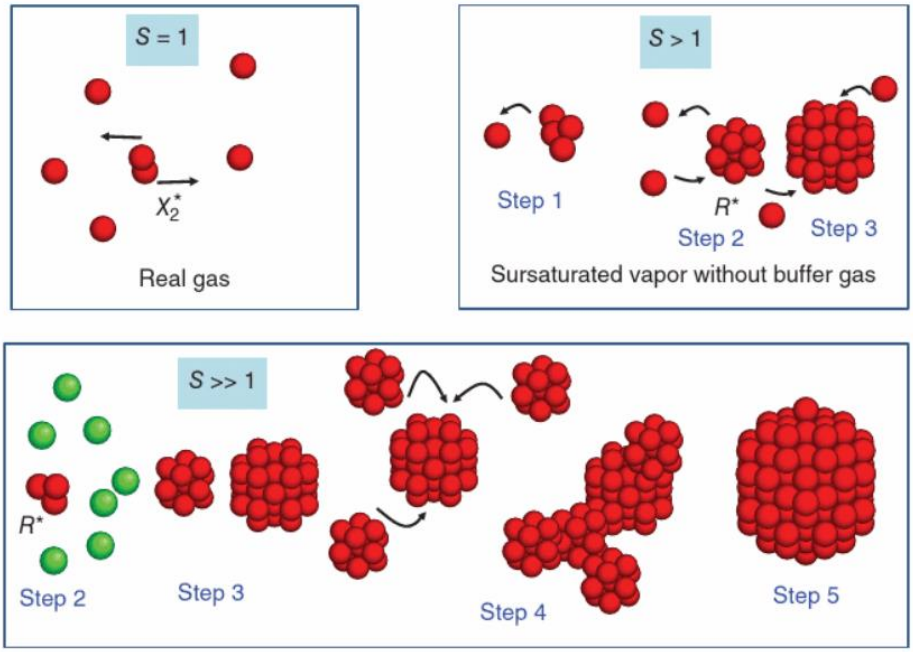

Figure 2.2: Schematic representation of nanoparticle formation in the gas phase under different supersaturation conditions. In a real gas at equilibrium (S=1), no nucleation occurs, and atoms remain independent in the gas phase. In a supersaturated vapor without buffer gas (S>1), nucleation begins, leading to the formation of critical nuclei (R^*) and subsequent growth of nanoparticles. (c) In a highly supersaturated vapor (S>>1) with the presence of a buffer gas, the formation of stable nuclei is enhanced, and the buffer gas helps in controlling energy dissipation, leading to a more controlled growth, coagulation (Step 4), and sintering (Step 5) of compact nanoparticle aggregates. Taken from [24].

The synthesis and deposition of nanoparticles via gas-phase aggregation follows a complex process that can be summarized in 6 steps [24]:

Step 1: Vaporization: The process begins with the vaporization of the target material, which is typically achieved through techniques such as laser ablation, magnetron sputtering, or thermal evaporation. The aim is to produce individual atoms or ions of the material in a vapor form, where they are free to move and interact in the gas medium.

Step 2: Homogeneous nucleation: Once the metal atoms are in the gas phase, nucleation occurs. Nucleation is the process where individual atoms begin to cluster together to form a "seed. This process is typically described by a three-body collision between two metal atoms (M) and a working gas atom (Ar, for instance). The role of the argon atom is to remove excess energy from the system, facilitating the stabilization of the newly formed metal dimer. The equation for this process is:

$$M + M + Ar \rightarrow M_2 + Ar \tag{2.1}$$

Where the argon atom removes excess energy, allowing the dimer (M_2) to stabilize.

As nucleation progresses, a critical-sized cluster R^* forms. If the cluster reaches this critical size, it becomes thermodynamically stable and can continue to grow. The critical size depends on the supersaturation ratio, as higher supersaturation values allow smaller clusters to stabilize.

Step 3: Condensation: After nucleation, the clusters grow through the condensation of additional atoms onto the stable nuclei. The classical nucleation theory helps describe this process, suggesting that growth occurs as the system seeks to minimize the free energy associated with the cluster's surface and volume.

$$\Delta G = \Delta G_{surface} + \Delta G_{volume} = 4\pi R^2 \Delta g_{surface} - \frac{4}{3}\pi R^3 \Delta g_{volume} \tag{2.2}$$

Where:

- $\Delta g_{surface}$ is the surface energy per unit area,
- Δg_{volume} is the volume energy per unit volume,
- R is the radius of the growing particle.

The critical radius R^*, at which the cluster becomes stable, is defined by the balance of surface tension and supersaturation:

$$R^* = \frac{2\sigma}{k_B T \, log \, S} \tag{2.3}$$

Once a stable nucleus forms, further condensation of metal atoms causes the particle to grow. The supersaturation ratio plays a critical role in determining the rate of growth, with higher supersaturation leading to more rapid condensation.

Step 4: coagulation of nanoparticles: After the formation of stable nuclei, these nanoparticles may collide and coagulate. Coagulation is primarily driven by Brownian motion, where thermal energy causes particles to move randomly within the gas medium. When two nanoparticles collide, they can either form loosely connected aggregates or sinter into more compact structures, depending on the energy conditions.

Coagulation often leads to the formation of larger particle clusters, which may remain loosely bound or undergo further densification. The balance between coagulation and subsequent sintering determines the final size and morphology of the nanoparticles.

Step 5: Sintering (formation of compact aggregates): During sintering, loosely bound aggregates undergo atomic diffusion, leading to the formation of more compact, dense structures. Sintering is the process by which atoms at the surfaces of neighboring particles migrate to reduce surface energy, ultimately densifying the nanoparticle clusters.

Sintering is influenced by temperature and the physical properties of the material. Higher temperatures increase the rate of diffusion, accelerating the sintering process. The final morphology and stability of the nanoparticles are largely determined at this stage.

Step 6: Deposition onto substrates: In the final step, nanoparticles are transported from the aggregation zone to the substrate for deposition.

Supersaturation creates the necessary conditions for homogeneous nucleation, where small clusters of atoms or molecules form spontaneously in the gas phase. The degree of supersaturation, alongside the presence of a buffer gas, plays a crucial role in determining the rate of nucleation, the size of the particles, and the overall morphology of the nanoparticle aggregates. A higher supersaturation ratio drives faster nucleation and more rapid particle growth, while the introduction of a buffer gas helps dissipate excess energy and ensures stable particle formation. Gas-phase aggregation provides

several key advantages, including the ability to synthesize high-purity nanoparticles without the need for surface ligands or solvents. This method is highly adaptable, allowing researchers to control nanoparticle size, composition, and morphology by tuning supersaturation levels and introducing buffer gases.

Among several gas phase aggregation techniques, Supersonic Cluster Beam Deposition (SCBD) offers a highly effective approach for producing nanoparticles with precise control over size and composition. The introduction of a buffer gas improves cluster growth by moderating the collision energy between particles, facilitating the formation of larger and more uniform nanoparticles. This stabilization is achieved through cooling and reduced kinetic energy during particle aggregation, allowing for more efficient growth and less premature agglomeration of particles. Such control is fundamental for applications in where particle uniformity and purity are paramount as reviewed in Section 1.2.

2.3 Molecular Beam Formation by Adiabatic Expansion

Before entering into details of supersonic cluster beam deposition, how to create a molecular beam will be discussed next. One method to create a molecular beam is to use a source or reservoir containing a gas at high pressure and temperature (P_0 and T_0 at the stagnation), a small orifice in the reservoir, and a low-pressure region downstream of the orifice, letting molecules in the pressurized cell to escape region of lower pressure. If the diameter of the orifice, d, is significantly smaller than the gas mean free path λ within the reservoir, the flow from the reservoir into the low-pressure region exhibits effusive characteristics. Conversely, if d is much larger than λ, then the orifice acts as a supersonic nozzle or jet [25]. The principle is illustrated in Figure 2.3.

The mean free path λ of the buffer gas in the cell determines the flow regime of the outgoing beam. There are two limiting regimes of flow: effusive and supersonic. The mean free path is given by:

$$\lambda = \frac{1}{\sqrt{2}n\sigma} \tag{2.4}$$

The collision cross-section σ for two spherical molecules with diameter d is given by:

$$\sigma = \pi d^2 \tag{2.5}$$

This cross-section represents the area through which a molecule must pass to collide with another molecule.

The number density n of molecules in an ideal gas is derived from the ideal gas law:

$$P = nk_BT \tag{2.6}$$

Where P is the pressure, k_B is the Boltzmann constant and T is the temperature.

Substituting the expression for n in Eq. 2.4:

$$\lambda = \frac{k_BT}{\sqrt{2}\pi d^2 P} \tag{2.7}$$

This equation highlights how λ increases with temperature and decreases with pressure, illustrating the sensitivity of molecular interactions to environmental conditions.

The regime between effusive and supersonic expansion in the context of gas dynamics and molecular beam generation can be effectively characterized by the Knudsen number (K_n). The Knudsen number is a dimensionless quantity that helps to determine the flow regime of a gas by comparing the mean free path of its molecules to a characteristic physical length scale, such as the diameter of an orifice or nozzle through which the gas is expanding:

$$K_n = \frac{\lambda}{d} \tag{2.8}$$

This dimensionless number categorizes the flow regimes of gases: Effusive and supersonic. For comparison, I will briefly review some properties of effusive and supersonic beams.

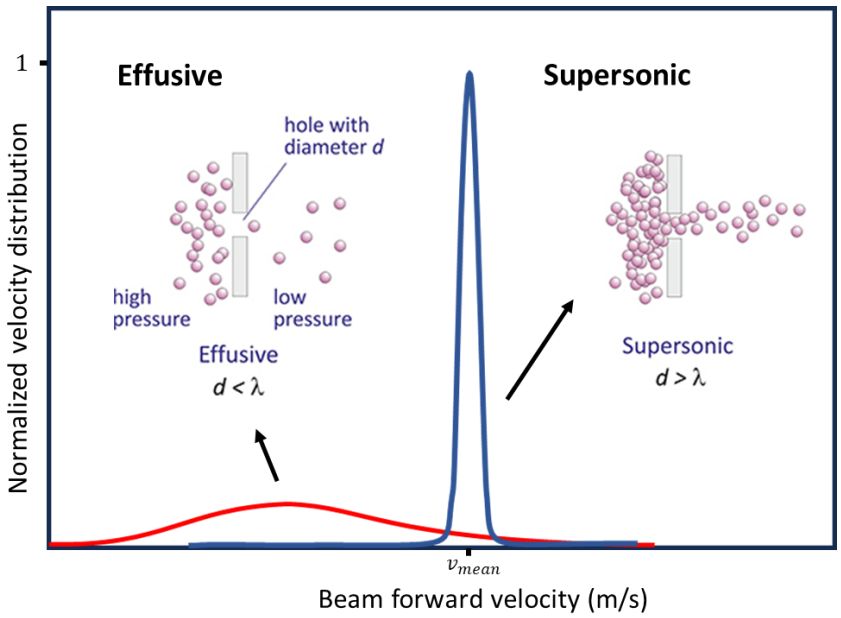

Figure 2.3. The diagram compares effusive and supersonic gas flow regimes through a small aperture based on the hole diameter (d) relative to the mean free path (λ) of gas molecules. In an effusive beam, $d < \lambda$, leading to a broad velocity distribution and a low mean forward velocity (red curve). In a supersonic beam, $d > \lambda$, leading to numerous collisions as the gas expands, narrowing the velocity distribution and significantly increasing the mean forward velocity (blue curve). Taken from [26].

2.3.1 Effusive Flow

In the effusive flow regime, characterized by a Knudsen number greater than one ($K_n > 1$), the mean free path length of the gas molecules is much larger than the characteristic dimension of the orifice or nozzle ($\lambda > d$). This condition means that gas molecules escape the reservoir into the low-pressure region without significant interaction with each other. The lack of collisions in and downstream of the orifice means that the velocity distribution of molecules in the resulting beam will be a Maxwellian distribution comparable to the reservoir temperature, T_0, prior the

expansion. Furthermore, the lack of collisions prevents any redistribution of the internal energies (rotational and vibrational) thus preserving the energy distribution identical with that in the reservoir.

For small nozzle sizes typically used, low backing pressures are required for the generation of effusive beams.

2.3.2 Supersonic Flow

In supersonic flow, characterized by a Knudsen number less than 1 ($K_n < 1$), the dynamics of gas expansion from a high-pressure reservoir through a small orifice into a vacuum exhibit distinct behavior. By increasing the stagnation pressure of the reservoir and decreasing the orifice diameter ($\lambda < d$), a molecular beam transitions into the supersonic expansion regime. Here, the mean free path of particles within the reservoir becomes smaller than the orifice diameter, resulting in numerous collisions during the expansion process. When the orifice diameter (d) is significantly larger than the mean free path, the escaping molecules experience frequent collisions, causing the expansion to be governed by gas dynamic equations similar to those utilized in aircraft design. As gas expands from the high-pressure stagnation region into a vacuum, the random velocities of gas atoms are diminished by adiabatic expansion, aligning their motion direction and speed. This process converts the enthalpy in the stagnation region into kinetic energy of the directed mass flow, as well as residual enthalpy, leading to a decrease in gas temperature (T) in accordance with the law of conservation of energy. This phenomenon is schematically depicted in Figure 2.3 (inset), illustrating the supersonic expansion of gas from a nozzle.

2.4 Supersonic Molecular Beams

In the realm of modern scientific research, supersonic molecular beams have emerged as a versatile and powerful tool for investigating the fundamental properties of molecules and clusters. These beams, characterized by their high directionality, low

internal temperatures, and narrow velocity distributions, have found widespread applications in spectroscopy, reaction dynamics, and surface science. This chapter delves into the fundamental principles of supersonic molecular beams.

To generate a supersonic jet, high-pressure gas is expanded through a sonic nozzle into a vacuum chamber. The setup includes a reservoir containing the working gas at a high pressure P_0 and a stagnation temperature T_0. The nozzle exit opens into a vacuum chamber maintained at a lower pressure P_b. The flow is driven by the pressure difference $(P_0 - P_b)$, achieving supersonic conditions when the pressure ratio P_0/P_b exceeds a critical value [27,28]:

$$\left(\frac{\gamma + 1}{2}\right)^{\gamma/(\gamma-1)} \tag{2.9}$$

where $\gamma = \frac{C_P}{C_V}$ is the ratio between the specific heats at constant pressure and volume. For all inert gases, the critical value is about 2, therefore if $P_0/P_b > 2$ the gas expansion proceeds with a supersonic character [29].

The supersonic expansion is adiabatic, meaning that no heat is exchanged with the surroundings. Consequently, as the gas expands and does work against the background pressure, its internal energy decreases, leading to a significant drop in temperature.

The rapid cooling during supersonic expansion is a key feature that distinguishes supersonic molecular beams from effusive beams. The temperature drop is accompanied by a decrease in the random thermal motion of the molecules and an increase in their directed velocity. This results in a highly directional beam with a narrow velocity distribution.

The Mach number (M), defined as the ratio of the flow velocity (u) to the local speed of sound (c), is a critical parameter in characterizing supersonic flow [30]:

$$M = \frac{u}{c} \tag{2.10}$$

The speed of sound in an ideal gas is related to its temperature (T) and molar mass (m) by:

$$c = \sqrt{\frac{\gamma P}{\rho}} = \sqrt{\frac{\gamma RT}{m}} \tag{2.11}$$

where R is the universal gas constant.

As the supersonic jet expands further into the vacuum chamber, the flow becomes more rarefied, and the frequency of collisions decreases. Eventually, the gas molecules reach a region where collisions become negligible. This region, characterized by a Mach number $M > 1$, is known as the zone of silence, as depicted in Figure 2.4 [27]. In this zone, the gas molecules move freely with a narrow velocity distribution and low internal temperatures.

As the jet interacts with the background gas in the vacuum chamber, it forms shockwaves. These are narrow regions where the flow velocity abruptly decreases, and the pressure and temperature increase sharply. The diagram illustrates the barrel shock and Mach disk shock, which are formed at the boundaries of the zone of silence. The Mach disk, the most prominent shockwave, marks the end of the zone of silence and the transition to subsonic flow.

The location of the Mach disk (x_M) from the nozzle exit can be estimated using the following empirical relation [31]:

$$x_M = 0.67d\left(\frac{P_0}{P_b}\right)^{\frac{1}{2}} \tag{2.12}$$

where d is the nozzle diameter.

During adiabatic expansion, the temperature (T) of a gas decreases as the gas performs work on its surroundings, following the principles of energy conservation. As gas expands from a high-pressure stagnation region into a vacuum through a small orifice, its random molecular velocities decrease, leading to a more uniform speed distribution among the gas molecules. The enthalpy in the stagnation region is thus converted into kinetic energy of the mass flow and residual enthalpy. The relationship between the Mach number and the stagnation to static temperature ratio is described by:

$$T = T_0 \left(1 + \frac{\gamma - 1}{2} M^2\right)^{-1} \tag{2.13}$$

In an ideal supersonic expansion, nearly all initial internal energy is converted into kinetic energy, making the final beam temperature negligible compared to the initial gas reservoir temperature ($T \ll T_0$) [29,32]. The maximum beam velocity (v_{max}) of a supersonic beam can be expressed as:

$$v_{max} = \sqrt{\left(\frac{\gamma}{\gamma - 1}\right) \frac{2kT_0}{m}} \tag{2.14}$$

This velocity is a function of the initial temperature, adiabatic index, and molecular mass. Noble gases typically employed in seeded supersonic nozzle sources, such as argon, helium, and neon, can reach maximum velocities of $557.9\, m/s$, $1771.0\, m/s$ and $784.9\, m/s$, respectively, under optimal expansion conditions.

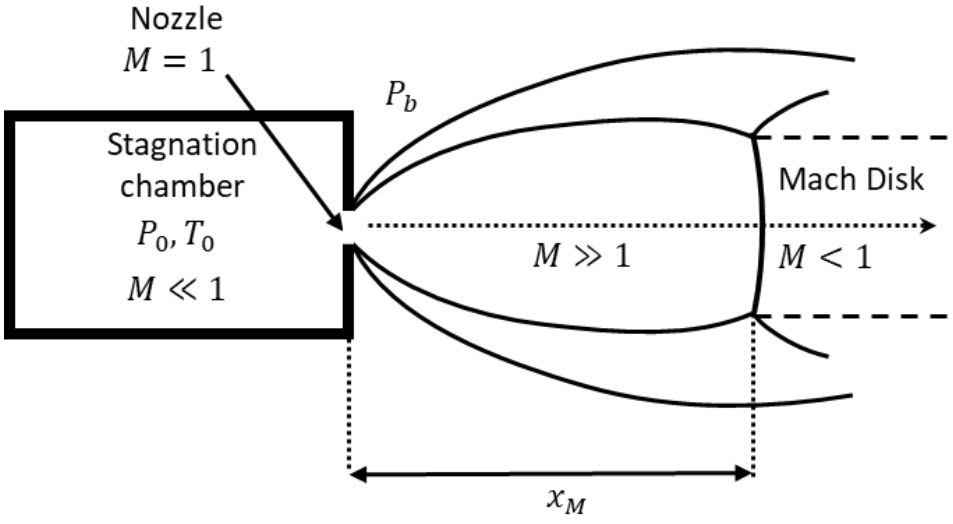

Figure 2.4: As depicted in the figure, The flow starts from rest with Mach number $M \ll 1$ and accelerates towards the nozzle, reaching sonic velocity ($M = 1$) at the nozzle given

a sufficiently high-pressure gradient. Further acceleration leads to supersonic velocities ($M > 1$).

The velocity distribution in the diagram show changes in velocity at different points along the jet, emphasizing the transition from subsonic to supersonic flow and the corresponding effects of shock waves and pressure adaptation.

2.4.1 Supersonic seeded cluster beam

The formation of a seeded molecular beam begins with the introduction of a small quantity of a target species, referred to as the "seed," into a carrier gas. The carrier gas, often a light monoatomic gas such as helium or argon, serves as a medium to facilitate the controlled expansion and cooling of the seed molecules as the gas mixture is expelled through a supersonic nozzle. This expansion process is central to defining the properties of the resulting molecular beam, particularly in applications related to atomic clusters [33,34].

During supersonic expansion, the gas mixture undergoes rapid adiabatic cooling, and this cooling is transferred to the seed molecules. This process significantly reduces the rotational and vibrational energy levels of the seed molecules, producing a beam with a high degree of translational energy while simultaneously achieving rotational cooling and alignment. The velocity of the molecules in the beam is influenced by a phenomenon known as "velocity slip," where the heavier seed molecules, through collisions with the faster carrier gas molecules, are accelerated to velocities approaching those of the carrier gas. This results in a narrow velocity distribution, which is essential for precise experimental control.

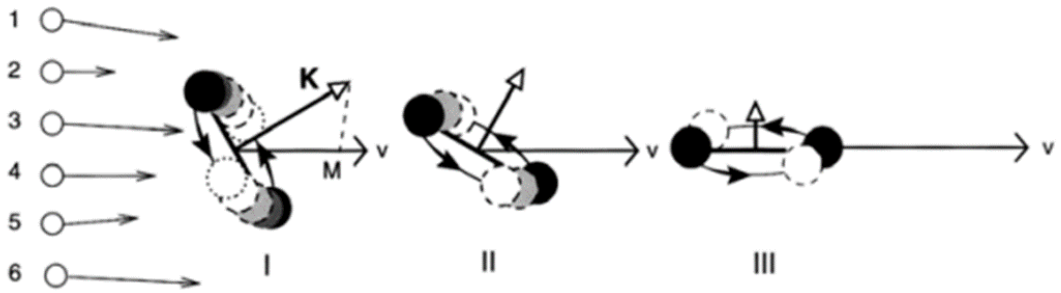

Figure 2.5. Classical depiction of acceleration, rotational cooling, and alignment in a supersonic expansion: A diatomic molecule (seed species) initially rotates randomly with respect to the flight direction $\boldsymbol{v}$ (Stage I). The molecule experiences multiple collisions with lighter atoms of a monoatomic carrier gas (e.g., helium or argon), leading to changes in its rotational angular momentum $\boldsymbol{K}$ and helicity $\boldsymbol{M}$ (the projection of $\boldsymbol{K}$ along $\boldsymbol{v}$). Collisions with small impact parameters (e.g., atoms 3 and 4) increase the seed molecule's translational velocity and reduce its rotational energy. Collisions with intermediate impact parameters (e.g., atoms 2 and 5) decrease the helicity $\boldsymbol{M}$ by bending the rotational plane. Larger impact parameter collisions (e.g., atoms 1 and 6) primarily deflect the molecule elastically without significantly altering its state. After sufficient collisions (Stage III), the seed molecules are left with minimal rotation, and the angular momentum vector $\boldsymbol{K}$ is uniformly distributed in a plane orthogonal to the velocity vector $\boldsymbol{v}$, signifying complete rotational cooling and alignment. Taken from [34].

Figure 2.5 shows a classical representation of this process. Initially, a diatomic molecule (representing the seed) is randomly oriented with respect to the flight direction $\boldsymbol{v}$ (Stage I). The rotational angular momentum vector $\boldsymbol{K}$ and its projection along v, denoted as the helicity M, describe the rotational state of the molecule. As the expansion begins, the seed molecule experiences multiple collisions with the lighter carrier gas atoms [34].

These collisions vary in impact parameter b, influencing the rotational and translational dynamics of the seed molecule. Collisions with small impact parameters (e.g., by atoms 3 and 4 in the figure) are particularly effective in increasing the translational velocity $\boldsymbol{v}$ of the seed molecule, thus contributing to the overall kinetic energy of the beam. These collisions also play a role in modifying the helicity M, with a tendency to reduce it as the rotational plane of the molecule aligns closer to the flight direction $\boldsymbol{v}$ (Stage II).

Intermediate collisions (e.g., by atoms 2 and 5) may bend the rotational plane of the seed molecule, leading to a gradual decrease in M. The progressive reduction in helicity is indicative of rotational cooling, where the molecule transitions from a high-energy rotational state to a lower-energy state, becoming increasingly aligned with the beam direction.

As the expansion continues, collisions with larger impact parameters (e.g., by atoms 1 and 6) become more elastic, meaning they primarily deflect the molecule without significantly altering its velocity or rotational state. This stage of the process (Figure 2.5, Stage III), illustrates how the seed molecules, after undergoing multiple collisions, reach a state of minimal rotation with low helicity M. In this state, the rotational angular momentum vector $\boldsymbol{K}$ is distributed uniformly in a plane orthogonal to the velocity vector $\boldsymbol{v}$.

The ability to achieve this state through careful control of the seeding and expansion process underpins the versatility and utility of seeded molecular beams in materials science, especially in the precise study and manipulation of atomic clusters.

By leveraging the properties of supersonic seeded beams, researchers have employed this technique for the production of atomic clusters with precise control over their size and energy characteristics. Various physical methods have been developed to produce the seed species used in these beams, including laser ablation and sputtering techniques. These approaches allow for the generation of a wide range of clusters, from simple metal clusters to more complex nanostructures. The next section will review cluster beam deposition (CBD) technique and the most common physical methods to produce the seeded species.

2.4.2 Pulsed supersonic beams

Pulsed supersonic beams have become a powerful implement in the field of molecular physics and chemistry, providing a method to produce highly collimated and internally cold molecular beams. This technique involves the rapid expansion of a high-pressure gas through a nozzle into a vacuum chamber, where the pulsed nature of the gas flow offers significant advantages over continuous supersonic beams.

The development of pulsed supersonic beams can be traced back to the early 1970s. Pioneering work by various research groups, including the significant contributions of Richard E. Smalley [35] and his colleagues in combining pulsed valves with laser vaporization, have led to advancements in supersonic seeded beams. These advancements were pivotal in enhancing the intensity and cooling of molecular beams, providing a foundation for their application in cluster beam deposition.

The generation of pulsed supersonic beams involves the use of specialized pulsed valves, such as the Even-Lavie valve. These valves operate by rapidly opening and closing, allowing controlled bursts of high-pressure gas to expand through a nozzle into a vacuum chamber. The General Valve Series 9 is another widely used device, which employs a solenoid to drive a Teflon cylinder with a conical tip, allowing the gas to expand through the nozzle.

The typical setup involves a pulsed valve connected to a high-pressure gas reservoir. Upon activation, the valve opens briefly (25–100 microseconds), allowing a controlled amount of gas to expand supersonically through a nozzle into the vacuum chamber. This rapid expansion results in a highly collimated beam with significantly reduced internal temperatures, which is critical for the formation of clusters.

Pulsed supersonic beams offer several distinct advantages over their continuous counterparts:

1. **Enhanced Control** Pulsed supersonic beams offer exceptional control over the duration and frequency of gas pulses, enabling precise synchronization with other experimental components such as lasers, detectors, magnetic fields, and electrical fields. This precise timing is crucial in cluster beam deposition, where the coordination of gas pulses with sputtering processes, induced by electrical discharges, can enhance the production and control of atomic clusters. The ability to fine-tune pulse parameters ensures optimized interaction between the beam and other experimental setups, leading to more reliable and reproducible results in complex experiments.
2. **Reduced Background Pressure**: Pulsed operation significantly reduces the background pressure in the vacuum chamber compared to continuous beams. This

is because the gas is introduced intermittently, allowing the vacuum pumps more time to evacuate the chamber between pulses, which can be important for the successful deposition of high-quality cluster assembled thin films.

3. **High Intensity and Cooling**: Although continuous beams can also achieve very low temperatures through careful design and operation, the rapid expansion of gas in pulsed supersonic beams leads to the formation of high-intensity beams with exceptionally low internal temperatures. These conditions are ideal for the production of atomic clusters with controlled size and shape.

By leveraging the precise control and high intensity offered by pulsed supersonic beams, Pulsed Microplasma cluster source (PMCS) has emerged as a versatile tool for the synthesis of diverse nanostructured materials. The combination of pulsed gas injection, electrical discharge, and supersonic expansion in PMCS allows for efficient generation of cluster-seeded supersonic beams with tailored properties. The PMCS used in this study will be discussed in Section 2.5.2.3.

2.5 Nanogranular films by cluster beam deposition

Cluster beam deposition (CBD) is a vacuum-based technique that relies on gas expansion to transport particles. These particles are carried in an inert gas through an orifice or nozzle, expanding into a beam that can be deposited onto various substrates. CBD has emerged as a versatile method for fabricating nanostructured and nanocomposite films, enabling precise control over cluster kinetics and leading to the development of advanced material properties.

This bottom-up approach to nanomaterial synthesis is rooted in the mechanisms of gas-phase particle synthesis, similar to those observed in aerosol synthesis and nanoparticle production. Clusters are built from individual atoms or molecules, with cluster embryos through physical means like condensation of a supersaturated vapor or through chemical reactions of gaseous precursors.

The roots of CBD trace back to gas aggregation techniques, a method employed since the 1930s. The first documented use of this technique was to produce a film of bismuth particles to serve as an optical filter. By the 1970s and 1980s, the concept underwent further exploration. The first beams of nanoscale clusters were produced during this time, initially focusing on noble-gas clusters, by Raoult and Farges [36] and later expanding to metallic clusters. Researchers like Hogg and Silbernagel, Sattler et al., Frank et al., and Takagi et al. explored metal evaporation in inert gas atmospheres. Notably, a 1976 review by Granqvist and Buhrmann significantly contributed to the analysis of the aggregation process of metallic clusters [37,38]. This review highlighted the mechanisms of nanoparticle formation and the potential applications of these materials. Nanoparticle synthesis via gas aggregation typically involves a vapor source within a vacuum chamber filled with an inert gas, such as argon or helium. Initial experiments employed resistive filament vapor sources; however, advancements have introduced thermal evaporation, sputtering, electron beam, and laser-based methods. Each technique presents distinct advantages and limitations, underscoring the versatility of cluster beam deposition (CBD) in materials research and development.

The kinetic energy of the deposited clusters plays a crucial role in determining the morphology and properties of the resulting films. As illustrated in Figure 2.6, based on the kinetic energy of the impinging clusters, CBD can be classified into three distinct regimes [22,39]:

Low energy (0.1-1 eV/atom): At this precise range, CBD facilitates the deposition of clusters without significant fragmentation. This preservation of structural integrity is due to the soft-landing collision on the substrate. The result is the formation of dendritic films, characterized by their large surface areas, akin to light-absorbing black films. Additionally, the film possesses less than one half of the bulk density, a significant outcome of this process.

Medium Energy (1-10 eV/atom): In this energy range, the cluster are deformed upon impact, leading to the formation of denser films with minimal cavities. These films achieve densities close to 80% of the bulk.

High Energy (>10 eV/atom): At high energies, the 'meteoric impact ', a metaphorical term used to describe the intense collision of clusters, the original cluster shape is destroyed upon impact. These clusters contribute to the formation of dense, almost bulk-density films, which are mirror-like and exhibit highly ordered and smooth surfaces.

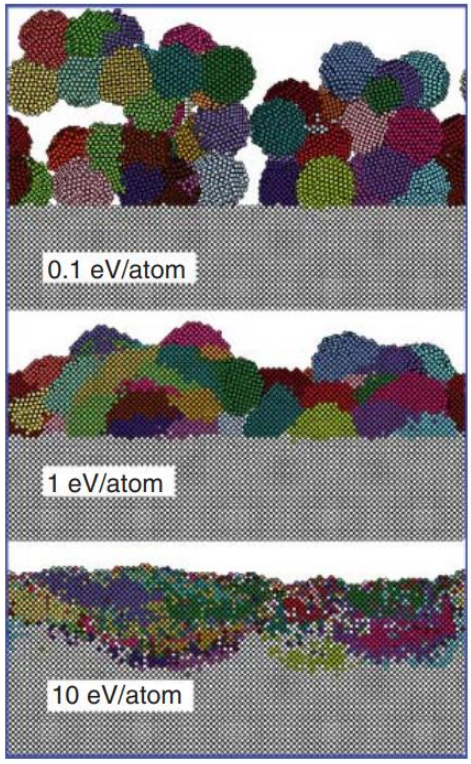

Figure 2.6: Molecular dynamics simulations illustrating the impact of molybdenum clusters (each containing 1043 atoms) onto a Mo (001) substrate at varying kinetic energies. The simulations reveal that low-energy impacts result in porous structures with clusters remaining largely intact, while high-energy impacts lead to the formation of smooth, compact films. Taken from [40].

In this context, CBD offers some unique possibilities for the control of the free incident clusters before deposition. A key example is Low Energy Cluster Beam Deposition (LECBD) which has emerged as a fundamental technique, enabling the formation of functional cluster-assembled nanostructured porous films. This is achieved by softly depositing clusters onto a substrate, ensuring they retain their structure and properties.

2.5.1 Low energy cluster beam deposition (LECBD)

LECBD is a sophisticated technique that focuses on the deposition of neutral clusters with very-low-energy per atom, produced in inert-gas condensation sources. This method is noted for its potential to finely control both the clusters in the gas phase and the deposition conditions. It is particularly advantageous for the production and deposition of nanoparticles in the 1-10 nm size range.

LECBD allows for the deposition of clusters with minimal energy transfer, typically around 0.1 eV/atom. This "soft landing" preserves the inherent structure of the free clusters, allowing them to act as building blocks in forming highly porous nanostructured materials.

The formation of nanoparticles involves complex processes where the physical conditions can greatly affect the size and properties of the resulting particles. One common method is the generation of a material vapor in a flow of inert gas, leading to supersaturation and subsequent condensation into nanoparticles. The conditions within the source, such as the supersaturation ratio, temperature, and pressure, play critical roles in determining the size distribution of these nanoparticles.

Various mechanisms are employed to eject material from the target in cluster sources, each with its own advantages and suitability depending on the type of material and the desired properties of the nanoparticles. Some of the main techniques used to produced atomic clusters will be reviewed next.

2.5.2 Low energy cluster sources

2.5.2.1 Laser vaporization cluster source

Laser Vaporization Cluster sources (LVCS) are considered as an advanced option for producing nanoparticles by rapidly vaporizing materials, even refractory materials. This technique, initially developed by R. Smalley [35] and his team, produces cold beams of clusters by quickly cooling the vaporized material through supersonic expansion. A key feature of this process is the synchronized operation of a

pulsed valve with a laser, which reduces the amount of carrier gas needed and allows for a more compact vacuum chamber design.

In typical LVCS setups (as illustrated in Figure 2.7), the process begins with the targeting of a material (rod or disk), using a high-powered laser, usually an Nd:YAG laser, which is capable of delivering pulses typically ranging from 30 to 100 $mJ/pulse$ depending the material [41–43]. The nanosecond laser pulses create a plasma contained within a small volume above the target, ensuring rapid and intense heating and vaporization of the target material. Following the vaporization phase, the vaporized material is synchronized with a pulse of inert gas flow (e.g., helium or argon), introduced at pressures of 5-9 bar some hundred microseconds before ablation. This gas rapidly thermalizes the vapor, leading to the condensation of the vapor into clusters. The gas then undergoes supersonic expansion which takes place at the exit of the source in the vacuum chamber through a typically 1 mm-diam nozzle, leading to produce cold beams of clusters [35,44].

Several variables influence the effectiveness of nanoparticle synthesis in LVCS. These include the plasma composition above the target, the choice of expansion gas, and its backing pressure. The timing of the gas pulse in relation to the laser pulse is particularly critical, as it affects the average gas pressure during the vaporization phase, thereby influencing the cooling rate and the subsequent condensation of the vapor into nanoparticles. This precise control over the conditions within the deposition process allows for the fine-tuning of nanoparticle size and distribution [45].

Furthermore, recent research has extended the utility of LVCS to the synthesis of mixed-metal clusters by a dual-target dual-laser vaporization source [46], opening new avenues for the creation of complex nanostructures with novel properties.

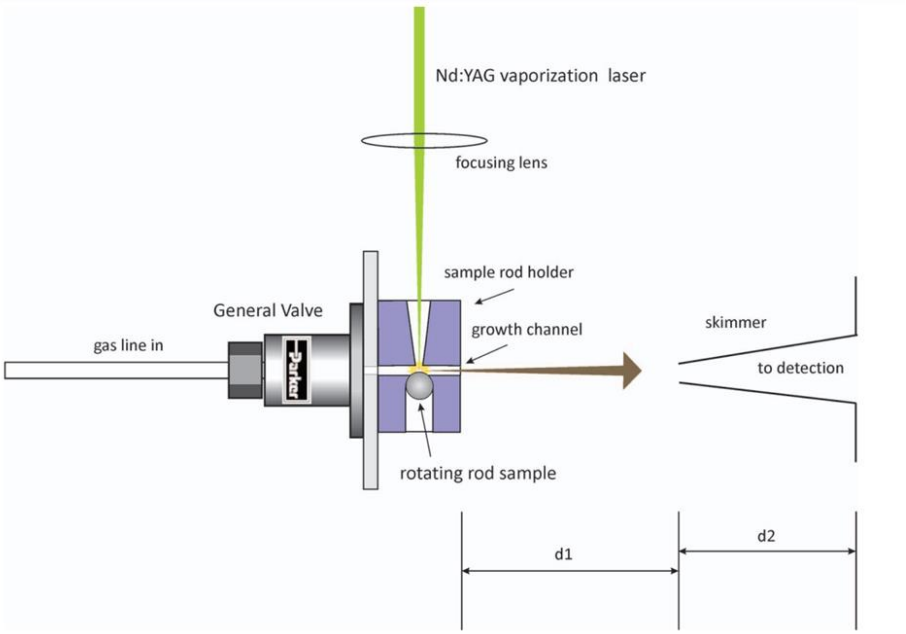

Figure 2.7: Schematic of a Laser Vaporization Cluster Source Setup. This figure illustrates the typical setup for a LVCS operation. It features a high-power laser directed at a target material, with a carrier gas inlet and a supersonic nozzle aligned with the vaporization site. Taken from [45].

2.5.2.2 Magnetron sputtering cluster source

Magnetron sputtering is a plasma-based technology where the process occurs inside a vacuum chamber. In this process, a target material, often a metal or alloy such as gold, silver, or titanium, is sputtered by the application of a high-voltage electric field, creating a plasma of an inert gas (typically Argon). The presence of a magnetic field perpendicular to the electric field increases the efficiency of the ion bombardment process, enhancing the sputtering rate due to longer ionization paths.

The combination of magnetron sputtering technique with gas condensation was reported in 1986 [47] and then further developed by Haberland and co-workers [48] . In gas phase aggregation sources, magnetron sputtering facilitates the formation of nanoparticles through the condensation of vaporized atoms in a controlled environment. The sputtered atoms ejected from the target material migrate through the

inert gas atmosphere and begin to lose energy. Upon reaching supersaturation, these atoms aggregate to form clusters, leading to nanoparticle formation. The process parameters, such as gas pressure, flow rate, and substrate temperature, play critical roles in determining the size, distribution, and morphology of the resulting nanoparticles.

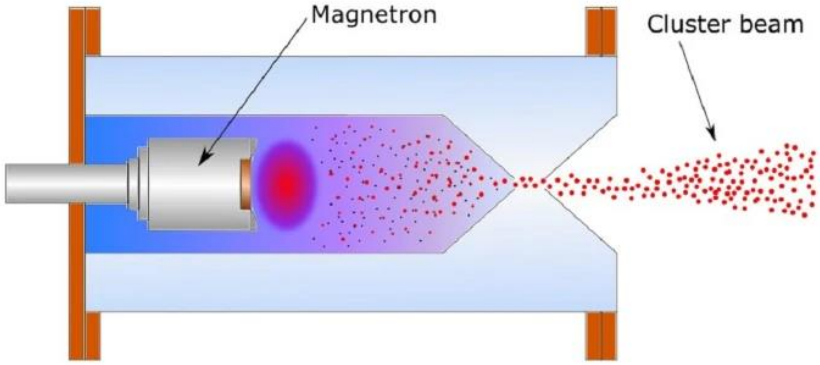

Figure 2.8. Schematic of a cluster beam deposition system integrating a magnetron sputtering cluster source. Taken from [49].

2.5.2.3 Pulsed Microplasma Cluster Source (PMCS)

The pulsed microplasma cluster source (PMCS) is a versatile tool for producing nanoparticles with high efficiency and control. It combines elements of sputtering sources and laser vaporization cluster sources (LVCSs) to overcome the limitations of each [50]. PMCS offers several advantages, including high flexibility in terms of the materials it can process and the ability to produce solvent-free nanoparticles in a vacuum environment [23]. The operational process of PMCS, like most cluster sources, comprises three stages. Initially, the target material is vaporized, followed by the thermalization of the vaporized material with the noble gas to form clusters, and finally, the resulting mixture is expelled from the source.

The PMCS is composed of a ceramic body with a channel drilled through it, intersecting a larger cylindrical cavity perpendicularly. The target rod, which acts as a cathode, is held within this channel and connected to the negative pole of a high-voltage power supply. The anode can be positioned within the cavity or opposite the cathode through the channel. In this PMCS prototype, the anode is located at the

nozzle. A solenoid pulsed valve, responsible for introducing inert carrier gas, is situated on one side of the cavity, while a nozzle is located on the opposite wall.

The valve, backed with a high gas pressure (typically up to 50 bars), releases brief pulses into the source cavity, with opening durations of approximately 200-300 microseconds. Upon valve opening, the substantial pressure differential generates a supersonic gas jet directed toward the cathode. A pulsed voltage of about 50 μs is applied across the electrodes, ionizing the gas to produce plasma. This plasma accelerates toward the cathode, where it ablates material that subsequently thermalizes and condenses to form clusters. The intense pressure gradient near the cathode surface creates aerodynamic confinement of the plasma within the source cavity, focusing the sputtering process to a cathode area of less than 1 mm^2, as confirmed by computational fluid dynamics simulations [51].Given the source cavity volume of approximately 2 cm^3 the internal pressure rises rapidly following each pulse. The pressure difference across the nozzle then propels the aerosol into the adjacent expansion chamber as a supersonic beam.

PMCS offers several advantages over other cluster sources. Its ability to confine the ablation plasma allows for efficient material vaporization and precise control over cluster growth. The pulsed nature of the process also contributes to its stability and reproducibility [52,53] . The size and morphology of the nanoparticles produced by PMCS can be controlled by adjusting various parameters during the synthesis process, such as the type and pressure of the inert gas, the discharge voltage and duration, and the geometry of the source cavity and nozzle.

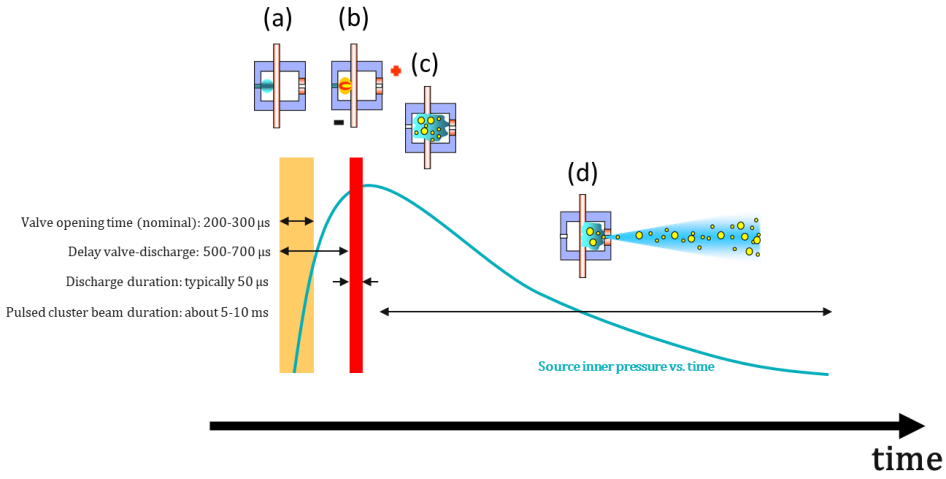

Figure 2.9. Operating principle of Pulsed Microplasma Cluster Source (PMCS). a) a pulse of inert gas is injected into the ceramic source body by a solenoid valve; b) a high-voltage is applied to a pair of electrodes, where the cathode is made of the material of interest (vertical bar) and the anode is the source nozzle, in order to ignite a pulsed electrical discharge; c) atoms are removed from the cathode by ion sputtering and afterwards they thermalize into the inert gas and aggregate in form of atomic clusters; d) driven by the pressure difference between the inner of the source and the vacuum deposition chamber, which the source is exposed to through a nozzle, a gas expansion takes place, carrying the atomic aggregates out of the source within a supersonic molecular beam.

II. EXPERIMENTAL FRAMEWORK AND METHODOLOGIES

CHAPTER 3. SUPERSONIC CLUSTER BEAM DEPOSITION PROTOTYPE

3.1 General design

3.1.1 Main prototype parts

During the first year of this PhD work, Supersonic Cluster Beam Deposition (SCBD) technique was introduced and established at the Luxembourg Institute of Science and Technology (LIST), designed and constructed with the support of the prototype team of LIST. My contributions involved assembling the vacuum system, designing the substrate holder, and implementing the setup for in-situ electrical and thickness measurements. Additionally, I was involved in designing deposition protocols within the graphical user interface (GUI) and participating in the testing of the prototype.

The SCBD system integrates a Pulsed Microplasma Cluster Source (PMCS) directly coupled to a combined expansion and deposition chamber. This design simplifies the apparatus by allowing the supersonic expansion of the cluster beam and its subsequent deposition to occur within the same chamber, thereby reducing system complexity.

The SCBD system comprises five main components, that will be discussed in subsequent sections:

Vacuum System: This system includes the vacuum chamber and a two-stage pumping configuration. The vacuum chamber maintains the ultra-high vacuum (UHV) environment necessary for high-purity deposition. The pumping system consists of a dry pump for achieving rough vacuum levels and a turbo pump to achieve and sustain UHV conditions (10^{-7} mbar).

Graphical User Interface (GUI): The GUI provides centralized control and monitoring, allowing real-time adjustments to parameters such as vacuum pressure and substrate positioning. The GUI also allows the recording of measurement protocols such as thickness by QCM, electrical measurements, time and pressure.

Cluster Source: The PMCS is employed to produce atomic clusters and is coupled to the vacuum chamber. The source includes a pulsed valve for precise gas input, a power supply to regulate voltage discharge, and aerodynamic lenses that filter and collimate the cluster beam for focused deposition.

Deposition Chamber: Serving as both the expansion and deposition area, the chamber houses the sample holder and manipulators for precise substrate positioning, facilitating customizable film deposition patterns and thickness control under UHV conditions.

3.1.2 Vacuum system

The SCBD prototype was assembled using a Kurt J. Lesker standard box vacuum chamber, built from 304 stainless steel with an aluminum door, ensuring a clean and durable environment suitable for high and ultra-high vacuum (UHV) conditions. The door is sealed with an FKM O-ring fitted into a dovetail groove, providing an effective vacuum seal essential for maintaining UHV. A rectangular viewport on the door allows for visual monitoring while maintaining UHV conditions.

A two-stage vacuum pumping system was installed to ensure optimal operating conditions. The initial vacuum was achieved using a Leybold ECODRY 35 plus dry pump, capable of delivering 35 m^3/h to establish a rough vacuum. Subsequently, a Leybold MAG W 1300 iP turbo pump, with a pumping speed of 1300 l/s, escalates the vacuum to UHV levels down to 10^{-7} mbar. This dual-stage approach minimizes residual gas presence, essential for high-purity cluster deposition.

The chamber is equipped with a rectangular viewport and multiple feedthroughs, accommodating the integration of pressure gauges, gas inlets and other instrumentation. These components are essential for real-time monitoring and control during the deposition process, ensuring precise manipulation of internal conditions.

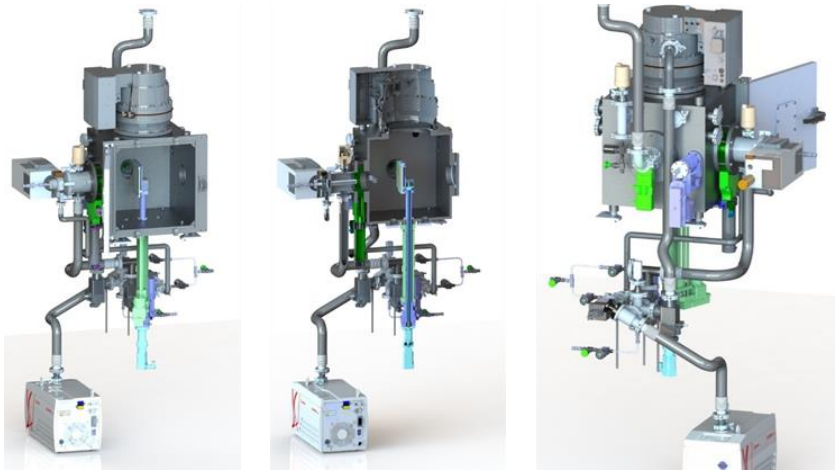

Figure 3.1. Rendering of the SCBD, illustrating the main components, including stainless steel vacuum chamber, two-stage vacuum pumping, cluster source, pulsed gas inlet, aerodynamic lenses, and a motorized substrate manipulator.

3.1.3 Graphical user interface (GUI)

The system's graphical user interface (GUI) serves as a control platform, enabling management and monitoring of the cluster beam deposition process. Key features include:

Monitoring Pumping Sequences: The GUI allows precise control over the pumping sequences, including automated venting and pumping cycles, ensuring safe and effective chamber pressure monitoring.

Rastering Protocols for Deposition: The interface enables programming of rastering patterns for substrate coverage, allowing users to define specific deposition areas and scan speeds. This feature is important for achieving uniform film thickness and desired coverage area. Additionally, the GUI allows users to record measurement protocols, including thickness by QCM, electrical measurements, and both time and pressure data, into a file.

Motor Control: The GUI provides detailed motor control for the motorized substrate manipulator, allowing for precise adjustments in substrate position and rotation for

deposition monitoring. This also enables accurate alignment and movement of the substrate relative to the cluster beam during deposition.

Turbo Pump Monitoring: Real-time monitoring of the turbo pump's parameters, such as rotational speed, temperature, and pressure levels, is available through the GUI.

Maintenance Protocols: The GUI includes a maintenance protocol that blocks the operation power supply. Also, a source venting protocol is included for the maintenance and replacement of a new precursor material.

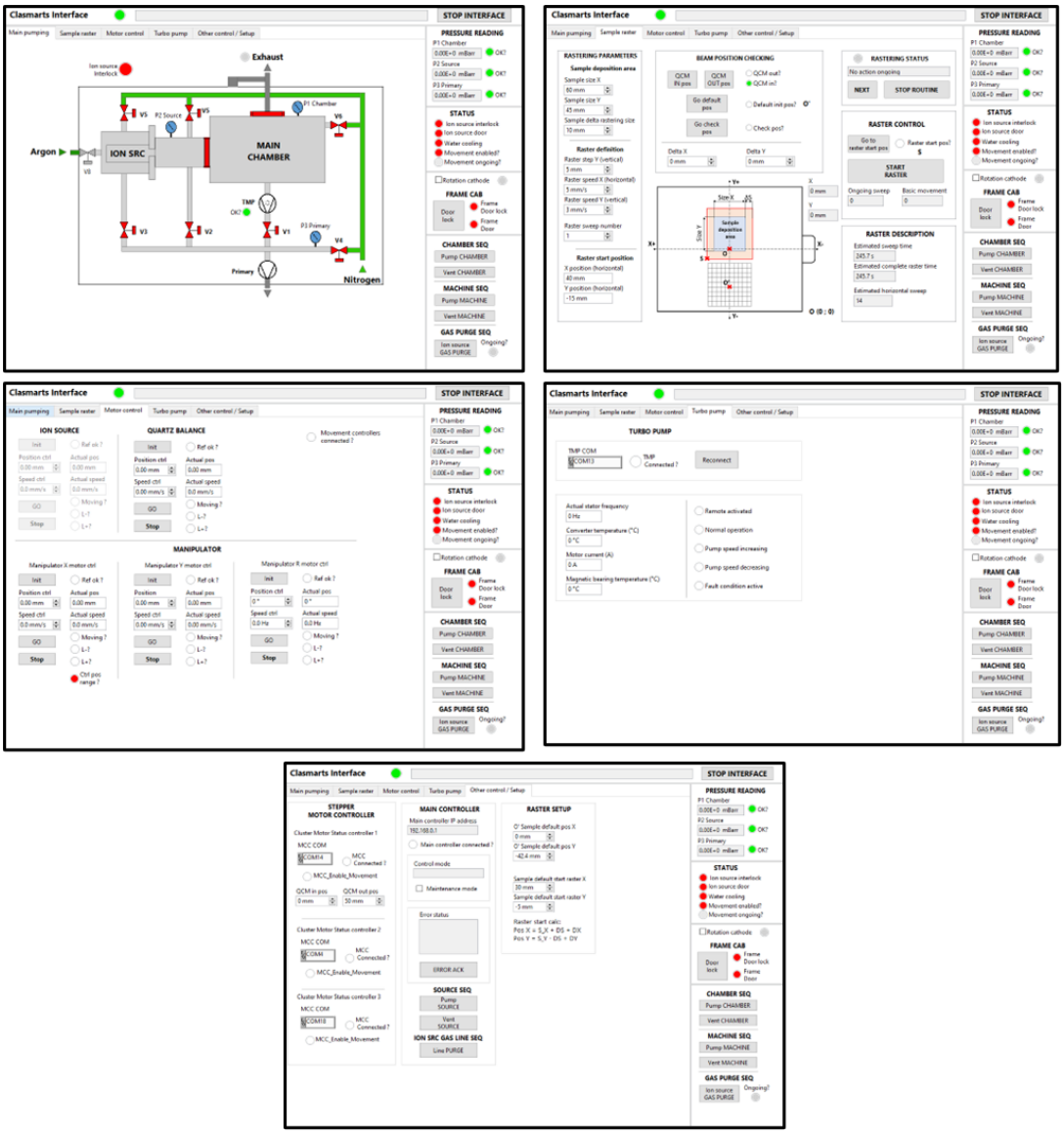

Figure 3.2. Screenshots of the main protocols included in the GUI or the SCBD system, providing control and monitoring over vacuum levels, substrate positioning and rastering protocols, maintenance protocols and real-time monitoring and data recording of thickness by QCM and current by electrometer. Screenshots of the Graphical User Interface (GUI) SCBD system, illustrating control and monitoring capabilities over vacuum levels, substrate positioning and rastering protocols, maintenance protocols, and real-time data recording of film thickness by QCM and current measurements using an electrometer.

3.2 Cluster Source

3.2.1 PMCS design

The Plasma Microplasma Cluster Source (PMCS) used in this thesis was designed to enable controlled production of atomic clusters by leveraging plasma ablation and supersonic expansion techniques, as detailed in Section 2.5.2.3 and previous studies. The primary components of the PMCS, as illustrated in Figure 3.3 and Figure 3.4, include:

High-Pressure Gas Inlet and Pulsed Valve: This assembly introduces inert gas (e.g., helium or argon) into the source cavity at pressures up to 50 bars. The pulsed valve operates with opening durations of approximately 200–300 microseconds, allowing precise control over gas pulses.

Source Cavity: A confined chamber (~2cm^3) where the injected gas forms a supersonic jet directed toward the cathode. The cavity's design ensures efficient gas flow and plasma formation.

Cathode and Anode Electrodes: The cathode, composed of the target material for cluster formation, and the anode are positioned within the source cavity. A pulsed voltage (typically 50 μs) applied between these electrodes ionizes the gas, generating plasma that ablates material from the cathode.

Nozzle: Located at the exit of the source cavity, the nozzle facilitates the supersonic expansion of the gas and ablated material into the expansion chamber. The nozzle's geometry is critical for controlling the cluster beam's characteristics. An aerodynamic lens system is employed to filter and focus the cluster beam, enhancing deposition precision on substrates.

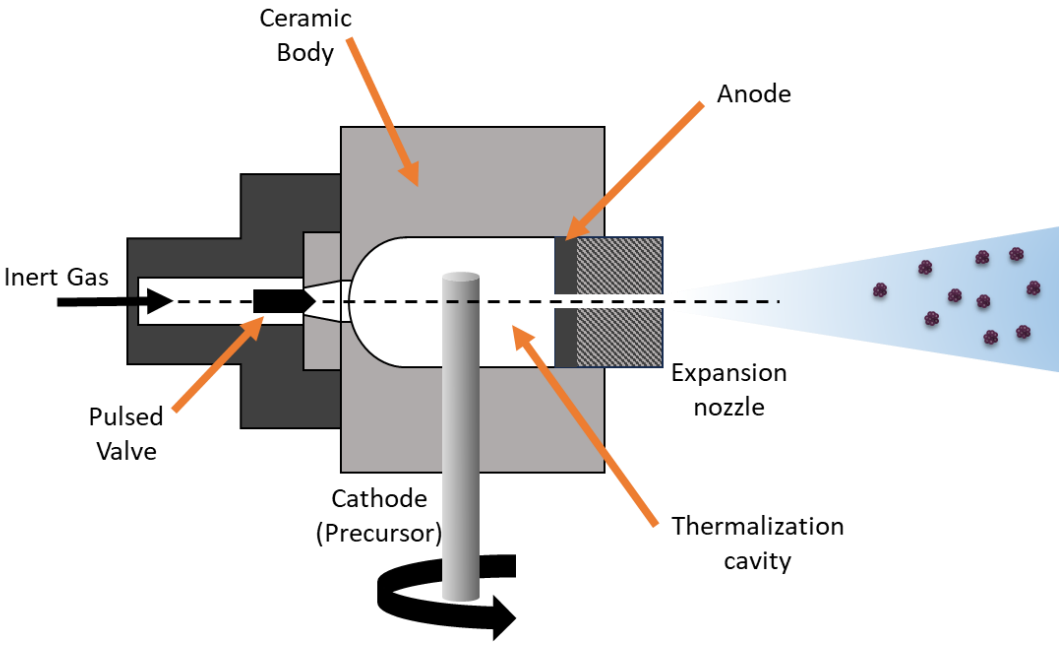

Figure 3.3. Schematic of the Pulsed Microplasma Cluster Source (PMCS) used for cluster production during my PhD work, illustrating its key components: (1) high-pressure gas inlet and pulsed valve for precise gas delivery; (2) source cavity where gas ionization and plasma generation occur; (3) cathode and anode electrodes; and (4) nozzle enabling supersonic expansion of the gas and ablated material Adapted from [50].

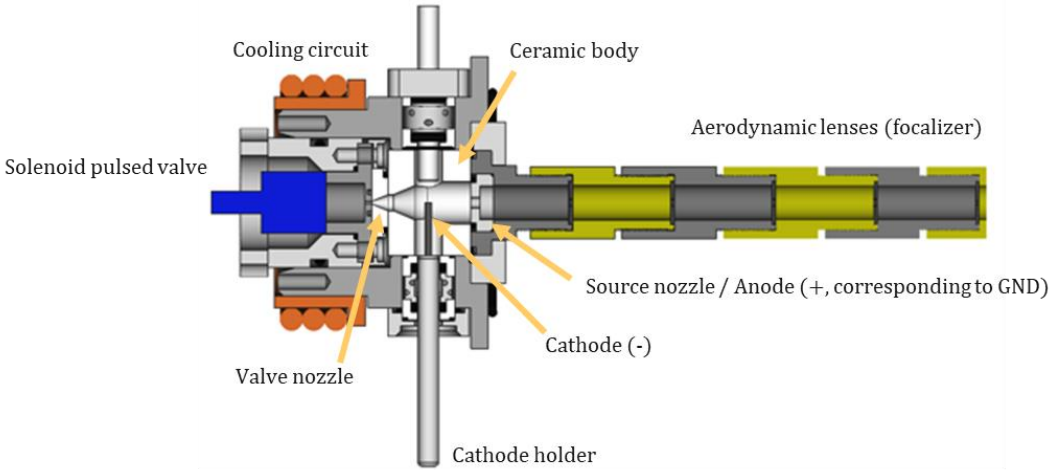

Figure 3.4. Detail of the PMCS (sectioned). Solenoid pulsed valve for gas injection; cathode (precursor material); cluster condensation cavity drilled in the ceramic body of the source; Source nozzle; aerodynamic lens system; water-cooling system.

3.2.2 Pulsed valve

In the PMCS, the solenoid-operated pulsed valve (General Valve Series 9) plays a critical role in controlling the precise delivery of inert gas into the condensation chamber. The valve is backed by a high-pressure gas supply (typically up to 50 bar), and its controlled bursts of gas create a supersonic jet that facilitates the rapid vaporization of the material in a well localized area of the cathode.

The valve, schematically shown in Figure 3.5, operates via electromagnetic actuation: when the coil assembly is energized, it generates a magnetic field that lifts the armature assembly and poppet, allowing gas flow into the chamber. Synchronization with the plasma discharge ensures precise timing of gas injection, which is essential for creating the optimal conditions for cluster formation. Once the coil is de-energized, the main spring and buffer spring return the poppet to its closed position, sealing the valve and stopping the gas flow.

Typical pulse durations range from a few hundred microseconds, carefully timed to synchronize with the electrical discharge. The pulse frequency, often set between 1 and 10 Hz, governs the rate of gas injection and cluster production. The O-ring ensures a tight seal, preventing gas leakage, while the stainless-steel construction allows the valve to withstand the high pressures and temperatures common in PMCS environments.

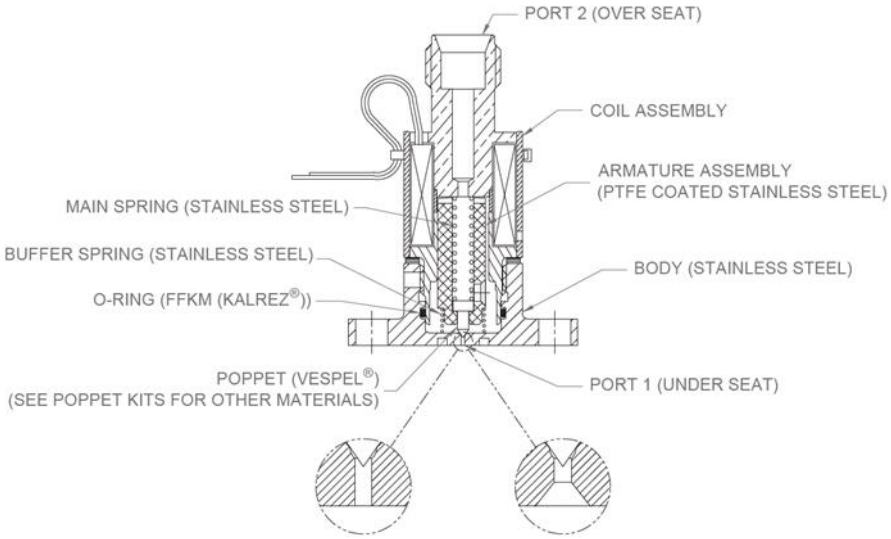

Figure 3.5. Cross-sectional diagram of the solenoid-operated pulsed valve used in the PMCS. The solenoid energizes to lift the poppet, allowing inert gas flow for precise control in cluster formation processes.

3.2.3 Power supply

The PMCS power supply (Figure 3.6) was designed to deliver controlled, high-voltage (500-800V) pulses for plasma generation. The power supply operates with resistors R1 (1 Ω, 1–2 kW) and R2 (5–10x R1, 300 W)** to limit the current between the cathode and anode. The cathode is connected through R1 to control the plasma current, while the anode is grounded to the vacuum chamber to maintain electrical stability.

In addition, external TTL (transistor-transistor logic) signals manage external events, such as triggering the pulsed valve. These signals, connected to the power supply's control ports, provide precise timing for both electrical pulses and gas flow, which is crucial for synchronizing the system. This configuration ensures effective control over plasma discharge and material ablation in the PMCS.

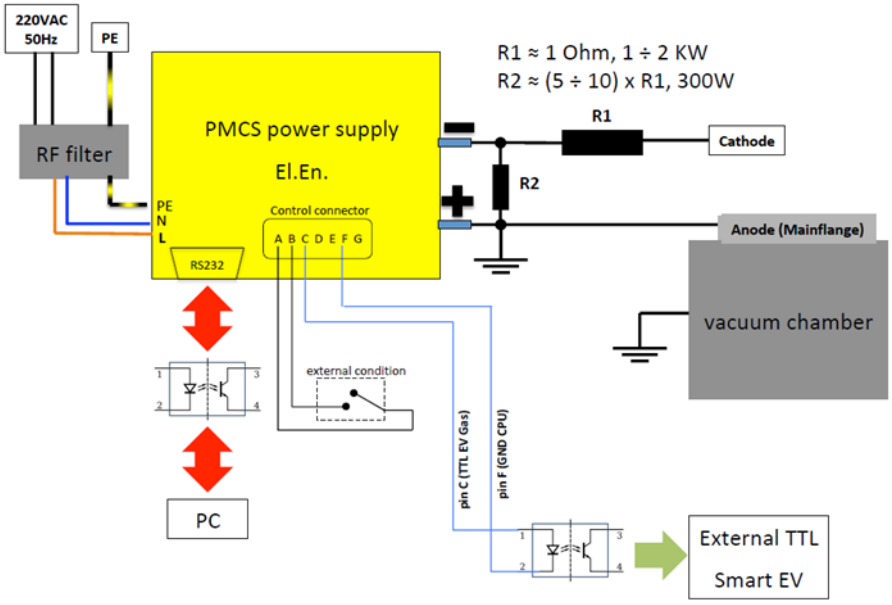

Figure 3.6. Diagram power supply employed in the PMCS.

3.2.4 Aerodynamic Lenses

Due to the stochastic nature of the cluster formation process, the resulting nanoparticle beam often exhibits a broad size distribution. To address this, aerodynamic size selection and focusing techniques derived from aerosol science can be employed prior to the supersonic expansion in vacuum, refining the nanoparticle beam and achieving a narrower size distribution.

A common method for achieving size selection is using an aerodynamic lens system [54]. Aerodynamic size selection is based on the principle that particles with different sizes and masses will respond differently to the drag forces exerted by a gas flow [23]. In a gas flow, larger particles tend to maintain their initial trajectories due to their higher inertia, while smaller particles are more easily deflected by the gas flow. This phenomenon is illustrated in Figure 3.7 a) and b), where the trajectories of 15 nm particles are simulated for different distances from the inlet. As the distance increases, the smaller particles are increasingly deflected away from the central axis.

This size-dependent deflection can be manipulated to separate particles based on their size by using aerodynamic lenses. Aerodynamic lenses consist of a series of axisymmetric contractions and enlargements of the aerosol flow passage. By adjusting

the geometry and operating conditions of the aerodynamic lens, it is possible to select a specific size range of nanoparticles and focus them into a narrow, collimated beam.

The parameter governing particle size selection in an aerodynamic lens is the Stokes number (St), a dimensionless parameter that relates the particle's response time to the characteristic time of the flow, which influences particle trajectories, as shown in Figure 3.7 c). The inertia of large particles ($St \gg 1$) exceeds the drag action of the gas streamlines that leads to their deposition on the walls of the lens. Very small particles ($St \ll 1$) closely follow the flow of the gas and become trapped in the vortices. Thus, intermediate-size particles with $St \sim 1$ have trajectories that are only slightly decoupled from the streamlines, allowing them to join the central beam and pass through a set of lenses.

The use of aerodynamic size selection and focusing in PMCS (Figure 3.4) offers several advantages. It allows for the production of nanoparticle beams with a narrower size distribution, which is important for many applications where precise control over particle size is required.

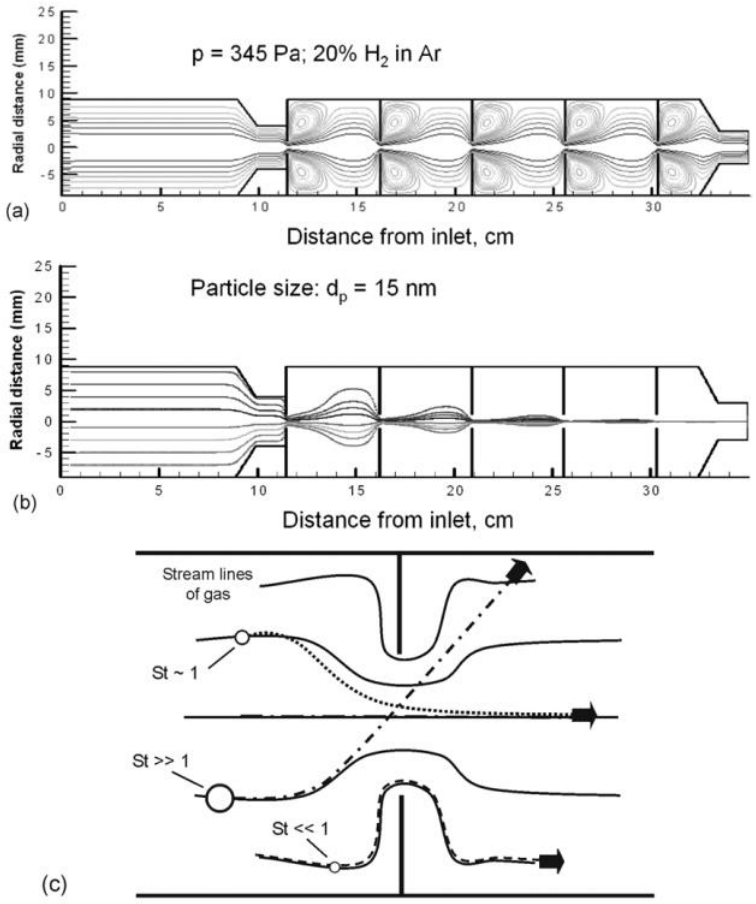

Figure 3.7. Simulation of the gas flow (a) and trajectories of 15 nm particles (b) in an aerodynamic lens system according to Gidwani and Di Fonzo et al. [55,56]. The particles are concentrated at the centre axis of the lens system, forming a beam. (c) basic principle of aerodynamic size-selection and focusing. Large particles, with high inertia ($S_t \gg 1$), deviate from the gas streamlines due to their greater inertia and tend to deposit on wall surfaces. Very small particles ($S_t \ll 1$) closely follow the gas flow. Particles of intermediate size have trajectories that only partially separate from the streamlines, allowing them to be concentrated at specific positions within the flow field [57,58]. Taken from [23].

3.3 Deposition chamber

3.3.1 Sample holder

The SCBD prototype employs a specialized deposition chamber engineered for precise and controlled film growth. Within this chamber, the cluster beam generated by the PMC is intercepted by a custom-designed sample holder (Figure 3.8 and Figure 3.9), where I contributed to the design and assembly. This holder accommodates various

substrates, including silicon wafers, interdigitated electrodes, and transmission electron microscopy (TEM) grids, allowing for flexible experimental configurations. Moreover, two quartz crystal microbalance (QCM) is integrated into the chamber QCM 1 which serves as sensor for materials deposition after maintenance of the source. The QCM 2 is integrated into the holder setup to provide continuous in-situ monitoring of the deposited material, enabling real-time measurement of nominal thickness and deposition rates. Additionally, a positioning grid for precise beam alignment after PMCS maintenance is included in the setup.

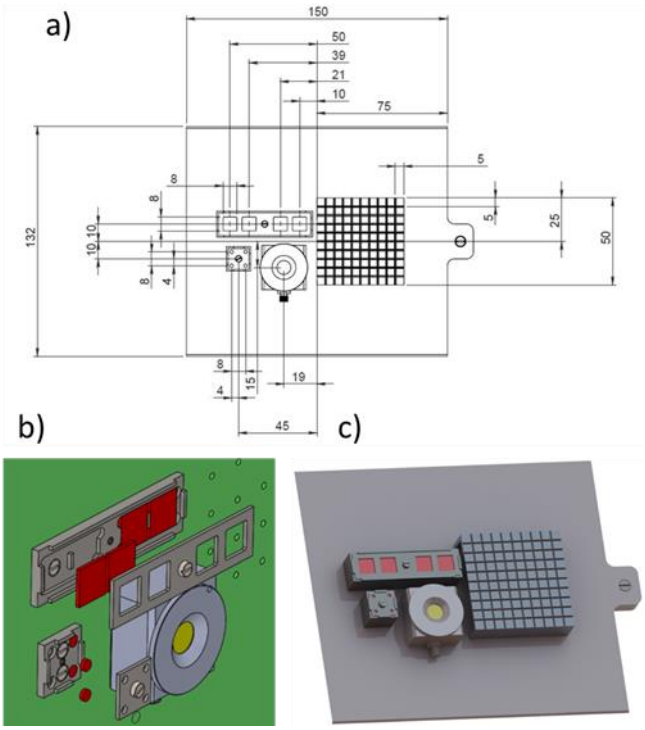

Figure 3.8. Design and assembly of the substrate holder for cluster beam deposition experiments. (a) Technical drawing of the substrate holder, showing the layout and dimensions of the substrate holder components. (b) Exploded view showing individual components, highlighting the modular design for easy assembly and customization. (c) Assembled 3D model of the substrate holder, illustrating the arrangement of components, including the positioning grid for precise beam alignment after PMCS maintenance.

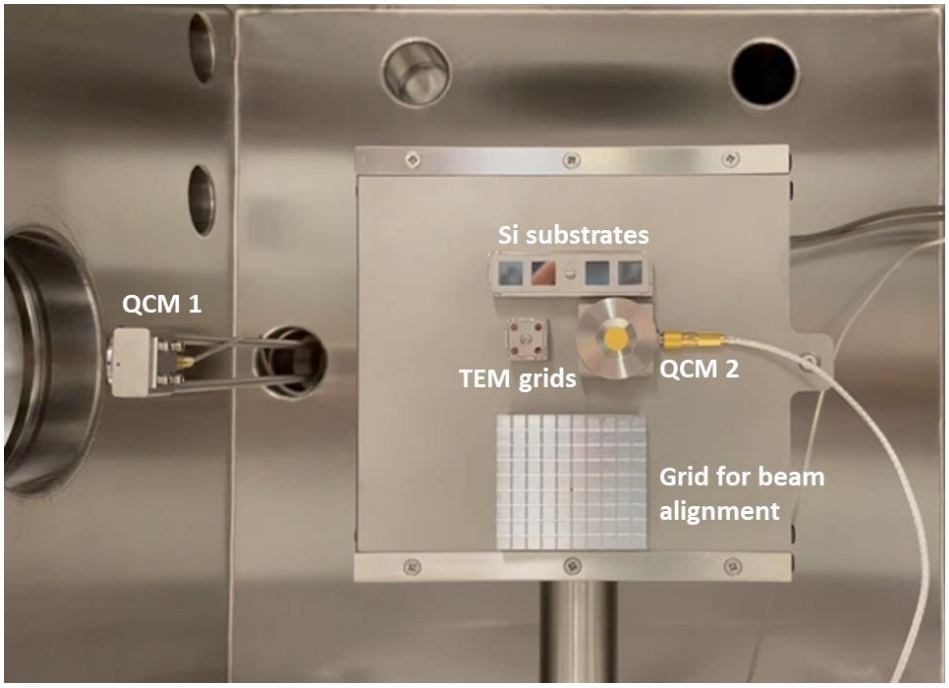

Figure 3.9. Picture of the custom-designed substrate holder within the SCBD chamber in view mode (90°), accommodating various substrates—including silicon wafers, interdigitated electrodes, and TEM grids—and integrating a quartz crystal microbalance (QCM2) for real-time monitoring of film deposition. QCM1 serves as a deposition sensor after maintenance of the PMCS.

3.3.2 Motorized manipulator

To ensure uniform film growth and enable the deposition of films over larger areas, the sample holder is equipped with two automated manipulators driven by stepper motors. One of these manipulators enable precise movement of the sample holder within the plane perpendicular to the cluster beam (along x and y axes). The second manipulator facilitates 90° rotation of the sample holder around its central axis. This rotation capability allows for the intermittent monitoring of the deposition process through a viewport integrated into the chamber as well as for beam alignment after maintenance of the PMCS.

By coordinating the movement of these manipulators during the deposition process, a rastering protocol can be implemented. This protocol, controlled by a custom LabVIEW program, involves the systematic and controlled movement of the sample

holder in a predefined pattern, effectively extending the deposition area beyond the dimensions of the cluster beam itself (Figure 3.10) up to 10 cm^2. This capability is important for depositing films onto substrates arranged in a linear configuration where the individual substrate dimensions must not exceed the beam diameter. Moreover, the implemented manipulators allow for the deposition of films onto large-area substrates by employing an appropriate 2D rastering protocol, which can be customized based on the desired coverage area.

The rastering speed and the distance between adjacent raster lines can be adjusted to control the film thickness and uniformity. In this work, the rastering speed was set to 5 mm/s, and the distance between raster lines was typically set 1 cm.

The integration of automated manipulators and the implementation of rastering protocols within the deposition chamber enhances the versatility and capabilities of the SCBD prototype, enabling the deposition of uniform cluster films onto a wide range of substrate configurations and sizes, from small TEM grids to substrates of larger area in comparison with the size of the beam.

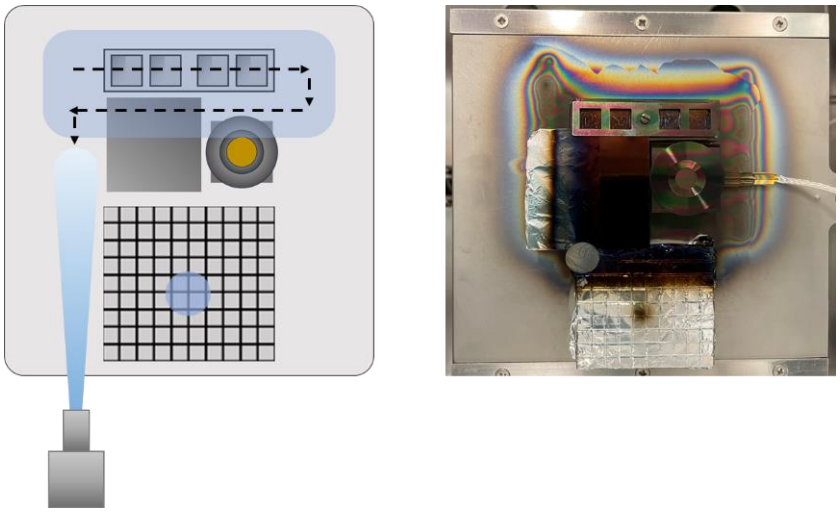

Figure 3.10. Rastering protocol for large-area deposition. The cluster beam is intercepted by the sample holder, which can move along the reference axes x and y. By horizontally moving the holder with incremental vertical steps, films can be deposited over areas up

to 10 cm^2. The GUI records in real time the amount of deposited material measured by the QCM as “bulk equivalent thickness”.

CHAPTER 4. MEASUREMENTS AND CHARACTERIZATIONS METHODS

4.1 In-situ electrical measurements

4.1.1 Interdigitated electrode's characteristics

The Interdigitated Electrodes (IDEs) used in this study were patterned by standard photography and lift-off process on 8-inch 500 µm thick Borofloat33 glass wafers. IDEs consist of 10 pairs of 100 µm width and 4 mm length fingers with 100 µm spacing. IDEs are connected to 5×5 mm² large contact pads. A set of 112 IDEs were patterned per wafer (Figure 4.1).

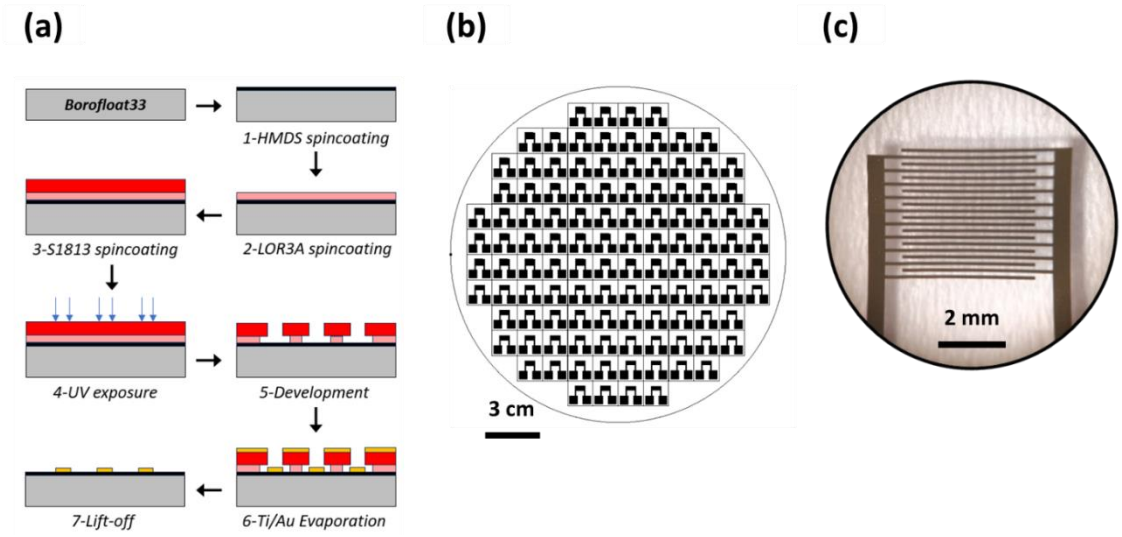

Figure 4.1 (a) IDEs patterning flow chart. (b) Design of the 112 IDE chips on 8-inch borofloat33 wafer. (c) picture of a single IDE.

HMDS adhesion promoter was first spincoated to enhance the adhesion of photoresists to glass. A LOR3A (Kayaku AM) / Shipley 1813 (Dow) photoresist bilayer was then spincoated, with respective thickness of 300 nm and 1.3 µm. The exposure was performed with an MLA 150 (Heidelberg Instruments GmbH) with a 375 nm laser wavelength and 84 mJ/cm² exposure density. Patterns where subsequently developed with MF319 developer (Dow). Titanium 15 nm / gold 200 nm layers were then

evaporated on top of the resist mask by e-beam evaporation (MEB 600HV, Plassys Bestek) with respective rates of 0.1 nm/s and 0.2 nm/s. The lift-off was performed with Remover PG (Kayaku AM) solvent, leading to the gold interdigitated electrodes and contact pads. Finally, 112 chips of 15×15 mm² containing single IDE were diced with a DAD 3350 saw (DISCO).

4.1.2 Setup for in-situ electrical and thickness measurements

In-situ electrical conduction analysis in correlation to deposited thickness is carried out logging current measurement from Picoammeter Keithley 6487 and thickness from the Quartz Crystal Microbalance Inficon SQM-160. Thanks to a fully motorized sample holder (2 translation axis), the Interdigitated Electrodes and the QCM detector (positioned side by side) are exposed to the cluster beam repeatedly. The overall setup of the electrical measurement is described in Figure 4.2.

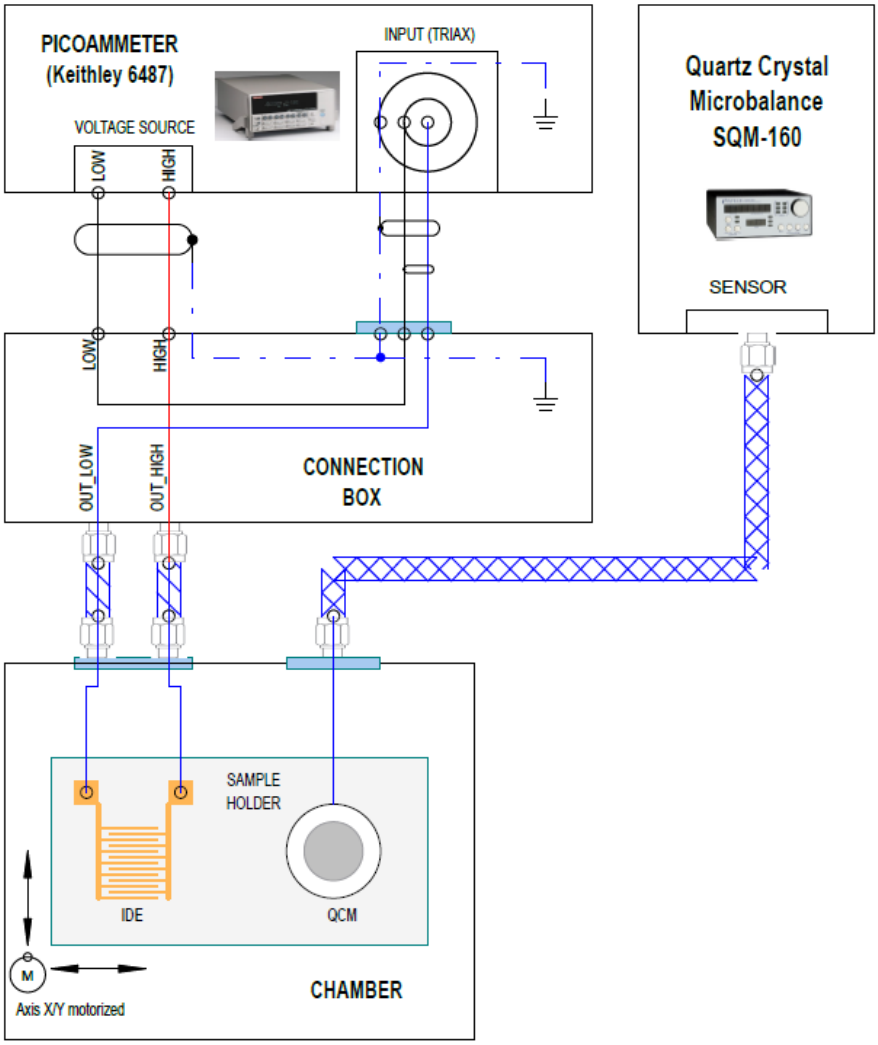

Figure 4.2: Schematic of the experimental setup for in-situ measurement of electrical conduction and deposited thickness.

Cables for the electrical measurement are shielded to the ground starting from the picoammeter. Inside the deposition chamber, electrical connections to the IDE are left ungrounded in the very last part, as shown in Figure 4.3.

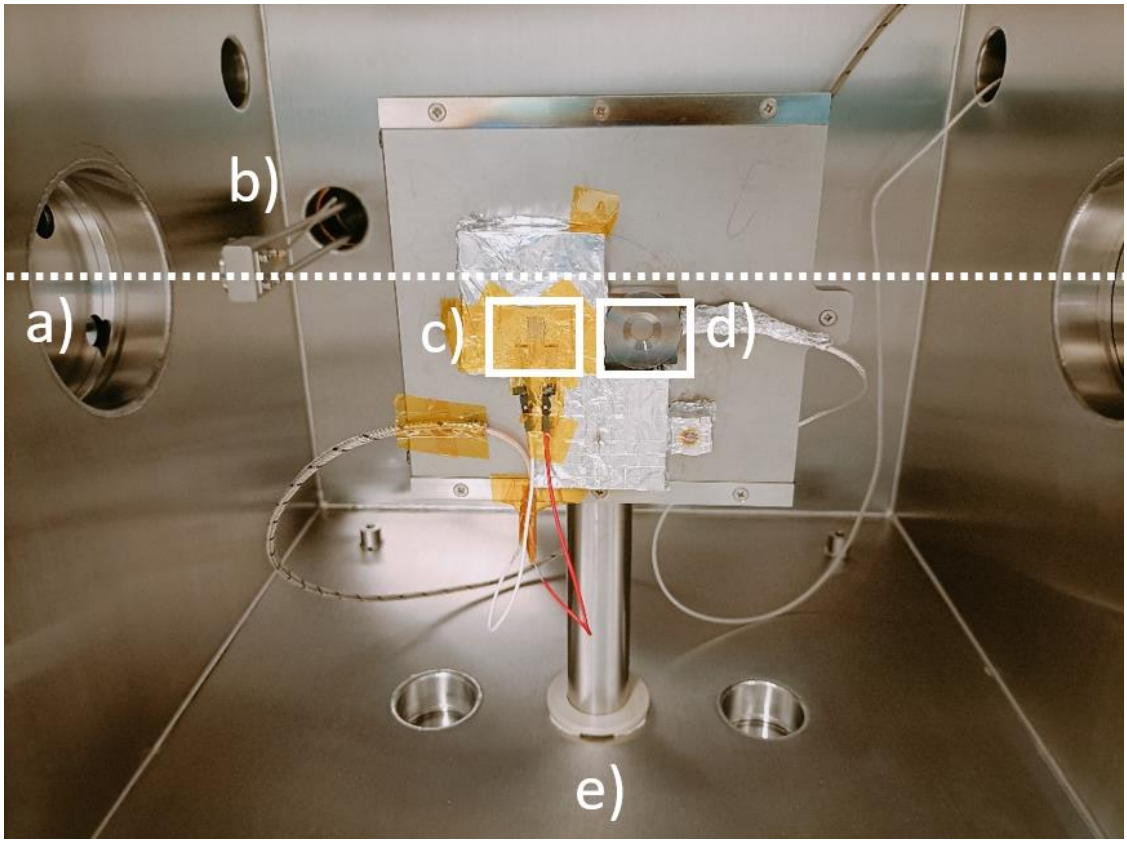

Figure 4.3: Internal view of the deposition chamber, showing the measurement setup: a) point of entrance of the cluster beam (dotted line shows beam axis); b) control QCM; c) IDE; d) main QCM; e) rotating support of the motorized sample holder (here anticlockwise rotated of 90° with respect to measurement position).

4.1.3 Experimental protocol for in-situ measurements

The process parameters of the PMCS used to produce the cluster-assembled films in this study were optimized according to the physical properties of the precursor materials, as detailed in Table 1. The base pressure in the deposition chamber was maintained at 1×10^{-7} mbar.

Specific adjustments were required for tin to prevent deformation of the tin rod during the deposition process. The pulse voltage and duration were set at the low-side limit of values allowed by the technique, and the diameter of the tin rod was increased to 3 mm, compared to the typical 2 mm diameter used for the other materials. Furthermore, the frequency (or repetition rate) was adjusted to tune the deposition rate.

For tungsten, a refractory metal characterized by a high melting point, the pulse voltage was increased to the maximum operational limits of the PMCS to ensure a sufficient sputter yield.

Table 1. Process parameters employed in the PMCS.

Material	**Carrier gas at 40 bar**	**Discharge voltage (V)**	**Pulse duration (μs)**	**Repetition rate (Hz)**
Sn (99.99% purity, Goodfellow)	Ne (Messer, 6.0)	500	30	2-4
Ni (99.99% purity, Goodfellow)	Ar (Messer, 6.0)	500	50	2-4
Pt (99.99% purity, Goodfellow)	Ar (Messer, 6.0)	500	50	2-4
W (99.99% purity, Goodfellow)	Ar (Messer, 6.0)	800	50	2-4

In PMCS operative conditions, the conversion of stagnation state enthalpy to beam kinetic energy during supersonic expansion of Neon and Argon determines a final velocity of about 900 m/s and 650 m/s respectively [29]. Sn Clusters at such velocity have a kinetic energy of 0.5 eV/atom, Pt and W clusters a kinetic energy of 0.4 eV/atom, and Ni clusters a kinetic energy of 0.12 eV/atom. These values must be considered as an upper limit, due to slipping effect occurring in seeded supersonic beams [29]. Silicon squares 1 x1 cm^2 and carbon coated TEM copper grids (200 mesh, Agar Scientific) were used as substrates for morphological characterization. The deposition process takes place at room temperature.

IDEs were connected to a picoammeter (Keithley 6487) operating with voltage bias of 10 mV. Such voltage value was intentionally chosen to prevent phenomena known as Electric Field Induced Evaporation (EFIE) and Electric Field Induced Surface Diffusion (EFISD) occurring at low film coverages during film growth [59,60] .

To establish a correlation between electrical conduction and thickness during film growth, I utilized a QCM beside the IDE, both mounted onto a custom-designed motorized sample holder, as described in [11]. A rastering protocol was implemented according to which IDE and QCM are repeatedly exposed to the cluster beam in such a way that both collect the same amount of material during each sweep [Figure 4.4a]. It is worth noting that QCM measures the deposited mass over detector area and, assuming the bulk density for the material, converts it to a thickness value. However, the real thickness of non-compact films, such as those ones formed in SCBD experiments, is higher than the values shown by the microbalance due to their lower density compared to the bulk material. To avoid misleading use of the word “thickness”, we will refer to QCM measurements as the "bulk equivalent thickness".

Figure 4.4b shows an example of raw data (corresponding to Sn), namely electrical current across IDE and thickness deposited onto QCM, where the stepwise trend of both current and thickness depends on repeating movements (rastering) of the sample holder hosting IDE and QCM, in front of the cluster beam. Cross correlation data are then progressively generated at the end of each sweep (Section 6.2).

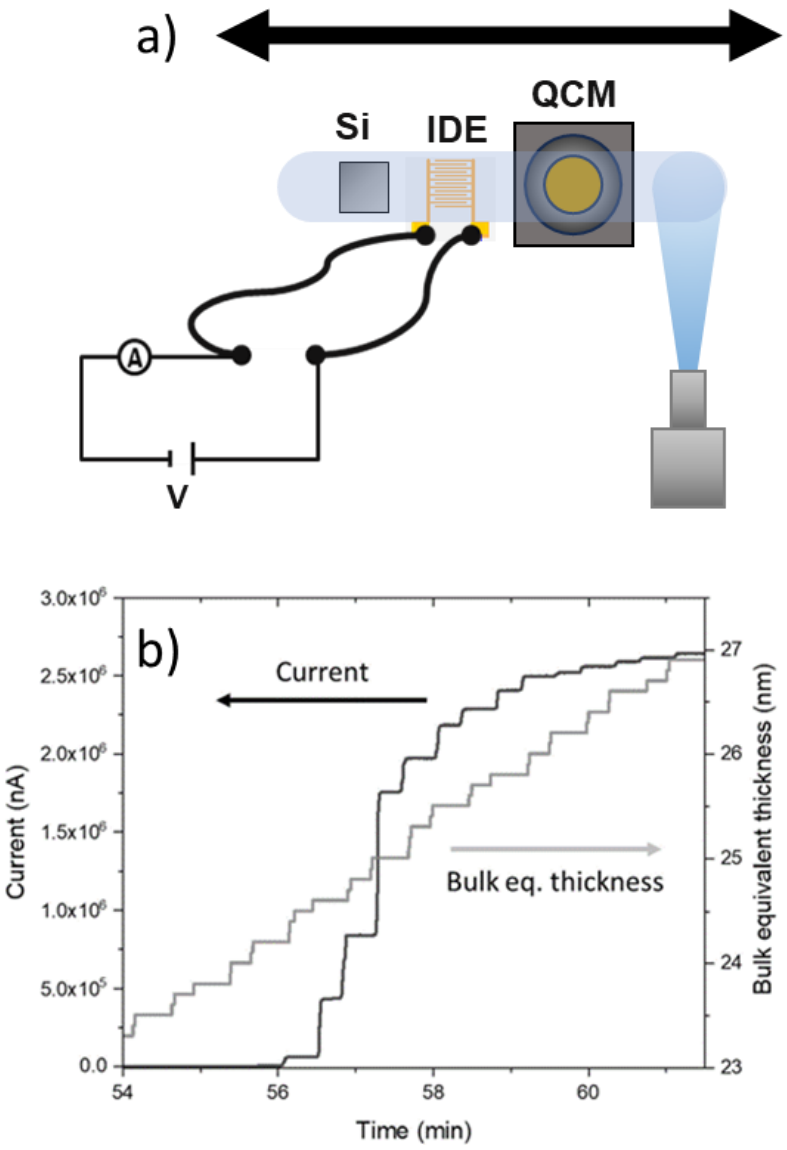

Figure 4.4. Experimental setup (a) to correlate the electrical conduction and thickness during film growth. IDE and QCM are repeatedly exposed to the cluster beam in such a way that both collect the same amount of material during each sweep. (b) Example of raw date corresponding to Sn, where the stepwise trend of both current and thickness depends on repeating movements (rastering) of the sample holder hosting IDE and QCM, in front of the cluster beam.

4.2 Ex-situ characterizations

4.2.1 Transmission electron microscopy (TEM)

The working principle of TEM is fundamentally similar to that of a light microscope; however, it employs electrons instead of photons to illuminate the specimen. The shorter wavelength of electrons, governed by the de Broglie equation ($\lambda = h/p$, where λ is the wavelength, h is Planck's constant, and p is the momentum), enables a substantially higher resolution down to a level of several Angstroms (~ 0.19 nm) [61,62].

Figure 4.5 illustrates the main components and the electron beam trajectory in a TEM instrument. The process begins with an electron gun, typically a tungsten filament (thermionic emission) or a field emission gun, which generates a stream of electrons [63]. These electrons are accelerated by a high voltage (typically 100-300 kV) towards the anode, creating a focused electron beam. The acceleration voltage can be modulated to control the electron energy and penetration depth, thereby influencing the image resolution and contrast [64].

The condenser lens system then focuses the electron beam onto the specimen, which is prepared as an ultrathin section or a dispersion on a support grid. As the electron beam interacts with the specimen, some electrons are transmitted through while others are scattered or absorbed, depending on the thickness and composition of the material. The degree of scattering depends on the atomic number of the elements present in the specimen, with heavier elements scattering more strongly. The scattered electrons can be further categorized into elastically scattered electrons, which retain their energy but change direction, and inelastically scattered electrons, which lose energy due to interactions with the specimen.

The transmitted and scattered electrons are then collected and processed to form different types of images. In bright-field (BF) imaging, the transmitted electrons are used to create an image that reveals the internal structure of the specimen. In dark-field (DF) imaging, only the scattered electrons contribute to the image, highlighting specific features or defects in the specimen [62,64].

The transmitted electrons pass through an objective aperture, which controls the contrast and resolution of the image, and then through a series of intermediate and

projector lenses. These lenses magnify the electron image and project it onto a fluorescent screen or a digital camera for visualization and recording.

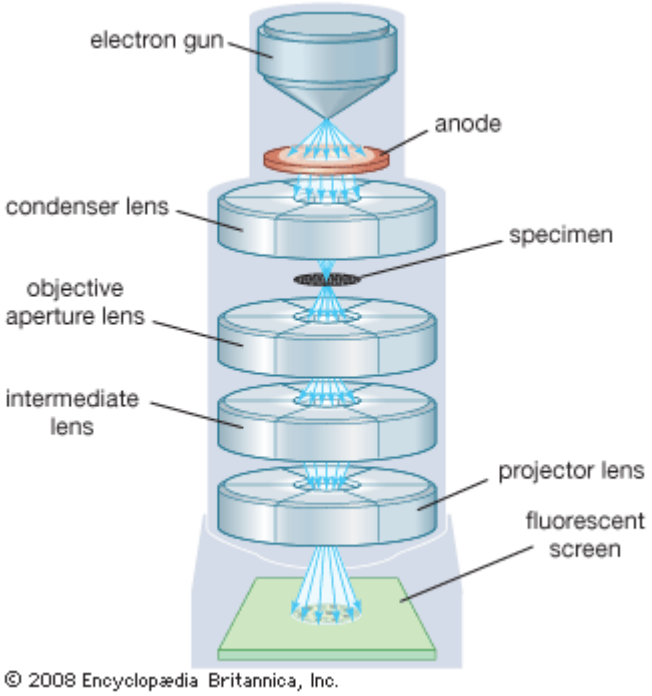

Figure 4.5: Schematic diagram illustrating the main components and electron beam path in a Transmission Electron Microscope (TEM). The transmitted and scattered electrons are then collected and magnified by objective, intermediate, and projector lenses to form an image on a fluorescent screen or a digital camera. Adapted from [65].

The overall morphology of the material at the nanoscale was characterized by Transmission Electron Microscopy (TEM) using a JEOL JEM-F200 cold FEG microscope operating at an acceleration voltage of 200 kV. Crystalline nanostructures were analyzed by direct spacing measurements on High-Resolution TEM (HRTEM) images as well as by Selected Area Electron Diffraction (SAED) using Digital Micrograph Software from Gatan (version v.3.50.3584.0) and D. Mitchell's script DiffTools.

Elemental mapping was obtained by X-ray Energy Dispersive Spectroscopy (EDS-X) in Scanning Transmission Electron Microscopy (STEM) mode.

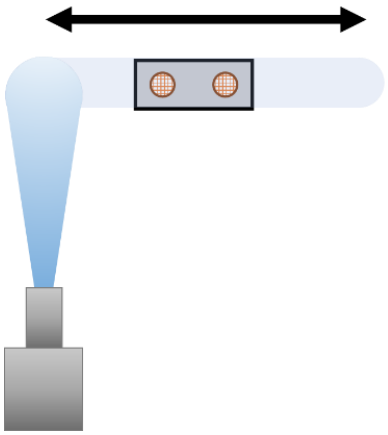

Figure 4.6. Protocol employed for the deposition of sub monolayer regime samples, where rastering protocol was monitored in parallel with the QCM in order to correlate the amount of deposited material with the coverage.

4.2.2 Atomic force microscopy (AFM)

Atomic Force Microscopy (AFM) is a high-resolution type of scanning probe microscopy that operates by scanning a cantilever with a sharp tip over the sample surface. The deflection of the cantilever, caused by interactions between the tip and the sample, is measured using a laser beam reflected from the top of the cantilever into a position-sensitive photodetector (Figure 4.7a). The deflection data is used to generate a topographical map of the surface. There are three primary modes of AFM operation: contact mode, tapping mode, and non-contact mode, each providing unique insights into the surface properties [66].

The fundamental relationship in AFM involves Hooke's Law, which relates the cantilever deflection to the force applied:

$$F = -kz \tag{4.1}$$

Where:

F is the force between the tip and the sample.

k is the spring constant of the cantilever.

z is the deflection of the cantilever.

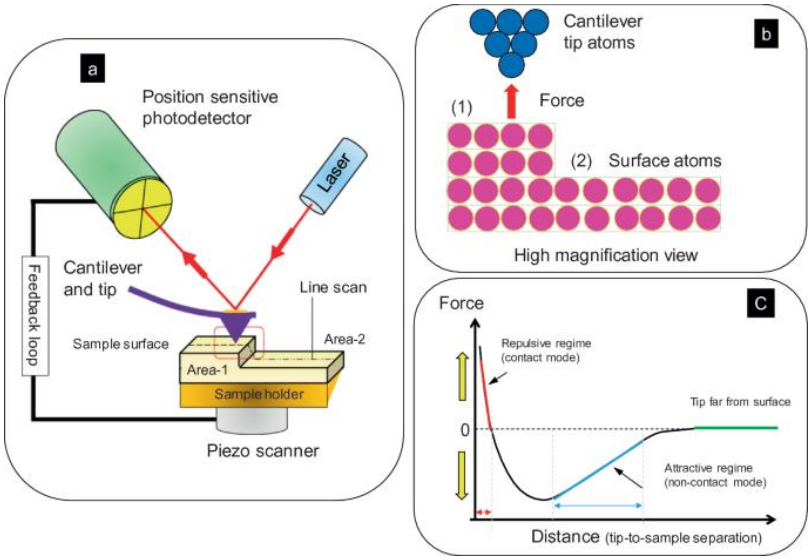

Figure 4.7. (a) Schematic of an AFM setup. The laser reflects off the cantilever into a position-sensitive photodetector, with a feedback loop ensuring constant interaction with the sample surface. The piezo scanner controls sample movement for line scanning across areas. (b) Interaction between the cantilever tip and surface atoms at high magnification, where force is exerted between the tip atoms and surface atoms. (c) Force vs. tip-to-sample distance plot, showing the repulsive regime (contact mode) and the attractive regime (non-contact mode), with forces switching based on tip-sample separation. Taken from [66].

By knowing k and measuring z, the force F can be calculated. This force is often in the range of piconewtons to nanonewtons, allowing for sensitive detection of surface features.

In Figure 4.7b, the average cantilever motion and force-distance curve show the repulsive regime in contact AFM and repulsive AM-AFM modes. In Figure 4.7d, the attractive AM-AFM mode is depicted, highlighting the attractive forces detected without the tip contacting the sample surface

1. **Contact Mode**: the AFM tip makes continuous contact with the sample surface. This mode is suitable for high-resolution imaging of hard surfaces but can cause damage to soft samples due to the frictional forces involved.

2. **Tapping Mode**: the cantilever oscillates near its resonant frequency, intermittently contacting the surface. This mode reduces the lateral forces on the sample, minimizing damage while maintaining high-resolution imaging capabilities.

3. **Non-contact Mode**: the cantilever oscillates above the sample surface without making contact. The tip detects the attractive van der Waals forces between the tip and the sample. This mode is ideal for imaging very soft or delicate surfaces without causing any damage.

AFM images were acquired in tapping mode at scan rates of 1 Hz with a resolution of 512 × 512 pixels from samples deposited on Si substrates. Semi-contact silicon AC160TS AFM tips (Olympus, Japan) with a cantilever spring constant of 26 N/m and tip apex radius of 7 nm were used. Surface topography of the deposit was acquired by maintaining the cantilever first resonance amplitude constant via the feedback loop of the AFM acting on the piezo Z direction. Software Mountains SPIP (Digital Surf, France) was exploited for images elaboration.

4.2.3 X-ray photoelectron spectroscopy (XPS)

X-ray Photoelectron Spectroscopy (XPS) provides quantitative and qualitative information about the elemental composition, empirical formula, chemical state, and electronic state of the elements within the material's surface.

XPS operates on the photoelectric effect principle. When a material is irradiated with X-rays, core electrons are ejected from the surface atoms. The kinetic energy of these ejected electrons is measured and used to calculate their binding energies, which are

characteristic of specific elements and their chemical states. The binding energy is given by:

$$E_B = h\nu - E_K - \phi \tag{4.2}$$

where E_B is the binding energy, $h\nu$ is the photon energy, E_K is the kinetic energy of the ejected electron, and ϕ is the work function of the spectrometer.

Figure 4.8b, illustrates the process of photoelectron emission where an X-ray photon interacts with an atom, resulting in the ejection of a core electron. The kinetic energy of this ejected electron is measured to determine the binding energy. The electron is ejected from the core levels (such as 1s, 2s, or 2p) of the atoms, and the binding energy E_B is a unique fingerprint for each element, allowing for elemental identification. The work function ϕ is the energy required to move an electron from the Fermi level to the vacuum level, and it is specific to the material of the spectrometer.

An XPS system consists of an X-ray source, an electron energy analyzer, and a detector. The X-ray source typically uses Al Kα (1486.6 eV) or Mg Kα (1253.6 eV) radiation. The electron energy analyzer (usually a hemispherical analyzer) separates electrons based on their kinetic energy, and the detector counts these electrons to generate a spectrum.

This technique is highly surface-sensitive, typically probing the top 1-10 nm of the material, as illustrated in Figure 4.8b. The use of Al Kα radiation is common due to its high photon energy, which is sufficient to eject core-level electrons from most elements. The emitted electrons are collected and passed through the electron energy analyzer, which filters them by kinetic energy before they reach the detector. This energy filtering is important as it enables the determination of the binding energy of the electrons, which is used to identify the elements and their chemical states.

The sensitivity of XPS to the topmost layers of the sample makes it an ideal tool for studying surface phenomena, such as oxidation, corrosion, and thin films. The information obtained can be used to infer the surface composition, thickness of oxide layers, and even the electronic structure of the materials.

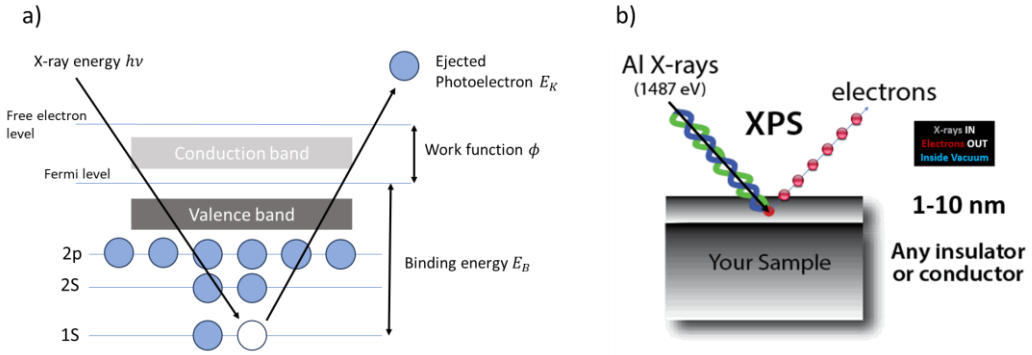

Figure 4.8. Illustration of the X-ray photoelectron spectroscopy (XPS) process. (a) An incident X-ray photon (energy hv) ejects a core-level electron (photoelectron) from the sample. The kinetic energy of the ejected photoelectron is measured and used to determine the binding energy of the electron in its original atomic orbital. (b) XPS experimental setup. Photoelectrons emitted from the sample's surface region (1-10 nm depth) are analyzed. This depth range arises from the short inelastic mean free path of photoelectrons without significant energy loss, making XPS a surface-sensitive technique. Taken from [67].

Tin, Ni and W oxidation states were investigated by XPS on Kratos Axis Ultra DLD spectrometer equipped with monochromatic Al Kα X-ray source (hν = 1486.6 eV) and operating at base pressure below 1×10^{-9} mbar. Analysis area was 700 μm × 300 μm and take-off angle 90°. High-resolution XPS spectra were acquired with 20 eV pass energy and step size of 0.1 eV for Sn 3d, Ni 2p and W 4f, and O 1s and C 1s. Energy step of valence band spectra was of 0.05 eV. Energy axis of high-resolution XPS spectra was referenced to adventitious C 1s at 285.0 eV, while for valence band spectra the energy axis was referenced to the Fermi level of a calibration gold foil.

III. RESULTS AND DISCUSSIONS

CHAPTER 5. FROM ISOLATED PARTICLES TO NANOGRANULAR FILMS

5.1 Morphological properties of isolated clusters

Aiming at determining first the size distribution of the nanoparticles composing the cluster-assembled films, low-coverage samples ensuring particle separation were produced and analyzed by low magnification TEM. TEM images of isolated clusters were analyzed using the particle analysis function in ImageJ (https://imagej.net/ij/), which allowed for the determination of the area, perimeter, and diameter of each individual particle. Images underwent first a thresholding process to differentiate nanoparticles from background. To improve the accuracy of this separation in the case of neighboring objects, watershed algorithms were employed. These approaches effectively eliminated any noise or artifacts, resulting in reliable particles identification. The particle size distribution was determined using the Feret diameter, defined as $\boldsymbol{P/\pi}$, where $\boldsymbol{P}$ is the measured contour. If on one hand this approach somehow loses the information about particle shape, on the other hand it allows to characterize in a simple way objects with spheroidal shapes as those observed in TEM images here and in the following as well.

Besides isolated nanoparticles, several agglomerates are visible in the images. As in most cases their irregular shapes can be traced back to the juxtaposition of the spheroidal shapes of single nanoparticles, I suggest that surface diffusion explains their presence.

Although a partial coalescence cannot be excluded at the point of contact of two particles, in such agglomerates the single particles maintain their individuality in what regards their dimensions, therefore they can be included in the statistics. The few objects whose shape is not spheroidal and cannot be reconstructed as juxtaposition of spheroidal shapes are not considered in the statistics. Particles size is reported as

"equivalent diameter", which is calculated by Feret diameter. Figure 5.1 a and b show an example of a low-magnification TEM image analyzed with the related particles tracking.

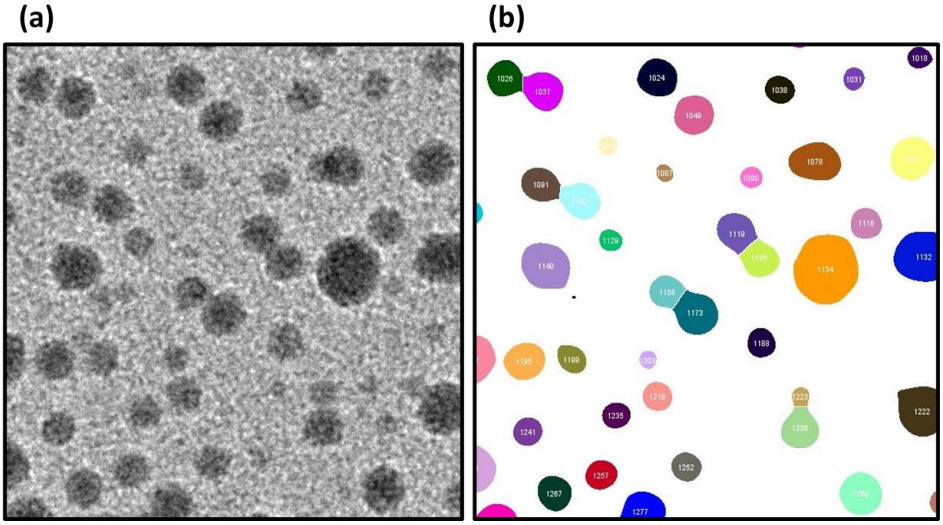

Figure 5.1. Example of low magnification TEM image (zoomed-in), corresponding to Sn, used for creating the particle size distribution. (b) Related image elaboration with the automatic recognition of spheroidal objects (white dots inside each object are actually the numerical labels for particles counting).

The histogram of nanoparticle sizes revealed a right-skewed distribution, characteristic of a log-normal distribution. This observation was further validated by fitting the data to a log-normal probability density function, described by the formula:

$$f(x, \overline{x}, \sigma) = \frac{1}{\sqrt{2\pi}x\sigma} e^{-\frac{1}{2}\left(\frac{ln(x)-ln(\overline{x})}{\sigma}\right)^2} \quad (5.1)$$

x represents the particle size, $\overline{x}$ is the median of the distribution (corresponding to the maximum of the distribution), and σ is the parameter that characterizes the width of the distribution [68].

The log-normal distribution arises when the logarithm of the variable of interest is normally distributed. This distribution is often observed in scenarios where the growth process involves multiplicative factors, such as in the gas-phase synthesis of nanoparticles. In such processes, the log-normal distribution indicates that particle

growth occurs through a parallel mechanism, involving the formation of initial particles (dimers) which then combine to form larger aggregates. Consequently, the size distribution is right-skewed, with most particles being smaller and a few significantly larger.

When plotted on a logarithmic scale, this distribution resembles a normal distribution, reflecting the underlying multiplicative nature of the growth process. This characteristic shape is a hallmark of the gas-phase synthesis process, where particle growth is governed by successive collisions and coalescence of smaller units. (See Section 2.2 for further details.) Thus, the observed log-normal distribution not only fits the data well but also provides insight into the fundamental processes driving the formation and growth of nanoparticles in the gas phase.

In the case of isolated Sn nanoparticles, it was observed that predominantly adopt a spherical shape with dimension ranging from 2 to 20 nm. The preference for spherical shape in Sn nanoparticles of this work, can be understood as a result of surface energy minimization during gas-phase growth combined with the lower cohesive energy of tin atoms in comparison with the aforementioned metals. The resulting histogram plot of Feret diameters was then fitted to a log-normal curve (Figure 5.2b), in line with what expected for size distribution of particles emerging from gas aggregation processes [37,69], returning mean at 7 nm, Log standard deviation of 0.48 nm, and R^2 0.94.

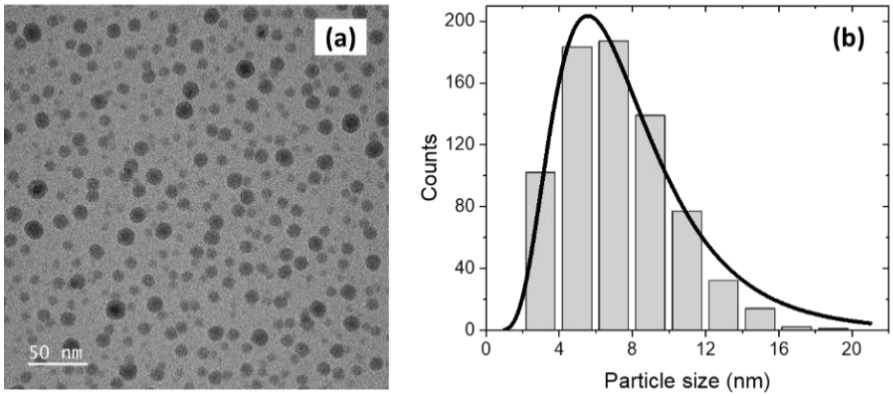

Figure 5.2 Example of low-magnification TEM image of isolated Sn nanoparticles, showing that they predominantly adopt a spherical shape; bulk equivalent thickness is 0.7 nm. (b) Size distribution and lognormal fit (black line) centered at 7 nm.

In the case of isolated Ni nanoparticles, low-magnification TEM images (Figure 5.3a) showing several hundreds of isolated nanoparticles were analyzed to obtain the size distribution. Besides isolated particles, several agglomerates are visible in the images. The few objects whose shape is not spheroidal and cannot be reconstructed as juxtaposition of spheroidal shapes are not considered in the statistics. It was observed that these Ni clusters predominantly adopt dimensions ranging from 2 to 12 nm. The resulting histogram plot of Feret diameters was then fitted to a log-normal curve (Figure 5.3Figure 5.2b), returning mean at 3.9 nm, Log standard deviation 0.33 nm, and R^2 0.94.

It is worth noting that particles fraction with diameter smaller than 5 nm constitutes more than half of the dataset. In the case of Nickel, this ultrasmall size range is poorly represented in literature, where sizes in the ten to several tens of nanometers range are typically investigated [70–73].

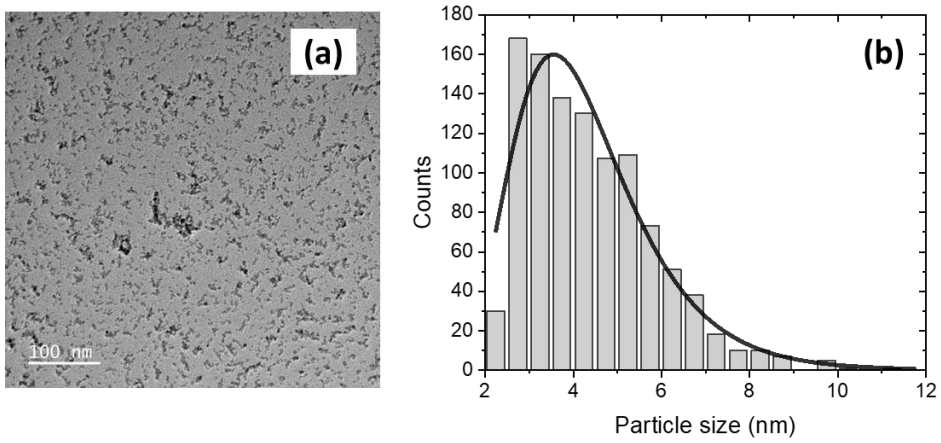

Figure 5.3. a) Example of low magnification TEM image of isolated Ni nanoparticles, used for obtaining the particle size distribution. b) Size distribution including lognormal fitting curve, centered at 3.9 nm.

In the case of isolated Pt nanoparticles, low-magnification TEM image (Figure 5.4a) show that Pt predominantly adopts a 'spheroidal' shape with dimensions ranging mainly from 2 to 4 nm. The resulting histogram of Feret diameters was fitted to a log-normal curve (Figure 5.4b), returning mean at 2.0 nm, Log standard deviation of 0.27 nm, and R^2 0.97.

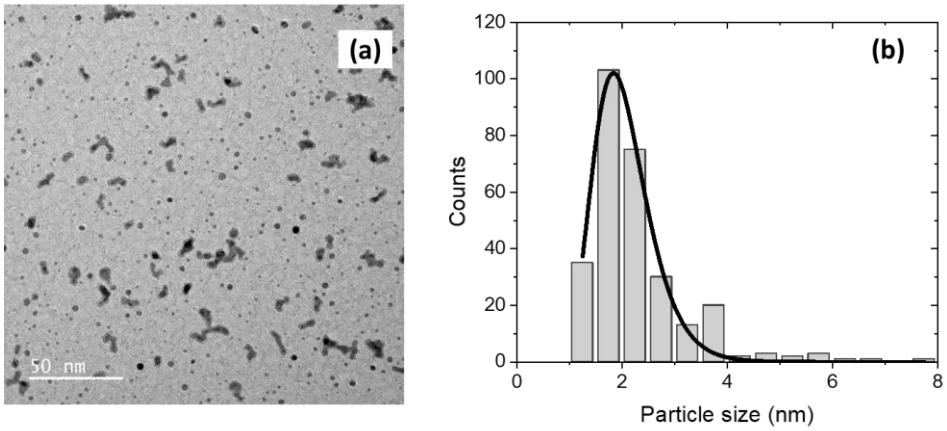

Figure 5.4. a) Example of low magnification TEM image of isolated Pt nanoparticles used to generate the particle size distribution. b) Size distribution including lognormal fitting curve, centered at 2.0 nm.

The good matching of the size distribution with the lognormal curve, which is typically shown by particles forming through gas-phase aggregation processes [24,29,37,74,75], suggests that the metallic clusters of Sn, Ni and Pt formed inside the PMCS follow the same mechanism: the sputtering of a metallic target by discharge-driven Ar or Ne ions produces a hot atomic vapor that thermalizes by collisions with the inert gas into PMCS body and aggregates in atomic clusters by homogeneous nucleation (steps b and c in Figure 2.9). The growth of Sn, Ni, Pt and W clusters into PMCS body proceeds until they are dragged out from the source by the expanding inert gas flow. At this point, clusters growth definitively ceases due to the occurrence of the collisionless molecular regime, following Ar supersonic expansion towards high vacuum (step d in Figure 2.9).

Furthermore, spherical shape formation in gas-phase aggregation is not universally observed across all materials. In fact, although spherical shape minimizes particle surface energy, other factors can play a role in determining particle final shape [76]. For instance, as shown in Figure 5.5 the shape of Iron (Fe), Platinum (Pt) and Vanadium (V) nanoparticles produced in gas-phase aggregation is strongly influenced by the specific conditions under which they are produced. In the case of Fe, studies by Zhao et al. [77] showed that Fe nanoparticles can grow into cubic shapes influenced by atomic diffusion behaviors on different surfaces ({100} and {110}), demonstrating the impact of kinetic factors and temperature in defining the final shape of the nanocluster. Similarly, controlled growth experiments by Xia et al. [78] have demonstrated a transition from octahedral to tetrahedral shapes in size-selected Pt nanocrystals, influenced by parameters like argon and helium gas flow rates and temperature, which affect the nucleation and growth pathway of the nanocrystals. Other studies by Kuzminova et al. [79] reported that low magnetron currents and aggregation pressures lead to the formation of cubic V nanoparticles, which is most likely connected with different kinetics growth modes on {100} and {110} surfaces of V. Conversely, higher magnetron currents and pressures result in the production of spherical-like nanoparticles (NPs) with highly irregular morphology. These factors underscore the complex interplay of process parameters in determining nanoparticle shape in gas-phase aggregation.

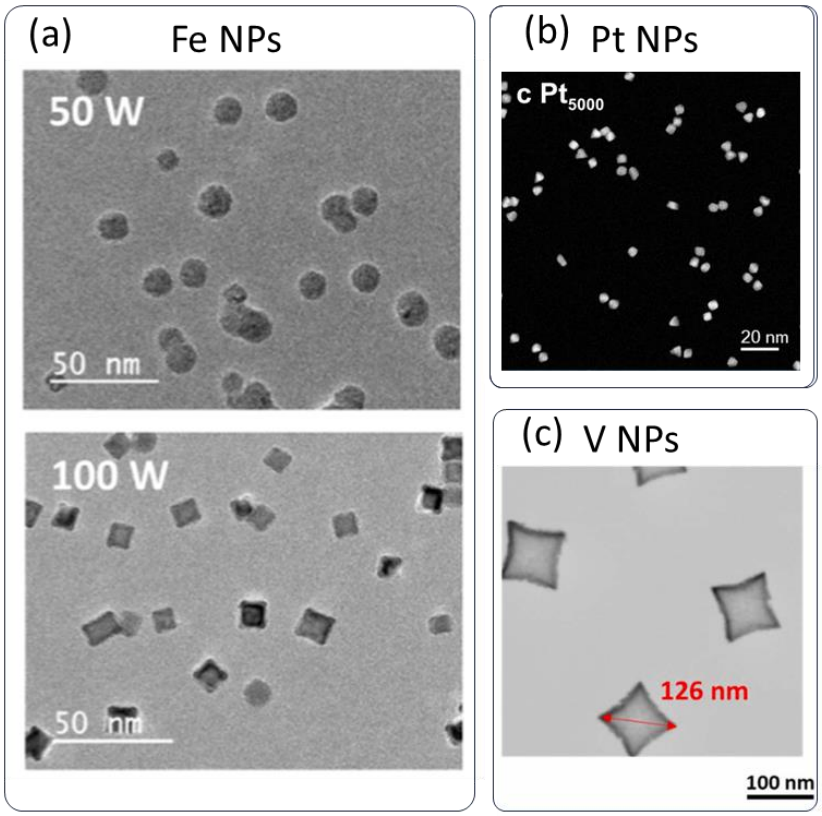

Figure 5.5. TEM and SEM examples of non-spherical NPs produced in the gas phase. (a) Fe, (b) Pt and (c) V. In (a) Fe NP shape can be altered by changing DC power. Taken from [77–79].

The preference for spherical shape in Sn nanoparticles of this work (Figure 5.6a), can be understood as a result of surface energy minimization during gas-phase growth combined with the lower cohesive energy of tin atoms in comparison with the aforementioned metals.

However, HR-TEM show evidence of non-spherical Pt particles (Figure 5.6b). Based on size-dependent shape trends reported in the literature, platinum nanoparticles predominantly adopt a truncated octahedral geometry, which is known to minimize surface energy by stabilizing {111} and {100} facets. This geometry is especially predominant in particles smaller than 2.5 nm. Given that the particles produced in this work by PMCS have a mean size of 2 nm, they are also expected to predominantly adopt a truncated octahedral shape.

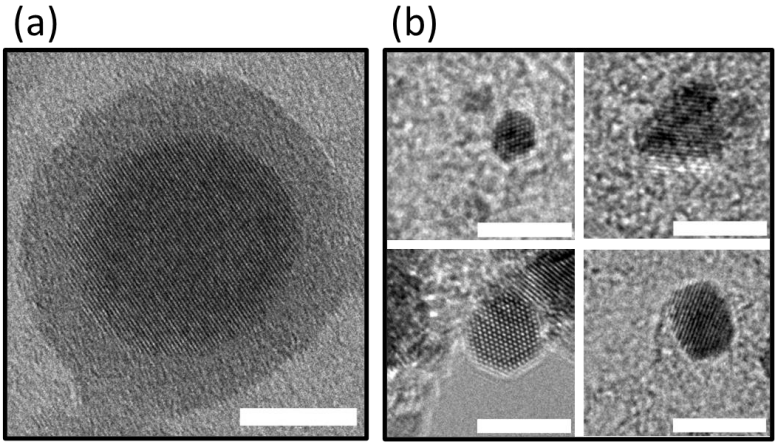

Figure 5.6. High magnification TEM images. (a) Primeval Sn particles display spherical shape while isolated Pt particles (b) show distinct non-spherical shapes. Scale bar 5 nm.

Moreover, gas-phase synthesis and simulation studies by Xia et al. [78] indicate that shape evolution of Pt nanoparticles follows a two-step growth process (). Initially, the truncated octahedron grows uniformly on all {100} facets, eventually forming a complete octahedron. Subsequently, further growth on only four of the {111} facets can result in the formation of tetrahedral shapes, as the symmetry of the octahedron is broken by preferential growth on selected facets. However, analysis by Ding et al. [80] of Pt particles synthesized via common wet impregnation (WI) methods, where no surface capping agents or stabilizers are used, suggests that additional shapes such as cuboctahedra and irregular polyhedra may form under certain conditions. This conclusion is supported by atomistic simulations, which show that such non-equilibrium shapes can emerge, particularly as particle sizes increase beyond 2 nm, reflecting a broader distribution of morphologies.

While initial comparisons suggest the presence of truncated octahedral as the predominant shape of particles produced in this work, evidence of other geometries such as tetrahedral shapes, indicates that further analysis is required to fully characterize the size-dependent morphology of the particles produced in this study. The role of kinetic factors in shaping these nanoparticles is critical, particularly in gas-phase synthesis, where rapid cooling and growth conditions can tune the size and shape. Controlling the growth and size distribution of nanoparticles in the gas phase is

essential for exploring their unique physical and chemical properties, which can be strongly influenced by their shape and size.

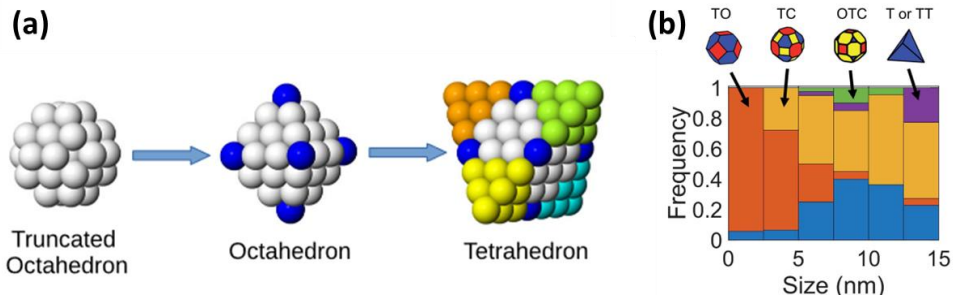

Figure 5.7. Schematic representation of the shape evolution of platinum nanoparticles produced in the gas-phase: starting with a truncated octahedron, growth on all {100} facets forms an octahedron, while selective growth on four {111} facets leads to a tetrahedron. Taken from [78]. The frequency distribution shown in figure (b) Size-dependent distribution of nanoparticle shapes based on frequency as a function of particle size. Truncated octahedra (TO) dominate at smaller sizes, while other shapes such as truncated cuboctahedra (TC), octahedral-truncated cuboctahedra (OTC), and tetrahedra (T or TT) emerge more frequently as size increases, particularly beyond 5 nm. Taken from [80].

5.2 From sub monolayer to 2D growth regime

To investigate the early stages of cluster-cluster interactions and the morphological evolution of cluster-assembled films during two-dimensional (2D) growth, TEM images were analyzed using ImageJ software. This analysis provides valuable information into the interaction and connectivity of atomic clusters at this early stage of aggregation. While site percolation models can interpret connectivity phenomena, they do not account for dynamic behaviors, such as diffusion. Experiments have shown evidence of fractal structures during first stages of the growth of films [81,82], therefore, other models such as cluster-cluster aggregation (CCA) and diffusion-limited aggregation (DLA) have been developed to model aggregation processes observed in colloids and aerosols.

Interestingly, both DLA and CCA models often result in the formation of structures exhibiting fractal properties. DLA aggregates are characterized by the development of dendritic-like branchings due to the attachment of individual particles diffusing through space and CCA aggregates form through the recursive attachment of clusters of particles, creating islands connected by bridges, also resulting in complex, fractal-like structures. However, CCA models are limited as they do not account for the continuous addition of new particles via deposition.

By incorporating deposition into aggregation models, the behavior of the particles can be modeled using various theoretical approaches. One such model is the Deposition-Diffusion-Aggregation (DDA) model, which effectively describes the behavior of atomic clusters during sub-monolayer film growth (Figure 5.8), elucidating the interplay of three fundamental processes [83,84]:

Deposition: Clusters land on the substrate at random locations. The deposition rate, controlled by experimental parameters, influences the film's density and structure. A normalized flux, Φ, is introduced, defined as the number of clusters deposited on the surface per unit area and unit time. While this flux is typically steady over time, certain experimental conditions may involve pulsing the flux—alternating it between a constant value and zero over specific intervals. This modulation of flux can substantially influence the growth dynamics of the film [85,86], as is the case for the films produced by a PMCS used in this work.

Diffusion: Deposited clusters can diffuse across the substrate surface. The diffusion coefficient, determined by factors like temperature and cluster-substrate interaction, affects the cluster mobility and arrangement. The model assumes Brownian motion (i.e., the particle undergoes a random walk on the substrate) for cluster diffusion.

Aggregation: Clusters in close proximity can aggregate to form larger islands. The aggregation process depends on cluster-cluster interactions and can lead to various film morphologies. While the DDA model simplifies this interaction by not considering coalescence or dissociation from the islands (stick irreversible), it offers a foundation for understanding the early stages of cluster aggregation.

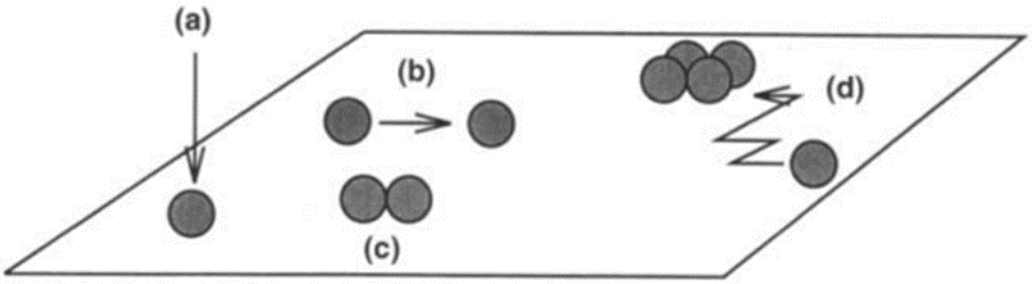

Figure 5.8: Schematic representation of the basic process considered in the DDA model: (a) deposition; (b and d) particle diffusion; and (c) aggregation. (b) represents a particle that diffuses and meets another particle to form a new island (a dimer in this case), while (d) correspond to a particle aggregating to an already existing island (growth process). Taken from [87].

This model, initially developed for atomic deposition, has been extended to describe the deposition of nanoparticles, where the size and interaction potential of the particles introduce additional complexities [83,87,88]. Furthermore, recent publications by Borghi et al., have employed this model to analyze the sub-monolayer growth dynamics in cluster-assembled films of zirconium [89] and gold [10] produced by SCBD, highlighting its versatility and applicability in advancing our understanding of nanoparticle deposition dynamics in the sub-monolayer or 2D growth.

In this chapter, I explore the dynamic interplay between deposition, diffusion, and aggregation of metallic particles on the carbon surface of TEM grids. The DDA model provides a fundamental framework for understanding the sub-monolayer growth of thin films and nanostructures on surfaces, highlighting the interplay of these three fundamental processes. Incorporating fractal analysis to TEM images at different coverages could provide insights into how the film's structural complexity evolves during deposition, potentially revealing a transition from isolated particles to interconnected clusters and percolating structures as particle interactions and

aggregation progress and has been described in previous publications by Jensen et al. [82,90,91].

The box-counting method, one of the most common techniques in fractal analysis, was employed to analyze complex structures observed during aggregation processes on substrates, as captured using Transmission Electron Microscopy (TEM) (Figure 5.10. This method assesses the complexity of a shape and aids in calculating the fractal dimensions. Employing ImageJ's FracLac plugin, the procedure involves systematically overlaying a series of progressively finer grids (the boxes) over an image (Figure 5.9). Data is collected by counting how many of these boxes contain any significant part of the image's details, with important details typically highlighted by contrasting black pixels against a non-essential white background. The analysis generates a plot of $log(N)$, the number of boxes intersecting the structure, versus $log(s)$, the size of each box. A linear relationship in this plot indicates a fractal pattern, and the slope of the best-fit line provides the fractal dimension.

This measure provided valuable information about the aggregation mechanism during cluster deposition, as will be discussed in the next section.

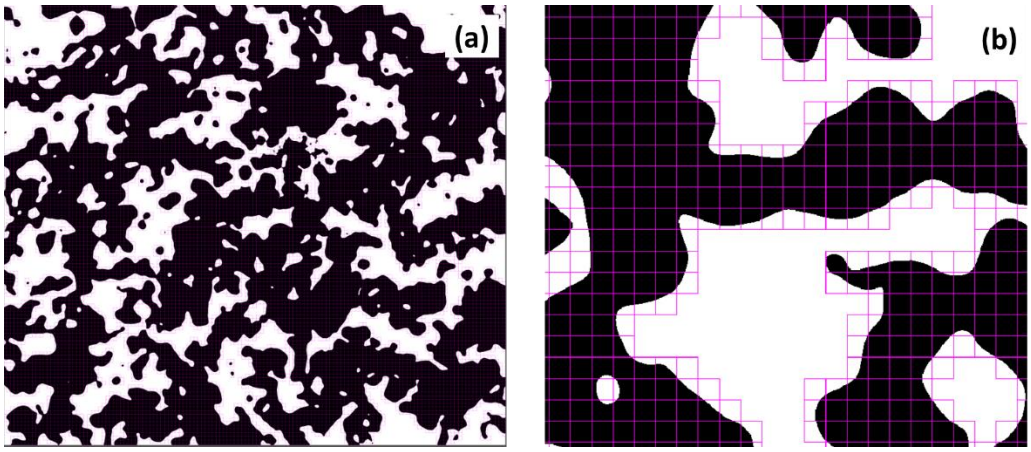

Figure 5.9. Example of TEM image of Pt films at ~63% surface coverage, binarized for fractal analysis. (a) reveals a complex, interconnected structure with a measured fractal dimension of 1.87, indicative of relatively high degree of structural complexity. (b) A zoomed-in view of (a), highlighting the application of the box-counting method to quantify the fractal dimension.

5.2.1 High melting point materials: the case of Ni, Pt and W

The morphological evolution of Pt thin films under varying coverage conditions, demonstrates the complex interplay between deposition, diffusion, and aggregation processes. This section elaborates on the transformation of isolated nanoparticles into more intricate structures with increasing coverage in correlation with bulk equivalent thickness.

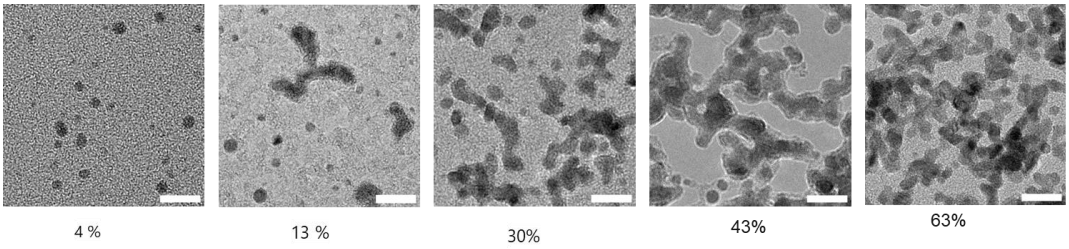

Figure 5.10. Evolution of coverage percentage by increasing the deposition time of Pt films, displaying branched structures that become more complex as coverage increases. The images were extracted from low magnification TEM images. Scale bar 5 nm

At 4% coverage, TEM images predominantly showcased isolated Pt nanoparticles on the substrate, ranging mainly from 1 to 5 nm, already described in Figure 5.4. The fractal dimension at this stage was measured to be 1.17, indicating a relatively simple and non-complex structure as these particles retained their primeval morphology, with minimal interaction and aggregation due to limited diffusion on the substrate, thus acting as several nucleation sites. It is noteworthy that in the soft-landing regime, a characteristic feature of SCBD, Pt clusters can become immobilized on surface defects. This immobilization further suppressed diffusion, thereby reducing the probability of particle-particle interaction and aggregation on the substrate at this early stage of deposition, however few aggregates were also observed.

As the coverage increased to 13%, the morphology of the Pt cluster film evolved gradually, displaying few complex branched-like shapes. This suggests that newly deposited nanoparticles tend to aggregate rather than merge upon interaction with others on the substrate. Although most clusters remained isolated, this stage marked the onset of early network formations due to hard aggregation, likely caused by partial or limited coalescence via necking, where interacting particles started forming branched-like shapes. The fractal dimension increased to 1.35, reflecting the increasing of structural complexity. This transition suggests that increasing particle

deposition, promotes the formation of more complex, branched structures as particles begin to aggregate and form initial networks.

At 30% coverage, significant morphological changes are evident, with branched-like structures becoming more prominent. The progressive deposition of nanoparticles leads to dendritic-like structures, with some dendritic objects beginning to interact. This stage highlights how Pt islands become increasingly interconnected, forming extensive dendritic patterns as the newly added primeval size particles stick to the existing islands. The fractal dimension of 1.63 obtained from the TEM image indicates a moderate level of aggregation complexity and partially filled structures, suggesting intricate, self-similar clustering with high surface area relative to volume, important for applications like catalysis

The TEM image at 44% surface coverage reveals a significant increase in the complexity and density of dendritic networks. This high coverage level promotes frequent interactions between incoming particles and existing islands, facilitating extensive growth and interlinking of branches. These extensive interactions result in large, interconnected networks that cover a substantial area of the surface. The measured fractal dimension of 1.74 aligns with the characteristics of DLA model, where particle aggregation is driven by random motion and subsequent sticking upon contact. In the context of cluster assembled films, as new particles are added and diffuse, they adhere to existing islands, forming fractal-like, dendritic structures. The high surface coverage further increases the frequency of interactions between newly added particles and islands, thus promoting the growth and interconnection between islands.

This DLA-like growth mechanism continues until a significant number of particles start to land within the existing islands, leading to an increase in their effective fractal dimension. At 63% coverage, the Pt films exhibit a highly intricate network of interconnected islands spanning across the entire observation area. This stage is characterized by nearly complete surface coverage, where new particle deposition primarily promotes the joining of islands and further complexification of the structure.

The fractal dimension at this stage reaches 1.87, indicating the highest level of structural complexity observed in this study for Pt sub monolayer films. This value approaches the fractal dimension of 1.9, typical of highly interconnected networks characteristic of fully developed percolation structures [81,82]. The percolation regime is reached when the deposited nanoparticles form a continuous network across the substrate, marking a critical transition point in film growth. At this stage, few isolated particles are observed as new particles predominantly deposit on top of existing islands, suggesting the onset of ballistic growth.

Ni and W films analyzed in this thesis also exhibit similar trends of aggregation in the sub monolayer, validating the DDA model. These materials display solid-like interactions that promote aggregation via necking. Similarly to the observed in Pt films, for tungsten at a high coverage of 71%, the fractal dimension is 1.9.

The observed morphological evolution of Pt, Ni, and W under varying coverage conditions aligns with the principles of the DDA model, encompassing the interplay of particle deposition, surface diffusion, and aggregation processes—key determinants of thin film growth and structural complexity. A defining characteristic of the DDA model is the irreversible sticking of particles upon contact, a phenomenon that drives the formation of aggregates and, ultimately, the intricate structures observed in the TEM images (Figure 5.11).

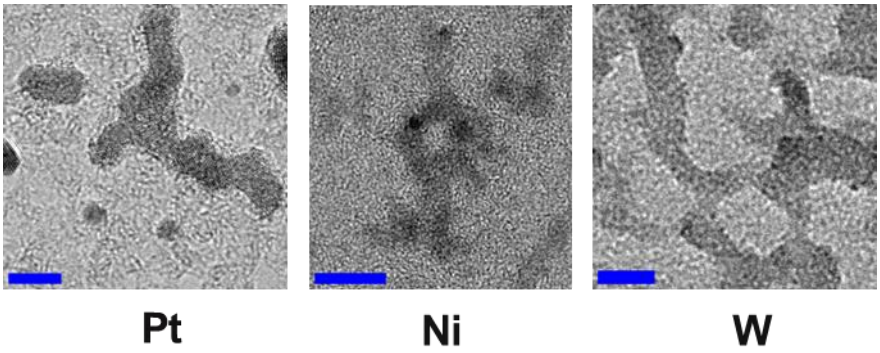

Figure 5.11. Comparative of sub-monolayer growth for the three high-melting point materials studied in this work, highlighting the formation of branched-like structures. Scale bar 5 nm.

Additionally, the soft-landing regime plays a significant role in maintaining the primeval morphology of nanoparticles. Sn, Pt, Ni and W clusters can become immobilized at surface defects, inhibiting diffusion and reducing particle-particle interactions. This immobilization is crucial in maintaining the discrete spreading of nanoparticles at low coverage, thereby ensuring their primeval morphology is largely retained then acting as nuclei sites.

5.2.2 Low melting point materials: the case of Sn

Atomic clusters do not always stick together without fusing, as was reported in the previous sections and references therein. Depending on their intrinsic properties and size, when two atomic clusters meet, they might coalesce. The coalescence of diffusing clusters upon mutual contact significantly influences the morphology of the resulting aggregate (Figure 5.12). This effect is particularly evident in the deposition of antimony (Sb) clusters onto a graphite surface. As the size of these initial clusters decreases from approximately 500 atoms to just four atoms, the morphology of the resulting structures shifts from fractal-like forms to more compact, spherical islands [92]. This transition underscores the critical influence of physical properties and cluster size on aggregate morphology.

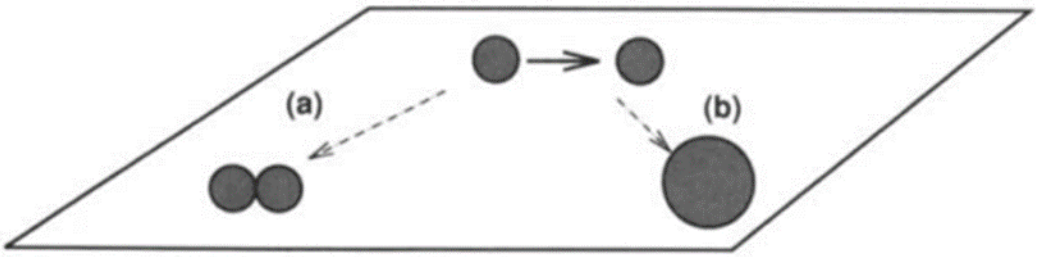

Figure 5.12: Possible interaction process for two clusters meeting on a surface. (a) aggregation, (b) fusion. For atoms, the only possibility is process (a) Taken from [87].

HRTEM images of very low coverage samples show tin NPs deposited by SCBD to have spherical shape with diameter in the range from few nm to around 20 nm. At larger coverage, NPs undergo coalescence phenomena leading to the formation of bigger units in which primeval particles are either completely melted or partially preserve their original identity.

Highly ordered crystalline planes are visible across the whole particles' core, whereas shells appear to be amorphous (This will be discussed in Section 5.4.2). Aiming at investigating coalescence phenomena, we carried out TEM analysis on samples at a level of coverage causing clusters to get in touch each other. In these conditions, we observed that the primary and spherical Sn clusters merge into larger nanoparticles having shapes evolving from original spherical ones towards spheroidal and oblong shapes, reminding the junction of two or more particles (Figure 5.13a).

Figure 5.13b shows the size distribution of nanoparticles that have undergone coalescence. Interestingly, size distribution reveals a bimodal character, whose component at small sizes matches well the size distribution of the original nanoparticles, as depicted in Figure 5.2, while an additional component at larger sizes appears. The presence of a component reminding the original one can be attributed to the fraction of particles not yet subjected to coalescence, while the new component, which exhibits a broader profile and is shifted towards larger sizes, represents the formation of islands resulting from the coalescence of multiple NPs. This observation suggests a gradual coalescence process, wherein new nanoparticles are continuously

deposited onto previous ones and contribute to the growth of progressively larger islands.

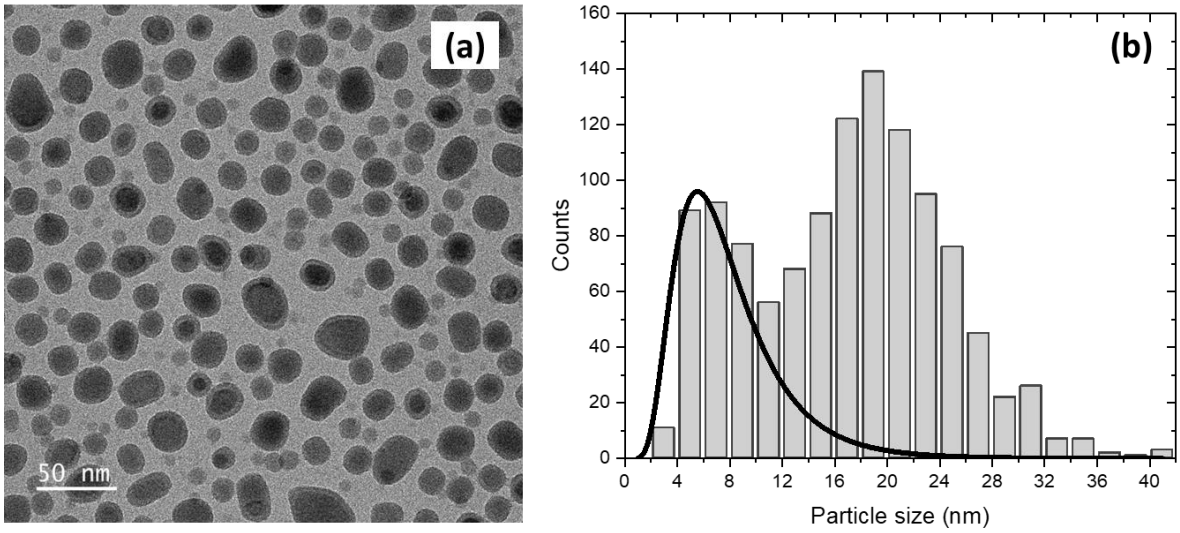

Figure 5.13. (a) TEM image showing a sample at larger degree of coverage than the one of Figure 5.2, where objects unveiling coalescence among two or more particles are visible; bulk equivalent thickness is 3.2 nm, deposition rate is 0.17 nm per rastering step. (b) Size distribution showing bimodal character. The first component matches well the size distribution of the initial nanoparticles, indicating that a fraction of particles remains uncoalesced. The second, broader component emerges at larger sizes, suggesting the formation of units due to the coalescence of at least two NPs. The superimposed black line represents the low-size component of a double lognormal fitting in which Mean and Log Standard Deviation have been kept fixed on values obtained from fitting in Figure 5.2b.

The coalescence of Sn NPs observed in TEM images can be attributed to two main factors: diffusion and juxtaposition. Due to their high surface-to-volume ratio, NPs inherently possess high surface energy [37]. Diffusive motion on the substrate can bring them into contact, leading to coalescence as a mean to reduce the total surface energy. Moreover, during the deposition process, NPs can also be juxtaposed onto one another, further inducing their contact and subsequent coalescence. This close proximity, combined with the system's tendency to minimize its total energy, drives the particles to merge and reduce their combined surface area. It is also noteworthy that since clusters are not deaccelerated before impinging on the substrate's surface, a part of their kinetic energy is available for further warming and structural

reorganization [69]. This phenomenon is particularly notable in the case of Sn clusters, which possess a lower melting point compared to their bulk counterparts [93,94].

According to computational studies performed by Grammatikopoulos et al. [95], dynamics of nanoparticle coalescence reveal a complex multistage process that can be classified into three stages: (i) interface formation; (ii) plastic deformation; (iii) spherization and recrystallization. Examples of Sn particles subjected to coalescence and "frozen" in each one of these stages can be identified by High-Resolution TEM (HRTEM) into the same cohort of particles, allegedly due to the distribution of energy characterizing particle-particle interactions.

The first stage, initial contact and interface formation, regards the formation of a sharp interface between the two particles upon contact, driven by the minimization of surface energy, where the individual crystal planes meet [37,96,97]. Figure 5.14a portraits two Sn NPs stuck in this stage, as it clearly shows the two well distinguished sets of crystalline planes separated by a sharp interface, in a dumbbell configuration. In the second stage, plastic deformation, the heat generated from the release of free surface energy induces a temporary melting of the interfaces [98,99]. This process, especially favored in nano-sized Sn due to its lowered melting point, allows full recrystallization across the two nanoparticle bodies. Figure 5.14b shows two Sn NPs stuck at this stage, highlighting the gradual disappearance of the neck and the progressive formation of a single crystal plane structure, indicative of the recrystallization process [97]. This is a critical aspect of the coalescence process, as it leads to the formation of a single and more stable configuration with enhanced crystallographic order. The final stage, slow spherization and completion of recrystallization, involves a slow relaxation process toward the thermodynamically stable structure, driven primarily by the thermal diffusion of surface atoms once the additional heat dissipates from the sintering process [100]. This migration led to a gradual rounding of the nanoparticle shape, culminating in a nearly spherical morphology, as in the case of Sn NPs shown in Figure 5.14c.

The effects of coalescence at further development stages of cluster-assembled Sn films have been investigated by AFM, which provided information on film morphology at the microscales. AFM images of films at increasing growth stages show a clear

progression of coalescence, where topological features evolve from spheroidal shapes to larger, irregular shapes. At short deposition times, AFM images show mostly spheroidal islands with dimensions in the range from 10 nm to 30 nm approximately (Figure 5.15a). Deformed particles can also be observed, indicating the early stages of coalescence. As deposition time increases, AFM images show an increasing fraction of deformed and larger islands (Figure 5.15b). Some small and spherical particles can still be observed. At longer deposition times, AFM images show mostly islands with complex geometries (Figure 5.15c). These islands are allegedly formed by the coalescence of multiple particles.

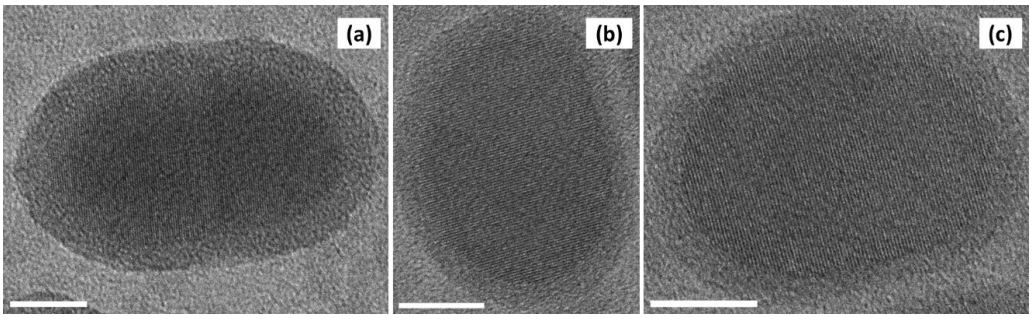

Figure 5.14. HRTEM images of Sn nanoparticles spotted at different stages of coalescence process. a) Formation of the interface between two Sn clusters, where the crystalline planes of each individual nanoparticle meet. b) Plastic deformation stage, where crystalline planes are in the process of realignment. c) Complete coalescence of the two particles is indicated by the disappearance of the interface and the formation of a single crystalline lattice where no defect is observed. Line pairs highlight crystalline plane orientations, while boxes emphasize interfaces. Scale bar at the bottom left of images is 10 nm in all cases.

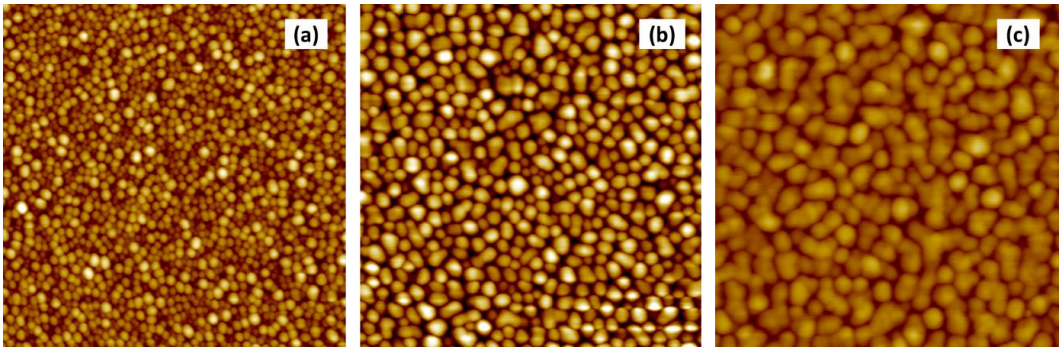

Figure 5.15. 1x1 μm AFM images showing the evolution of island-like film morphology with increasing deposition time. (a) At short deposition times, predominantly spheroidal islands with dimensions ranging from 10 nm to 30 nm are observed. In some cases, signs of deformation are visible, indicating early coalescence stages. Thickness is 10.2 nm. (b) As the deposition time increases, the fraction of deformed and larger islands increases. Thickness is 21.5 nm. (c) With longer deposition times large islands with complex shapes appear, resulting from the coalescence of multiple particles. Thickness is 39.2 nm.

5.3 3D growth regime

Scaling concepts are essential in understanding the growth behaviour and surface morphology of thin films, particularly in the study of cluster-assembled materials. These materials display distinct surface roughness and growth dynamics, which can be characterized using atomic force microscopy (AFM) and analysed through scaling laws. This chapter provides an overview of scaling fundamentals and applies them to the 3D growth regime of cluster-assembled films, focusing on the relationship between surface roughness and film thickness.

In cluster-assembled films, the deposition process involves the direct transfer of clusters onto a substrate, where they adhere and aggregate to form a film. The surface roughening arises from the stochastic nature of cluster landing, diffusion, and aggregation processes. Unlike atomic deposition, where individual atoms can diffuse over significant distances before finding an energetically favourable site, clusters have limited mobility due to their larger mass and size. This limited diffusion leads to a more pronounced surface roughness as the film grows [101].

The roughening is further influenced by factors such as deposition rate, cluster size distribution, and substrate temperature. High deposition rates increase the flux of

clusters arriving at the substrate, enhancing the probability of clusters landing on top of existing ones, which contributes to surface roughness. The size distribution of clusters also plays a significant role; a broad distribution can lead to uneven surface features due to the varying sizes of clusters aggregating on the surface.

The quantitative characterization of surface roughness in cluster-assembled films is often described using the root-mean-square (RMS) roughness, which depends on the film thickness or deposition time t. The RMS roughness is defined as:

$$w = \sqrt{\frac{1}{L}\sum_{i=1}^{L}\left[h(i,t) - \bar{h}(t)\right]^2} \tag{5.2}$$

Where $h(i,t)$ is the height of column i at time t and L is the system size [102].

Roughness scaling laws provide insights into the universal behavior of surface growth processes. In cluster-assembled films, the scaling exponents can deviate from those observed in atomic deposition due to the unique aggregation mechanisms of clusters. The dynamic scaling hypothesis proposes that the RMS roughness scales with the lateral length scale L and time t as [102,103]:

$$w = L^{\alpha} f\left(\frac{t}{L^{z}}\right) \tag{5.3}$$

In this equation, α is the roughness exponent, z is the dynamic exponent, and f is a scaling function. In the early stages of film growth, when $t \ll L^{z}$, the roughness grows as:

$$w \sim t^{\beta} \tag{5.4}$$

with the growth exponent $\beta = \alpha/z$. The value of these scaling exponents uniquely determines the universality class of the growth process. Universality classes such as Edwards-Wilkinson (EW) [104] and Kardar-Parisi-Zhang (KPZ) [105] are distinguished by their specific sets of exponents. Various growth models, including random deposition (RD), ballistic deposition (BD), and random deposition with

surface relaxation (RDSR), are associated with distinct stochastic growth rules based on nearest or second nearest neighbor interactions (Figure 5.16).

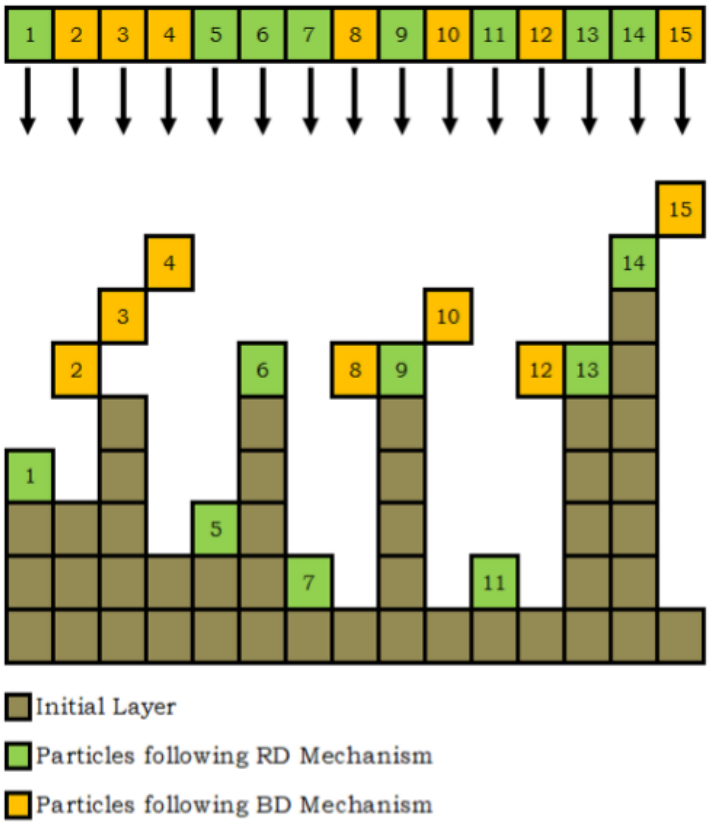

Figure 5.16. Representation of a 1+1-dimensional deposition scheme, featuring Random Deposition (RD) and Ballistic Deposition (BD) mechanisms. Taken from [106].

Except for the RD model, which involves independent particle deposition without surface interactions, all other models incorporate interactions that influence surface morphology. The RDSR model falls within the linear EW universality class, whereas the BD model belongs to the nonlinear KPZ universality class. The scaling exponents for these universality classes vary between 1+1 and 2+1 dimensions, reflecting how dimensionality impacts the growth dynamics and resulting surface roughness.

Surface morphology of films resulting from Nickel, Platinum and Tungsten cluster assembling was characterized by AFM, as shown in Figure 5.17. I calculated the surface roughness of several samples displaying different thickness, following the approach adopted with other cluster-assembled materials [11,89,107,108]. Raw images $1 \times 1\ \mu m^2$ were first corrected from tilt with a line by line fit, then roughness

(RMS) was calculated according to ISO 25178. The thickness was systematically measured at the step created by the masking. In correspondence of the step a larger area ($15 \times 15\ \mu m^2$) was scanned to avoid taking into account misleading elements close to the step edge (e.g. presence of boulders or diffusion of nanoparticles below the mask). Figure 5.17c shows an example of height profile extracted from the AFM image of Figure 5.17.a. Mean height difference between pristine silicon and surface of cluster-assembled film was used to estimate the thickness. Figure 5.17d shows the height distribution of the AFM image of Figure 5.17a, where the sharp peak on the left refers to the substrate region while the broad peak refers to the film region.

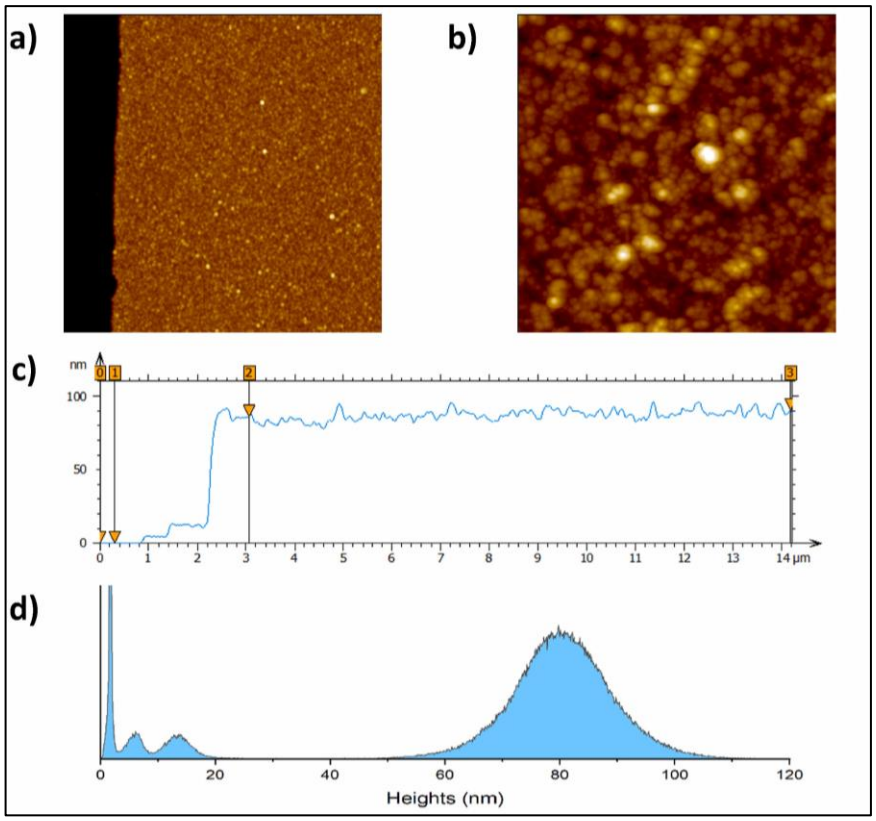

Figure 5.17. a) Example of AFM image, corresponding to Ni films showing the edge of the film where thickness is measured; the side of the image is 15 µm. b) Surface morphology by AFM where roughness is evaluated; the side of the image is 1 µm. c) Example of height profile from image a). d) Height distribution of image a); standard deviations at substrate

level (sharp peak at the left) and at film surface level (broader peak on the right) are 0.11 and 6.45 nm, respectively.

The linear distribution of data points in the log-log plot (Figure 5.18) of roughness vs. thickness suggests an underneath power-law relationship $w \sim t^{\beta}$, whose fitting returns an exponent growth value of $\beta = 0.46$ for Pt, $\beta = 0.41$ for Ni, and $\beta = 0.31$ for W.

As conditions for this analysis are fulfilled, namely (1) lateral scan size much larger than lateral size of morphological features under investigation and (2) constant deposition rate providing linear dependence of thickness with time, the observed exponent suggests, for cluster-assembled Pt, Ni and W films, a growth mechanism in agreement with the ballistic deposition model. In ballistic deposition, clusters adhere to the substrate where they land without significant lateral movement, leading to surface roughening due to limited surface diffusion. The observed β values are higher than the theoretical predictions for ballistic deposition in lower-dimensional models, which are $\beta \approx 0.33$ in 1+1 dimensions and $\beta \approx 0.24$ in 2+1 dimensions. The higher exponents suggest that three-dimensional aggregation dynamics and possibly enhanced shadowing effects in cluster deposition that contribute to increased surface roughness beyond what theoretical models predict.

Notably, studies by Borghi et al. [10] report a $\beta \approx 0.4$ for cluster-assembled films of gold, highlighting that the value is the same by using Ar or He as process gas. This value aligns closely with our results, reinforcing the consistency of ballistic deposition as the governing mechanism in cluster-assembled films.

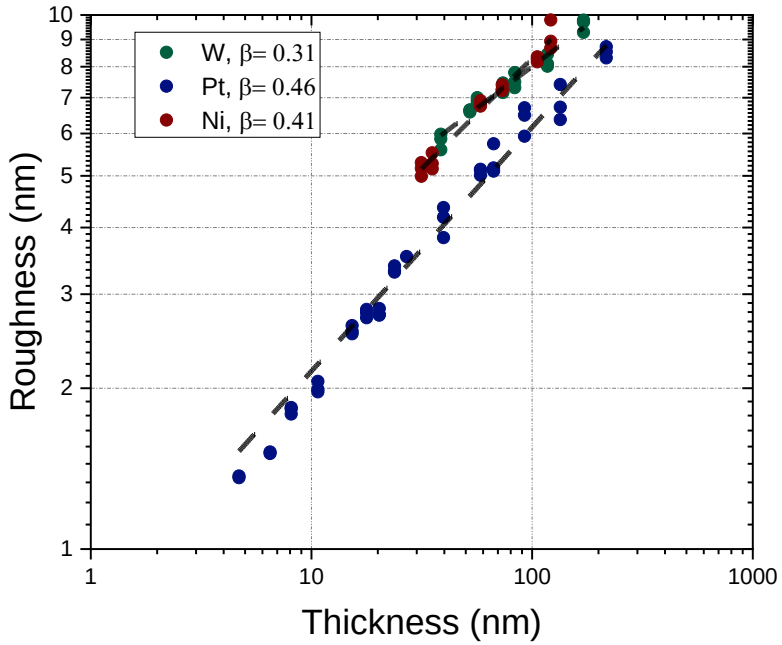

Figure 5.18. Log-log plot of roughness vs. thickness; power law fitting returns an exponent value of 0.31, 0.41 and 0.46 for W, Ni and Pt, respectively.

Despite the clear result on ballistic growth mechanism, it is matter of discussion to what extent ex-situ characterizations of morphological features at such level of detail, as the use of β values from fit of surface roughness vs. thickness to decide about system dimensionality, are truly representative of in-vacuum dynamics leading to the formation of a film by metal clusters assembling. In fact, oxidation is expected to affect cluster's structure, as discussed in detail in the following, and one can argue whether such changes could not weaken the link between ex-situ data and in-vacuum growth dynamics. Assuming that the link is valid is a rather strong hypothesis that implies constraints on the effects of oxidation on clusters morphology.

Nevertheless, no matter the details of system dimensionality, to the purpose of this analysis is the confirmation of a ballistic growth regime for cluster-assembled films brings important consequences: absence of clusters diffusion in the investigated thickness range, soft-assembling and related memory effect, and -above all-film porosity. In fact, this last allows assuming that air exposure and oxidation process occur on particles assembled in form of a porous film basically the same way of

isolated particles, making the comparison of collective results from XPS on films and localized results from TEM on single particles meaningful. By comparing direct AFM measurements of the thickness with bulk-equivalent values shown by QCM, average film porosity can be estimated around 70–80%.

5.4 Oxidation of isolated metallic clusters and cluster-assembled films

5.4.1 Cabrera-Mott oxidation model

The oxidation of metallic nanoparticles involves a series of complex mechanisms influenced by factors such as particle size, structure, and the surrounding environment. At its core, the process involves the interaction between the metal's surface, oxygen, and the subsequent diffusion of ions through an oxide layer.

The initial stages of oxidation typically begin with the adsorption of oxygen molecules on the nanoparticle surface, where oxygen dissociates and reacts with surface metal atoms to form an oxide. This oxidation involves the transfer of electrons from metal atoms, resulting in metal cations (M^{2+}) which diffuse toward the nanoparticle surface, while oxygen anions (O^{2-}) diffuse inward (Figure 5.19). In these early stages, the Cabrera-Mott theory provides a theoretical framework for describing the rapid formation of a thin oxide layer [109,110]. According to this model, an electric field develops between the metal cations and oxygen anions, driving the migration of metal ions outward and oxygen inward. The electric field significantly accelerates the initial oxidation process, but as the oxide layer thickens, this field diminishes, leading to a slower oxidation rate.

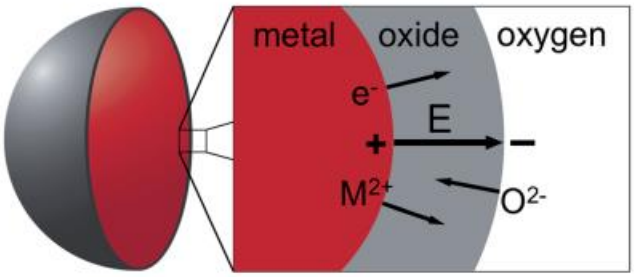

Figure 5.19: Schematic representation of the oxidation mechanism in metallic nanoparticles. The diagram shows the formation of an oxide layer driven by the electrostatic field generated by electron transfer, leading to the diffusion of metal cations (M^{2+}) outward and oxygen anions (O^{2-}) inward, following the Cabrera-Mott model Taken from [111,112].

At the nanoscale, this oxidation process can proceed rapidly due to the increased surface area-to-volume ratio, making the oxidation kinetics highly dependent on particle size. Smaller nanoparticles tend to oxidize more quickly due to the enhanced diffusion and surface energy effects. In many bulk metals, the oxide layer is passivating, meaning that it impedes further oxidation once a certain thickness is reached, but in nanoscale systems, the oxide layer often exhibits different properties, such as defects and vacancies, that can influence its passivating behavior.

A common outcome of nanoparticle oxidation is the formation of core-shell structures, where a metal core is encased by an oxide shell [111,112]. As oxidation continues, the metal core gradually diminishes while the oxide shell grows. Oxygen continues to diffuse through the oxide layer to reach the metal core, and the process becomes increasingly diffusion-limited as the shell thickens. This core-shell formation is prevalent in metal nanoparticles such as indium and tin.

In many cases, the diffusion of metal atoms and oxygen ions is not symmetric, leading to unique structural changes within the nanoparticle such as hollow structures due to the Kirkendall effect [111,113,114]. As illustrated in Figure 5.20, this phenomenon occurs when there is a significant difference in the diffusion rates of metal cations and oxygen anions through the growing oxide layer. Typically, metal cations diffuse outward at a faster rate than oxygen anions diffuse inward. This discrepancy in diffusion creates vacancies at the interface between the metal core and the oxide shell. Over time, these vacancies merge and form voids within the nanoparticle. As the

process continues, the metal core is gradually consumed, leaving behind a hollow structure encased in an oxide shell.

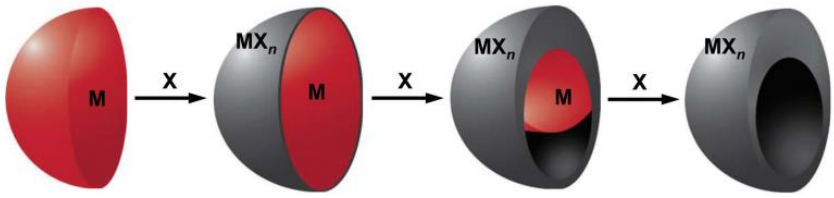

Figure 5.20. Illustration of hollow nanoparticle formation through the Kirkendall effect. The outward diffusion of metal cations (M) exceeds the inward diffusion of reactive species (X), resulting hollow of nanoparticle. Taken from [111].

The following sections will discuss the structure and mechanism behind oxidation of isolated particles and cluster assembled films.

5.4.2 The case of Sn: core-shell structures and intermediate oxides

HRTEM images of very low coverage samples show tin NPs deposited by SCBD to have spherical shape with diameter in the range from few nm to around 20 nm. At larger coverage, NPs undergo coalescence phenomena leading to the formation of bigger units in which primeval particles are either completely melted or partially preserve their original identity, as visible in the distribution of intra-particle crystalline planes. Figure 5.21a and b show examples of HRTEM images, where spherical single particles as well as one deformed particle following coalescence phenomena are visible. We noticed that particles with dimensions smaller than around 10 nm have uniform grey shade while larger ones show darker core and lighter shell, the latter presenting a rather uniform thickness of about 4 nm, independently on particle size. Highly ordered crystalline planes are visible across the whole particles' core, whereas shells appear to be amorphous. We suppose that core–shell structure stems from room temperature oxidation, taking place at the venting of deposition chamber and subsequent exposure to atmospheric air, for which core is expected to be metallic tin while shell tin oxide. Top right insert of Figure 5.21b displays the Fast Fourier Transform (FFT) of an area located in the core of a particle, where spots pattern is ascribable to metallic β-tin with tetragonal structure. Given the thickness of the alleged oxide shell, particles smaller than about 10 nm -appearing of light grey uniform colour- are

supposed to be fully oxidized. We carried out elemental mapping (EDS-X coupled to STEM) that confirmed the expected distribution of oxygen and tin, as shown in Figure 5.21c, where light green colour refers to oxygen-rich regions while red to tin-rich ones. It is worth noting that such compositional mapping shows smaller particles as identical in colour to shells of larger particles, suggesting their full oxidation.

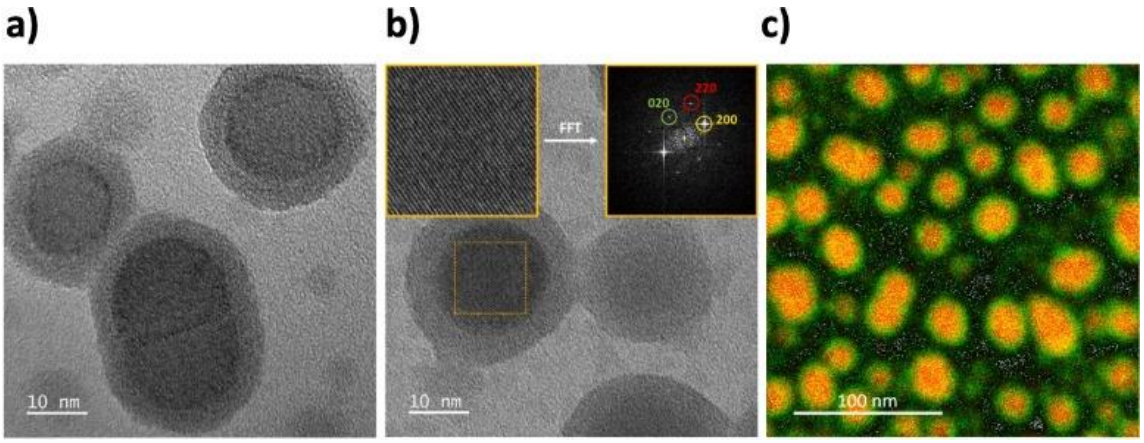

Figure 5.21. a) HRTEM image of Sn sample by SCBD, showing various spherical nanoparticles as well as an ovoidal one following partial coalescence. Core-shell structure is visible in larger particles, while smaller ones seem to have homogeneous structure. b) Same as a), where top left insert shows a zoom-in of the area within the orange dashed square displayed on the main image, while top right insert shows the FFT of this same area, indicating metallic β-tin with tetragonal structure (main spots are labelled with corresponding crystalline planes). c) Elemental map by STEM-coupled EDS-X of the same sample at lower magnification, showing oxygen-rich regions in green and tin-rich region in red.

Aiming at further clarifying the crystalline nature of Sn nanoparticles, Selected Area Electron Diffraction (SAED) was carried out on cohorts of about one hundred isolated particles, in low-coverage samples like those ones shown in Figure 5.21a and b. Electron diffraction pattern (Figure 5.22) confirms FFT indications, as the signature of metallic tetragonal β-tin is identified. SAED experimental data of Sn nanoparticles by SCBD, summarized in Table 2, match well values of bulk metallic tin, therefore excluding major size-effects on crystallographic properties of metallic tin at such dimensions. No diffraction pattern ascribable to phases other than tetragonal metallic

β-tin is visible, confirming that oxide phase of nanoparticles' shell is amorphous, as suggested by HRTEM images.

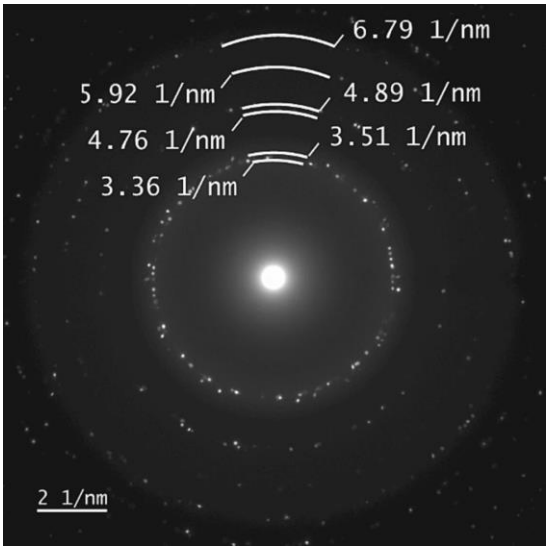

Figure 5.22. Electron diffraction pattern generated by a group of about one hundred isolated Sn particles from low-coverage samples. Radii of rings hosting diffraction spots are shown in the image, while complete crystallographic analysis is reported in Table 2.

Table 2. Crystallographic analysis results and comparison with data of bulk metallic tin (PDF card 00-004-0673).

1/d (nm^{-1})	**d (nm)**	**Plane (h k l)**	**d_{bulk} (nm)**
3.36	0.2924	(2 0 0)	0.2915
3.51	0.2801	(1 0 1)	0.2793
4.76	0.2070	(2 2 0)	0.2062
4.89	0.2008	(2 1 1)	0.2017
5.92	0.1658	(3 0 1)	0.1659
6.79	0.1481	(1 1 2)	0.1484

TEM analysis has been carried out on samples with exposure to air limited to 10 min as well as on samples with more than one month exposure: both sample typologies showed the exact same traits, which suggested that room temperature oxidation process of tin NPs takes place on a few-minutes time scale at most, leaving afterwards a basically stable structure/composition. Albeit happening at room temperature, as mentioned in the introduction, NPs surface curvature and alleged large density of surface defects are elements promoting oxidation dynamics and accounting for reaching of stable configurations within a short timescale. XRD, XPS, and Raman spectroscopy data reported in the following are collected on samples experiencing about one month exposure to air, therefore fully stabilized with respect to oxidation process.

As deposition proceeds, the condition of isolated particles gives way to the formation of a cluster-assembled film. Although cluster beam deposition typically preserves the identity of primeval clusters into the film, which is therefore characterized by a nanogranular structure, in the case of low melting point materials as tin this is questionable. In fact, the dissipation of clusters kinetic energy at the impact in combination with the reduced latent heat of fusion of tin NPs [93] is expected to favour coalescence, as indeed already discussed in Section 5.2.2, and the formation of a nanostructured film where original clusters and coalescence-induced larger structures coexist.

Grazing incidence XRD characterization of samples having "bulk equivalent thickness"[1] of 50 nm unveiled spectra dominated by metallic β-tin with tetragonal structure, space group $I4_1/amd$ (Figure 5.23.), in agreement with FFT analysis of HRTEM images (Figure 5.21b) and SAED results (Figure 5.22); no other ordered phases are visible. Absence of peaks ascribable to oxide phases suggests that most of them are amorphous and prospective ordered oxide phases are below the limit of detection of the equipment.

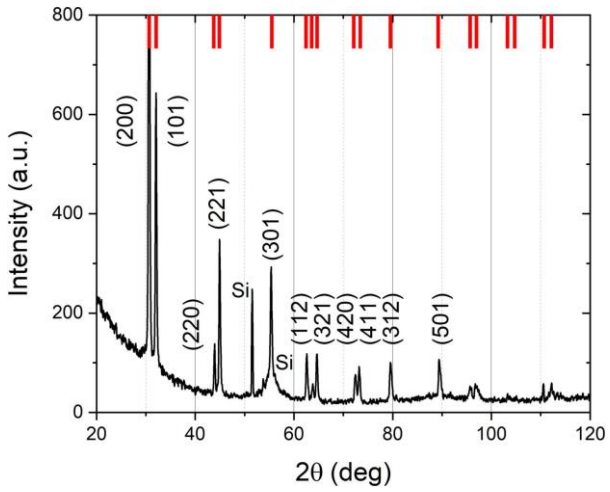

Figure 5.23. XRD spectrum of cluster-assembled Sn film. Red bars show expected peak positions of tetragonal β-tin (space group I41/amd), which sample spectrum perfectly matches to. Main peaks are labelled with corresponding crystallographic planes. Peak at 52 deg and bump at 55 deg are attributed to silicon substrate (Si label).

An average size of crystalline domains has been calculated following a Rietveld Size -Strain Analysis and resulted to be >150 nm. Such value highlights the importance of coalescence phenomena among metallic tin NPs during SCBD. By comparing average crystallite dimension from XRD and "bulk equivalent thickness" from QCM, where the former is three times the latter, it can indeed be inferred that tin layers by SCBD grow in form of separated 3D islands, following coalescence phenomena, instead of a flat 2D film. Beside literature evidence about similar systems [115–117], island-based growth has been also recently confirmed by in-situ electrical transport experiments carried out onto cluster-assembled tin films, and related Atomic Force Microscopy characterizations [118].

Interestingly, intra-islands regions ensure effective exposure of the whole islands to oxidation process, while islands dimension from several tens up to more than one hundred nanometres ensure the existence of a "metallic reservoir" large enough to survive Cabrera-Mott oxidation process. In this respect, metallic Sn islands by SCBD represent a favourable architecture for the study of oxidation of tin nanostructures, as inner metallic core and outmost surfaces exposed to oxygen excess define two limit

conditions among which a complete oxidation gradient is expected to set, as schematically shown in Figure 5.24.

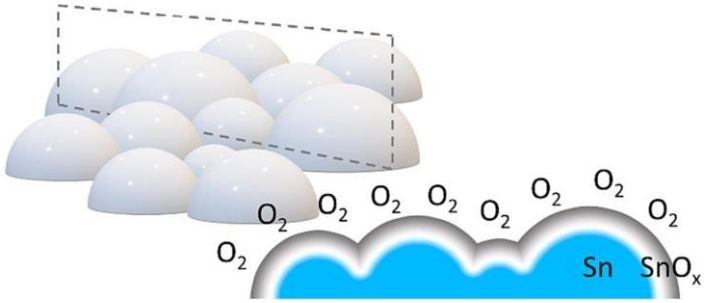

Figure 5.24. Schematic representation of Sn islands formed by clusters coalescence in high vacuum, which subsequently undergo oxidation by air exposure. Islands cross section along dashed plane highlights the oxidation gradient, which is expected to form between metallic cores and outmost surfaces exposed to oxygen excess.

XRD unveiled that crystallites are subjected to a micro-strain of (0.161 ± 0.005) %. Micro-strain can have several causes, including residual stresses, dislocations, vacancies, grain boundaries [119], and all of them can be induced or amplified by the three main phases of sample preparation: (i) gas-phase nucleation/growth of Sn clusters; (ii) clusters impact during film growth; (iii) oxidation process. The observation of a micro-strain value as low as 0.16 % resulting from the pile-up of all possible micro-strain causes mentioned above remarkably suggests that the three main phases of sample preparation have not a severe impact on them.

Oxidation states of island-structured tin samples identical to XRD ones -in terms of thickness and oxygen exposure time- have been investigated by XPS. Core level Sn $3d_{5/2}$ has been specifically analysed, unveiling the presence of all oxidation states, namely Sn^0, Sn^{2+}, and Sn^{4+}, through their respective peaks, positioned at 484.7 eV, 486.2 eV, and 487.1 eV (Figure 5.25a), in agreement with published results [120,121]. This confirms the observed core–shell structures to be made of tin metallic core and tin oxide shell, as deduced from TEM analysis. Since XPS depth of analysis in tin and tin oxide, estimated to be 6.9 nm with TPP-2 M equation [122], is larger than shell thickness, semi-quantitative comparison of Sn^{2+} and Sn^{4+} components of Sn $3d_{5/2}$ peak is allowed, and the ratio of the area of Sn^{4+} component over Sn^{2+} one returns 0.9. Although depth distribution of Sn^{2+} and Sn^{4+} oxidation states cannot be inferred, this

value anyway remarkably suggests that the two states are present with very similar abundance into oxide shell.

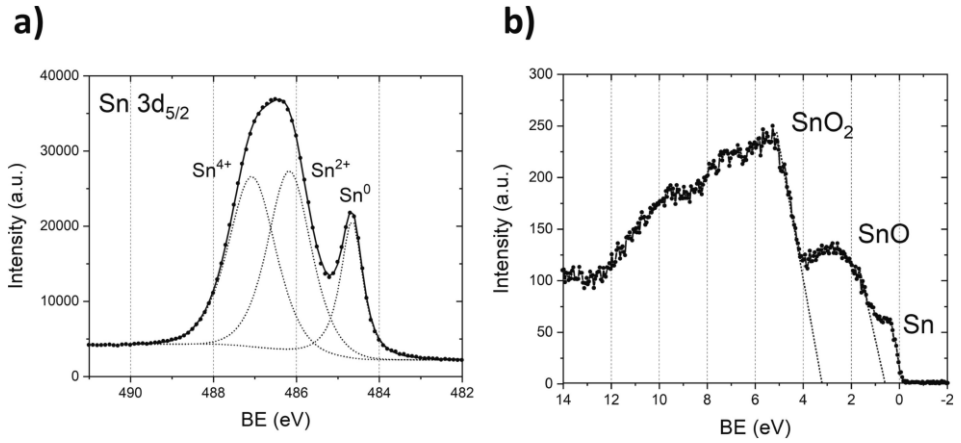

Figure 5.25. a) XPS spectrum of Sn $3d_{5/2}$ core level, showing contributions from metallic tin (Sn^0) and both oxidation states Sn^{2+} and Sn^{4+} at 484.7 eV, 486.2 eV, and 487.1 eV, respectively. b) Valence band analysis confirming results from core levels analysis. Dashed lines extrapolate to binding energy (BE) axis the edges of main structures centred at 5.2 eV and 2.9 eV, to estimate distance of valence band top of the two species from Fermi level E_F, positioned at 0 eV.

Due to the presence of several overlapped components, the analysis of oxygen O 1s peak is particularly challenging. In facts, in addition to the two oxide components of oxygen atoms bonded to Sn^{2+} and Sn^{4+}, the observation of silicon in XPS survey scan, due to the accessibility of the substrate enabled by islands-like film structure (Figure 5.24), introduces a third oxide component in O 1s peak, while the observation of adventitious carbon allegedly indicates the presence of various organic moieties, which might also include hydroxyl groups. In these conditions multi-peak fitting is untrustworthy, making O 1s peak poorly informative in regard to our discussion. For this reason, O 1s is not reported here.

Valence band analysis confirmed outcomes of Sn $3p_{5/2}$ core level analysis, as spectral features ascribable to metallic tin (Sn), $Sn^{2+}O$ (SnO), and $Sn^{4+}O_2$ (SnO_2) are visible (Figure 5.25b). Valence band spectrum is characterized by broad structures among which we focus on those ones centred at around 5.2 eV and 2.9 eV, as well as on plateau at 0.4–0.7 eV with edge reaching 0 eV on binding energy (BE) axis, i.e.,

system's Fermi level E_F. The latter is the signature of metallic tin; the structure at 2.9 eV stems from hybrid state of Sn 5s and Sn 5p and is attributed to SnO; while the structure at 5.2 eV stems from O 2p level and is attributed to SnO_2 [123–125]. By extrapolating the edge of 5.2 eV and 2.9 eV structures to estimate the distance of valence band top levels of the two components from E_F, values of 3.2 eV and 0.6 eV are obtained, respectively. Even if the structure of tin oxides valence band is still in itself subject of investigation, these values are consistent with a material composition hosting at the same time SnO_2 and SnO (and metallic Sn) [126,127].

If on one hand the presence of both oxidation states Sn^{2+} and Sn^{4+} with similar abundance was clearly demonstrated by electron spectroscopy, on the other hand nothing can be said about their distribution along radial direction. Nevertheless, the presence of a metallic core and the exposure of particles' topmost surface to oxygen-rich atmosphere, suggest that an oxidation gradient might be expected, as already proposed in Figure 5.24, where oxygen abundant phase, i.e., SnO_2, is predominantly present towards the surface, while SnO is predominantly present towards metallic core, according to Cabrera-Mott diffusion of oxidizing species. At this point, an intriguing question arose regarding the alleged presence of intermediate oxides within such oxidation gradient. In this respect, it is worth noting that intermediate oxides are actually made of a combination of the two oxidation states of Sn atoms (and related oxygen atoms): for instance, Sn_3O_4 is the short version for $Sn^{2+}{}_2O_2Sn^{4+}O_2$.

As clearly pointed out by Eifert et al. [128], Raman spectroscopy provides substantial advantage in respect to XRD when dealing with the identification tin oxide phases, particularly intermediate ones. In fact, as it probes crystal dynamic properties, namely phonon profile, which strongly depend on local bonding structure and -in addition- is sensitive to the number of atoms per unit cell, Raman spectroscopy can distinguish among tin oxide phases even if their (static) structural units, which determine XRD, are very similar. In addition, being insensitive to metals, in the case of metal-core/oxide-shell structures Raman spectroscopy is expected to selectively collects information from oxide shells only (though, we argue that a synergic action is anyway played by nanoscale metallic cores in diffusing Rayleigh photons, thus improving Raman scattering yield).

Figure 5.26 shows Raman spectrum over a broad frequency range. In the low frequency region (up to 300 cm^{-1}), we identify the two peaks expected for SnO (114 and 209 cm^{-1}), the peak expected for SnO_2 (123 cm^{-1}), but also several other intense modes at 140, 169 and 239 cm^{-1}, which clearly demonstrate that an additional polymorph is present. We assign them to Sn_3O_4 based on the remarkable match with the frequencies calculated and experimentally observed by Eifert et al. [128] for this polymorph. The choice of an excitation wavelength of 442 nm, corresponding to photon energy of 2.8 eV, aligns well with the optical bandgap of Sn_3O_4 [129,130]. Consequently, a higher Raman yield can be expected from Sn_3O_4, which would make this phase particularly visible even if it might be present in small amount with respect to other phases. In high frequency region (expanded in Figure 5.26), modes are broader and assignments less conclusive in general, nevertheless observed features can be reconciled with the presence of SnO, SnO_2 and Sn_3O_4. Table 3 summarizes the observed modes with their assignment to a phase, a mode symmetry, and their comparison with the computed/measured frequencies reported in [128].

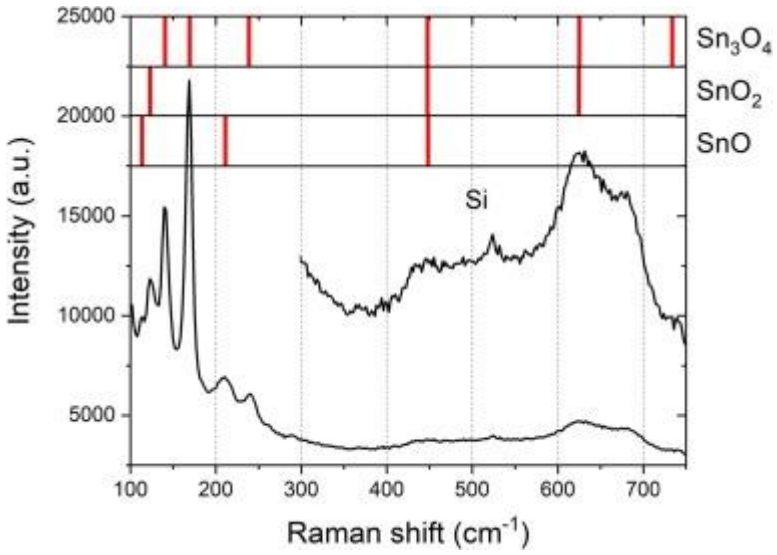

Figure 5.26. Raman spectrum of cluster-assembled Sn film upon room temperature oxidation. Red bars show the vibrational modes ascribable to main oxide phases SnO and SnO_2, as well as to intermediate oxide Sn_3O_4. Broad structure in the 400–800 cm^{-1} range

is expanded to favour identification of the various contributions. Full list of peaks is reported in Table 3.

Table 3. Raman shift peaks assignment in comparison with theoretical and experimental data in [128].

Raman shift (cm^{-1}) **This work**	**Phase**	**Mode**	**Raman shift (cm^{-1})** **Theor.** [128]	**Raman shift (cm^{-1})** **Exp.** [128]
114	SnO	E_{1g}	115	115
123	SnO_2	B_{1g}	129	(not detectable)
140	Sn_3O_4	A_g	140	140
169	Sn_3O_4	A_g or B_g	170, 172	170
209	SnO	A_{1g}	217	211
239	Sn_3O_4	A_g	247	238
446	$SnO/SnO_2/Sn_3O_4$			
626	SnO_2	A_{1g}	624	639
	Sn_3O_4	A_g	632	627
677	?			
734	Sn_3O_4	B_g	718	700

The clear observation of the Sn_3O_4 signature confirms this phase spontaneously forms upon oxidation of metallic Sn NPs at room temperature. We propose that the intermediate oxide Sn_3O_4 is located between SnO_2 and SnO in NPs shell, along

inwards radial direction from NP surface to metallic core, as consequence of Cabrera-Mott inward oxygen drift at room temperature.

5.4.3 The case of Ni: hollow particles by Kirkendall effect

The analysis of isolated Ni clusters by HRTEM and SAED unveils the massive presence of ordered phases. Several inter-plane distances were measured in real-space HRTEM images as well as deducted from reciprocal-space diffractograms, as shown in Figure 5.27. According to the literature and to crystallographic databases, inter-plane distances confirm XPS results regarding the presence of metallic Nickel and NiO, in both cases in cubic phase (PDF numbers 01-089-1729 and 00-047-1049 respectively) [131,132], as summarized in Table 4. On the contrary, unambiguous indications about ordered phases of Ni(OH)2 cannot be collected, suggesting that hydroxide is mostly present as amorphous phase. Regions where metallic Ni is identified are always surrounded by NiO, which protects the metallic core from further oxidation. Similarly to XPS, HRTEM analysis was accomplished more than one month after deposition, during which samples have been stored in atmospheric conditions. We therefore assume that any short- and mid-term oxidation dynamic has come to an end and the observed structures are stable in time. By transferring this result, obtained on isolated particles, to the cluster-assembled films, where metallic particles touch each other during film growth and can partially coalesce at the point of contact, we foresee that a metallic network interconnecting the majority of clusters composing the film could survive the oxidation process. In this case, we would deal with a topologically complex metallic conductor, whose charge transport properties worth to be investigated, the perspective of electrochemical and sensing applications. This will be discussed in CHAPTER 6.

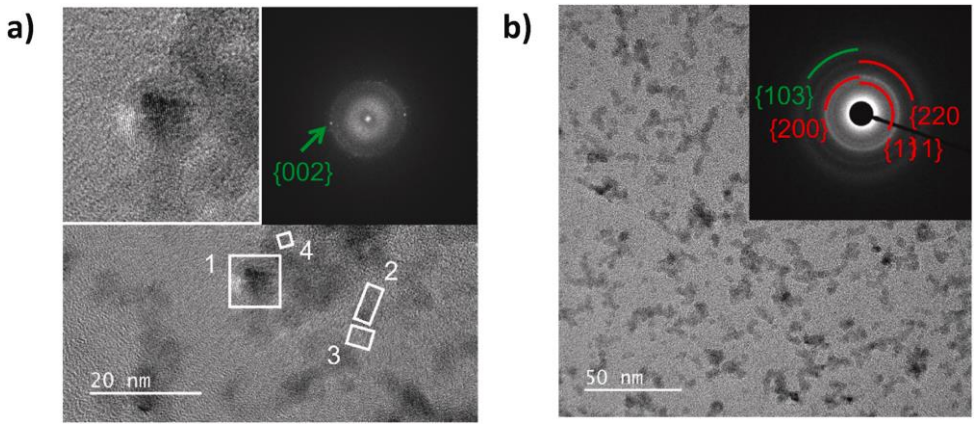

Figure 5.27: a) TEM image showing the nanostructure of the material and highlighting the regions where direct measurements of crystalline spacing was performed (numbered white frames); top left inset shows the magnification of area 1 while top right one shows the Fast Fourier Transform (FFT) carried out on the entire picture, where dots related to metallic Nickel (002) symmetry are clearly visible. b) TEM image at lower magnification where SAED was carried out; top right inset shows the obtained diffraction pattern, where the main crystalline symmetries of metallic Nickel (green) and NiO (red) observed are reported.

Table 4. Summary of results of crystallographic analysis carried out on HRTEM and SAED images, showing that the ordered phases identified are ascribable to metallic Ni and NiO only, both in cubic symmetry. Positions in first column refer to the labelled white boxes in Figure 5.27a; FFT method applied to the whole image refers to Figure 5.27a too. Data from diffraction-based method (SAED) applied to the whole image refer to Figure 5.27b.

Position	**Method**	**d-spacing [nm]**	**Species**	***hkl* indexes**	**d-spacing Ref. [nm]**	**Error**
1	Direct	0.2184	Ni	002	0.2165	1.1%
2	Direct	0.2178	Ni	002	0.2165	0.6%
3	Direct	0.2253	Ni	100	0.2295	1.8%
4	Direct	0.2068	NiO	200	0.2084	0.8%
Whole Image	FFT	0.2185	Ni	002	0.2165	0.9%

Whole Image	SAED	0.2425	NiO	111	0.2407	0.7%
Whole Image	SAED	0.2096	NiO	200	0.2084	0.5%
Whole Image	SAED	0.1496	NiO	220	0.1474	1.5%
Whole Image	SAED	0.1217	Ni	103	0.1222	0.4%

Interestingly, the presence of intra-particle ordered phases of Ni and NiO is observed although the deposition is done at room temperature and no post-deposition annealing step is performed. We suppose that the cubic phase of the particles' metallic cores traces back to the original structure of the deposited clusters, before air exposure, which in turn forms inside the cluster source, during nucleation and growth following cathode sputtering by the high-energy pulsed electrical discharge (steps b and c in Figure 2.9). In addition, we suppose that the cubic phase of metallic Ni promotes the ordered growth of NiO shells during air exposure at room temperature, taking advantage of the release of the heat of formation of the oxide (240 kJ/mol). Grain boundaries within metallic clusters are expected to play a role in Ni cations diffusion feeding oxidation process at the surface and in the "path towards oxidation" followed by a specific particle, which in some cases leads to a fully oxidized particle while in other cases preserves a metallic core. Regarding the $Ni(OH)_2$ outer shell, no evidence of ordered phases is identified and its amorphous nature is then proposed. We argue that the mismatch between the simple NiO cubic symmetry and the complex symmetries of the two mostly known polyforms of $Ni(OH)_2$ (i.e. trigonal one and water-intercalating layers "turbostratic" one, named β and α respectively [133]) prevents triggering the growth of ordered $Ni(OH)_2$ onto NiO.

Beside core-shell structures, it was noted that samples include several objects having contrast features in TEM images that are compatible with hollow structures, where a spheroidal shell surrounds a central void, sometimes rather irregular. White arrows in Figure 5.28a point to some of them. Figure 5.28b and c shows examples of HRTEM images where core-shell structures and hollow structures are contemporary observed. If on one hand the observation of hollow structures in not surprising, as in-line with the well-known behaviour of Ni nanoparticles undergoing oxidation upon the Kirkendall effect (according to which, outwards radial flow of metallic ions dominates on inwards flow of oxidizing species and the final result is indeed an oxide shell surrounding a void [134–138]), on the other hand in the samples here described the phenomenon takes place without the intervention of any high-temperature process.

The coexistence of core-shell structures and Kirkendall hollow structures within the same dimensional range suggests that the spontaneous, room temperature reaction of metallic Ni nanoparticles with air can either get to a complete oxidation of the nanoparticle or end at some intermediate level, preserving a metallic residue. The particle dimension per-se seems not to be enough to define unambiguously the oxidation process outcome and, even if the fully oxidized configuration -either hollow or compact-is expected to be the thermodynamically favoured one, the very-slow kinetics due to room temperature in some cases can stop the oxidation process before completion.

At this stage it is not possible to explain why in some cases the fully hollow structure is reached while in others it is not, apart from ascribing this to the variety of the structures of Nickel clusters -albeit their very similar dimensions-at the beginning of the oxidation process, for which some are more prone than others to complete it. We propose that this variety of cluster structures arises from the sudden, and likely out of equilibrium, “freezing” of gas-phase cluster growth due to supersonic expansion, before deposition (step d of Figure 2.9). This hypothesis may suggest considering SCBD as a way to prepare and deposit a complex ensemble of nanoparticles with similar ultrafine dimensions but different intra-particle structures, thanks to the freezing of metastable crystallographic configurations.

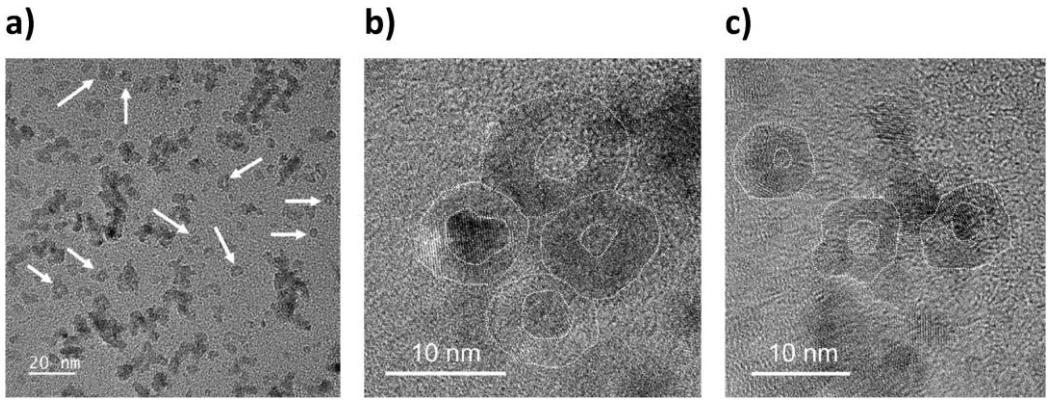

Figure 5.28: a) TEM image highlighting the presence of hollow structures (white arrows). b) c) HRTEM images showing in detail hollow structures as well as core-shell ones. Image b) is the same of the inset in Figure 5.27.

From XPS survey spectrum (Figure 5.29), only Nickel (27.9 at.%), Oxygen (39.3 at.%) and Carbon (32.8 at. %) are present at the surface of the samples. No other contaminant than Carbon, attributed to adventitious carbon, nor the substrate contribution are detected. Even though XPS is well suited for the characterization of nanometric scale structures thanks to an analysis depth limited to 5–10 nm, identifying and quantifying Nickel-based phases (which can include metal phase, oxides and hydroxides) is challenging. Indeed, as for many transition metals, it has been demonstrated that chemical states cannot be represented by single contributions [139–141]. Multiplet splitting resulting from shake-up and plasmon loss structures as well as inter-atomic and non-local coupling or screening effects must be considered [139,140]. Four relative maxima can be observed on the Ni $2p_{3/2}$ spectrum at 852.3 eV, 854.0 eV, 855.7 eV and 861.0 eV that clearly reveal the presence of several Ni-based phases in the sample (Figure 5.29). Comparing to the reference spectra of NiO_x samples published in literature [139,142–146], the first peak can undoubtably be attributed to metallic Ni. The next two maxima energy positions roughly correspond to NiO, however their intensity ratio is not in agreement with a pure NiO phase meaning that at least a third phase as $Ni(OH)_2$ and NiOOH has to be considered as they both present a single and wide peak around 856.0 eV. The maximum observed around 861.0 eV corresponds to satellites structures as previously described and should be taken into account for a better accuracy of the fitting. The Ni $2p_{3/2}$ experimental spectra of the cluster assembled samples has been reconstructed with a linear combination of reference spectra (Ni, NiO, $Ni(OH)_2$ and NiOOH (γ-NiOOH and α-NiOOH)) extracted

from data published elsewhere [142]. Remarkably, Major et al. already published this fitting approach for nickel compounds [147]. The spectra line shapes of these reference samples have been depicted by Biesinger et al. with a set of peaks that has been used in the present work to draw the spectra of the various NiO_x phases [142]. These spectra were recorded on reference materials with an Axis Ultra DLD equipment, with both the same acquisition parameters and spectra background removal method as the material investigated in this study. The spectra fitting parameters (i.e. FWHM, peak energy separation and relative intensities of the set of peaks) were strictly maintained constant so that the shape of each reference spectrum was fixed. Only the intensity and the energy position of these overall envelops, were allowed to vary to respectively determine the relative proportion of each phase in the film and to compensate for the eventual differential charge effects between the various phases or towards the adventitious carbon used for spectra energy calibration. Clusters are found to mainly consist of metallic Ni, NiO and $Ni(OH)_2$ (nickel hydroxide), with atomic fractions around 20%, 45% and 35%, respectively. No NiOOH was found whatever the line shape considered, i.e. γ-NiOOH and α-NiOOH.

Interestingly, we note that the Ni, NiO and $Ni(OH)_2$ line shapes are respectively located at −0.4 eV, +0.0 eV and +0.8 eV of the position of the reference spectra of the bulk materials [147]. Since in poorly-conducting samples electron transfer from the substrate after the photo-ionisation process leads to a gradient in charge distribution, the potential across the section of clusters in the topmost layer can explain the observed energy shifts, suggesting that the species towards external environment is $Ni(OH)_2$, which lies onto NiO, which in turn lies onto metallic Ni.

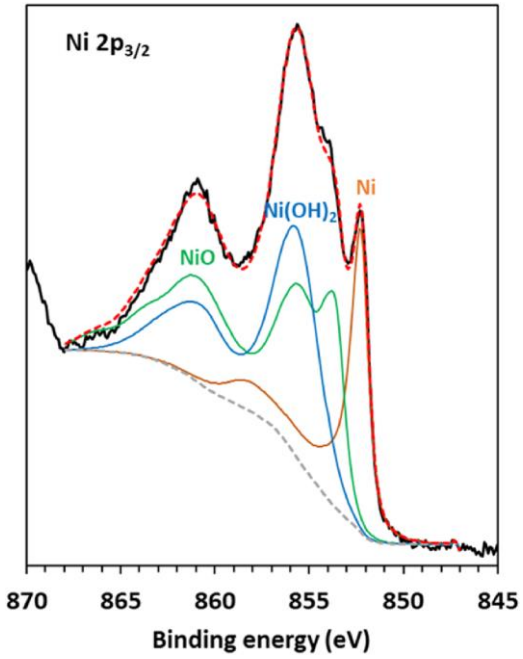

Figure 5.29. Ni $2p_{3/2}$ XPS spectrum of Nickel cluster-assembled films. The black line, the red and the grey dashed lines are the experimental spectrum, the fitting reconstruction and the Shirley background, respectively. The Ni $2p_{3/2}$ spectrum is curve fitted with reference spectra from bulk samples published elsewhere [142].

Even if a contribution to the oxidation of Ni clusters during the deposition by the 1×10^{-7} mbar background gas cannot be excluded, NiO and $Ni(OH)_2$ are supposed to mainly arise from spontaneous reactions due to air exposure at room temperature and atmospheric pressure. Referring to what is observed on flat surface of metallic Nickel exposed to the atmosphere, (i) oxygen dissociative chemisorption, (ii) oxide nucleation, (iii) lateral growth of NiO islands and (iv) islands coalescence steps are supposed to proceed also on Ni nanoparticles until a complete NiO layer passivates the metallic surface, while a subsequent reaction between the oxide layer and airborne water molecules leads to hydroxide formation [148–152]. Studies on planar surfaces report about the stability of the Ni–NiO–$Ni(OH)_2$ configuration in air at atmospheric pressure, where the layer of oxide and hydroxide has a total thickness slightly above 1 nm [149]. Clearly, the spheroidal shape of Nickel clusters of the present study -with particles dimensions of few nanometers-sets a substantial geometrical difference with respect to planar surfaces, and the high density of grain boundaries and crystalline defects, which favour the diffusion of species during the oxidation process, can

promote the metal-oxide interface formation and evolution [151,153,154]. Nevertheless, the observation of metallic Nickel surviving the oxidation suggests that in a fraction of particles the oxidation is not complete, and the presence of core-shell structures can be envisaged.

Finally, regarding the link between ex-situ data on films morphology and in-vacuum growth dynamics mentioned in Section 5.3: assuming the validity of this link implies that the effect of oxidation on Nickel clusters structure reported above is not affecting the scaling law describing the collective morphology of the cluster-assembled films. This is a delicate point deserving to be further investigated through dedicated in-situ experiments.

5.4.4 The case of W: oxidation gradients

The XPS spectrum (Figure 5.30) indicates that WO_3 is the predominant oxidation state, with major peaks observed at approximately $35.6\,eV$ and $37.7\,eV$, corresponding to the $W\ 4f_{7/2}$ and $W\ 4f_{5/2}$ spin-orbit components of tungsten trioxide. This result is consistent with the high reactivity of tungsten under ambient conditions, where exposure to oxygen rapidly leads to the formation of a stable WO_3 layer on the surface. WO_3 is well-documented as the most thermodynamically stable phase under these conditions due to its complete oxidation state (W^{6+}) [155–159].

In addition to WO_3, the spectrum reveals the presence of lower oxidation states, specifically WO_2 (W^{4+}) and W_2O_5 (W^{5+}). The WO_2 peaks are located around $34.1\,eV$ for $W\ 4f_{7/2}$ and $36.3\,eV$ for $W\ 4f_{5/2}$, while W_2O_5 peaks are observed near $34.8\,eV$ and $36.9\,eV$ for $W\ 4f_{7/2}$ and $W\ 4f_{5/2}$, respectively. These sub-stoichiometric oxides suggests that the oxidation process may have been incomplete or that some regions of the film are less oxidized [157–162].

A minor peak corresponding to W^0 is also detected, indicating that some regions of the tungsten remain unoxidized. This peak appears around $31.5\,eV$ for $W\ 4f_{7/2}$ and $33.7\,eV$ for $W\ 4f_{5/2}$ [157,159]. The persistence of metallic tungsten is likely due to limited oxygen diffusion into the innermost regions of the tungsten clusters or within densely packed grains where oxygen diffusion is significantly hindered.

The observed distribution of oxidation states across the tungsten cluster-assembled films suggests the presence of an oxidation gradient, heavily influenced by the nanostructured nature of the films. These films, formed through the soft assembly of tungsten clusters, exhibit a porous structure with varying grain sizes, contributing to non-uniform oxidation throughout the material. To further understand this oxidation gradient, it is helpful to compare it with the oxidation behavior of tungsten nanoparticles as detailed in recent studies.

In the study by Arnas et al. [163], tungsten nanoparticles generated via conventional DC magnetron discharges developed a distinct core-shell structure after approximately 46 days of air exposure. The cores of these nanoparticles, ranging from 15 to 30 nm, predominantly exhibited the $\beta - W$ phase, surrounded by an amorphous oxide shell up to 6 nm thick. This core-shell configuration suggests an analogous oxidation behavior in the tungsten clusters or grains within the films. Just as the nanoparticles develop an oxide shell while maintaining a metallic core, the tungsten clusters in the films likely undergo a similar oxidation process, resulting in the formation of a WO_3 surface layer while the core retains a lower oxidation state or remains metallic. This comparison provides valuable insights into the oxidation behaviour of cluster-assembled tungsten films, and similarly to the cluster assembled tin films studied in this work [164], I propose an analogous oxidation mechanism characterized by an oxidation gradient evolving from metallic W, to WO_2, to W_2O_5, to WO_3 resulting from room temperature exposure to air.

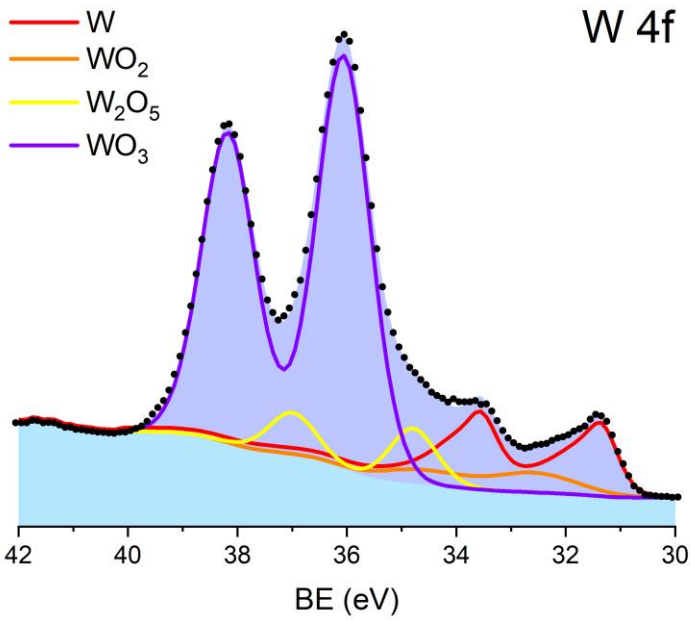

Figure 5.30: W 4f XPS spectrum of tungsten cluster-assembled films oxidized in air at room temperature. The deconvoluted peaks correspond to metallic tungsten (W, red), tungsten dioxide (WO_2, W^{4+}, orange), tungsten pentoxide (W_2O_5, W^{5+}, yellow), and tungsten trioxide (WO_3, W^{6+}, purple).

The observed oxidation gradient and the presence of multiple tungsten oxide phases within the film have significant implications for the material's properties. For instance, the mixture of WO_3 with WO_2 and W_2O_5 could result in a material with heterogeneous electrical properties. The residual metallic tungsten also suggests that the film could maintain some conductive pathways, which might be beneficial in applications where a balance between conductivity and oxidation resistance is required (this will be discussed in Section 7.2.3).

CHAPTER 6. IN-SITU ELECTRICAL TRANSPORT

6.1 Percolation theory

Percolation theory provides a fundamental framework for understanding the relationship between morphological characteristics and electrical conduction in nanogranular metallic films. This theory studies the formation conductive pathways within a system, , where elements, such as particles in a lattice, occupy specific sites, with each occupied site representing a particle. A percolation threshold is reached when these occupied sites create an unbroken pathway, establishing connectivity throughout the entire system [165,166].

The basic model in 2D Percolation Theory is the bond percolation model on a square lattice. In this model, each edge (or bond) between adjacent sites (or nodes) is randomly occupied with probability p or unoccupied with probability $1-p$. Alternatively, the site percolation model considers each site to be occupied with probability p and unoccupied with probability $1-p$. Both models exhibit a critical threshold p_c at which a giant connected cluster appears, spanning the entire lattice. This critical probability is central to the theory and determines the transition between a non-percolating and a percolating phase [167].

In the context of this work, percolation theory serves as a fundamental framework for elucidating the relationship between morphological properties and electrical conduction in cluster-assembled metallic films. By monitoring the electrical current and bulk equivalent thickness in situ, we can observe the evolution of electrical transport properties as a function of thickness or time. Figure 6.1 illustrates this behavior, highlighting three distinct regions: the insulator region, where sparse particle distribution prevents electrical current flow; the percolation region, where conductance increases sharply as a connected network of particles forms; and the continuous region, where high conductance is achieved through the progressive formation of continuous conductive paths.

The critical concentration of conductive particles, or percolation threshold p_c, is a pivotal factor in determining the onset of conductance. For a 2D lattice site percolation, this threshold is 59.27%. Near this threshold, the electrical conductivity G scales with the relation

$$G \sim (p - p_c)^t \tag{6.1}$$

Where the exponent t has a universal value and it dependents on the system's dimensionality [168].

When dealing with nanogranular metal films, the classical concept of geometrical contact, central to percolation theory, requires careful re-evaluation. While traditional percolation theory assumes that conducting particles are categorized either electrically connected, with finite inter-particle conductance, or entirely disconnected. This binary approach is suitable for composites with large conducting particles. However, in nanostructured materials with particle sizes limited to a few nanometers, this clear demarcation is less applicable. As metal particles come into contact, conductive pathways emerge, and reaching a critical coverage fraction of the conductive phase induces a notable rise in conductivity. This increase is driven by a combination of percolation within the evolving metallic network and electron tunneling across isolated particles. With further increases in the fraction of metal particles, tunneling or hopping effects diminish in importance compared to percolation [9].

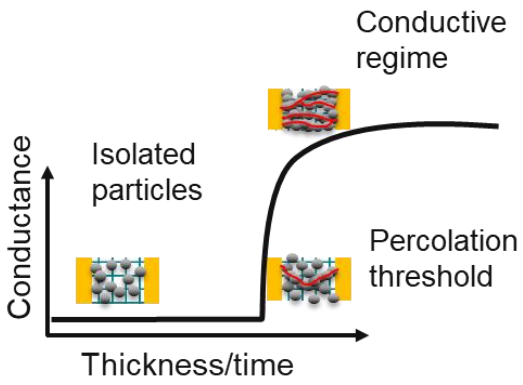

Figure 6.1. Illustration of a percolation curve showing the evolution of conductance as a function of material thickness or time. Initially, isolated particles avoid electrical current flow. As thickness/time increases, the system reaches the percolation threshold, where conductive paths begin to form between particles. Beyond this threshold, conductance

rapidly increases, indicating the transition to the conductive regime, where a fully interconnected network is established.

Figure 6.2a shows an example of raw data, namely electrical current across IDE and thickness deposited onto QCM, where the stepwise trend of both current and thickness depends on repeating movements (rastering) of the sample holder hosting IDE and QCM, in front of the cluster beam (already commented in Section 4.1.3). Cross correlation of current and thickness data accumulated at the end of each sweep (Figure 6.2b) qualitatively shows the well-known behavior of electrical conduction of thin metallic films as a function of substrate coverage, where three distinct regimes are observed: (i) insulating phase, (ii) percolation phase, and (iii) three-dimensional conduction beyond percolation.

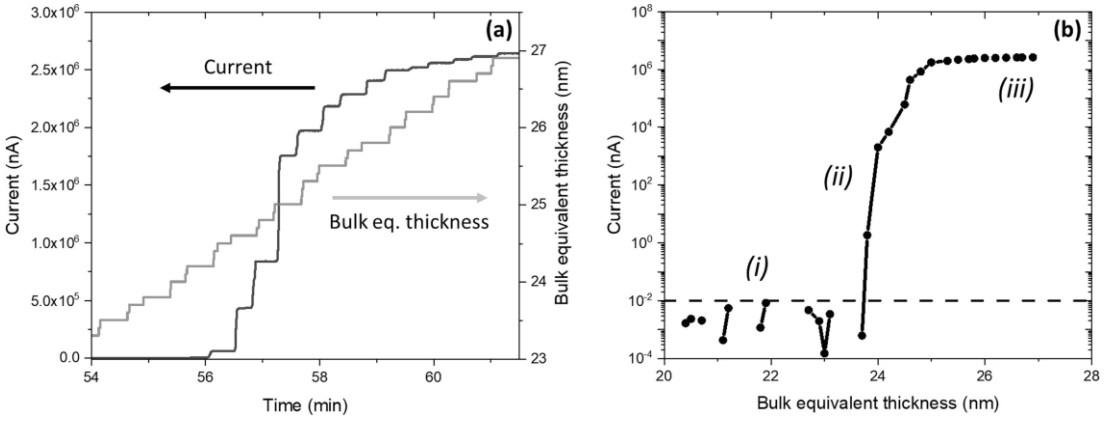

Figure 6.2. (a) Example of raw data corresponding to Sn during in-situ measurement of deposited thickness and electrical current through the growing film; deposition rate is 0.17 nm per rastering step. (b) Current as function of the thickness obtained by cross-correlation of raw data values at the end of each rastering step. Dashed line shows background level due to noise inherent to the electrical readout setup.

In the initial stage, the system exhibits an insulating behavior, indicative of isolated Sn NPs on the substrate. Due to noise inherent to the electrical readout setup, current measurements are reliable if larger than 10 pA (dashed line in Figure 6.2b). As deposition proceeded, current through IDE remains below background level for thickness smaller than 24 nm. The transition to the percolation phase is marked by a sudden onset in conductance upon reaching a particular deposited thickness value, slightly below 24 nm in this example, indicating the percolation threshold. From this

point on, deposition causes nanoparticles to get each other into contact, creating a conductive network, where progressively more pathways are available for current to flow. Beyond the percolation phase, the electrical conduction exhibits a steady rise, although at a lower rate, indicative of the formation of a stable, three-dimensional conducting network, which grows in thickness as deposition proceeds.

Section 6.2 will be focused on the electrical characterization at percolation in correlation of the aggregation mechanism occurring in the sub-monolayer regime, as discussed in Section 5.2.

6.2 Electrical characterization at percolation

6.2.1 High melting point materials: the cases of Ni, Pt and W

This section presents the electrical characterization at the percolation threshold for Ni, Pt, and W, with a primary focus on Pt as the reference material. The analysis of Pt serves as a basis for understanding the percolation behavior in these high melting point materials. Where relevant, comparative discussions of the results for Ni and W will be introduced to emphasize material-specific differences and similarities in their electrical properties at the percolation threshold. These comparisons will provide insights into how variations in material properties, such as particle size and surface interactions, influence the percolation behavior of each material.

In analogous way as in the example of Sn films described in Section 6.1, cross correlation of current and thickness data accumulated at the end of each sweep for Pt cluster assembled films (Figure 6.3), qualitatively shows the well-known behavior of electrical conduction of cluster assembled-films metallic films as a function of thickness.

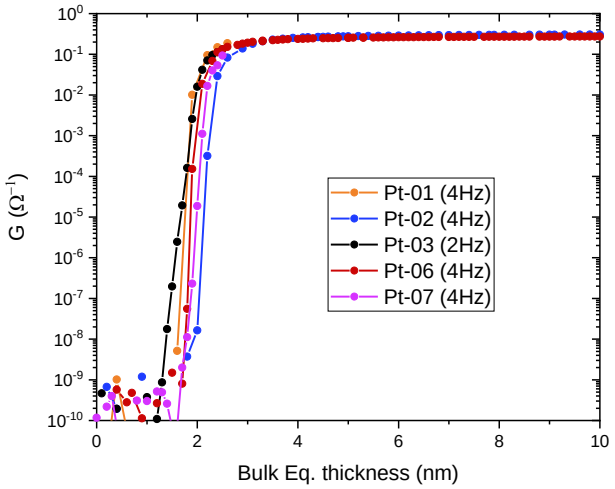

Figure 6.3. In-situ conductance of cluster-assembled Pt films as a function of the thickness. Regardless of the deposition rate the onset occurs at a narrow thickness value of 1.3-1.8 nm.

In the initial stage of deposition, the system remains in an insulating phase, where Pt clusters begin to interact on the substrate, forming early aggregates of nanoparticles. During this phase, the current measured across the interdigitated electrodes remains below the background level for thicknesses smaller than approximately 1.3 nm, indicating the absence of a continuous conductive path which avoids electrical current to flow.

As deposition continues, a sharp increase in conductance signifies the transition to the percolation phase, occurring within a narrow thickness range of 1.3 to 1.8 nm. At this point, the deposited nanoparticles come into contact, forming an interconnected conductive network. As deposition progresses, more conductive pathways are established, facilitating larger current flow. Beyond the percolation phase, the electrical conduction continues to rise steadily, albeit at a slower rate. This phase indicates the formation and thickening of a stable, three-dimensional conductive network as deposition of clusters progresses. This will be discussed further in Section 6.3.

Samples were deposited at a repetition rate of 2 Hz and 4 Hz and there was no evidence to suggest that this parameter influenced the thickness at which percolation occurs, nor did it shift the percolation threshold to a different thickness value. Additionally, the

thickness range at which percolation occurs, closely matches the size of the nanoparticles (~2.0 nm), suggesting that the percolation threshold is directly linked to the dimensions of the particles.

In comparative studies evaluating the conductance behavior of Ni and W as a function of bulk-equivalent thickness, the percolation onset in Ni films is observed at thickness values within the narrow range of 1.4-2.1 nm, similar to those of Pt films. W films exhibit a lower percolation onset, ranging between 0.7-1.0 nm. This trend also supports the idea that the percolation threshold is significantly influenced by factors such as material properties, particle size, and surface interactions, suggesting a correlation between the percolation onset and particle size. In support to these observations, studies by Yamamuro et al. [169] and Borghi et al. [10], highlight that smaller particles are more effective in forming large, well-connected regions during film growth, reaching percolation at lower thickness values. Based on these reports and the trends observed in my results, it can be assumed that if the thickness at which the percolation onset occurs is slightly larger than the particle size, as observed in Pt and Ni, where the mean size of the particles are 2.0 and 3.9, respectively (see Section 5.1), this suggest that tungsten particles produced in this work are likely slightly larger than 1 nm.

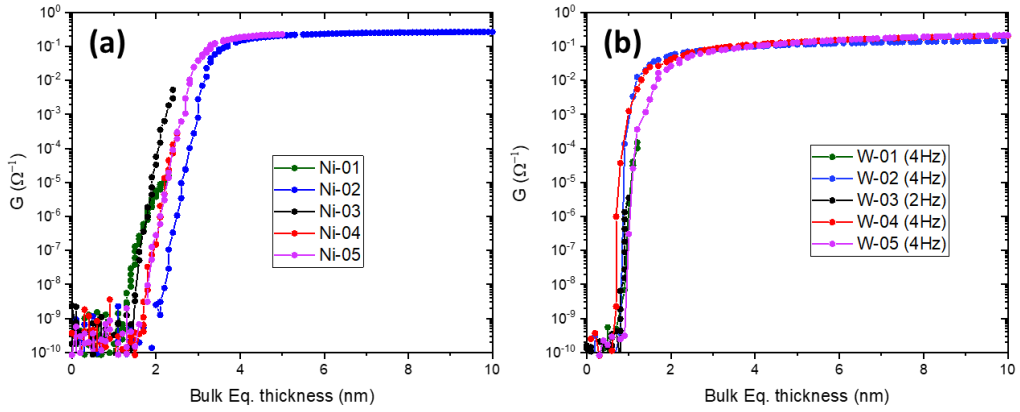

Figure 6.4. Electrical behavior at percolation for Ni (a) and W (b). Similarly to Pt films, the onset of conductance occurs at narrow thickness values regardless the deposition rate.

Furthermore, the distinct behavior of the percolation onset, where deposition rate does not affect the thickness value at which the onset of conductance occurs, can be explained by the aggregation mechanism in the sub-monolayer, as was discussed in Section 5.2.1. Unlike what is observed in Sn, where primary particles coalesce upon contact, the high melting point materials studied in this thesis exhibit a different aggregation mechanism. In these materials, limited coalescence occurs, where particles form necks rather than fully merging. This results in a more complex film morphology in the sub-monolayer, characterized by dendritic-like structures that become increasingly complex as deposition progresses, confirming that the early stages of aggregation can be described by DDA.

These dendritic structures further form percolation paths when surface coverage exceeds at least 60%, which contrasts with standard percolation theory. The fractal dimensions of 1.87 and 1.9 (a value of 1.9 is in fact indicative of percolation in fractals), calculated for Pt and W, at surface coverages of 63% and 71%, respectively (see Section 6.2.1), were obtained at bulk equivalent thicknesses of 1.2 nm for Pt and 1.1 nm W, matching the values of the conductance onset. This suggests that the percolation process mechanism in these materials can be effectively modeled using the continuum percolation framework, which typically occurs at around 68% coverage.

6.2.2 Low melting point materials: the case of Sn

As can be observed in Figure 6.5, the abrupt transition from insulating behavior to 3D conducting behavior, taking place at a thickness remarkably larger than particles dimension and within a thickness variation as small as about 1 nm, suggests that Sn clusters undergo coalescence (discussed in Section 5.2.2), forming electrically non-connected 3D islands that grow due to the deposition of additional particles until the point when a minor amount of deposited material causes them to suddenly connect electrically.

Aiming at investigating coalescence phenomena, we carried out TEM analysis on samples at a level of coverage causing clusters to get in touch each other. In these conditions, we observed that the primary and spherical Sn clusters merge into larger nanoparticles having shapes evolving from original spherical ones towards spheroidal and oblong shapes, reminding the junction of two or more particles (Figure 5.13a).

The observations of coalescence phenomena of this study are consistent with the findings of S.A. Brown's group, who has previously reported coalescence of Sn NPs during film growth by gas-phase aggregation system based on magnetron sputtering at room temperature [170–172]. They successfully inhibited in-situ Sn NPs coalescence by forming an oxide shell during the deposition in vacuum by means of proper air injection through a needle valve. Such controlled partial oxidation during the deposition enabled them to reach the conduction onset at shorter times but with the conductance increasing more slowly. Even if enabling coalescence control, this oxidation-based approach obviously modifies the nature of the material.

Departing from the fact that the onset of conductance can be varied by controlling the coalescence of Sn NPs, we carried out a series of experiments where we adjusted the deposition rate in the PMCS, by playing with the number of pulse repetitions in the range of 2-4 Hz. We supposed that a faster cluster deposition with respect to diffusion and coalescence dynamics might in fact create the condition for percolative paths to form in advance, i.e. at lower deposited thickness, while coalescence is still ongoing.

In-situ electrical measurements revealed that indeed a higher deposition rate shifts the percolation threshold at smaller thicknesses (Figure 6.5).

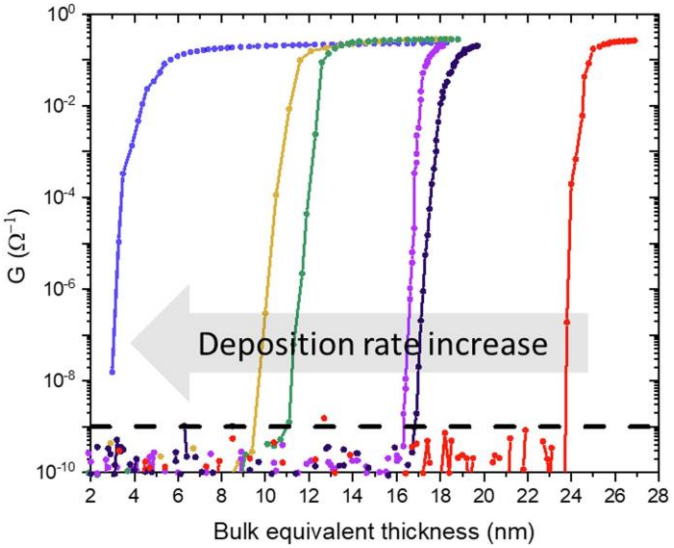

Figure 6.5. In-situ conductance of cluster-assembled Sn films as a function of the thickness. Deposition rate from 0.17 to 0.32 nm per rastering step. As the deposition rate increases, the percolation threshold shifts towards lower film thicknesses, indicating the formation of the conductive network requires a minor amount of material. This suggests that different microstructures are formed. Dashed line shows background level due to noise inherent to the electrical readout setup. The applied voltage on the IDEs was 10 mV for all experiments. Colors link data of this figure to data of Figure 6.8a.

A close look at electrical current raw data shows that each step of current increase, due to IDE passing in front of the cluster beam, is followed by a slight decrease in current, taking place during the time IDE is not exposed to the cluster beam (Figure 6.6). This observation suggests that, while percolation phase is ongoing, particles coalescence can cause a partial loss of conductive pathways because a fraction of neighboring particles electrically connected are pulled apart when they coalesce with other particles. Assuming the variation (decrease) of the number of percolation paths dn in the time interval dt is proportional to the number of percolating path n available at time t, i.e., $dn = -\frac{1}{\tau}n(t)dt$, where τ has the meaning of a time constant, an exponential fitting can be applied to the decreasing part of each current step of Figure 6.6. This analysis yields a time constant of $\tau = 11 \pm 1\ s$, which is believed to represent a sort of characteristic time of the disruption of percolation paths due to coalescence dynamics. These current decreasing dynamics are very well perceivable

in high deposition rate experiments (as the one Figure 6.6 refers to), while are not in low deposition rate experiments.

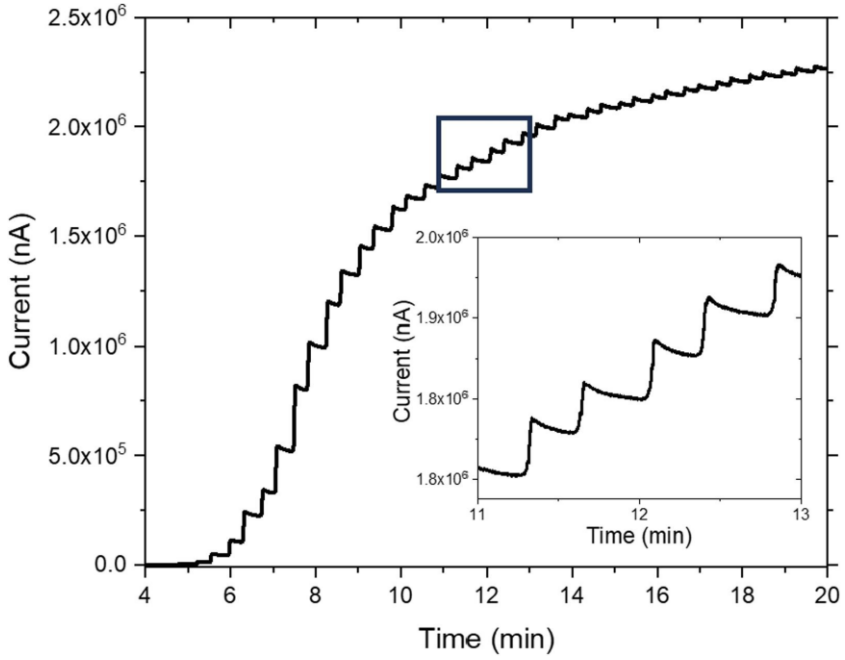

Figure 6.6. Raw data of in- situ electrical current measurements during film growth (high deposition rate case, 0.32 nm per rastering step). The inset highlights the slight decreasing of electrical current across IDE during the time interval when IDE is not exposed to the cluster beam.

On one hand, as the deposition rate increases, the percolation threshold shifts towards lower film thicknesses, indicating that a minor amount of material is necessary for the formation of the conductive network. On the other hand, slower deposition rates shift the percolation threshold towards higher film thicknesses, which can be attributed to the increased time available for coalescence to favor the formation of 3D separated islands, thus delaying the creation of interconnected electrical pathways on the substrate.

Interestingly, these results suggest that the deposition rate can have an important effect in the final microstructure of the films, as low deposition rate might favor more compact, 3D island wise film microstructure, while high deposition rate might favor more ramified, porous film microstructure. This observation can be understood by considering the time dynamics of cluster deposition and coalescence in determining the resultant morphology of the film. We suppose that at low deposition rate

conditions, the average time interval between the arrival of clusters is longer than the time required for coalescence to take place. Therefore, the process of formation of thermodynamically stabilized compact spheroidal shape prior the subsequent interaction with another deposited cluster tends to prevail. This leads to a dense and potentially more stable structure. In contrast, for samples grown at high deposition rate, the shorter average interval between successive cluster depositions might prevent coalescence process to complete: two nanoparticles do not have time to fully merge into a single compact shape before the arrival of the next cluster nearby, which -once in contact- makes energetically unfavorable the completion of ongoing coalescence, leading to the formation of a less-compact and more-ramified structure.

In line with indications coming from in-situ electrical conduction, evidence of the role of deposition rate in determining film microstructure can be also inferred from size distributions of objects appearing in TEM images of samples having the same amount of mass (same bulk equivalent thickness) but deposited with different deposition rate, as shown in Figure 6.7. At a thickness of 3.2 nm (much smaller than primeval particle size, meaning low coverage and particles well separated each other), no relevant differences are visible in size distributions obtained at low and high deposition rates, the former operating the cluster source at 2 Hz repetition rate while the latter at 4 Hz (Figure 6.7a and Figure 6.7c). Bimodal character of these distributions has been already commented in regard to Figure 5.13.

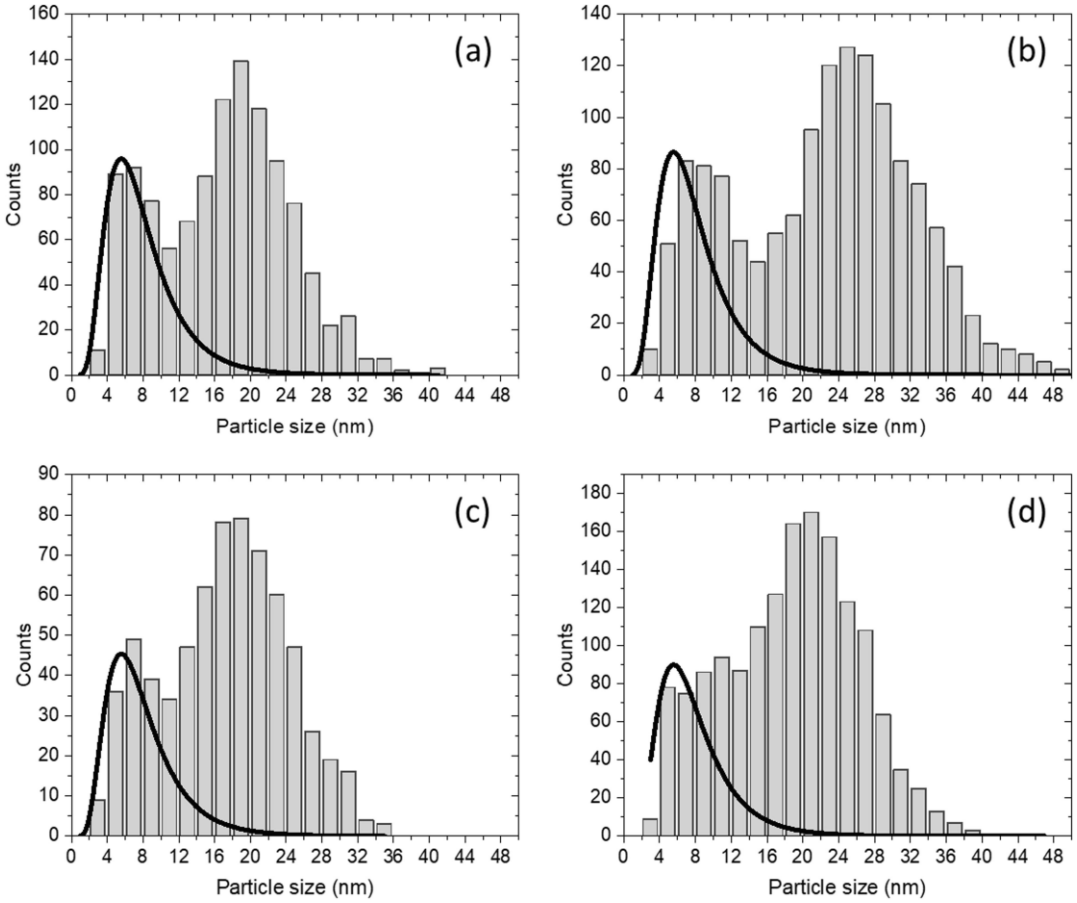

Figure 6.7. Evolution of size distribution histograms of Sn NPs with amount of deposited NPs for low deposition rate (cluster source operated at 2Hz) and high deposition rate (cluster source operated at 4Hz), highlighting the different impact of coalescence. a) and c): Samples of same thickness (3.2 nm) obtained at low deposition rate (2 Hz) and high deposition rate (4 Hz) respectively, showing very similar bimodal distributions with small-size component of non-coalesced clusters and large-size component of coalesced particles centered around 18-20 nm. b) and d): same as a) and c) at larger thickness (6 nm). Here differences among distributions appear, where high deposition rate one (d) unveils remarkably smaller objects than low deposition rate one (b). In all cases black curve reproduces lognormal fitting of small-size component keeping fixed fit parameters of Figure 5.2 fitting.

When considering larger thickness (6 nm, Figure 6.7b and d), size distributions of samples obtained at low and high deposition rates differentiate. Sample obtained at low deposition rate, where coalescence is supposed to impact the most on film microstructure, shows a shift from 18-20 nm to 24-26 nm of the center of large-size component and a basically unchanged small-size component. Instead, sample obtained at high deposition rate shows a broad, unstructured size distribution positioned at remarkably smaller dimensions, as if coalescence process be somehow hampered.

Essentially, Figure 6.7 b and d show that given a certain amount of material deposited, low deposition rate generates larger and allegedly more compact island-like objects, while high deposition rate smaller objects allegedly arranged in a less compact, granular structure. An indirect though unambiguous confirmation of this picture is provided by oxidation experiments, discussed in Section 6.4.

6.3 Resistivity evolution beyond electrical percolation.

At the end of the percolation phase, which is characterized by a variation of the electrical current of several orders of magnitude within a thickness variation as small as few nanometers, the increasing trend of electrical conduction drops, indicating the beginning of the conduction phase dominated by 3D pathways network. As discussed in Section 6.2, in this phase conductance increase is still present due to further adding of material on topmost film surface, which contributes to develop the 3D pathways network, but the order of magnitude of conductance stabilizes at the same value, irrespectively of the deposition rate and of the position of the percolation threshold.

Film resistivity can be calculated from conductance and thickness data, showing values for 3D conduction phase that are almost three orders of magnitude larger than the one of their bulk counterparts (Figure 6.8), in line with what observed in cluster-assembled films of other metals [9–11]. It is suggested that such deviation in respect to bulk lies in the nanoscale granular composition and highly defected nature of the cluster-assembled films. It is worth noting that in the case of Sn cluster-assembled films, coalescence might reduce the density of defects compared to films made of materials with higher melting points. However, the tendency of Sn clusters to coalesce can result in the formation groups or regions of islands in ohmic contact that are barely interconnected with another groups, resulting in a reduced amount of material actively participating in the electrical conduction.

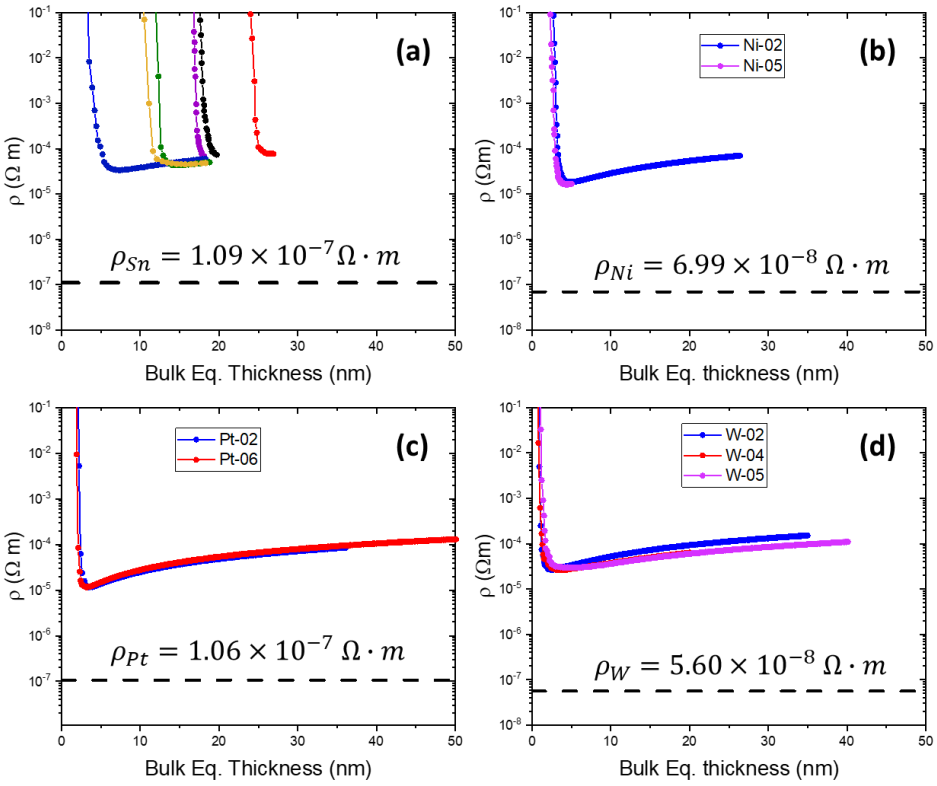

Figure 6.8. Resistivity of Sn, Ni, Pt and W cluster-assembled films in 3D conduction regime showing values almost three orders of magnitude larger than their bulk counterparts (dashed lines). This huge deviation is attributed to the nanoscale granular structure and defected nature of these films, alongside, in the case of Sn (a), the impact of cluster coalescence forming island-like structures, which reduce the amount of active material for electrical conduction.

Similarly to what reported by Barborini et al. [11] in the case of Fe, Pd, Nb, W and Mo, also resistivity of cluster-assembled films of Sn, Ni, Pt and W in 3D conduction phase is not constant with respect to thickness increasing. As proposed, in 3D conduction regime interconnection between clusters of the upper-most layers progressively decreases contributing to the resistivity increase with thickness. Such progressive decrease of clusters interconnection is consistent with the model of ballistic growth characterizing films by SCBD. A power law $\rho \sim t^{\alpha}$, where ρ is the resistivity, t the thickness, and α the power law exponent, has been identified for all investigated metals Fe, Pd, Nb, W, and Mo, with exponent values between 0.41 and 0.78. As shown in Figure 6.9, the films studied in this thesis exhibit a similar power-law behavior with exponents α of 0.96, 0.93, and 0.85-87 for Pt, Ni, and W films,

respectively. However, Sn films exhibited a somewhat lower range of exponents, between 0.76 and 0.78.

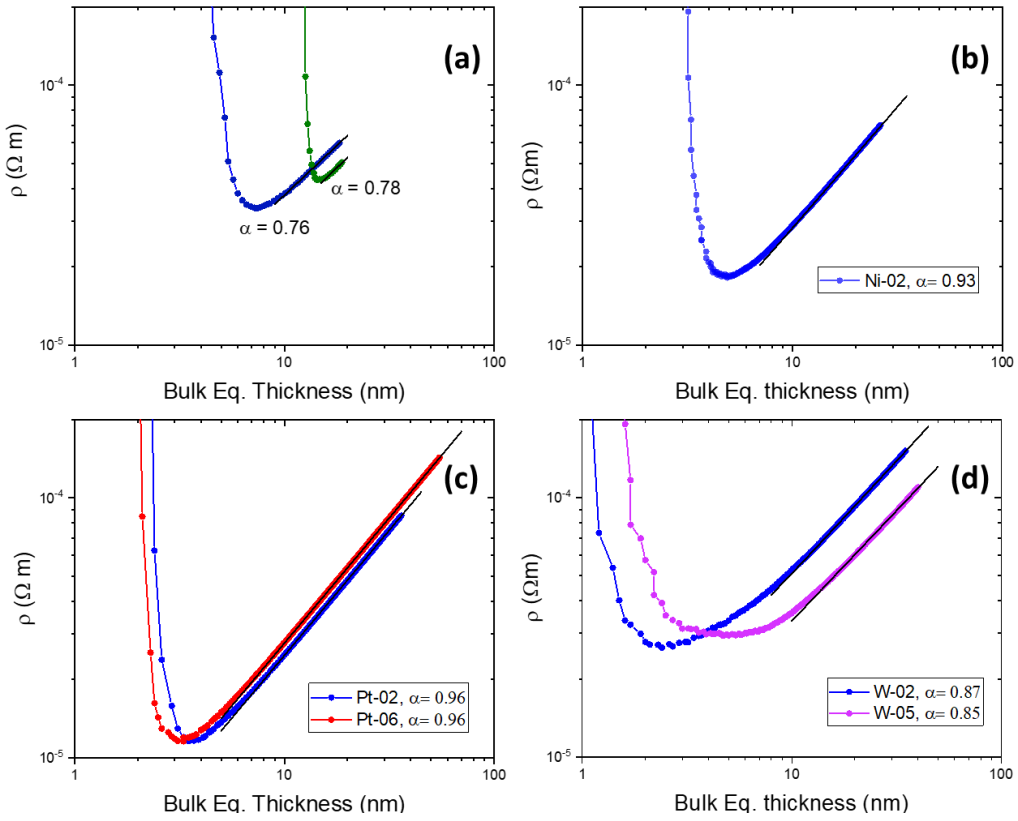

Figure 6.9. Log-log plot of resistivity of the cluster-assembled films as function of thickness (same data of Figure 6.8), unveiling that a power law describes the behavior of resistivity and thickness. Data fitting returns power law exponent values α ranging from 0.76 and 0.96.

In nanogranular films, the incomplete coalescence of clusters results in a high density of grain boundaries. These boundaries act as strong scattering centers, significantly reducing electron mobility and contributing to the large increase in resistivity compared to bulk materials. This effect is well captured by the Mayadas-Shatzkes (MS) model [8], which describes how grain boundary scattering becomes more pronounced as the grain size remains small and the grain boundary density increases.

As film thickness increases, additional factors contribute to the continued rise in resistivity. The surface roughness, which increases with thickness following a power-

law characterized by the roughness exponent β, enhances electron scattering at the film surface. This mechanism is described by the Fuchs-Sondheimer (FS) model [4], where rougher surfaces lead to more diffuse scattering of electrons.

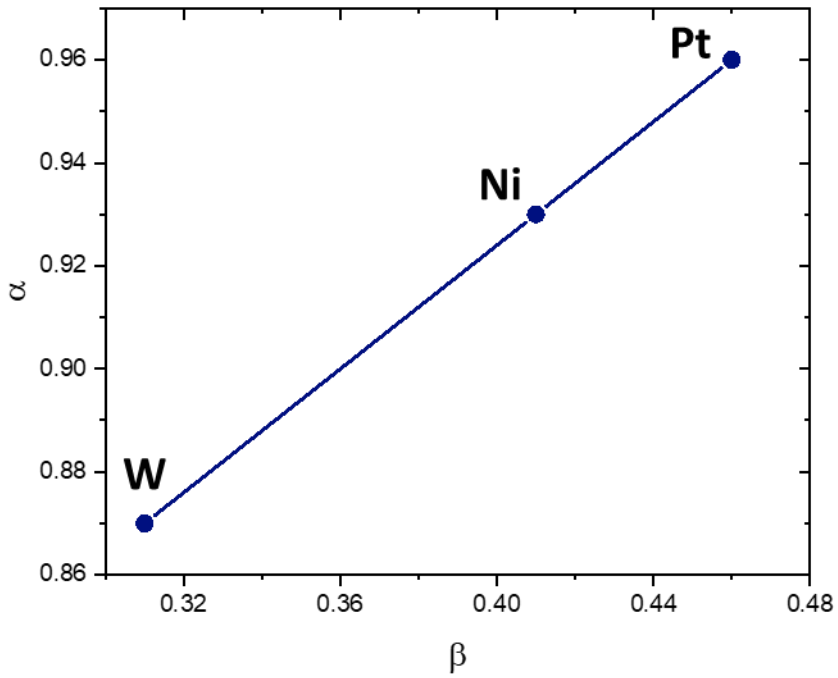

Figure 6.10. resistivity exponent α vs. roughness exponent β for cluster-assembled films of Pt, Ni and W. The linear trend suggests that higher roughness exponents correlate with larger resistivity exponents, highlighting the influence of surface morphology on electrical properties.

The correlation between the power-law exponents β (roughness) and α (resistivity) shows a relationship between surface morphology and electrical behavior of the different materials studied: Pt, Ni, and W films. As thickness increases, roughness grows following a power-law trend, and this increase in roughness can be linked to the rise in resistivity. Figure 6.10 shows the relationship between the power-law exponents β and α. The linear relationship between the two exponents highlights that the evolution of surface morphology plays a critical role in determining the electrical behavior of these cluster-assembled films, with larger growth exponents driving steeper increases in resistivity, suggesting that as roughness increases, it enhances the surface scattering, contributing to the observed resistivity evolution.

The overall resistivity behaviour of the films can be effectively modelled by a combination of surface and grain boundary scattering [173]:

$$\rho = \rho_0 \left(1 + \frac{3\lambda}{8t}(1-p)\right) + \rho_0 \left(\frac{3\lambda}{8D}\left(\frac{R}{1-R}\right)\right) \tag{6.2}$$

Grain boundary scattering, represented by the second term, accounts for the large deviation from bulk resistivity, while surface roughness (first term) contributes to the resistivity increase with thickness. While this combined model captures the key trends in resistivity, further refinement is needed to better understand the contributions of each scattering mechanism.

In addition to grain boundary and surface scattering, porosity, which is approximately 70−80%, plays a substantial role in further increasing the resistivity. The porous structure introduces numerous voids within the film, which effectively reduces the conductive cross-sectional area available for electron transport. This reduction forces electrons to traverse more complex paths to avoid non-conductive regions, which significantly disrupts direct electron transport. Moreover, porosity not only impedes this transport but also intensifies the effects of both grain boundary and surface scattering by extending the electron pathways and heightening the probability of scattering events at the remaining conductive regions.

As the thickness of the films increases, the evolving morphology, particularly the decreasing interconnection between clusters in the upper-most layers, further limits electron transport. This behavior, consistent with ballistic growth, leads to fewer conductive pathways and an overall increase in resistivity. The diminishing interconnection between clusters, combined with the scattering effects of grain boundaries, surface roughness, and porosity, drives the resistivity behavior observed in these films. This highlights the complex nanoscale features and highly defected nature on the electrical properties of films assembled by metallic clusters

6.4 Impact of oxidation on electrical transport

A confirmation of the hypothesis according to which deposition rate affects the microstructure of cluster-assembled Sn films is provided by the behavior electrical conduction during film oxidation. So far, all electrical measurements presented were collected in-situ, in high vacuum condition ($<1 \times 10^{-7}$ mbar). At the end of deposition, the venting of the chamber causes the exposure of the film to oxygen and its impact on electrical conduction can be monitored in real time. Figure 6.11 shows the conductance of films having the same final thickness of about 20 nm but obtained with different deposition rates. Interestingly, the conductance behavior of the two samples diverges significantly during the air exposure: the sample grown at a high deposition rate shows a decrease of conductance of almost two orders of magnitude during the first 80 min of air exposure, while the sample grown at a low deposition rate did not show any significant decrease in conductance within the same timeframe.

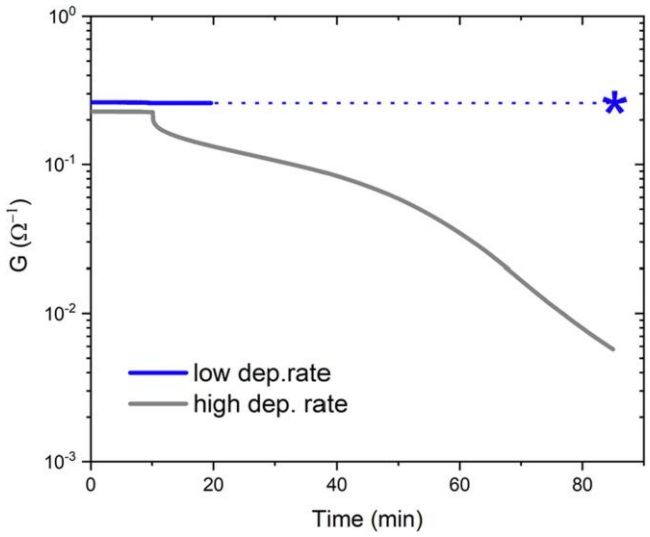

Figure 6.11. Comparison of conductance behavior during air exposure of two samples grown at low and high deposition rate, 0.17 and 0.32 nm per rastering step, respectively. Data acquisition of blue curve was stopped after 10 min from venting and repeated as single measurements afterwards: no change was observed after 4 months. the completely different trend of the two samples suggests the former to be more compact

and maintaining the metallic character, while the latter to be more porous therefore mostly prone to oxidation.

We speculate that this observation provides a clear indication of the diverse microstructures achievable by varying the deposition rate. A higher deposition rate promotes the creation of a porous and less densely packed structure, thereby facilitating the oxidation process due to increased surface area and structural irregularities. Conversely, samples deposited at a lower rate exhibit minimal changes in conductance, implying that oxidation is confined to the surface of their more compact, island-like structure. In these samples, metallic conductance persists throughout the monitored period and remains largely unchanged even after several months.

6.5 Electrical transport before percolation

The electrical properties of cluster assembled films, particularly their current-voltage (IV) characteristics, exhibit interesting behavior as the film transitions from a discontinuous, insulating state to a continuous, conducting state at the percolation threshold. Understanding the IV characteristics of these films, particularly before they reach the percolation threshold, is crucial for their applications in sensors, electronic devices, and catalytic systems. This section explores the IV characteristics of cluster-assembled films before the percolation threshold. Before this threshold, the film consists of isolated clusters or small networks of clusters separated by small gaps, which leads to distinct electrical behavior compared to post-percolation films.

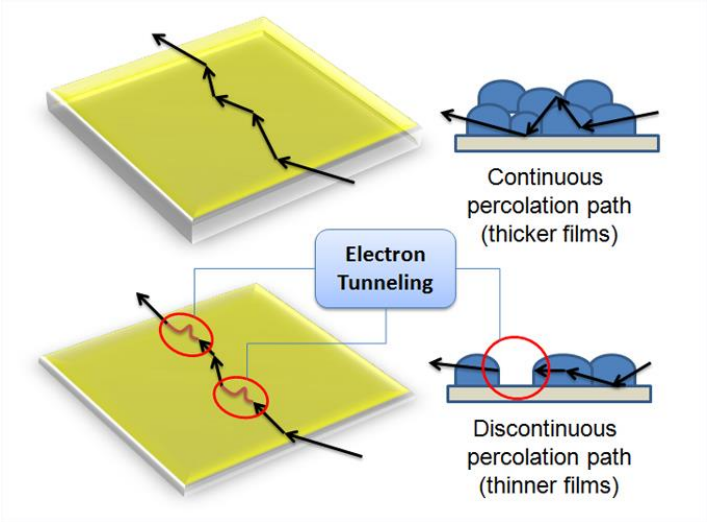

Figure 6.12. Illustration of electron tunneling in thin films, contrasting the continuous percolation paths in thicker films (top) with the discontinuous paths in thinner films (bottom). The continuous pathways in thicker films enable efficient electron flow, while the discontinuous paths in thinner films create barriers, affecting conductivity. Taken from [174].

6.5.1 Tunneling

Tunneling current is a quantum mechanical phenomenon where electrons pass through an energy barrier that they could not cross under classical physics. This process is central to understanding charge transport in nanoscale systems, particularly in structures like metal-insulator-metal (MIM) junctions. Simmons' model [175], developed in the 1960s, provides a theoretical framework to describe tunneling current in such systems.

The probability of tunneling depends on the thickness and height of the barrier. In MIM junctions, the tunneling current is highly sensitive to the barrier's properties and the voltage applied across the junction.

Simmons' model describes the tunneling current (I) in a MIM junction as a function of the applied voltage (V), barrier thickness (d), and barrier height (ϕ). The model assumes a rectangular potential barrier and uniform voltage drop across it. The tunneling current density J is given by [175]:

$$I \sim \left(\phi_B - \frac{eV}{2}\right) \exp\left[-\frac{2(2m)^{\frac{1}{2}}}{\hbar}\alpha\left(\phi_B - \frac{eV}{2}\right)^{\frac{1}{2}} d\right] - \left(\phi_B + \frac{eV}{2}\right) \exp\left[-\frac{2(2m)^{\frac{1}{2}}}{\hbar}\alpha\left(\phi_B + \frac{eV}{2}\right)^{\frac{1}{2}} d\right] \quad (6.3)$$

Simmons' model has been widely validated in various experimental setups, particularly in structures where tunneling dominates electron transport. Applications include tunnel junctions, scanning tunneling microscopy (STM), and memristive devices. However, the model assumes ideal conditions, such as a perfectly rectangular barrier and neglects real-world imperfections like barrier inhomogeneities or scattering.

6.5.2 High melting point materials

In order to perform the I-V measurements of the Ni, Pt, and W films, deposition was stopped before the onset of conductance.

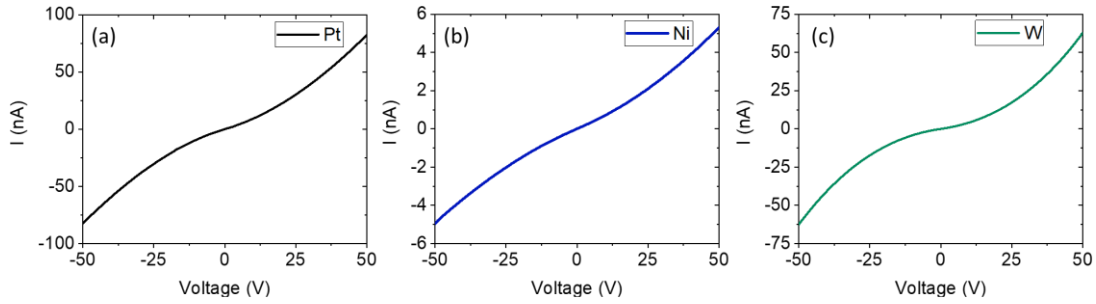

Figure 6.13. I-V characteristics near percolation at 1.3, 1.6 and 0.8 of nominal thickness for Pt, Ni and W films, respectively. The three cases show a non-ohmic trend, indicating tunnelling as the primary transport mechanism.

The current-voltage (I-V) characteristics of cluster-assembled metallic films (Pt, Ni, and W) with nominal thicknesses of 1.3 nm, 1.6 nm, and 0.8 nm, respectively, exhibit nonlinearity, indicating tunnelling as the primary transport mechanism. In these films, near the percolation threshold, electron conduction occurs through tunneling between isolated dendritic islands, where gaps act as barriers. The field-dependent nonlinear

current response confirms the discontinuous nature of the films, with charge transport governed by quantum tunneling across nanoscale gaps. This tunneling behavior is consistent across all three materials, highlighting their similar conduction mechanisms in this regime.

The absence of hysteresis in the I-V curves of cluster-assembled Pt films (Figure 6.14), even with the applied voltage sweep up to ±50 V, indicates that the tunneling mechanism is stable and unaffected by structural changes. This stability is notable because, at the tunneling gaps (typically sub-nanometric) between metallic islands, electric fields in the range of 10–50 V/nm should be sufficient to induce effects such as electric field-induced surface diffusion (EFISD) and/or electric field-induced evaporation (EFIE) [60]. In metals, EFISD typically occurs at field strengths around 1–20 V/nm, where surface atoms on metallic islands can migrate, potentially altering the tunneling distance. Similarly, EFIE can occur at even higher fields, around 30–50 V/nm, where atoms might be ejected from the surface, further changing the structure of the tunneling paths.

The absence of hysteresis due to the structural stability observed in the Pt films during the I-V sweep is similarly reproducible in the Ni and W films, confirming that electron tunneling between metallic islands remains stable and consistent across all three materials. This stability can be explained by the complex percolation tunneling network, which comprises numerous parallel and series tunnelling paths. In such a network, even if slight modifications occur in individual tunneling paths due to EFISD or EFIE, the overall conduction remains unaffected. The numerous pathways within the device compensate for these changes, and the robust connectivity between metallic islands ensures that small structural changes are absorbed by the network as a whole, maintaining stable and reversible tunneling behavior without hysteresis.

Furthermore, as shown in Figure 6.14 (b) for the case of Pt films, increasing the nominal thickness from 1.7 nm to 1.9 nm, and then 2.0 nm, leads to a corresponding increase in the overall current in the I-V curves. This increase is expected, as additional material enhances the connectivity between metal islands, allowing more efficient charge transport. However, the persistence of nonlinearity in the IV characteristics indicates that, even at these nominal thicknesses, the films remain near the percolation

threshold, with conductance still dominated by tunneling rather than transitioning to ohmic conduction. This suggests that the additional material increases the complexity of the tunneling network, rather than fully bridging the gaps between the metallic islands. Although not shown here, similar behavior is observed in Ni and W films. Additionally, these observations suggest that the onset of conductance analyzed in Section 6.2 correspond to percolation with tunneling [176], allowing conduction even when no continuous pathway exists, since quantum-mechanical tunneling allows electrical trans-port even before onset of percolation.

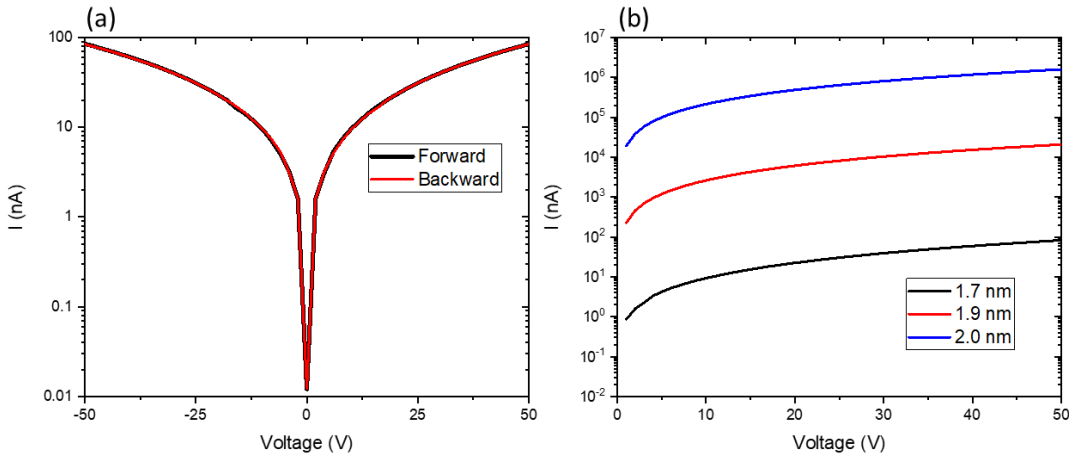

Figure 6.14. Semi log I-V plot of Pt films (a) showing stable, non-hysteretic tunneling behavior. (b) With increasing nominal thickness, the IV characteristics show higher overall current due to added material. The persistence of nonlinearity indicates that tunneling remains dominant, as the film approaches but does not fully reach percolation.

Although the Simmons model can provide a general framework for interpreting the I-V characteristics in tunneling junctions, the model is based on the concept of a uniform, continuous tunnelling barrier, typically applied to describe electron transport in systems like metal-insulator-metal junctions. In cluster-assembled films near the percolation threshold, the situation is far more complex. The transport mechanism involves tunnelling across a network of metallic islands separated by irregular, non-uniform gaps, where the barrier heights and tunnelling distances vary significantly.

This variability in the tunnelling paths, combined with the percolation nature of the network (comprising numerous parallel and series paths), introduces a level of

complexity that the Simmons model cannot capture. As a result, while the I-V characteristics may follow a general nonlinear trend similar to that predicted by the Simmons model, the constants derived from fitting do not have physical relevance. The model oversimplifies the reality of the inhomogeneous tunnelling barriers, leading to discrepancies in the calculated parameters. Therefore, a more refined model is needed to account for the varying geometries and tunnelling conditions across the network, which lead to the nonlinear I-V behavior observed in these films.

6.5.3 Low melting point materials

6.5.3.1 Coalesced particles

As described in Section 6.2.2 percolation threshold can be shifted lo larger values when coalescence dynamics is faster than the arrival of newly particles. Clusters were deposited intentionally at a low deposition rate until reaching a thickness of $\sim 27\ nm$. This deposition process allowed the initial clusters to coalesce into larger particles. (see section 5.2.2). The I-V measurements were conducted within voltage ranges of ±1V, ±2V, and ±4V, under vacuum conditions and at room temperature.

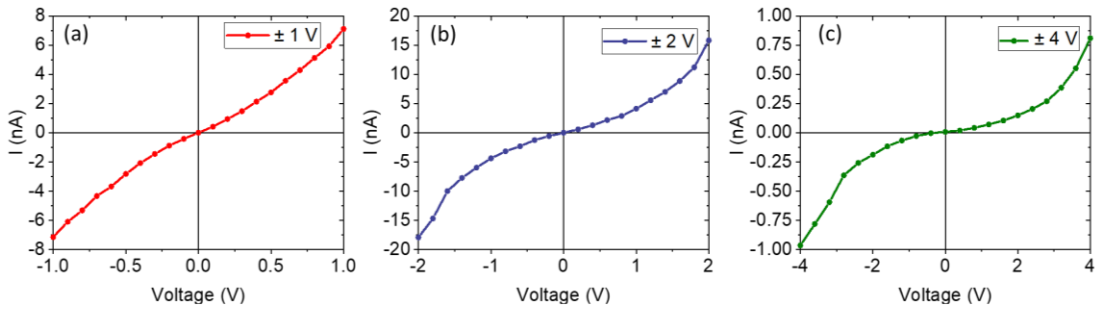

Figure 6.15.. I-V characteristics of Sn films (~27 nm thick) composed of coalesced nanoparticle islands, showing non-ohmic behavior with a systematic decrease in current magnitude with subsequent I-V measurement, indicating a voltage-induced modification of the film's morphology.

Initial I-V measurements exhibited a clear non-ohmic behavior, characterized by a non-linear increase in current as the applied voltage varied from -1V to 1V. The current ranged from -7 nA to 7 nA, forming a symmetric and continuous curve around the

origin. This non-linearity suggests quantum tunneling effects, where electrons tunnel through potential barriers present in the gaps within the Sn cluster network. The I-V curve was reproducible across repeated measurements within the same voltage range, indicating stability of the films under the applied bias.

Extending the voltage range to ±2V and ±4V further highlighted the non-ohmic behavior. While the I-V curves remained symmetric and repeatable (in the same voltage range), an interesting observation was the systematic decrease in overall current magnitude at higher voltages. For instance, the current at 1 V during the ±2 V measurement was lower than that observed during the initial ±1 V range. This trend continued when extending to the ±4 V range. This decrease in current with increasing voltage suggests changes in the morphology of the tunneling gaps, marking a difference with the case of high-melting point materials.

The consistent non-ohmic behavior and voltage-dependent current reduction can be explained by considering tunneling mechanisms and the influence of electric fields. In Sn cluster-assembled films, electrons can tunnel through potential barriers formed by gaps or regions between clusters. However, in previous chapters it was demonstrated that coalescence can affect the formation of tunneling path through the network The probability of tunneling is highly sensitive to the barrier width and height, which can be affected by the applied voltage.

Recent studies have demonstrated that strong electric fields can induce nanoscale evaporation-like processes, known as electric field-induced evaporation (EFIE). Specifically, the threshold values of EFISD and EFSE reported for Sn are $\sim 1\ V/nm$ and $\sim 25\, V/nm$ [170,171], respectively. This phenomenon could effectively enlarge gaps between nanoparticle networks, increasing the barrier width and reducing tunneling current i.e. the electric field at higher voltages likely causes partial evaporation or migration of surface atoms, leading to reduced tunneling probabilities and thus lower currents. EFIE could play a significant role in the more pronounced current reduction observed at higher voltage ranges.

Additionally, the experimental data in Figure 6.15 exhibits similarities to the report by Sotthewes et al. [177] on scanning tunneling microscopy, where increasing the gap

width between the tip and sample results in a decrease in overall current. This further reinforces the notion that the enlargement of gaps between clusters due to electric field induced is a contributing factor to the observed current reduction.

6.5.3.2 Small particles

Clusters were deposited intentionally at a high deposition rate until reaching a thickness 10 nm, indicating that the initial clusters underwent limited coalescence.

One of the first observations was that, in contrast to networks formed by coalesced particles, the I-V curves were not always repetitive at the same voltage range, as can be observed in Figure 6.16. This behavior suggests a more complex conduction mechanism in Sn films with regulated coalescence. Initially, the I-V measurements were conducted in the range of ±1V. The first performed I-V curve (in blue) ranged from approximately -10 μA to 10 μA. In a consecutive I-V measurement within the same voltage range (in green), an increase in conductance was observed (-15 μA to 15 μA), suggesting a modification of the tunnelling gaps. Extending the voltage range to ±3V (in orange) resulted in an even larger increase in conductance further confirming a modification of the tunnelling gaps within the film, contrasting with the previous case of coalesced particles where the increasing of voltage range in the I-V curve resulted in a decreasing of the current.

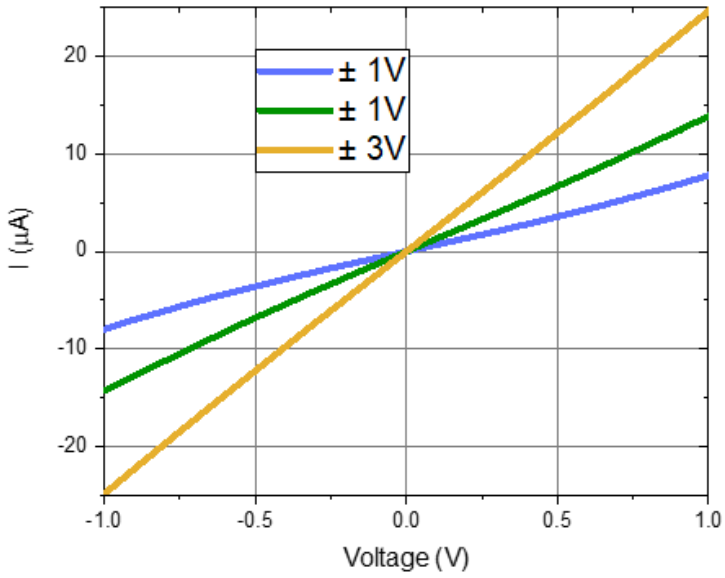

Figure 6.16. I-V characteristics of Sn films below 10 nm displaying evident non-linear behavior and conductance switching which becomes more evident as voltage range in the I-V is increased. This behavior will be further discussed in Section 7.2.1.

The observed conductance modulation to higher conductance values with successive voltage applications, align with the study by Bose et al. [171] on stable self-assembled atomic-switch networks for neuromorphic applications. They investigated Sn nanoparticle networks with a controlled oxidized shell, observing non-linear current-voltage characteristics suggestive of quantum tunnelling. Similarly, they observed conductance modulation with successive electric field applications. This conductance modulation can be explained by the voltage application inducing Electric Field Induced Evaporation (EFIE) and Electric Field Induced Surface Diffusion (EFISD) of the surface atoms, thus forming some kind of hillock that reduces the width of the tunneling gaps which is mainly observed in films composed of islands below 20 nm [176].

6.5.4 Fowler Nordheim tunneling

Fowler-Nordheim (FN) tunneling is a quantum mechanical process that occurs under high electric fields (Figure 6.17(b)), where electrons tunnel through a triangular potential barrier in a metal-insulator-metal (MIM) junction. In contrast, at lower fields, direct tunneling dominates, where electrons tunnel through a more rectangular barrier.

Understanding the transition between these regimes and the resulting current-voltage behavior is significant in characterizing tunneling in nanoscale devices, such as memristors and tunneling diodes [177–179].

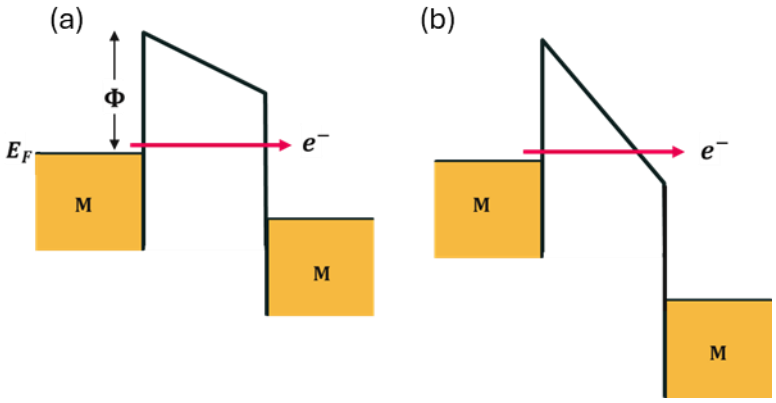

Figure 6.17. Energy band diagrams depicting (a) Direct tunneling through a rectangular barrier at low voltage. (b) Fowler-Nordheim tunneling through a triangular barrier under a strong electric field. Taken from [180].

Direct tunneling: At lower voltages, direct tunneling occurs when the potential barrier remains nearly rectangular. The current density for direct tunneling I is given by:

$$I \propto Vexp\left(-\frac{2d\sqrt{2m\phi}}{\hbar}\right) \tag{6.4}$$

Fowler-Nordheim: In FN tunneling, a strong electric field distorts the potential barrier into a triangular shape, reducing the barrier thickness and facilitating electron tunneling. The current density I for FN tunneling is expressed as:

$$I \propto V^2exp\left(-\frac{4d\sqrt{2m\phi^3}}{3\hbar eV}\right) \tag{6.5}$$

The transition between direct tunneling and FN tunneling occurs at a specific voltage V_t, where the potential barrier changes from rectangular to triangular due to the applied electric field. This transition is observed on the FN plot, where the curve shifts from a nonlinear region at low fields (dominated by direct tunneling) to a linear regime at higher fields, characteristic of FN tunneling.

In practical terms, V_t is identified as the voltage at which the plot of $\ln(I/V^2)$ vs. $1/V$ becomes linear, then FN tunneling is expected to dominate. Below V_t, slope rises exponentially, direct tunneling is thought to occur.

This can be summarized as:

$$\ln\left(\frac{I}{V^2}\right) \propto \begin{cases} \ln\left(\frac{1}{V}\right) & (V < V_t): Direct\ tunneling \\ -\frac{1}{V} & (V > V_t): FN\ tunneling \end{cases} \tag{6.6}$$

Error! Reference source not found. and **Error! Reference source not found.** show the FN analysis for Pt (high-melting-point) and Sn (low-melting-point) materials, respectively. In the case of Pt films, the FN plot shows a logarithmic curve, characteristic of direct tunneling. The absence of an inflection point in the FN plot indicates that direct tunneling is the dominant mechanism for electron transport across the entire voltage range up to 50 V, with no transition to FN tunneling. This behavior is consistent with the findings from Ebrahimpour et al. [181] in their study of gold nanoparticle films, where no transition to FN is observed even at voltages of 200 V due the presence of numerous tunnelling paths maintained stable direct tunnelling across a wide voltage range. However, a notable change occurs when the films are annealed. As the inter-particle distance increases due to coalescence during annealing, the number of available tunnelling paths is reduced, and the films exhibit a clear transition from direct to FN tunnelling. In Pt films produced in this work, the absence of FN tunnelling confirms that their structure, with numerous tunneling paths, is robust enough to maintain direct tunneling even under high electric fields. This highlights the critical role of the dendritic-like 2D film morphology and the availability of tunnelling paths play in determining the dominant electron transport mechanism.

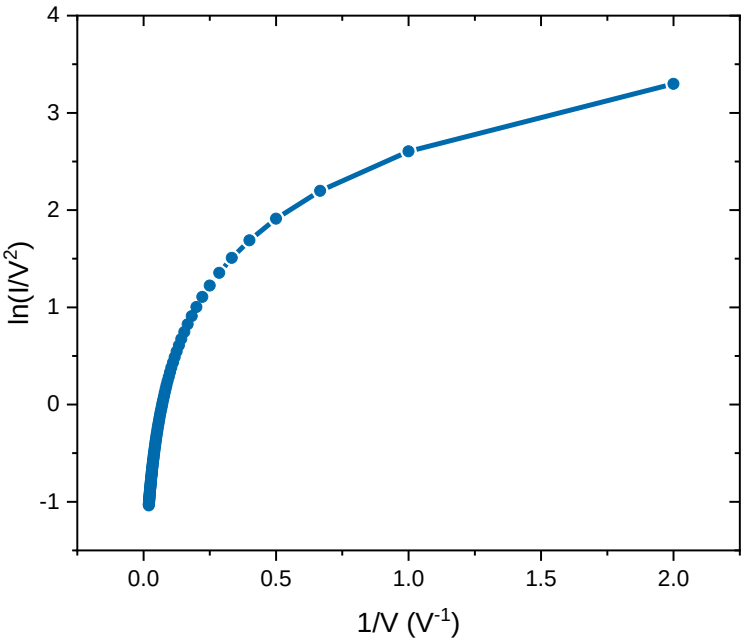

Figure 6.18. Fowler Norheim plot corresponding to the IV characteristics of Pt films near percolation in Figure 6.13 (a). The absence of an inflection point indicates the absence of FN tunnelling.

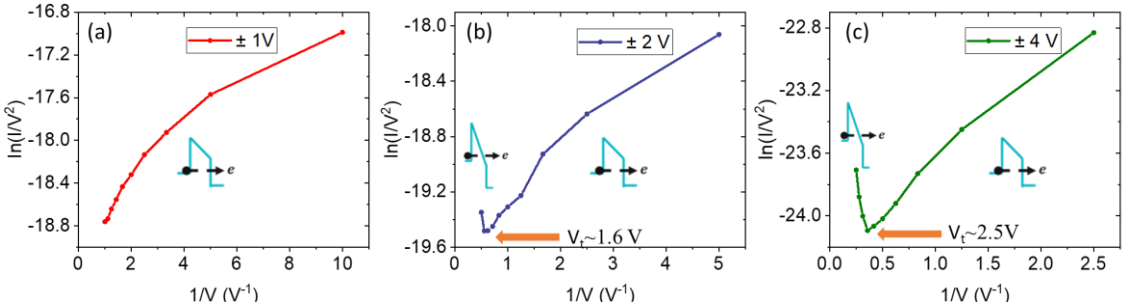

Figure 6.19. Fowler–Nordheim plots of a selected set of I-V's, corresponding to Figure 6.15. (b) and (c) show transition voltages at 1.6 and 2.5, for consecutive I-V's of 2 Vand 4 V, respectively, indicating the shift from direct to FN tunneling.

The analysis of Sn films, where the structure is influenced by coalescence, demonstrates a clear transition from direct to FN tunneling at lower voltages, with V_t observed at approximately 1.2 V and 2 V in the 2-volt and 4-volt IV's, respectively. This shift in V_t can be linked to the enlargement of the tunneling gap induced by the

increased applied electric field (as discussed in Section 6.5.3). As the tunneling gap widens, the likelihood of direct tunneling decreases, since direct tunneling is primarily distance-dependent, where electrons can tunnel through a thin potential barrier. When the barrier thickens with increased gap width, the probability of direct tunneling falls exponentially. Consequently, a stronger electric field is required to transition to FN tunneling, where the barrier shape becomes triangular under the field's influence, enabling electrons to "field emit" through the barrier.

The shift in V_t due to gap increase aligns with previous findings. Beebe et al. [179] reported that in metal-molecule junctions, as the tunnelling gap widens, the transition voltage shifts upward. This occurs because the increased gap leads to a thicker tunnelling barrier, making direct tunnelling less probable and requiring a higher electric field to transition to FN tunnelling. Similarly, Xiang et al. [182] found that in nanoelectrode junctions, FN tunnelling dominates as the energy barrier decreases at shorter tunnelling distances. However, as the gap width increases, the field required to overcome the barrier increases, shifting V_t to higher values. This supports the idea that the tunnelling distance directly influences the transition to FN tunnelling.

Furthermore, Sotthewes et al. [177] demonstrated that in ultra-high vacuum scanning tunnelling microscopy (UHV-STM) junctions, V_t increases with widening tunnelling gap, requiring a stronger electric field to enable FN tunnelling as the barrier thickens. Their findings highlight that V_t is not solely determined by barrier height, but it is also sensitive to other factors, such as the tunneling distance. This correlation underscores the importance of gap width in electron transport mechanisms, aligning with Sn films in this work, where similar shifts in V_t were observed with changes in tunnelling distance by field-induced gap modification. The transition at low voltages from direct to FN tunneling observed in Sn films also corroborates that much less tunneling paths contribute to the electron transport in comparison to high melting points materials.

CHAPTER 7. PERSPECTIVES

7.1 Bimetallic clusters and chemiresistive gas sensing

7.1.1 Synthesis of bimetallic atomic clusters

In PMCS bimetallic atomic clusters can be produced using two primary approaches: either a single target containing both metallic species at specified ratios and two-electrode configuration where the individual metals are vaporized separately. Though, complex configurations in other sources exist by using custom made targets or two target configurations to determine the atomic ratio, have been widely employed to ensure efficient co-deposition and mixing of the metals in the gas phase.

In this thesis, bimetallic Pt-Sn clusters were produced using two distinct methods. First, a sintered target containing both Pt (10 at%) and Sn (90 at%) was employed to ensure the formation of well-mixed atomic vapor (Figure 7.1a). The second method was a two-electrode configuration, in which Pt and Sn were vaporized close to each other (Figure 7.1b). This approach was designed to increase the proportion of Pt in the vaporized material, allowing for a direct comparison with the results from the single sintered target.

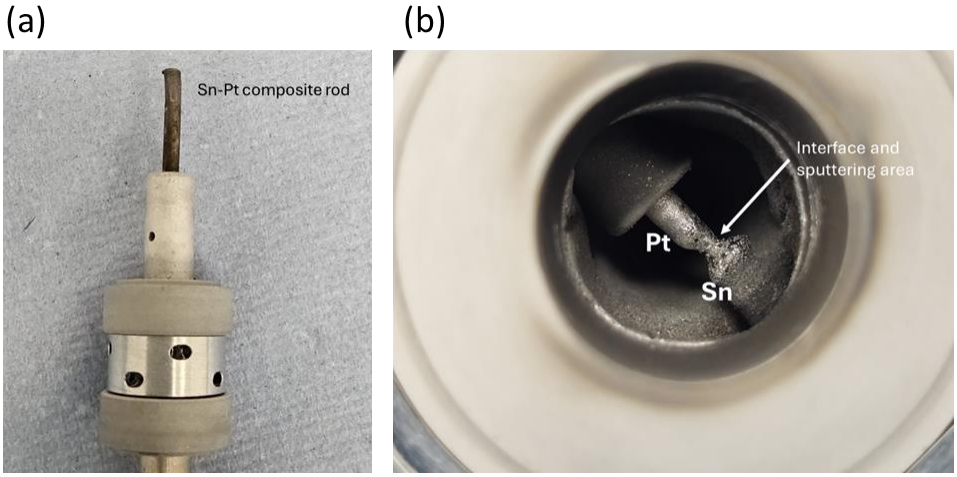

Figure 7.1. (a) Composite cathode containing Pt (10 at%) and Sn (90 at%). (b) Two-electrode configuration for the production of Sn-Pt nanoparticles, where the interface of the cathodes was fixed in the sputtering region.

Furthermore, the relationship between surface energy and particle size is critical in controlling nanoparticle formation, as shown in Figure 7.2. Metals with higher surface energies typically form the core of bimetallic structures, while metals with lower surface energies tend to migrate to the surface, leading to core-shell configurations. In larger particles, this surface energy differential becomes more pronounced, leading to well-defined phase segregation or layered structures.

Understanding the surface energy dynamics and nucleation mechanisms during gas-phase synthesis provides insight into how to control the structural evolution of Pt-Sn nanoparticles, enabling their use in applications requiring specific elemental distribution and morphological properties.

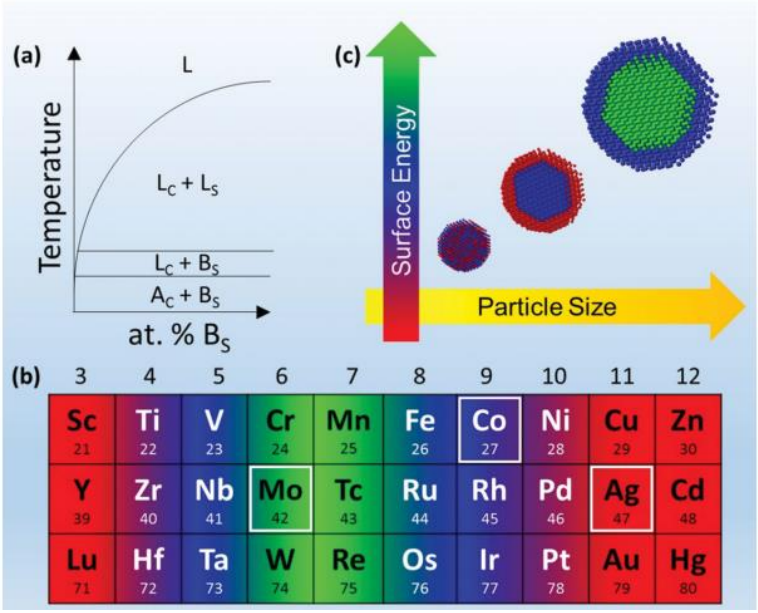

Figure 7.2. (a) Schematic phase diagram showing regions of liquid immiscibility and core-shell formation regimes, (b) Relative surface energies of metals from groups 3-12, where higher surface energy elements (blue) tend to form the core and lower surface energy elements (red) form the shell, (c) Core-shell formation concept indicating how particle size and surface energy determine structural outcomes. Taken from [183].

In the first case, Pt-Sn nanoparticles were synthesized using a sintered target containing Pt and Sn. Elemental mapping by EDS (Figure 7.3) of the resulting nanoparticles revealed that Pt atoms were relatively dispersed throughout the Sn-rich particle. This distribution can be attributed to the nucleation, and condensation of an initial well-mixed vapor of both metals in the gas phase, which facilitates atomic integration.

Although elemental mapping revealed that while Pt was generally spread throughout the Sn matrix, in some cases a distinct trend of Pt migrating toward the core of Sn-rich particles was observed. This suggests that Pt diffuses through the Sn particles, driven by surface energy minimization. Due to its higher surface energy (~2.49 J/m^2), Pt seeks energetically favourable positions in the core, while Sn, with its lower surface energy (~0.72 J/m^2), remains more concentrated at the outer regions [183,184]. This inward diffusion of Pt through the Sn matrix results in a core-shell-like structure, where Pt gradually localizes at the core.

Additionally, the rapid cooling during gas-phase synthesis significantly influences the final structure. Although the initial vapor phase is well-mixed, the fast-cooling rates trap Pt atoms in non-equilibrium positions throughout the Sn-rich particles, preventing full segregation to the core. This kinetic trapping contributes to the observed particle distribution and helps explain the incomplete phase separation seen in some particles.

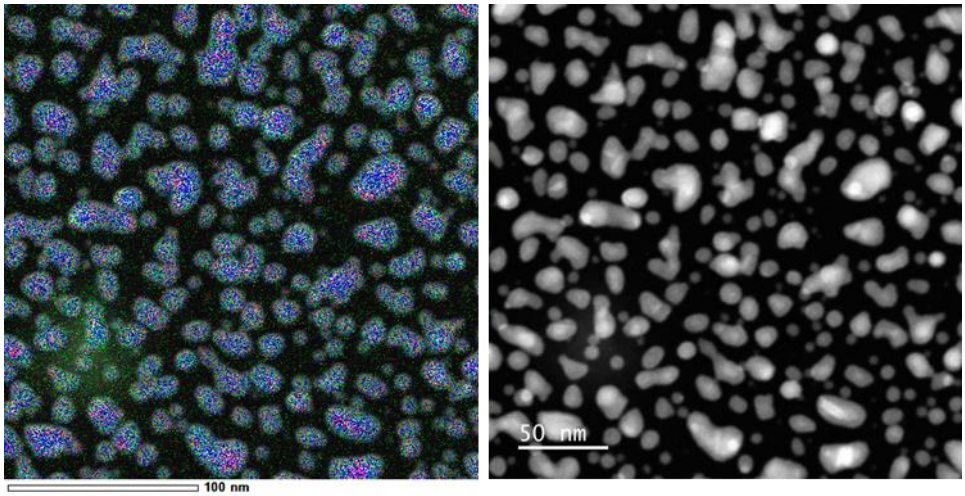

Figure 7.3 Elemental analysis by STEM-EDS of the Sn-Pt composite cathode, showing a generally uniform Pt (red) distribution within the Sn (blue) matrix, with some instances of Pt migrating toward the core, as Pt, with higher surface energy, diffuses inward, while Sn remains concentrated at the surface. Oxygen is shown in green.

In the second case, Pt and Sn were sputtered from a two-electrode configuration, Elemental mapping of the nanoparticles produced in this configuration exhibited clear phase segregation, suggesting that the two metals nucleated separately, forming primeval particles reminiscent to the pure Sn and Pt cluster formation, although partial mixed phases are also observed.

Upon deposition on the substrate, primeval Sn and Pt segregated particles can diffuse and meet. This interaction can lead to the “encapsulation” of Pt by Sn, forming core-shell structures post-deposition. The mobility of Sn allowed it to migrate and form a shell around the Pt clusters, driven by the surface energy differential between Pt and Sn. Pt, with its higher surface energy, tended to migrate toward the core, while Sn stabilized the outer surface of the particle, reducing the overall system energy. This is

consistent with previously observed behaviours in gas-phase synthesis, where substrate interactions play a role in final particle morphology, specifically, Vernieres et al. [185] report the wetting of Au particles on Fe particles, thus forming Au-Fe core-shell structures. It is also important to note that in my experiments core-shell formation may not only occur post-deposition but could also arise during the gas-phase synthesis.

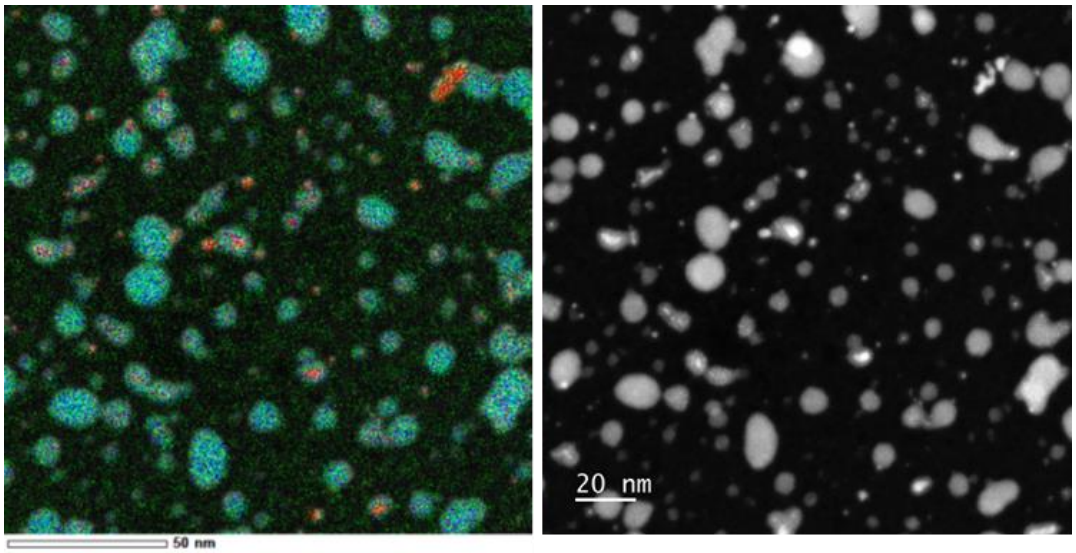

Figure 7.4. Elemental STEM-EDS mapping of Pt-Sn nanoparticles synthesized from separate precursors, displaying clear phase segregation with distinct Pt-rich (red) and Sn-rich (blue) regions, with oxygen (green) also indicated. Core-shell structures appear as Sn encapsulates Pt clusters upon deposition, while Pt satellites form from Pt clusters adhering to Sn surfaces without full integration.

In addition to core-shell structures, Pt satellites are frequently observed. These satellites are alleged to result from the interaction of Pt clusters with coalesced Sn particles on the substrate, where Pt remained attached to the Sn surface but did not fully integrate into the Sn matrix, as the Sn particles reduced their surface energy due to the previous coalescence.

The differences between the two precursor methods highlight the critical role of nucleation dynamics, surface energy and post-deposition interactions. In the composite precursor case, the initial mixing of Pt and Sn atoms in the vapor phase facilitated co-nucleation, resulting in particles with better atomic mixing. Furthermore, rapid cooling

prevented segregation of Pt migrating to the core. This further highlights the impact of non-equilibrium conditions on the structural outcomes of these nanoparticles.

In the separate precursor method, the segregation of Pt and Sn is more evident, likely due to independent nucleation, but some mixed phases are also observed. The interaction between Pt and Sn particles on the substrate on determining the final morphology, with some core-shells or Pt satellites attached to coalesced Sn particles.

These results underscore the importance of precursor configuration, particle size, surface energy minimization and miscibility in determining the final nanoparticle structure, contributing to a deeper understanding of bimetallic nanoparticle formation under non-equilibrium conditions.

7.1.2 Gas sensing

Chemiresistive gas sensors are among the most widely researched and utilized sensors due to their relatively simple design, cost-effectiveness, and high sensitivity. These sensors function based on the principle that the electrical resistance of a semiconducting material changes when gas molecules adsorb onto its surface. This change in resistance can be directly correlated with the concentration of the target gas. The capability to integrate these sensors with electronic devices has facilitated their widespread application in fields such as environmental monitoring, industrial safety, and healthcare [186,187].

The performance of chemiresistive gas sensors is significantly dependent on the properties of the sensing material. Metal oxides, particularly tin oxide (SnO_2), zinc oxide (ZnO), and tungsten oxide (WO_3), are the most extensively studied materials in this domain. Among these, SnO_2 stands out due to its inherent stability and high sensitivity to various reducing gases. Recent advancements in this field have focused on enhancing these materials by doping, nanostructuring, and forming hybrid composites to increase surface area and improve the gas-sensing interaction [188–190].

The fundamental mechanism of chemiresistive gas sensors revolves around the interaction between the gas molecules and the surface-adsorbed oxygen species on the semiconducting material. In case of n-type semiconductors like SnO_2 (Figure 7.5), oxygen molecules adsorb on the sensor's surface and capture electrons from the conduction band, forming negatively charged oxygen species (O^-, O_2^-, or O_2^{2-}). This adsorption process depletes electrons in the material, increasing its resistance. When a reducing gas, such as carbon monoxide (CO), is introduced, it reacts with the adsorbed oxygen ions, releasing electrons back into the conduction band, thereby lowering the resistance of the sensor. Conversely, the adsorption of oxidizing gases, such as nitrogen dioxide (NO_2), will further withdraw electrons, leading to an increase in resistance [188,191–193].

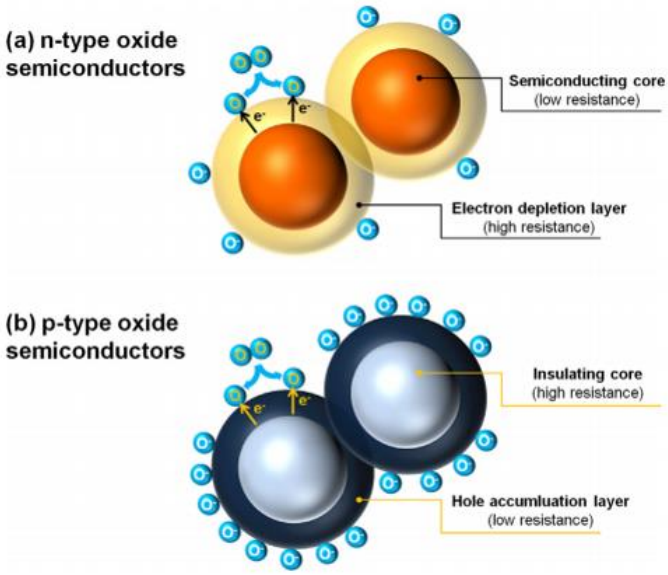

Figure 7.5. The figure shows the gas sensing mechanisms in (a) n-type and (b) p-type oxide semiconductors. In n-type, gas adsorption forms an electron depletion layer, increasing resistance. In p-type, a hole accumulation layer forms upon gas exposure, reducing resistance. These resistance changes are key to detecting gases. Taken from [194].

Despite their advantages, chemiresistive sensors face several challenges, including cross-sensitivity to multiple gases, high operating temperatures, and issues related to long-term stability. These challenges have encouraged ongoing research into the development of advanced materials and sensor architectures. The incorporation of

catalytic materials such as Pt and Pd has proven effective in enhancing the selectivity and lowering the operational temperatures of these sensors [195].

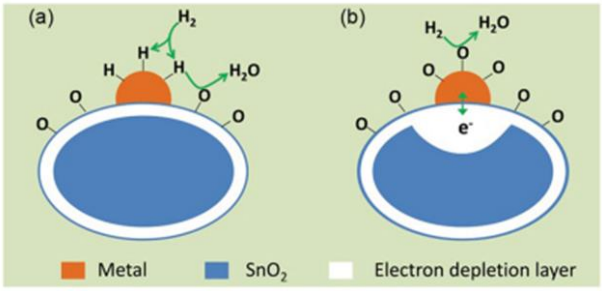

Figure 7.6. Schematic representation of noble metal-assisted gas sensing in SnO_2. In (a), H_2 molecules approach the noble metal catalyst on the SnO_2 surface, where they dissociate and form water (H_2O) with surface oxygen. In (b), the interaction leads to the release of electrons into the SnO_2, reducing the electron depletion layer and lowering the resistance of the sensor. This electron transfer from the metal catalyst to the SnO_2 surface enhances the sensor's response to H_2 gas. Taken from [195].

For instance, Pt doping in SnO_2 significantly enhances its gas sensing capabilities, particularly for hydrogen (H_2) detection, through a combination of different mechanisms. In the presence of Pt nanoparticles, hydrogen molecules first adsorb onto the Pt surface, where they dissociate into atomic hydrogen. This atomic hydrogen then migrates, or "spills over," onto the SnO_2 surface as illustrated in Figure 7.6a. Here, the hydrogen atoms interact with adsorbed oxygen species, leading to the release of electrons into the conduction band of SnO_2. This interaction reduces the electron depletion layer at the surface of SnO_2 (Figure 7.6b), thereby decreasing its electrical resistance [195,196].

The process is further enhanced by the formation of a Schottky barrier at the Pt-SnO_2 interface, which modulates electron flow between the Pt and the semiconductor. When hydrogen interacts with the Pt, the barrier height decreases, facilitating easier electron transfer, which amplifies the change in resistance. Additionally, Pt acts as a catalyst that lowers the activation energy for these reactions, enabling the sensor to operate effectively at lower temperatures, which is beneficial for practical applications requiring rapid response and high sensitivity [193,197].

These combined effects make Pt-doped SnO_2 sensors highly effective for detecting hydrogen at low concentrations, with quick response times and improved selectivity. The integration of Pt into SnO_2 highlights the potential for noble metal doping to enhance the performance of metal oxide-based gas sensors, positioning these materials as critical components in industrial and environmental monitoring systems [193,198].

Furthermore, nanostructuring the sensing layers through soft assembly of atomic clusters into cluster-assembled films offers significant advantages in enhancing gas sensor performance, such as higher surface-to-volume ratio that is key for effective gas interaction and adsorption.

Although significant advancements have been achieved by doping/decoration SnO_2 with noble metals such as platinum and palladium [199–202], which have markedly enhanced gas sensing capabilities, the potential of incorporation or embedding of noble metal in metal oxide nanoparticles has rarely been considered [203] and these structures in gas sensing remain relatively underexplored.

In this study, preliminary results are presented on the gas-sensing behavior of SnO2-Pt cluster-assembled films. These films were synthesized via co-deposition of Sn and Pt, as described in section 7.1.1. To investigate their sensing properties, the films were exposed to 1% H_2 in air under controlled conditions at different temperatures. Prior to gas exposure, the films were annealed in a flow of 100 sccm of air at 250°C for several hours to stabilize the current and ensure uniform surface conditions.

During the sensing experiments, the films were subjected to alternating gas pulses: 120 seconds of air, followed by 60 seconds of 1% H_2 in air, both at a flow rate of 100 sccm. The electrical response was monitored by measuring the change in current under a constant applied voltage of 0.5 V. This current variation, shown in Figure 7.7, reflects the dynamic interaction between the Sn-Pt films and the gases at different temperatures, highlighting the temperature-dependent gas-sensing behavior of the films, influenced by the synergistic effects of Pt catalysis and the porous nanostructure

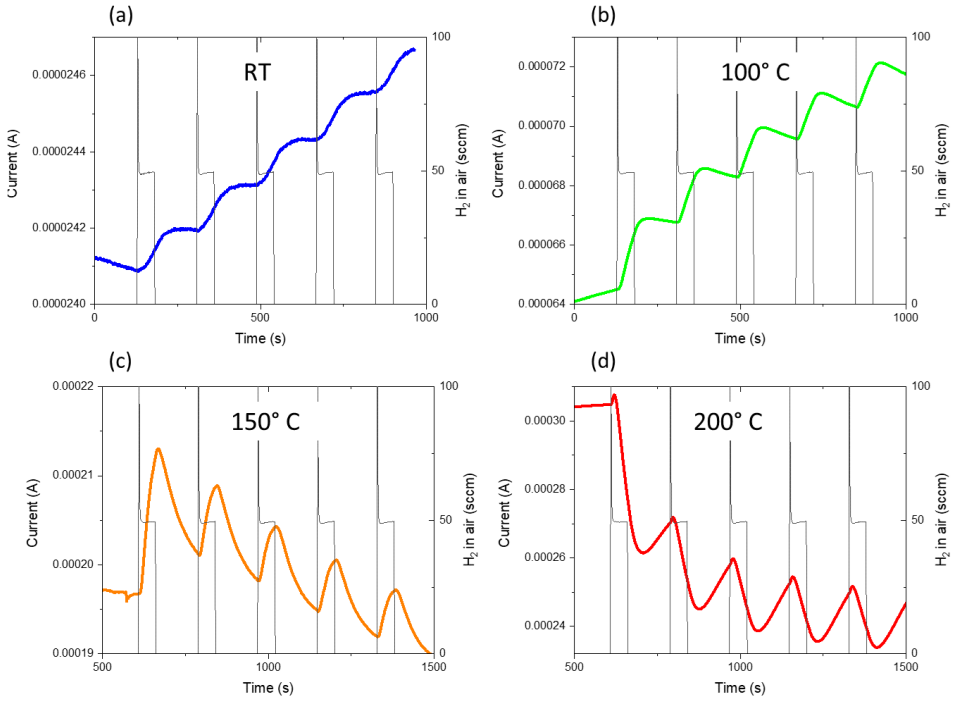

Figure 7.7. Current response of Sn-Pt films (produced by two-cathode approach) to H_2 at different temperatures (Rt, 100°C, 150°C, and 200°C), demonstrate clear temperature-dependent behaviors.

At RT and 100°C, the current increases steadily with each H_2 pulse. This rise is attributed to the interaction between H_2 and adsorbed oxygen species on the SnO_2 surface. Hydrogen reacts with adsorbed oxygen ions (e.g., O^- or O_2^-), releasing trapped electrons back into the conduction band, which increases conductivity. Pt plays a catalytic role by facilitating the dissociation of H_2 into atomic hydrogen, further enhancing the reduction of surface oxygen. The porous structure of the film, combined with the catalytic activity of Pt, increases the effective surface area, improving the gas response sensitivity.

At these lower temperatures, the re-adsorption of oxygen when the gas flow switches to air is relatively slow, resulting in minimal recovery of the current between pulses. The stepwise increase in current, particularly at 100°C, indicates that the desorption of oxygen and its replacement by H_2 is dominant, leading to a higher electron density in the conduction band.

At 150°C, the current response exhibits periodic increases during H_2 exposure and drops when the flow switches to air. This pattern reflects the faster kinetics of oxygen desorption and re-adsorption at elevated temperatures. The H_2 pulses cause the reduction of surface oxygen, temporarily increasing the conductivity, but once the flow switches to air, oxygen quickly re-adsorbs, re-establishing the surface depletion layer and reducing the electron density. This behaviour aligns with studies showing that at moderate temperatures, the balance between oxygen adsorption/desorption and gas interaction becomes more pronounced, with SnO_2 sensors showing a reversible response to H_2 and air cycles. At 200°C the sensing behavior deviates in comparison with the measurements at lower temperatures and further analysis are needed to better understand the hydrogen sensing mechanisms at different temperatures.

The porous structure of the films plays a crucial role in enhancing the gas-sensing response. The porous architecture increases the sensor's surface area, improving gas diffusion and interaction with surface-active sites, which is critical for both the reduction and re-adsorption of oxygen. Moreover, the addition of Pt enhances the dissociation of H_2 and modulates the surface chemistry by forming active catalytic sites, which improves the sensor's sensitivity and selectivity to H_2 at different temperatures.

As these are preliminary results, further refinements of experimental parameters, such as H_2 concentration, exposure times, and sensor fabrication conditions, are still necessary. Future work will focus on optimizing these parameters to enhance sensor performance, particularly in terms of sensitivity, response time, and selectivity to H_2 in complex gas environments as well as the mechanism behind the different responses.

7.2 Non-linear memristive electrical transport

Memristors, a term derived from "memory resistor," represent the fourth fundamental passive circuit element, joining resistors, capacitors, and inductors. Initially conceptualized by Leon Chua in 1971, memristors became a physical reality in 2008 with the demonstration by HP Labs [204,205]. These devices have gained significant attention due to their unique properties, including non-volatility, low power

consumption, and the ability to mimic synaptic behavior, making them highly promising for next-generation computing architectures, especially in neuromorphic and memory applications.

A memristor's fundamental operation is based on the relationship between the time integral of current and the time integral of voltage, linking charge and flux. This unique characteristic allows memristors to retain their resistance level even after the power is turned off, a feature that distinguishes them from traditional resistive devices. The resistance change is typically governed by ion migration, phase transitions, or charge trapping/de-trapping mechanisms, depending on the material system and device structure used [206].

The integration of cluster-assembled films into memristors presents several advantages due to their unique electrical properties which can vary with factors such as coverage, oxidation, and the intrinsic properties of the materials themselves. Moreover, the ability to precisely control the size and composition of clusters allows for the engineering of films with customized electronic properties, which is crucial for optimizing memristor performance.

Recent research highlights the work of S. Brown's group and P. Milani's group, who have explored the resistive switching behavior in cluster-assembled thin films near and beyond the percolation threshold, respectively. Furthermore, switching behavior in oxidized cluster-assembled films seem to be unexplored. In this context, the switching behavior of WO_x cluster-assembled films is also explored in this thesis.

7.2.1 The case of films near percolation

S. Brown's group [170–172,176] has demonstrated resistive switching in Sn nanoparticulate films, where 7 nm particles coalesce to form larger aggregates approximately 20 nm in diameter, fabricated using a magnetron sputtering cluster source. These films are carefully engineered to be near the electrical percolation threshold, the critical point where a fully connected network of nanoclusters begins to emerge (Figure 7.8). The observed resistive switching in these films is attributed to the stochastic formation and destruction of

nanojunctions, where these conductive filaments are formed between gaps of neighbouring clusters under an applied voltage.

The application of voltage sweeps or pulses triggers several key mechanisms, including Electric Field Induced Evaporation (EFIE) and Electric Field Induced Surface Diffusion (EFISD) of surface atoms. These processes lead to the formation of atomic-scale wires within the tunnel gaps present in the percolating network. Additionally, van der Waals forces, which are independent of the applied electric field, can further drive the formation of atomic-scale connections between particles. As the gaps between non-connected particles decrease, the local electric field strength increases, which in turn promotes the formation of these atomic-scale wires, thus increasing the conductance.

However, the high electrical currents that flow through the newly formed nanojuctions, causes electromigration-induced breakdown and disconnection of these atomic-wires, resulting in a decreasing in conductance. This dynamic process creates conductive pathways of varying lengths, leading to the observed resistive switching behavior. Interestingly, this behavior has parallels with neuron firing patterns, as it exhibits long-range temporal correlations similar to those found in the brain's cortex, a phenomenon that has been further explored in studies involving Ag nanoparticle networks [207].

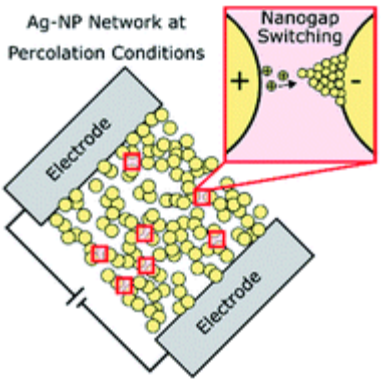

Figure 7.8. Schematic of an Ag nanoparticle (Ag-NP) network near percolation, illustrating the formation of conductive pathways between electrodes. Inset highlights nanogap switching, where electric field-induced atomic rearrangements bridge gaps between nanoparticles, enabling stochastic conductance changes within the network. Taken from [207].

Here as described in Sections 6.2.2 and 6.5.3, high deposition rate was employed until reaching ~10 nm. I-V measurements were conducted at room temperature to investigate the electrical behavior of the Sn nanoparticle films. As shown in Figure 6.16, the I-V curves exhibited non-linear characteristics and evidence of conductance switching after a consecutive IV pulse. Preliminary results in Figure 7.9 show the conductance (G) as a function of time under a series of voltage pulses (I-Vs from 1-10 V), with stepwise increases in G representing stochastic switching events typical in atomic-switch networks (ASNs) [170,171]. These events are driven by electric-field-induced atomic rearrangements within the nanoparticle network. The inset I-V curve illustrates that switching becomes more pronounced at higher voltages, where atomic-scale conductive filaments are more likely to form, enhancing conductance. This behavior associates with EFISD and EFIE mechanisms.

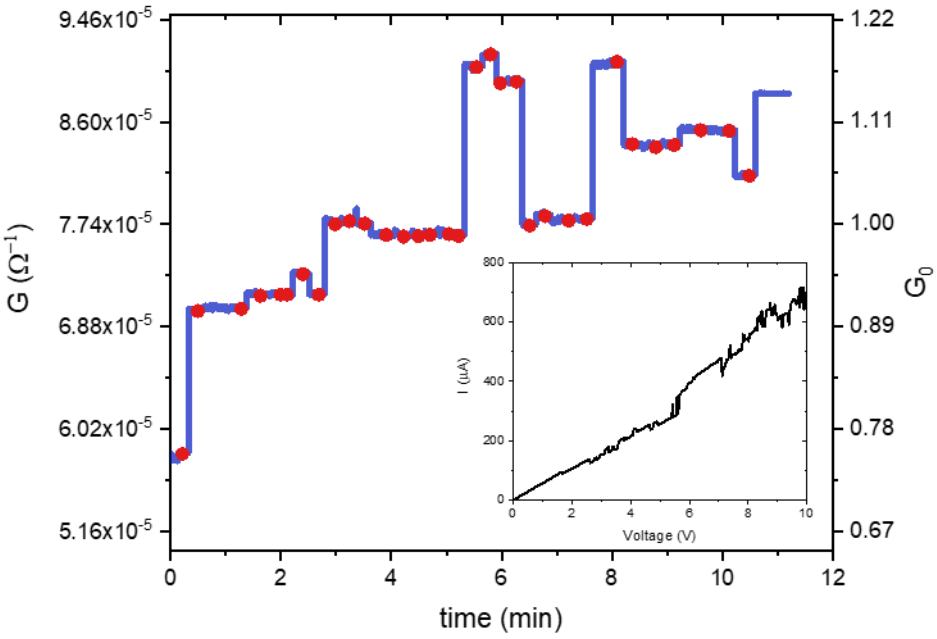

Figure 7.9. Conductance G vs. time under IV pulses (1-10 V), showing stochastic switching events in a self-assembled atomic-switch network. Stepwise conductance increases are due to electric field-induced atomic rearrangements forming conductive

filaments. Inset: I-V curve highlights more pronounced switching at higher voltages, consistent with EFISD and EFIE mechanisms.

Our findings on the non-Ohmic behavior and quantum tunneling in the I-V characteristics of cluster-assembled tin films align with the study by Bose et al. [171] on stable self-assembled atomic-switch networks for neuromorphic applications. They investigated Sn nanoparticle networks with a controlled oxidized shell, observing non-linear current-voltage characteristics suggestive of quantum tunneling. Their research also delved into the stochastic switching mechanisms associated with increases and decreases in device conductance in Sn NP networks highlighting that conductance modulation with electric field stimuli is essential for synaptic learning capability in neuromorphic systems. This expands our understanding of the complex electrical behavior of cluster-assembled films before the percolation threshold. Their research supports our observation of non-Ohmic behavior and quantum tunneling in the I-V characteristics of tin films.

7.2.2 The case of films beyond percolation

P. Milani's group [9,10,208–211] has observed resistive switching in Au cluster-assembled films produced using a PMCS, with the films studied beyond the percolation threshold. One would expect that increasing the film's thickness beyond the percolation threshold would lead to a uniform, metal-like ohmic conductivity, resembling that of bulk materials. However, these films exhibit unusual electrical and structural properties due to the retention of individual cluster morphologies, which results in a high density of grain boundaries that significantly deviate from expected bulk properties.

Figure 7.10 illustrates the complex resistive switching behavior in these films, initiated when an electric current passes through a film characterized by a non-uniform arrangement of grains and a high inter-grain boundary density (state 1). The localized Joule heating from the current flow increases the mobility of the grains. This mobility facilitates grain rearrangement and reorientation, effectively reducing local resistance through the sintering of grains and elimination of defects (state 2).

As the resistance decreases, the increase in current density further elevates the local temperature, leading to enhanced electromigration and eventual breakdown of electrical connections between grains. This results in a sharp rise in resistance (state 3), followed by a decrease in current density. The decrease in current density allows the system to cool and stabilize, potentially leading back to state 1, where new electrical pathways can form. This dynamic reconfiguration is responsible for the complex resistive switching and spiking behavior observed in these films beyond the percolation threshold. The ability to precisely control this behavior with an externally applied voltage allows for tailored functionality in devices for unconventional computing, highlighting its potential in fields where adaptable and responsive properties are of interest.

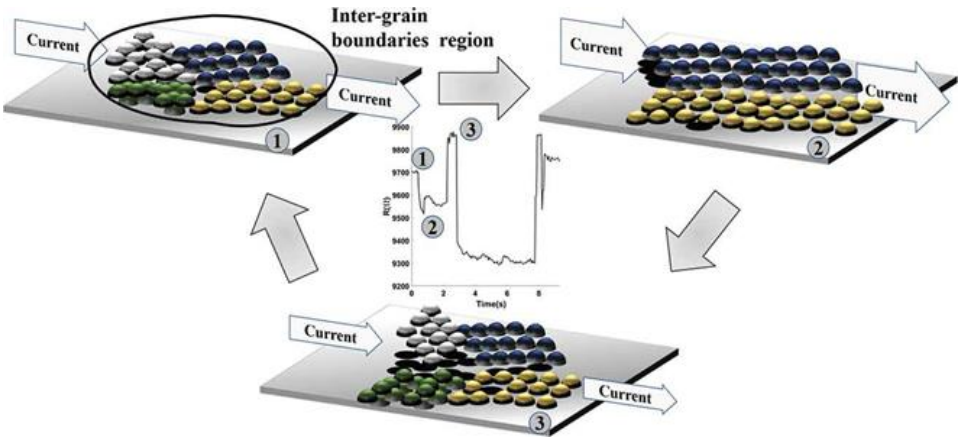

Figure 7.10. Schematic representation of atomic rearrangements at a single grain boundary under current flow, driving resistive switching events. Different colors indicate regions with distinct crystalline orientations. (1) Initial configuration. (2) Grain boundary configuration after current flow and Joule heating. (3) Breakdown of connectivity due to high current density, leading to a redistribution of current flow that promotes further atomic migration and reformation of electrical paths (returning to 1). Taken from [9].

Here, I present preliminary evidence of the resistive switching behavior of Ni nanoparticle films (~5 nm) beyond the electrical percolation threshold. Building on

previous studies of Au cluster-assembled films, electrical characterization of the Ni films revealed a non-ohmic behavior, consistent with earlier findings. The Ni films exhibit a complex resistive switching mechanism that is significantly influenced by the applied voltage.

As shown in Figure 7.10, the conductance G undergoes a stepwise change, with red dots marking the application of IV pulses of 1 V and 2 V. The conductance shows both increases and decreases following the pulses, indicating dynamic changes in the film's conductance state. The decreases in conductance after certain pulses suggest the creation of resistive barriers due to grain boundary rearrangements or defect migration. Conversely, the increases in conductance after the pulses, can be attributed to the re-establishment of conductive pathways through localized atomic reorganization. These distinct, reversible steps reflect a non-linear resistive switching behavior, as observed in previous studies on nanogranular Au films, where the applied electric field modulates the conductive network in response to the structural dynamics of the film.

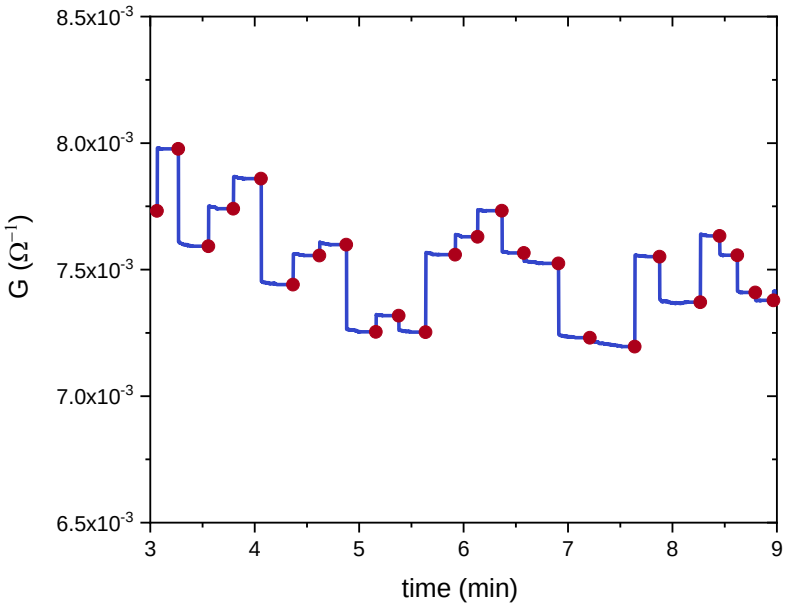

Figure 7.11. Time evolution of conductance (G) in Ni cluster-assembled films under periodic IV pulses of 1 V and 2 V, marked by red dots. The stepwise conductance changes indicate a resistive switching behavior, with both increases and decreases attributed to dynamic rearrangement of grain boundaries and defect migration.

These initial observations of resistive switching in Ni cluster-assembled films provide promising evidence of their potential for advanced electronic applications. However, further refinements in fabrication and a more comprehensive understanding of the switching mechanisms are necessary to fully exploit the unique properties of these films for practical device integration.

7.2.3 The case of partially oxidized films

Metal oxide (MOx) based resistance switching devices have emerged as a promising candidate for next-generation non-volatile memory (NVM) and neuromorphic computing applications, owing to their simple structure, scalability, low power consumption, and compatibility with CMOS technology. A key feature of these devices is their ability to exhibit both volatile and non-volatile resistance switching behaviors, which can be leveraged for different functionalities [206,212,213].

Non-volatile resistance switching in MOx is typically attributed to the formation and rupture of conductive filaments composed of oxygen vacancies or metal ions within the oxide layer. The application of an external electric field induces the migration of these defects, leading to a change in the device resistance that persists even after the removal of the field. This phenomenon has been extensively studied for resistive random-access memory (RRAM) applications, where the two resistance states represent the binary '0' and '1'.

Volatile resistance switching, on the other hand, is characterized by a reversible change in resistance that occurs only in the presence of an applied electric field. This behavior is often associated with the trapping and de-trapping of charge carriers at defect sites or interfaces within the MOx layer. While volatile switching has traditionally been considered a drawback for NVM applications, it has recently gained attention for its potential in neuromorphic computing, where it can emulate the synaptic plasticity of biological neurons.

The ability to control and tune the volatile and non-volatile switching characteristics of MOx devices through material engineering, device design, and operating conditions

opens up exciting possibilities for future applications. For instance, multi-level resistance states can be achieved by carefully controlling the filament formation and rupture processes, enabling high-density data storage. Furthermore, the volatile switching behavior can be exploited to implement various synaptic functions, such as short-term and long-term potentiation/depression, paving the way for hardware-based neural networks.

Despite the significant progress made in understanding and controlling resistance switching in MOx, several challenges remain to be addressed before their widespread adoption. These include improving the device reliability and endurance, reducing the switching variability, and understanding the underlying physical mechanisms at the nanoscale. Additionally, further research is needed to explore novel MOx materials and device architectures that can offer enhanced performance and functionality.

Among various MOx materials, WOx has gained significant attention due to its unique properties that make it well-suited for resistance switching applications. Its rich defect chemistry, including oxygen vacancies and tungsten ions, facilitates the formation and rupture of conductive filaments, enabling both volatile and non-volatile switching behaviors [214–216]. Furthermore, WOx exhibits excellent stability, making it a practical choice for device integration.

The resistive switching behavior of cluster-assembled WO3-x thin films was investigated through a series of I-V measurements. These films were oxidized in air, resulting in a mixed-phase composition as confirmed by XPS (section 5.4.4).

Figure 7.12 (a) shows the current response of the WOx film under consecutive I-V pulses from 0 to -20 V. With each pulse, the current incrementally increases in the negative direction, suggesting a cumulative increase in conductance with each applied pulse. When pulsing stops, the current gradually decays, returning to its original baseline. This decay implies that the conductance state is temporary and dependent on continuous stimulation, suggesting volatile behavior. The smooth, cumulative increase in current with each pulse points to an analog-type response, where conductance modulation is gradual and continuous.

Figure 7.12 (b) shows the I-V response over six consecutive cycles from 0 to -20 V and back to 0 V. Each cycle produces a higher current, reflecting a progressive increase in conductance across cycles. The cumulative conductance enhancement, without abrupt transitions, supports an analog switching mechanism. Based on the volatile characteristics observed in Figure 7.12 (a), it is inferred that this progressive increase in conductance would also decay if cycling were to stop, indicating a combination of analog and volatile characteristics.

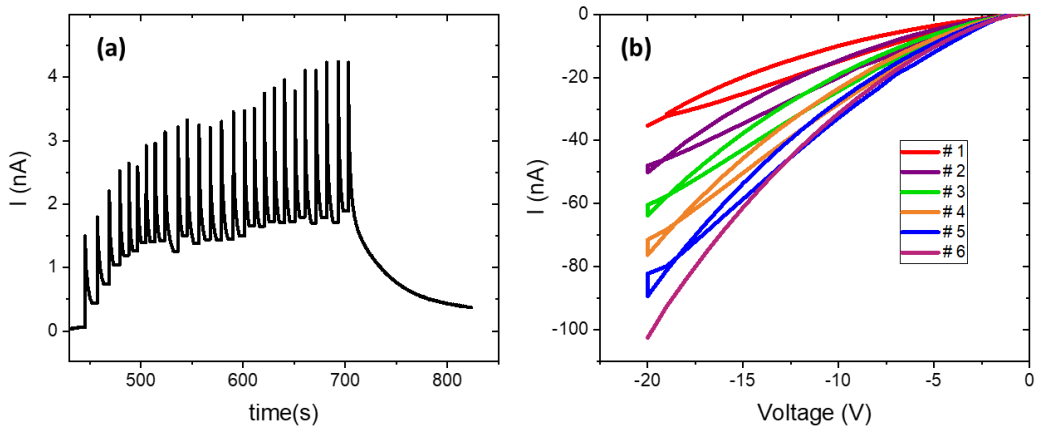

Figure 7.12. (a) Current response of cluster-assembled WOx films under consecutive I-V pulses from 0 to -20 V. Each pulse results in a cumulative increase in conductance, with conductance gradually decaying back to the baseline level when pulsing stops, indicating analog and volatile switching behavior. (b) I-V response of cluster-assembled WOx films under six consecutive cycles from 0 to -20 V and back to 0 V. Each cycle leads to a progressive increase in conductance, supporting analog switching. The volatile nature of conductance is inferred from the gradual decay observed in (a).

The analog and volatile switching behaviour observed in the WOx films is facilitated by their cluster-assembled structure and mixed-phase composition. The porous morphology and the presence of multiple tungsten oxidation states create pathways that enhance oxygen vacancy mobility and redistribution within the film.

Under the applied negative bias, oxygen vacancies migrate toward the electrode interface, modulating the Schottky barrier and resulting in a gradual, cumulative

increase in conductance. This analog switching arises from the smooth and incremental conductance changes with each pulse or cycle, rather than sharp transitions.

When the voltage is removed, the vacancies diffuse back into the bulk, leading to a volatile response where the conductance returns to its baseline level. This temporary conductance enhancement resembles short-term memory effects, indicative of a non-permanent switching state.

This behavior aligns with findings by Hu et al. [214] and Yang et al. [215,216], where similar WOx-based devices exhibited analog and volatile switching through oxygen vacancy dynamics. The reversible, vacancy-based modulation in these WOx films allows for temporary, multi-level conductance states that emulate synaptic plasticity, making them suitable for neuromorphic applications.

Although evidence of non-volatile resistive switching was observed in thicker samples studied in this thesis, still further analyses are needed to clearly distinguish the mechanisms involved and confirm the stability and endurance of these states under extended cycling conditions.

CHAPTER 8. CONCLUSIONS

Through this PhD work, the Supersonic Cluster Beam Deposition (SCBD) technique was introduced and established at the Luxembourg Institute of Science and Technology (LIST), where during the first year I participated in assembling the vacuum system, designing the substrate holder, installing the setup for in-situ electrical and thickness measurements, and designing deposition protocols within the graphical user interface (GUI). These contributions led to the building of an advanced experimental platform that allowed precise control over deposition parameters and real-time monitoring of film growth, enabling in situ investigation of electrical transport properties of cluster-assembled thin films during growth.

Building upon this groundwork, the general objective of this thesis was to investigate the correlation between morphological and electrical transport properties in cluster-assembled thin films of Sn, Pt, Ni, and W deposited using the new SCBD prototype. Such metals were selected in order to have low melting point ones and high melting point ones, as well as some more prone to oxidation and some less. By studying the structural evolution and electrical behaviour from the sub-monolayer to the thin film regime, I aimed to deepen the understanding of thin film growth mechanisms and establish how morphological features impact electrical transport properties.

My study confirms that the sub-monolayer growth of Pt, Ni, and W thin films adheres to the Deposition Diffusion Aggregation (DDA) model. This model describes how particles undergoing random motion (diffusion) stick irreversibly upon contact, leading to the formation of aggregates. Such aggregates evolve towards interconnected dendritic structures as surface coverage increases. This morphological progression is quantitatively characterized by an increase in the fractal dimension (Df), indicating that the film's morphology becomes more complex and interconnected as growth proceeds.

Dendritic structures form percolation paths when surface coverage exceeds 59% the value foreseen by standard percolation theory. In Pt and W films, the onset of conductance occurs at nominal thickness values of about 1.5 nm and 0.9 nm,

respectively. The fractal dimensions calculated at similar thicknesses from TEM images are 1.87 for Pt and 1.9 for W—values indicative of percolation in fractal systems—and correspond to surface coverages of 63% for Pt and 71% for W. This suggests that the percolation process in these materials can be effectively modelled using the continuum percolation framework, which occurs at around 68% coverage.

In contrast, Sn films exhibit markedly different behaviour due to their lower melting point, which influences both morphology and electrical transport. Instead of following the DDA model, Sn nanoparticles demonstrate liquid-like interactions at early deposition stages, leading to coalescence into larger, ovoidal islands rather than forming dendritic-like structures. Coalescence affects the percolation threshold, occurring at larger thicknesses around 24 nm, under low deposition rates conditions. By manipulating the deposition rate—a parameter easily controlled via the cluster source repetition rate—I observed a significant change in Sn film morphology. Higher deposition rates influence the coalescence dynamics, preventing complete merging of particles and shifting the percolation threshold to a value as low as 3 nm. This change in morphology directly impacts electrical transport properties, as evidenced by substantial variations in conductance, and demonstrates how deposition parameters can be used to tailor the correlation between structure and electrical behaviour in low melting point materials.

During the three-dimensional (3D) growth regime, Pt, Ni, and W cluster-assembled films exhibit a power-law relationship between surface roughness and thickness, with exponent values between 0.31−0.46, indicative of ballistic growth mechanism. In ballistic growth, particles travel in straight paths before adhering to the surface, leading to highly porous structures. This morphological characteristic is closely linked to electrical transport properties. The films display resistivity values approximately 2–3 orders of magnitude higher than their bulk counterparts, attributed to the granular nature of the films and electron scattering at grain boundaries and interfaces. I also observed that in the 3D conduction regime, resistivity varies non-linearly with thickness, following a power law with exponent values between 0.76−0.96. This behavior is consistent with observations in other cluster-assembled metal films produced by SCBD and is attributed to the gradual decrease in interconnections within

the uppermost layers of the film during growth, as dictated by ballistic growth dynamics.

Additionally, in the sub-percolation regime, the cluster-assembled metallic films exhibit nonlinear current-voltage (I-V) characteristics, indicating that quantum tunnelling is the primary charge transport mechanism across nanoscale gaps between islands. This behavior is consistent across all the studied materials, highlighting a common conduction mechanism in this regime. However, Fowler-Nordheim tunnelling currents were observed only in Sn films with voltage transition values between 1.6−2.5 V, suggesting that microstructural differences resulting from coalescence affect the tunnelling behavior. In contrast, high melting point films exhibit stable direct tunnelling without transitioning to Fowler-Nordheim tunnelling across a wide voltage range of 50 V, likely due to the presence of numerous tunnelling paths.

The oxidation behavior of Ni and Sn films further distinguishes their structural evolution. In Ni films, X-ray Photoelectron Spectroscopy (XPS) and Transmission Electron Microscopy (TEM) analysis reveal the formation of core-shell structures where metallic Ni cores are encapsulated by $NiO/Ni(OH)_2$ shells. The preservation of cubic crystalline symmetry in both core and shell suggests that the ordered metallic phase exists prior to deposition, and the oxide shell forms with the same symmetry upon room-temperature air exposure. Notably, the observation of both core-shell and fully hollow Ni nanoparticles indicates the occurrence of the Kirkendall effect, where different diffusion rates between Ni cations and oxygen anions lead to void formation within particles. This phenomenon affects the microstructure and, consequently, the electrical transport properties by introducing voids and modifying pathways for conduction. These findings imply that particle size alone is insufficient to predict oxidation outcomes at room temperature; instead, inter-particle structural differences, such as grain boundary density and internal defects, play crucial roles.

In contrast, Sn films oxidize to form core-shell structures with an oxidation gradient transitioning from metallic Sn to SnO, Sn_3O_4, and finally SnO_2. Raman spectroscopy provides unequivocal evidence of the spontaneous formation of Sn_3O_4 at room temperature, aligning with theoretical predictions that this intermediate phase is energetically favored during the oxidation of Sn nanostructures. The incomplete

oxidation due to the larger size of Sn islands results in residual metallic cores that maintain electrical conductivity, but the oxide shell and the morphology of the islands influence the overall transport properties of the film.

Building on our findings with single-metal systems, I also explored the production of bimetallic nanoparticles of Sn and Pt using a composite cathode and a two-cathode configuration. The rational being to obtain, upon exposure to air, a combination of the standard oxide used for chemoresistive gas sensing (SnO2) with a catalytic metal (Pt), which should promote heterogeneous catalysis surface reactions and enhance gas sensing properties. Preliminary analyses using Scanning Transmission Electron Microscopy (STEM) coupled with Energy-Dispersive X-ray Spectroscopy (EDS) provided insights into the different characteristics of bimetallic nanoparticles generated with the different cathode configurations. The ability to tailor structural and compositional properties in bimetallic systems can open new avenues for material design, offering synergistic effects that could enhance catalytic activity and sensing performance.

Preliminary studies of Pt-SnOx films for gas sensing applications in respect to hydrogen detection have shown interesting results. I in fact observed that device temperature qualitatively affects the impact of hydrogen on film conductivity, which increases at low temperature, while decreases at high temperature. Further investigations are needed to better understand the hydrogen sensing mechanisms. Future work should focus on systematic studies of Pt-SnOx films under varying temperatures, exploring how bimetallic composition and nanoparticle configuration affect sensing behaviour, response times, and sensitivity.

Additionally, preliminary results revealed non-linear electrical conduction and conductance switching upon the application of external voltage across all studied materials. According to the scientific literature, I propose that also in the case of cluster-assembled films by SCBD, (1) in Sn films near the percolation threshold conductance switching is driven by the formation and disruption of atomic-scale wires, (2) in Ni and Pt films beyond the percolation threshold, switching occurs due to atomic rearrangements at single grain boundaries, and (3) in WO_x films, volatile switching is facilitated by oxygen vacancy migration. On one hand, these diverse switching

mechanisms occurring in cluster-assembled films by SCBD require additional investigation. On the other hand, they highlight the versatility of the method and its potential for tailored applications for unconventional computing.

The successful implementation of SCBD at LIST has proven highly effective in producing nanogranular films composed of diverse ensembles of particles from different materials. The results obtained during this PhD demonstrate that by understanding the relationship between film morphology and electrical transport, we can deliberately engineer thin films with tailored electrical characteristics. Fine-tuning deposition conditions thus enables the production of films optimized for specific applications in electronics, energy storage, sensing, and catalysis.

REFERENCES

[1] S. Kasap, C. Koughia, H. Ruda, R. Johanson, Electrical Conduction in Metals and Semiconductors, in: Springer Handbook of Electronic and Photonic Materials, Springer US, Boston, MA, 2006: pp. 19–45. https://doi.org/10.1007/978-0-387-29185-7_2.

[2] N.W. Ashcroft, N.D. Mermin, S. Rodriguez, Solid State Physics, Am J Phys 46 (1978) 116–117. https://doi.org/10.1119/1.11117.

[3] J.M. Ziman, Electrons and Phonons, Oxford University Press, 2001. https://doi.org/10.1093/acprof:oso/9780198507796.001.0001.

[4] K. Fuchs, The conductivity of thin metallic films according to the electron theory of metals, Mathematical Proceedings of the Cambridge Philosophical Society 34 (1938) 100–108. https://doi.org/10.1017/S0305004100019952.

[5] E.H. Sondheimer, The mean free path of electrons in metals, Adv Phys 1 (1952) 1–42. https://doi.org/10.1080/00018735200101151.

[6] R.S. Smith, E.T. Ryan, C.-K. Hu, K. Motoyama, N. Lanzillo, D. Metzler, L. Jiang, J. Demarest, R. Quon, L. Gignac, C. Breslin, A. Giannetta, S. Wright, An evaluation of Fuchs-Sondheimer and Mayadas-Shatzkes models below 14nm node wide lines, AIP Adv 9 (2019). https://doi.org/10.1063/1.5063896.

[7] Y. Namba, Resistivity and Temperature Coefficient of Thin Metal Films with Rough Surface, Jpn J Appl Phys 9 (1970) 1326. https://doi.org/10.1143/JJAP.9.1326.

[8] A.F. Mayadas, M. Shatzkes, Electrical-Resistivity Model for Polycrystalline Films: the Case of Arbitrary Reflection at External Surfaces, Phys Rev B 1 (1970) 1382–1389. https://doi.org/10.1103/PhysRevB.1.1382.

[9] M. Mirigliano, P. Milani, Electrical conduction in nanogranular cluster-assembled metallic films, Adv Phys X 6 (2021). https://doi.org/10.1080/23746149.2021.1908847.

[10] F. Borghi, M. Mirigliano, D. Dellasega, P. Milani, Influence of the nanostructure on the electric transport properties of resistive switching cluster-assembled gold films, Appl Surf Sci 582 (2022) 152485. https://doi.org/10.1016/j.apsusc.2022.152485.

[11] E. Barborini, G. Corbelli, G. Bertolini, P. Repetto, M. Leccardi, S. Vinati, P. Milani, The influence of nanoscale morphology on the resistivity of cluster-assembled nanostructured metallic thin films, New J Phys 12 (2010) 073001. https://doi.org/10.1088/1367-2630/12/7/073001.

[12] K. Kamata, T. Aihara, K. Wachi, Synthesis and catalytic application of nanostructured metal oxides and phosphates, Chemical Communications 60 (2024) 11483–11499. https://doi.org/10.1039/D4CC03233K.

[13] J. Wang, Z. Li, R. Li, H. Wang, Y. Wu, X. Liu, Z. Lu, Nanoporous Metals Based on Metallic Glasses: Synthesis, Structure and Functional Applications, Acta Metallurgica Sinica (English Letters) 36 (2023) 1573–1602. https://doi.org/10.1007/s40195-023-01597-6.

[14] J.E. Ellis, S.E. Crawford, K.-J. Kim, Metal–organic framework thin films as versatile chemical sensing materials, Mater Adv 2 (2021) 6169–6196. https://doi.org/10.1039/D1MA00535A.

[15] J. Jia, Y. Lan, Synthesis, Characterization, and Applications of Nanomaterials for Energy Conversion and Storage, Molecules 28 (2023) 7383. https://doi.org/10.3390/molecules28217383.

[16] F. Baletto, R. Ferrando, Structural properties of nanoclusters: Energetic, thermodynamic, and kinetic effects, Rev Mod Phys 77 (2005) 371–423. https://doi.org/10.1103/RevModPhys.77.371.

[17] R. Ferrando, J. Jellinek, R.L. Johnston, Nanoalloys: From Theory to Applications of Alloy Clusters and Nanoparticles, Chem Rev 108 (2008) 845–910. https://doi.org/10.1021/cr040090g.

[18] T. Tsukamoto, Recent advances in atomic cluster synthesis: a perspective from chemical elements, Nanoscale 16 (2024) 10533–10550. https://doi.org/10.1039/D3NR06522G.

[19] Y. Wang, D. Wang, Y. Li, Rational Design of Single-Atom Site Electrocatalysts: From Theoretical Understandings to Practical Applications, Advanced Materials 33 (2021). https://doi.org/10.1002/adma.202008151.

[20] M.-C. Daniel, D. Astruc, Gold Nanoparticles: Assembly, Supramolecular Chemistry, Quantum-Size-Related Properties, and Applications toward Biology, Catalysis, and Nanotechnology, Chem Rev 104 (2004) 293–346. https://doi.org/10.1021/cr030698+.

[21] A.T. Bell, The Impact of Nanoscience on Heterogeneous Catalysis, Science (1979) 299 (2003) 1688–1691. https://doi.org/10.1126/science.1083671.

[22] H. Haberland, Clusters of Atoms and Molecules, Springer Berlin Heidelberg, Berlin, Heidelberg, 1994. https://doi.org/10.1007/978-3-642-84329-7.

[23] K. Wegner, P. Piseri, H.V. Tafreshi, P. Milani, Cluster beam deposition: a tool for nanoscale science and technology, J Phys D Appl Phys 39 (2006) R439–R459. https://doi.org/10.1088/0022-3727/39/22/R02.

[24] Y. Huttel, Gas-Phase Synthesis of Nanoparticles, Wiley, 2017. https://doi.org/10.1002/9783527698417.

[25] J.M. Hayes, G.J. Small, Supersonic Jets, Rotational Cooling, and Analytical Chemistry, Anal Chem 55 (1983) 565A-574A. https://doi.org/10.1021/ac00255a784.

[26] C. Vallance, Collision rates in gases, in: An Introduction to the Gas Phase, Morgan & Claypool Publishers, 2017: pp. 6-1-6–7. https://doi.org/10.1088/978-1-6817-4692-0ch6.

[27] G. Scoles, Atomic and Molecular Beam Methods, n.d.

[28] R. Campargue, Atomic and Molecular Beams, Springer Berlin Heidelberg, Berlin, Heidelberg, 2001. https://doi.org/10.1007/978-3-642-56800-8.

[29] P. Milani, S. Iannotta, Cluster Beam Synthesis of Nanostructured Materials, Springer Berlin Heidelberg, Berlin, Heidelberg, 1999. https://doi.org/10.1007/978-3-642-59899-9.

[30] G. Sanna, G. Tomassetti, Introduction to Molecular Beams Gas Dynamics, PUBLISHED BY IMPERIAL COLLEGE PRESS AND DISTRIBUTED BY WORLD SCIENTIFIC PUBLISHING CO., 2005. https://doi.org/10.1142/p387.

[31] H.I. Ashkenas, F.S. Sherman, The Structure and Utilization of Supersonic Free Jets in Low Density Wind Tunnels, in: 1965. https://api.semanticscholar.org/CorpusID:93121606.

[32] T.E. Wall, Preparation of cold molecules for high-precision measurements, Journal of Physics B: Atomic, Molecular and Optical Physics 49 (2016) 243001. https://doi.org/10.1088/0953-4075/49/24/243001.

[33] V. Aquilanti, D. Ascenzi, D. Cappelletti, M. de Castro, F. Pirani, Natural Alignment and Cooling in Seeded Supersonic Free Jets: Experiments and a Quantum Mechanical View, in: Atomic and Molecular Beams, Springer Berlin Heidelberg, Berlin, Heidelberg, 2001: pp. 263–272. https://doi.org/10.1007/978-3-642-56800-8_17.

[34] P.A. Skovorodko, Simulation Of The Parameters Of Seeded Molecular Beam, in: AIP Conf Proc, AIP, 2005: pp. 857–862. https://doi.org/10.1063/1.1941642.

[35] T.G. Dietz, M.A. Duncan, D.E. Powers, R.E. Smalley, Laser production of supersonic metal cluster beams, J Chem Phys 74 (1981) 6511–6512. https://doi.org/10.1063/1.440991.

[36] B. Raoult, J. Farges, Electron Difraction Unit with Supersonic Molecular Beam and Cluster Beam, Review of Scientific Instruments 44 (1973) 430–434. https://doi.org/10.1063/1.1686150.

[37] C.G. Granqvist, R.A. Buhrman, Ultrafine metal particles, J Appl Phys 47 (1976) 2200–2219. https://doi.org/10.1063/1.322870.

[38] O. Kylián, D. Nikitin, J. Hanuš, S. Ali-Ogly, P. Pleskunov, H. Biederman, Plasma-assisted gas-phase aggregation of clusters for functional nanomaterials, Journal of Vacuum Science & Technology A 41 (2023). https://doi.org/10.1116/6.0002374.

[39] P. Mélinon, G. Fuchs, B. Cabaud, A. Hoareau, P. Jensen, V. Paillard, M. Treilleux, Low-energy cluster beam deposition : do you need it ?, Journal de Physique I 3 (1993) 1585–1603. https://doi.org/10.1051/jp1:1993202.

[40] H. Haberland, History, Some Basics, and an Outlook, in: Gas-Phase Synthesis of Nanoparticles, Wiley, 2017: pp. 1–21. https://doi.org/10.1002/9783527698417.ch1.

[41] P. Milani, W.A. deHeer, Improved pulsed laser vaporization source for production of intense beams of neutral and ionized clusters, Review of Scientific Instruments 61 (1990) 1835–1838. https://doi.org/10.1063/1.1141103.

[42] K.S. Molek, T.D. Jaeger, M.A. Duncan, Photodissociation of vanadium, niobium, and tantalum oxide cluster cations, J Chem Phys 123 (2005). https://doi.org/10.1063/1.2050650.

[43] M.A. Duncan, SPECTROSCOPY OF METAL ION COMPLEXES: Gas-Phase Models for Solvation, Annu Rev Phys Chem 48 (1997) 69–93. https://doi.org/10.1146/annurev.physchem.48.1.69.

[44] A. Perez, P. Melinon, V. Dupuis, P. Jensen, B. Prevel, J. Tuaillon, L. Bardotti, C. Martet, M. Treilleux, M. Broyer, M. Pellarin, J.L. Vaille, B. Palpant, J. Lerme, Cluster assembled materials: a novel class of nanostructured solids with original structures and properties, J Phys D Appl Phys 30 (1997) 709–721. https://doi.org/10.1088/0022-3727/30/5/003.

[45] M.A. Duncan, Invited Review Article: Laser vaporization cluster sources, Review of Scientific Instruments 83 (2012). https://doi.org/10.1063/1.3697599.

[46] W. Bouwen, P. Thoen, F. Vanhoutte, S. Bouckaert, F. Despa, H. Weidele, R.E. Silverans, P. Lievens, Production of bimetallic clusters by a dual-target dual-laser vaporization source, Review of Scientific Instruments 71 (2000) 54–58. https://doi.org/10.1063/1.1150159.

[47] S. Yatsuya, T. Kamakura, K. Yamauchi, K. Mihama, A New Technique for the Formation of Ultrafine Particles by Sputtering, Jpn J Appl Phys 25 (1986) L42. https://doi.org/10.1143/JJAP.25.L42.

[48] H. Haberland, M. Karrais, M. Mall, Y. Thurner, Thin films from energetic cluster impact: A feasibility study, Journal of Vacuum Science & Technology A: Vacuum, Surfaces, and Films 10 (1992) 3266–3271. https://doi.org/10.1116/1.577853.

[49] G. Sanzone, J. Yin, H. Sun, Scaling up of cluster beam deposition technology for catalysis application, Front Chem Sci Eng 15 (2021) 1360–1379. https://doi.org/10.1007/s11705-021-2101-7.

[50] E. Barborini, P. Piseri, P. Milani, A pulsed microplasma source of high intensity supersonic carbon cluster beams, J Phys D Appl Phys 32 (1999) L105–L109. https://doi.org/10.1088/0022-3727/32/21/102.

[51] H.V. Tafreshi, P. Piseri, G. Benedek, P. Milani, The Role of Gas Dynamics in Operation Conditions of a Pulsed Microplasma Cluster Source for Nanostructured Thin Films Deposition, J Nanosci Nanotechnol 6 (2006) 1140–1149. https://doi.org/10.1166/jnn.2006.139.

[52] P. Piseri, A. Podestà, E. Barborini, P. Milani, Production and characterization of highly intense and collimated cluster beams by inertial focusing in supersonic expansions, Review of Scientific Instruments 72 (2001) 2261–2267. https://doi.org/10.1063/1.1361082.

[53] G. Bongiorno, C. Lenardi, C. Ducati, R.G. Agostino, T. Caruso, M. Amati, M. Blomqvist, E. Barborini, P. Piseri, S. La Rosa, E. Colavita, P. Milani, Nanocrystalline Metal/Carbon Composites Produced by Supersonic Cluster Beam Deposition, J Nanosci Nanotechnol 5 (2005) 1072–1080. https://doi.org/10.1166/jnn.2005.161.

[54] P. Liu, P.J. Ziemann, D.B. Kittelson, P.H. McMurry, Generating Particle Beams of Controlled Dimensions and Divergence: I. Theory of Particle Motion in Aerodynamic Lenses and Nozzle Expansions, Aerosol Science and Technology 22 (1995) 293–313. https://doi.org/10.1080/02786829408959748.

[55] F. Di Fonzo, A. Gidwani, M.H. Fan, D. Neumann, D.I. Iordanoglou, J.V.R. Heberlein, P.H. McMurry, S.L. Girshick, N. Tymiak, W.W. Gerberich, N.P. Rao, Focused nanoparticle-beam deposition of patterned microstructures, Appl Phys Lett 77 (2000) 910–912. https://doi.org/10.1063/1.1306638.

[56] A. Gidwani, Studies of Flow and Particle Transport in Hypersonic Plasma Particle Deposition and Aerodynamic Focusing. , University of Minnesota, 2003.

[57] O.F. Hagena, W. Obert, Cluster Formation in Expanding Supersonic Jets: Effect of Pressure, Temperature, Nozzle Size, and Test Gas, J Chem Phys 56 (1972) 1793–1802. https://doi.org/10.1063/1.1677455.

[58] J.F. De La Mora, P. Riesco-Chueca, Aerodynamic focusing of particles in a carrier gas, J Fluid Mech 195 (1988) 1. https://doi.org/10.1017/S0022112088002307.

[59] A. Sattar, S. Fostner, S.A. Brown, Quantized Conductance and Switching in Percolating Nanoparticle Films, Phys Rev Lett 111 (2013) 136808. https://doi.org/10.1103/PhysRevLett.111.136808.

[60] M. Olsen, M. Hummelgård, H. Olin, Surface Modifications by Field Induced Diffusion, PLoS One 7 (2012) e30106. https://doi.org/10.1371/journal.pone.0030106.

[61] R.F. Egerton, The Transmission Electron Microscope, in: Physical Principles of Electron Microscopy, Springer International Publishing, Cham, 2016: pp. 55–88. https://doi.org/10.1007/978-3-319-39877-8_3.

[62] B. Fultz, J. Howe, Transmission Electron Microscopy and Diffractometry of Materials, Springer Berlin Heidelberg, Berlin, Heidelberg, 2013. https://doi.org/10.1007/978-3-642-29761-8.

[63] D.B. Williams, C.B. Carter, The Transmission Electron Microscope, in: Transmission Electron Microscopy, Springer US, Boston, MA, 2009: pp. 3–22. https://doi.org/10.1007/978-0-387-76501-3_1.

[64] J. Mast, E. Verleysen, V.-D. Hodoroaba, R. Kaegi, Characterization of nanomaterials by transmission electron microscopy: Measurement procedures, in: Characterization of Nanoparticles, Elsevier, 2020: pp. 29–48. https://doi.org/10.1016/B978-0-12-814182-3.00004-3.

[65] transmission electron microscope, Https://Www.Britannica.Com/Technology/Transmission-Electron-Microscope (n.d.).

[66] S. Akhtar, Applications of Atomic Force Microscopy in Corrosion Research, in: Recent Developments in Analytical Techniques for Corrosion Research, Springer International Publishing, Cham, 2022: pp. 187–201. https://doi.org/10.1007/978-3-030-89101-5_9.

[67] Physics of XPS, Https://Xpslibrary.Com/Physics-of-Xps/ (n.d.).

[68] A.Yu. Olenin, Mechanisms of metal nanoparticle formation, Nanotechnol Russ 7 (2012) 238–242. https://doi.org/10.1134/S1995078012030123.

[69] R. Alayan, L. Arnaud, A. Bourgey, M. Broyer, E. Cottancin, J.R. Huntzinger, J. Lermé, J.L. Vialle, M. Pellarin, G. Guiraud, Application of a static quadrupole deviator to the deposition of size-selected cluster ions from a laser vaporization source, Review of Scientific Instruments 75 (2004) 2461–2470. https://doi.org/10.1063/1.1764607.

[70] J. Yu, W. Yuan, H. Yang, Q. Xu, Y. Wang, Z. Zhang, Fast Gas–Solid Reaction Kinetics of Nanoparticles Unveiled by Millisecond In Situ Electron Diffraction at Ambient Pressure, Angewandte Chemie International Edition 57 (2018) 11344–11348. https://doi.org/10.1002/anie.201806541.

[71] J.G. Railsback, A.C. Johnston-Peck, J. Wang, J.B. Tracy, Size-Dependent Nanoscale Kirkendall Effect During the Oxidation of Nickel Nanoparticles, ACS Nano 4 (2010) 1913–1920. https://doi.org/10.1021/nn901736y.

[72] J.A. Medford, A.C. Johnston-Peck, J.B. Tracy, Nanostructural transformations during the reduction of hollow and porous nickel oxide nanoparticles, Nanoscale 5 (2013) 155–159. https://doi.org/10.1039/C2NR33005A.

[73] R. Sainju, D. Rathnayake, H. Tan, G. Bollas, A.M. Dongare, S.L. Suib, Y. Zhu, *In Situ* Studies of Single-Nanoparticle-Level Nickel Thermal Oxidation: From Early Oxide Nucleation to Diffusion-Balanced Oxide Thickening, ACS Nano 16 (2022) 6468–6479. https://doi.org/10.1021/acsnano.2c00742.

[74] J. Söderlund, L.B. Kiss, G.A. Niklasson, C.G. Granqvist, Lognormal Size Distributions in Particle Growth Processes without Coagulation, Phys Rev Lett 80 (1998) 2386–2388. https://doi.org/10.1103/PhysRevLett.80.2386.

[75] F. Siviero, E. Barborini, C. Boragno, R. Buzio, E. Gnecco, C. Lenardi, P. Piseri, S. Vinati, U. Valbusa, P. Milani, In situ investigation of the first stages of growth of cluster-assembled carbon films by scanning tunnelling microscopy, Surf Sci 513 (2002) 381–388. https://doi.org/10.1016/S0039-6028(02)01786-7.

[76] B. Molleman, T. Hiemstra, Size and shape dependency of the surface energy of metallic nanoparticles: unifying the atomic and thermodynamic approaches, Physical Chemistry Chemical Physics 20 (2018) 20575–20587. https://doi.org/10.1039/C8CP02346H.

[77] J. Zhao, E. Baibuz, J. Vernieres, P. Grammatikopoulos, V. Jansson, M. Nagel, S. Steinhauer, M. Sowwan, A. Kuronen, K. Nordlund, F. Djurabekova, Formation Mechanism of Fe Nanocubes by Magnetron Sputtering Inert Gas Condensation, ACS Nano 10 (2016) 4684–4694. https://doi.org/10.1021/acsnano.6b01024.

[78] Y. Xia, D. Nelli, R. Ferrando, J. Yuan, Z.Y. Li, Shape control of size-selected naked platinum nanocrystals, Nat Commun 12 (2021) 3019. https://doi.org/10.1038/s41467-021-23305-7.

[79] A. Kuzminova, A. Hanková, N. Khomiakova, M. Cieslar, O. Kylián, Tailoring the shape of vanadium nanoparticles produced by gas aggregation source, Vacuum 206 (2022) 111545. https://doi.org/10.1016/j.vacuum.2022.111545.

[80] R. Ding, I.M. Padilla Espinosa, D. Loevlie, S. Azadehranjbar, A.J. Baker, G. Mpourmpakis, A. Martini, T.D.B. Jacobs, Size-dependent shape distributions of platinum nanoparticles, Nanoscale Adv 4 (2022) 3978–3986. https://doi.org/10.1039/D2NA00326K.

[81] L. Bardotti, P. Jensen, A. Hoareau, M. Treilleux, B. Cabaud, Experimental Observation of Fast Diffusion of Large Antimony Clusters on Graphite Surfaces, Phys Rev Lett 74 (1995) 4694–4697. https://doi.org/10.1103/PhysRevLett.74.4694.

[82] P. JENSEN, A.-L. BARABÁSI, H. LARRALDE, S. HAVLIN, H. EUGENE STANLEY, A FRACTAL MODEL FOR THE FIRST STAGES OF THIN FILM GROWTH, Fractals 04 (1996) 321–329. https://doi.org/10.1142/S0218348X96000431.

[83] P. Jensen, A.-L. Barabási, H. Larralde, S. Havlin, H.E. Stanley, Deposition, diffusion, and aggregation of atoms on surfaces: A model for nanostructure growth, Phys Rev B 50 (1994) 15316–15329. https://doi.org/10.1103/PhysRevB.50.15316.

[84] P. Jensen, A.-L. Barabási, H. Larralde, S. Havlin, H. Eugene Stanley, Connectivity of diffusing particles continually deposited on a surface: relation to LECBD experiments, Physica A: Statistical Mechanics and Its Applications 207 (1994) 219–227. https://doi.org/10.1016/0378-4371(94)90376-X.

[85] P. Jensen, B. Niemeyer, The effect of a modulated flux on the growth of thin films, Surf Sci 384 (1997) L823–L827. https://doi.org/10.1016/S0039-6028(97)00254-9.

[86] P. Jensen, N. Combe, Understanding the growth of nanocluster films, Comput Mater Sci 24 (2002) 78–87. https://doi.org/10.1016/S0927-0256(02)00167-2.

[87] P. MELINON, V. PAILLARD, V. DUPUIS, A. PEREZ, P. JENSEN, A. HOAREAU, J.P. PEREZ, J. TUAILLON, M. BROYER, J.L. VIALLE, M. PELLARIN, B. BAGUENARD, J. LERME, FROM FREE CLUSTERS TO CLUSTER-ASSEMBLED MATERIALS, Int J Mod Phys B 09 (1995) 339–397. https://doi.org/10.1142/S021797929500015X.

[88] P. Jensen, A.-L. Barabási, H. Larralde, S. Havlin, H. Eugene Stanley, Connectivity of diffusing particles continually deposited on a surface: relation to LECBD experiments, Physica A: Statistical Mechanics and Its Applications 207 (1994) 219–227. https://doi.org/10.1016/0378-4371(94)90376-X.

[89] F. Borghi, A. Podestà, C. Piazzoni, P. Milani, Growth Mechanism of Cluster-Assembled Surfaces: From Submonolayer to Thin-Film Regime, Phys Rev Appl 9 (2018) 044016. https://doi.org/10.1103/PhysRevApplied.9.044016.

[90] P. Jensen, A.-L. Barabási, H. Larralde, S. Havlin, H.E. Stanley, Growth and percolation of thin films: A model incorporating deposition, diffusion and

aggregation, Chaos Solitons Fractals 6 (1995) 227–236. https://doi.org/10.1016/0960-0779(95)80029-G.

[91] P. Jensen, A.-L. Barabási, H. Larralde, S. Havlin, H.E. Stanley, Model incorporating deposition, diffusion, and aggregation in submonolayer nanostructures, Phys Rev E 50 (1994) 618–621. https://doi.org/10.1103/PhysRevE.50.618.

[92] B. Yoon, V.M. Akulin, Ph. Cahuzac, F. Carlier, M. de Frutos, A. Masson, C. Mory, C. Colliex, C. Bréchignac, Morphology control of the supported islands grown from soft-landed clusters, Surf Sci 443 (1999) 76–88. https://doi.org/10.1016/S0039-6028(99)00988-7.

[93] S.L. Lai, J.Y. Guo, V. Petrova, G. Ramanath, L.H. Allen, Size-Dependent Melting Properties of Small Tin Particles: Nanocalorimetric Measurements, Phys Rev Lett 77 (1996) 99–102. https://doi.org/10.1103/PhysRevLett.77.99.

[94] M. Liu, R.Y. Wang, Size-Dependent Melting Behavior of Colloidal In, Sn and Bi Nanocrystals, Sci Rep 5 (2015) 16353. https://doi.org/10.1038/srep16353.

[95] P. Grammatikopoulos, M. Sowwan, J. Kioseoglou, Computational Modeling of Nanoparticle Coalescence, Adv Theory Simul 2 (2019). https://doi.org/10.1002/adts.201900013.

[96] P. Grammatikopoulos, C. Cassidy, V. Singh, M. Sowwan, Coalescence-induced crystallisation wave in Pd nanoparticles, Sci Rep 4 (2014) 5779. https://doi.org/10.1038/srep05779.

[97] M. José-Yacamán, C. Gutierrez-Wing, M. Miki, D.-Q. Yang, K.N. Piyakis, E. Sacher, Surface Diffusion and Coalescence of Mobile Metal Nanoparticles, J Phys Chem B 109 (2005) 9703–9711. https://doi.org/10.1021/jp0509459.

[98] K.E.J. Lehtinen, M.R. Zachariah, Energy accumulation in nanoparticle collision and coalescence processes, J Aerosol Sci 33 (2002) 357–368. https://doi.org/10.1016/S0021-8502(01)00177-X.

[99] H. Zhu, Sintering processes of two nanoparticles: A study by molecular dynamics simulations, Philos Mag Lett 73 (1996) 27–33. https://doi.org/10.1080/095008396181073.

[100] L.J. Lewis, P. Jensen, J.-L. Barrat, Melting, freezing, and coalescence of gold nanoclusters, Phys Rev B 56 (1997) 2248–2257. https://doi.org/10.1103/PhysRevB.56.2248.

[101] P. Jensen, Growth of nanostructures by cluster deposition: Experiments and simple models, Rev Mod Phys 71 (1999) 1695–1735. https://doi.org/10.1103/RevModPhys.71.1695.

[102] A.-L. Barabási, H.E. Stanley, Fractal Concepts in Surface Growth, Cambridge University Press, 1995. https://doi.org/10.1017/CBO9780511599798.

[103] F. Family, T. Vicsek, Scaling of the active zone in the Eden process on percolation networks and the ballistic deposition model, J Phys A Math Gen 18 (1985) L75–L81. https://doi.org/10.1088/0305-4470/18/2/005.

[104] S.F. Edwards, D.R. Wilkinson, The surface statistics of a granular aggregate, Proceedings of the Royal Society of London. A. Mathematical and Physical Sciences 381 (1982) 17–31. https://doi.org/10.1098/rspa.1982.0056.

[105] M. Kardar, G. Parisi, Y.-C. Zhang, Dynamic Scaling of Growing Interfaces, Phys Rev Lett 56 (1986) 889–892. https://doi.org/10.1103/PhysRevLett.56.889.

[106] S.K. Das, D. Banerjee, J.N. Roy, Stochastic Study of Random-Ballistic Competitive Growth Model in 2 + 1 Dimension and Related Scaling Exponents, Journal of The Institution of Engineers (India): Series D 104 (2023) 777–784. https://doi.org/10.1007/s40033-022-00408-z.

[107] A. Podestà, F. Borghi, M. Indrieri, S. Bovio, C. Piazzoni, P. Milani, Nanomanufacturing of titania interfaces with controlled structural and functional properties by supersonic cluster beam deposition, J Appl Phys 118 (2015). https://doi.org/10.1063/1.4937549.

[108] F. Borghi, M. Milani, L.G. Bettini, A. Podestà, P. Milani, Quantitative characterization of the interfacial morphology and bulk porosity of nanoporous cluster-assembled carbon thin films, Appl Surf Sci 479 (2019) 395–402. https://doi.org/10.1016/j.apsusc.2019.02.066.

[109] N. Cabrera, N.F. Mott, Theory of the oxidation of metals, Reports on Progress in Physics 12 (1949) 308. https://doi.org/10.1088/0034-4885/12/1/308.

[110] A.T. Fromhold, E.L. Cook, Kinetics of Oxide Film Growth on Metal Crystals: Thermal Electron Emission and Ionic Diffusion, Physical Review 163 (1967) 650–664. https://doi.org/10.1103/PhysRev.163.650.

[111] B.D. Anderson, J.B. Tracy, Nanoparticle conversion chemistry: Kirkendall effect, galvanic exchange, and anion exchange, Nanoscale 6 (2014) 12195–12216. https://doi.org/10.1039/C4NR02025A.

[112] A. Ermoline, E.L. Dreizin, Equations for the Cabrera–Mott kinetics of oxidation for spherical nanoparticles, Chem Phys Lett 505 (2011) 47–50. https://doi.org/10.1016/j.cplett.2011.02.022.

[113] Y. Yin, R.M. Rioux, C.K. Erdonmez, S. Hughes, G.A. Somorjai, A.P. Alivisatos, Formation of Hollow Nanocrystals Through the Nanoscale Kirkendall Effect, Science (1979) 304 (2004) 711–714. https://doi.org/10.1126/science.1096566.

[114] W. Wang, M. Dahl, Y. Yin, Hollow Nanocrystals through the Nanoscale Kirkendall Effect, Chemistry of Materials 25 (2013) 1179–1189. https://doi.org/10.1021/cm3030928.

[115] X. Yu, P.M. Duxbury, G. Jeffers, M.A. Dubson, Coalescence and percolation in thin metal films, Phys Rev B 44 (1991) 13163–13166. https://doi.org/10.1103/PhysRevB.44.13163.

[116] A. Sattar, S. Fostner, S.A. Brown, Quantized Conductance and Switching in Percolating Nanoparticle Films, Phys Rev Lett 111 (2013) 136808. https://doi.org/10.1103/PhysRevLett.111.136808.

[117] V.A. Timofeev, V.I. Mashanov, A.I. Nikiforov, I.D. Loshkarev, D. V. Gulyaev, V.A. Volodin, A.S. Kozhukhov, O.S. Komkov, D.D. Firsov, I. V. Korolkov, Study of structural and optical properties of a dual-band material based on tin oxides and GeSiSn compounds, Appl Surf Sci 573 (2022) 151615. https://doi.org/10.1016/j.apsusc.2021.151615.

[118] J.E. Martinez Medina, J. Polesel-Maris, A.M. Philippe, P. Grysan, N. Bousri, S. Girod, E. Barborini, The role of coalescence and ballistic growth on in-situ electrical conduction of cluster-assembled nanostructured Sn films, Appl Surf Sci 664 (2024) 160268. https://doi.org/10.1016/j.apsusc.2024.160268.

[119] Y. Zhao, J. Zhang, Microstrain and grain-size analysis from diffraction peak width and graphical derivation of high-pressure thermomechanics, J Appl Crystallogr 41 (2008) 1095–1108. https://doi.org/10.1107/S0021889808031762.

[120] F.A. Akgul, C. Gumus, A.O. Er, A.H. Farha, G. Akgul, Y. Ufuktepe, Z. Liu, Structural and electronic properties of SnO2, J Alloys Compd 579 (2013) 50–56. https://doi.org/10.1016/j.jallcom.2013.05.057.

[121] M. Fondell, M. Gorgoi, M. Boman, A. Lindblad, An HAXPES study of Sn, SnS, SnO and SnO2, J Electron Spectros Relat Phenomena 195 (2014) 195–199. https://doi.org/10.1016/j.elspec.2014.07.012.

[122] S. Tanuma, C.J. Powell, D.R. Penn, Calculations of electron inelastic mean free paths, Surface and Interface Analysis 37 (2005) 1–14. https://doi.org/10.1002/sia.1997.

[123] J.-M. Themlin, M. Chtaïb, L. Henrard, P. Lambin, J. Darville, J.-M. Gilles, Characterization of tin oxides by x-ray-photoemission spectroscopy, Phys Rev B 46 (1992) 2460–2466. https://doi.org/10.1103/PhysRevB.46.2460.

[124] K. Nose, A.Y. Suzuki, N. Oda, M. Kamiko, Y. Mitsuda, Oxidation of SnO to SnO_2 thin films in boiling water at atmospheric pressure, Appl Phys Lett 104 (2014) 091905. https://doi.org/10.1063/1.4867654.

[125] A. Nikiforov, V. Timofeev, V. Mashanov, I. Azarov, I. Loshkarev, V. Volodin, D. Gulyaev, I. Chetyrin, I. Korolkov, Formation of SnO and SnO2 phases during the annealing of SnO(x) films obtained by molecular beam epitaxy, Appl Surf Sci 512 (2020) 145735. https://doi.org/10.1016/j.apsusc.2020.145735.

[126] Q.-J. Liu, Z.-T. Liu, L.-P. Feng, First-principles calculations of structural, electronic and optical properties of tetragonal SnO2 and SnO, Comput Mater Sci 47 (2010) 1016–1022. https://doi.org/10.1016/j.commatsci.2009.11.038.

[127] L. Grządziel, M. Krzywiecki, A. Szwajca, A. Sarfraz, G. Genchev, A. Erbe, Detection of intra-band gap defects states in spin-coated sol-gel SnO_x nanolayers by photoelectron spectroscopies, J Phys D Appl Phys 51 (2018) 315301. https://doi.org/10.1088/1361-6463/aacf3a.

[128] B. Eifert, M. Becker, C.T. Reindl, M. Giar, L. Zheng, A. Polity, Y. He, C. Heiliger, P.J. Klar, Raman studies of the intermediate tin-oxide phase, Phys Rev Mater 1 (2017) 014602. https://doi.org/10.1103/PhysRevMaterials.1.014602.

[129] M. Li, R. Tan, R. Li, W. Song, W. Xu, Effects of pH on the microstructures and optical properties of Sn3O4 crystals prepared by hydrothermal method, Ceram Int 40 (2014) 11381–11385. https://doi.org/10.1016/j.ceramint.2014.02.118.

[130] S.D. Balgude, Y.A. Sethi, B.B. Kale, N.R. Munirathnam, D.P. Amalnerkar, P. V. Adhyapak, Nanostructured layered Sn_3O_4 for hydrogen production and dye degradation under sunlight, RSC Adv 6 (2016) 95663–95669. https://doi.org/10.1039/C6RA20058C.

[131] S. Chakrabarti, D. Carolan, B. Alessi, P. Maguire, V. Svrcek, D. Mariotti, Microplasma-synthesized ultra-small NiO nanocrystals, a ubiquitous hole transport material, Nanoscale Adv 1 (2019) 4915–4925. https://doi.org/10.1039/C9NA00299E.

[132] A. Kotta, E.-B. Kim, S. Ameen, H.-S. Shin, H.K. Seo, Communication—Ultra-Small NiO Nanoparticles Grown by Low-Temperature Process for

Electrochemical Application, J Electrochem Soc 167 (2020) 167517. https://doi.org/10.1149/1945-7111/abcf51.

[133] D.S. Hall, D.J. Lockwood, C. Bock, B.R. MacDougall, Nickel hydroxides and related materials: a review of their structures, synthesis and properties, Proceedings of the Royal Society A: Mathematical, Physical and Engineering Sciences 471 (2015) 20140792. https://doi.org/10.1098/rspa.2014.0792.

[134] Y. Yin, R.M. Rioux, C.K. Erdonmez, S. Hughes, G.A. Somorjai, A.P. Alivisatos, Formation of Hollow Nanocrystals Through the Nanoscale Kirkendall Effect, Science (1979) 304 (2004) 711–714. https://doi.org/10.1126/science.1096566.

[135] C.M. Wang, D.R. Baer, L.E. Thomas, J.E. Amonette, J. Antony, Y. Qiang, G. Duscher, Void formation during early stages of passivation: Initial oxidation of iron nanoparticles at room temperature, J Appl Phys 98 (2005). https://doi.org/10.1063/1.2130890.

[136] H.J. Fan, U. Gösele, M. Zacharias, Formation of Nanotubes and Hollow Nanoparticles Based on Kirkendall and Diffusion Processes: A Review, Small 3 (2007) 1660–1671. https://doi.org/10.1002/smll.200700382.

[137] W. Wang, M. Dahl, Y. Yin, Hollow Nanocrystals through the Nanoscale Kirkendall Effect, Chemistry of Materials 25 (2013) 1179–1189. https://doi.org/10.1021/cm3030928.

[138] B.D. Anderson, J.B. Tracy, Nanoparticle conversion chemistry: Kirkendall effect, galvanic exchange, and anion exchange, Nanoscale 6 (2014) 12195–12216. https://doi.org/10.1039/C4NR02025A.

[139] A.P. Grosvenor, M.C. Biesinger, R.St.C. Smart, N.S. McIntyre, New interpretations of XPS spectra of nickel metal and oxides, Surf Sci 600 (2006) 1771–1779. https://doi.org/10.1016/j.susc.2006.01.041.

[140] H.A.E. Hagelin-Weaver, J.F. Weaver, G.B. Hoflund, G.N. Salaita, Electron energy loss spectroscopic investigation of Ni metal and NiO before and after

surface reduction by Ar+ bombardment, J Electron Spectros Relat Phenomena 134 (2004) 139–171. https://doi.org/10.1016/j.elspec.2003.10.002.

[141] A.P. Grosvenor, B.A. Kobe, M.C. Biesinger, N.S. McIntyre, Investigation of multiplet splitting of Fe 2p XPS spectra and bonding in iron compounds, Surface and Interface Analysis 36 (2004) 1564–1574. https://doi.org/10.1002/sia.1984.

[142] M.C. Biesinger, B.P. Payne, L.W.M. Lau, A. Gerson, R.St.C. Smart, X-ray photoelectron spectroscopic chemical state quantification of mixed nickel metal, oxide and hydroxide systems, Surface and Interface Analysis 41 (2009) 324–332. https://doi.org/10.1002/sia.3026.

[143] ThermoFisherScientific online spectra database. , Https://Www.Thermofisher.Com/Fr/Fr/Home/Materials-Science/Learning-Center/Periodic-Table/Transition-Metal/Nickel.Html (n.d.).

[144] The international XPS database, Https://Xps-Database.Com/Nickel-Ni-Z28-Chemicals/ (n.d.).

[145] A.N. Mansour, Characterization of NiO by XPS, Surface Science Spectra 3 (1994) 231–238. https://doi.org/10.1116/1.1247751.

[146] A.N. Mansour, Characterization of β -Ni(OH)2 by XPS, Surface Science Spectra 3 (1994) 239–246. https://doi.org/10.1116/1.1247752.

[147] G.H. Major, N. Fairley, P.M.A. Sherwood, M.R. Linford, J. Terry, V. Fernandez, K. Artyushkova, Practical guide for curve fitting in x-ray photoelectron spectroscopy, Journal of Vacuum Science & Technology A 38 (2020). https://doi.org/10.1116/6.0000377.

[148] K.H. Rieder, A combined SIMS-AES/LEED study of the room-temperature oxidation of Ni(110) and Ni(111) surfaces, Applications of Surface Science 2 (1978) 74–84. https://doi.org/10.1016/0378-5963(78)90007-7.

[149] E.S. Lambers, C.N. Dykstal, J.M. Seo, J.E. Rowe, P.H. Holloway, Room-temerature oxidation of Ni(110) at low and atmospheric oxygen pressures, Oxidation of Metals 45 (1996) 301–321. https://doi.org/10.1007/BF01046987.

[150] D.S. Hall, D.J. Lockwood, C. Bock, B.R. MacDougall, Nickel hydroxides and related materials: a review of their structures, synthesis and properties, Proceedings of the Royal Society A: Mathematical, Physical and Engineering Sciences 471 (2015) 20140792. https://doi.org/10.1098/rspa.2014.0792.

[151] Y. Unutulmazsoy, R. Merkle, D. Fischer, J. Mannhart, J. Maier, The oxidation kinetics of thin nickel films between 250 and 500 °C, Physical Chemistry Chemical Physics 19 (2017) 9045–9052. https://doi.org/10.1039/C7CP00476A.

[152] A.P. LAGROW, N.M. ALYAMI, D.C. LLOYD, O.M. BAKR, E.D. BOYES, P.L. GAI, *In situ* oxidation and reduction of triangular nickel nanoplates via environmental transmission electron microscopy, J Microsc 269 (2018) 161–167. https://doi.org/10.1111/jmi.12621.

[153] J. Yu, W. Yuan, H. Yang, Q. Xu, Y. Wang, Z. Zhang, Fast Gas–Solid Reaction Kinetics of Nanoparticles Unveiled by Millisecond In Situ Electron Diffraction at Ambient Pressure, Angewandte Chemie International Edition 57 (2018) 11344–11348. https://doi.org/10.1002/anie.201806541.

[154] K. Koga, M. Hirasawa, Anisotropic growth of NiO nanorods from Ni nanoparticles by rapid thermal oxidation, Nanotechnology 24 (2013) 375602. https://doi.org/10.1088/0957-4484/24/37/375602.

[155] F.S. Manciu, J.L. Enriquez, W.G. Durrer, Y. Yun, C. V. Ramana, S.K. Gullapalli, Spectroscopic analysis of tungsten oxide thin films, J Mater Res 25 (2010) 2401–2406. https://doi.org/10.1557/jmr.2010.0294.

[156] O. Gurcuoglu, D. Evecan, E. Ozkan Zayim, Synthesis and characterization of tungsten oxide films by electrodeposition with various precursors and electrochromic device application, Journal of Solid State Electrochemistry 19 (2015) 403–413. https://doi.org/10.1007/s10008-014-2605-x.

[157] K. Zhang, W. Zhao, X. Sheng, Ion-gated tungsten oxide based electrochemical transistors with subthreshold slopes approaching the thermodynamic limit, Applied Physics A 129 (2023) 728. https://doi.org/10.1007/s00339-023-07005-1.

[158] W.C. Chien, Y.R. Chen, Y.C. Chen, A.T.H. Chuang, F.M. Lee, Y.Y. Lin, E.K. Lai, Y.H. Shih, K.Y. Hsieh, Chih-Yuan Lu, A forming-free WO<inf>x</inf> resistive memory using a novel self-aligned field enhancement feature with excellent reliability and scalability, in: 2010 International Electron Devices Meeting, IEEE, 2010: pp. 19.2.1-19.2.4. https://doi.org/10.1109/IEDM.2010.5703390.

[159] W.-T. Wu, J.-J. Wu, J.-S. Chen, Resistive Switching Behavior and Multiple Transmittance States in Solution-Processed Tungsten Oxide, ACS Appl Mater Interfaces 3 (2011) 2616–2621. https://doi.org/10.1021/am200430y.

[160] S. Corby, L. Francàs, A. Kafizas, J.R. Durrant, Determining the role of oxygen vacancies in the photoelectrocatalytic performance of WO_3 for water oxidation, Chem Sci 11 (2020) 2907–2914. https://doi.org/10.1039/C9SC06325K.

[161] Z. Sun, S. Bhattacharjee, M. Xiao, W. Li, M.O. Hill, R.A. Jagt, L.-V. Delumeau, K.P. Musselman, E. Reisner, J. MacManus-Driscoll, Low-temperature open-atmosphere growth of WO_3 thin films with tunable and high-performance photoresponse, J Mater Chem C Mater 12 (2024) 4779–4791. https://doi.org/10.1039/D3TC02257A.

[162] C. Martin, H. Hijazi, Y. Addab, B. Domenichini, M.E. Bannister, F.W. Meyer, C. Pardanaud, G. Giacometti, M. Cabié, P. Roubin, Tungsten oxide thin film bombarded with a low energy He ion beam: evidence for a reduced erosion and W enrichment, Phys Scr T170 (2017) 014019. https://doi.org/10.1088/1402-4896/aa89c1.

[163] C. Arnas, A. Chami, L. Couëdel, T. Acsente, M. Cabié, T. Neisius, Thermal balance of tungsten monocrystalline nanoparticles in high pressure magnetron discharges, Phys Plasmas 26 (2019). https://doi.org/10.1063/1.5095932.

[164] J.E. Martinez Medina, A.M. Philippe, J. Guillot, C. Vergne, Y. Fleming, E. Barborini, Intermediate tin oxide in stable core-shell structures by room temperature oxidation of cluster-assembled nanostructured Sn films, Appl Surf Sci 658 (2024) 159846. https://doi.org/10.1016/j.apsusc.2024.159846.

[165] B. Bollobás, O. Riordan, Percolation, Cambridge University Press, 2006. https://doi.org/10.1017/CBO9781139167383.

[166] S.R. Broadbent, J.M. Hammersley, Percolation processes, Mathematical Proceedings of the Cambridge Philosophical Society 53 (1957) 629–641. https://doi.org/10.1017/S0305004100032680.

[167] G. Grimmett, Percolation, Springer Berlin Heidelberg, Berlin, Heidelberg, 1999. https://doi.org/10.1007/978-3-662-03981-6.

[168] S. Kirkpatrick, Percolation and Conduction, Rev Mod Phys 45 (1973) 574–588. https://doi.org/10.1103/RevModPhys.45.574.

[169] S. Yamamuro, K. Sumiyama, T. Hihara, K. Suzuki, Geometrical and electrical percolation in nanometre-sized Co-cluster assemblies, Journal of Physics: Condensed Matter 11 (1999) 3247–3257. https://doi.org/10.1088/0953-8984/11/16/006.

[170] A. Sattar, S. Fostner, S.A. Brown, Quantized Conductance and Switching in Percolating Nanoparticle Films, Phys Rev Lett 111 (2013) 136808. https://doi.org/10.1103/PhysRevLett.111.136808.

[171] S.K. Bose, J.B. Mallinson, R.M. Gazoni, S.A. Brown, Stable Self-Assembled Atomic-Switch Networks for Neuromorphic Applications, IEEE Trans Electron Devices 64 (2017) 5194–5201. https://doi.org/10.1109/TED.2017.2766063.

[172] S. Shirai, S.K. Acharya, S.K. Bose, J.B. Mallinson, E. Galli, M.D. Pike, M.D. Arnold, S.A. Brown, Long-range temporal correlations in scale-free neuromorphic networks, Network Neuroscience 4 (2020) 432–447. https://doi.org/10.1162/netn_a_00128.

[173] D. Gall, The search for the most conductive metal for narrow interconnect lines, J Appl Phys 127 (2020). https://doi.org/10.1063/1.5133671.

[174] Laboratory for Energy & Nano Sciences (LENS), Https://Www.Lens-Online.Net/Meet-Amro/ (n.d.).

[175] J.G. Simmons, Generalized Formula for the Electric Tunnel Effect between Similar Electrodes Separated by a Thin Insulating Film, J Appl Phys 34 (1963) 1793–1803. https://doi.org/10.1063/1.1702682.

[176] J.B. Mallinson, S. Shirai, S.K. Acharya, S.K. Bose, E. Galli, S.A. Brown, Avalanches and criticality in self-organized nanoscale networks, Sci Adv 5 (2019). https://doi.org/10.1126/sciadv.aaw8438.

[177] K. Sotthewes, C. Hellenthal, A. Kumar, H.J.W. Zandvliet, Transition voltage spectroscopy of scanning tunneling microscopy vacuum junctions, RSC Adv 4 (2014) 32438. https://doi.org/10.1039/C4RA04651J.

[178] J.M. Houston, The Slope of Logarithmic Plots of the Fowler-Nordheim Equation, Physical Review 88 (1952) 349–349. https://doi.org/10.1103/PhysRev.88.349.

[179] J.M. Beebe, B. Kim, J.W. Gadzuk, C. Daniel Frisbie, J.G. Kushmerick, Transition from Direct Tunneling to Field Emission in Metal-Molecule-Metal Junctions, Phys Rev Lett 97 (2006) 026801. https://doi.org/10.1103/PhysRevLett.97.026801.

[180] S. Zhou, K. Chen, M.T. Cole, Z. Li, M. Li, J. Chen, C. Lienau, C. Li, Q. Dai, Ultrafast Electron Tunneling Devices—From Electric-Field Driven to Optical-Field Driven, Advanced Materials 33 (2021). https://doi.org/10.1002/adma.202101449.

[181] Z. Ebrahimpour, N. Mansour, Annealing effects on electrical behavior of gold nanoparticle film: Conversion of ohmic to non-ohmic conductivity, Appl Surf Sci 394 (2017) 240–247. https://doi.org/10.1016/j.apsusc.2016.10.041.

[182] D. Xiang, Y. Zhang, F. Pyatkov, A. Offenhäusser, D. Mayer, Gap size dependent transition from direct tunneling to field emission in single molecule junctions, Chemical Communications 47 (2011) 4760. https://doi.org/10.1039/c1cc10144g.

[183] M.A. Koten, P. Mukherjee, J.E. Shield, Core-Shell Nanoparticles Driven by Surface Energy Differences in the Co-Ag, W-Fe, and Mo-Co Systems, Particle & Particle Systems Characterization 32 (2015) 848–853. https://doi.org/10.1002/ppsc.201500019.

[184] R. Tran, Z. Xu, B. Radhakrishnan, D. Winston, W. Sun, K.A. Persson, S.P. Ong, Surface energies of elemental crystals, Sci Data 3 (2016) 160080. https://doi.org/10.1038/sdata.2016.80.

[185] J. Vernieres, S. Steinhauer, J. Zhao, P. Grammatikopoulos, R. Ferrando, K. Nordlund, F. Djurabekova, M. Sowwan, Site-Specific Wetting of Iron Nanocubes by Gold Atoms in Gas-Phase Synthesis, Advanced Science 6 (2019). https://doi.org/10.1002/advs.201900447.

[186] G. Korotcenkov, The role of morphology and crystallographic structure of metal oxides in response of conductometric-type gas sensors, Materials Science and Engineering: R: Reports 61 (2008) 1–39. https://doi.org/10.1016/j.mser.2008.02.001.

[187] T. Lin, X. Lv, S. Li, Q. Wang, The Morphologies of the Semiconductor Oxides and Their Gas-Sensing Properties, Sensors 17 (2017) 2779. https://doi.org/10.3390/s17122779.

[188] X. Kang, N. Deng, Z. Yan, Y. Pan, W. Sun, Y. Zhang, Resistive-type VOCs and pollution gases sensor based on SnO2: A review, Mater Sci Semicond Process 138 (2022) 106246. https://doi.org/10.1016/j.mssp.2021.106246.

[189] J.M. Xu, J.P. Cheng, The advances of Co 3 O 4 as gas sensing materials: A review, J Alloys Compd 686 (2016) 753–768. https://doi.org/10.1016/j.jallcom.2016.06.086.

[190] A. Kar, A. Patra, Recent development of core–shell SnO_2 nanostructures and their potential applications, J. Mater. Chem. C 2 (2014) 6706–6722. https://doi.org/10.1039/C4TC01030B.

[191] Y.-F. Sun, S.-B. Liu, F.-L. Meng, J.-Y. Liu, Z. Jin, L.-T. Kong, J.-H. Liu, Metal Oxide Nanostructures and Their Gas Sensing Properties: A Review, Sensors 12 (2012) 2610–2631. https://doi.org/10.3390/s120302610.

[192] E.M. Materon, F.R. Gómez, N. Joshi, C.J. Dalmaschio, E. Carrilho, O.N. Oliveira, Smart materials for electrochemical flexible nanosensors: Advances and applications, in: Nanosensors for Smart Manufacturing, Elsevier, 2021: pp. 347–371. https://doi.org/10.1016/B978-0-12-823358-0.00018-6.

[193] V. Shah, J. Bhaliya, G.M. Patel, P. Joshi, Room-Temperature Chemiresistive Gas Sensing of SnO2 Nanowires: A Review, J Inorg Organomet Polym Mater 32 (2022) 741–772. https://doi.org/10.1007/s10904-021-02198-5.

[194] H.-J. Kim, J.-H. Lee, Highly sensitive and selective gas sensors using p-type oxide semiconductors: Overview, Sens Actuators B Chem 192 (2014) 607–627. https://doi.org/10.1016/j.snb.2013.11.005.

[195] J. Zhang, X. Liu, G. Neri, N. Pinna, Nanostructured Materials for Room-Temperature Gas Sensors, Advanced Materials 28 (2016) 795–831. https://doi.org/10.1002/adma.201503825.

[196] B.K.S. Reddy, P.H. Borse, Review—Recent Material Advances and Their Mechanistic Approaches for Room Temperature Chemiresistive Gas Sensors, J Electrochem Soc 168 (2021) 057521. https://doi.org/10.1149/1945-7111/abf4ea.

[197] V.R. Naganaboina, S.G. Singh, Chemiresistive gas sensors: From novel gas-sensing materials to electrode structure, Chemical Physics Reviews 4 (2023). https://doi.org/10.1063/5.0151356.

[198] C. Liu, Q. Kuang, Z. Xie, L. Zheng, The effect of noble metal (Au, Pd and Pt) nanoparticles on the gas sensing performance of SnO_2 -based sensors: a case

study on the {221} high-index faceted SnO_2 octahedra, CrystEngComm 17 (2015) 6308–6313. https://doi.org/10.1039/C5CE01162K.

[199] K. Hu, F. Wang, H. Liu, Y. Li, W. Zeng, Enhanced hydrogen gas sensing properties of Pd-doped SnO2 nanofibres by Ar plasma treatment, Ceram Int 46 (2020) 1609–1614. https://doi.org/10.1016/j.ceramint.2019.09.132.

[200] P.M. Bulemo, D.-H. Kim, I.-D. Kim, Controlled synthesis of electrospun hollow Pt-loaded SnO2 microbelts for acetone sensing, Sens Actuators B Chem 344 (2021) 130208. https://doi.org/10.1016/j.snb.2021.130208.

[201] S. Steinhauer, E. Lackner, F. Sosada-Ludwikowska, V. Singh, J. Krainer, R. Wimmer-Teubenbacher, P. Grammatikopoulos, A. Köck, M. Sowwan, Atomic-scale structure and chemical sensing application of ultrasmall size-selected Pt nanoparticles supported on SnO_2, Mater Adv 1 (2020) 3200–3207. https://doi.org/10.1039/D0MA00244E.

[202] L.-Y. Zhu, L.-X. Ou, L.-W. Mao, X.-Y. Wu, Y.-P. Liu, H.-L. Lu, Advances in Noble Metal-Decorated Metal Oxide Nanomaterials for Chemiresistive Gas Sensors: Overview, Nanomicro Lett 15 (2023) 89. https://doi.org/10.1007/s40820-023-01047-z.

[203] N.J. Pineau, S.D. Keller, A.T. Güntner, S.E. Pratsinis, Palladium embedded in SnO2 enhances the sensitivity of flame-made chemoresistive gas sensors, Microchimica Acta 187 (2020) 96. https://doi.org/10.1007/s00604-019-4080-7.

[204] L. Chua, Memristor-The missing circuit element, IEEE Transactions on Circuit Theory 18 (1971) 507–519. https://doi.org/10.1109/TCT.1971.1083337.

[205] D.B. Strukov, G.S. Snider, D.R. Stewart, R.S. Williams, The missing memristor found, Nature 453 (2008) 80–83. https://doi.org/10.1038/nature06932.

[206] N. Carstens, M.-I. Terasa, P. Holtz, S. Kaps, T. Strunskus, A. Hassanien, R. Adelung, F. Faupel, A. Vahl, Memristive Switching: From Individual Nanoparticles Towards Complex Nanoparticle Networks, in: 2024: pp. 219–239. https://doi.org/10.1007/978-3-031-36705-2_9.

[207] N. Carstens, B. Adejube, T. Strunskus, F. Faupel, S. Brown, A. Vahl, Brain-like critical dynamics and long-range temporal correlations in percolating networks of silver nanoparticles and functionality preservation after integration of insulating matrix, Nanoscale Adv 4 (2022) 3149–3160. https://doi.org/10.1039/D2NA00121G.

[208] M. Mirigliano, F. Borghi, A. Podestà, A. Antidormi, L. Colombo, P. Milani, Non-ohmic behavior and resistive switching of Au cluster-assembled films beyond the percolation threshold, Nanoscale Adv 1 (2019) 3119–3130. https://doi.org/10.1039/C9NA00256A.

[209] M. Mirigliano, B. Paroli, G. Martini, M. Fedrizzi, A. Falqui, A. Casu, P. Milani, A binary classifier based on a reconfigurable dense network of metallic nanojunctions, Neuromorphic Computing and Engineering 1 (2021) 024007. https://doi.org/10.1088/2634-4386/ac29c9.

[210] M. Mirigliano, D. Decastri, A. Pullia, D. Dellasega, A. Casu, A. Falqui, P. Milani, Complex electrical spiking activity in resistive switching nanostructured Au two-terminal devices, Nanotechnology 31 (2020) 234001. https://doi.org/10.1088/1361-6528/ab76ec.

[211] F. Mambretti, M. Mirigliano, E. Tentori, N. Pedrani, G. Martini, P. Milani, D.E. Galli, Dynamical stochastic simulation of complex electrical behavior in neuromorphic networks of metallic nanojunctions, Sci Rep 12 (2022) 12234. https://doi.org/10.1038/s41598-022-15996-9.

[212] K. Udaya Mohanan, Resistive Switching Devices for Neuromorphic Computing: From Foundations to Chip Level Innovations, Nanomaterials 14 (2024) 527. https://doi.org/10.3390/nano14060527.

[213] S.S. Kundale, G.U. Kamble, P.P. Patil, S.L. Patil, K.A. Rokade, A.C. Khot, K.A. Nirmal, R.K. Kamat, K.H. Kim, H.-M. An, T.D. Dongale, T.G. Kim, Review of Electrochemically Synthesized Resistive Switching Devices: Memory Storage, Neuromorphic Computing, and Sensing Applications, Nanomaterials 13 (2023) 1879. https://doi.org/10.3390/nano13121879.

[214] H. Hu, A. Scholz, C. Dolle, A. Zintler, A. Quintilla, Y. Liu, Y. Tang, B. Breitung, G.C. Marques, Y.M. Eggeler, J. Aghassi-Hagmann, Inkjet-Printed Tungsten Oxide Memristor Displaying Non-Volatile Memory and Neuromorphic Properties, Adv Funct Mater 34 (2024). https://doi.org/10.1002/adfm.202302290.

[215] R. Yang, K. Terabe, Y. Yao, T. Tsuruoka, T. Hasegawa, J.K. Gimzewski, M. Aono, Synaptic plasticity and memory functions achieved in a WO $_{3-x}$-based nanoionics device by using the principle of atomic switch operation, Nanotechnology 24 (2013) 384003. https://doi.org/10.1088/0957-4484/24/38/384003.

[216] R. Yang, K. Terabe, T. Tsuruoka, T. Hasegawa, M. Aono, Oxygen migration process in the interfaces during bipolar resistance switching behavior of WO $_{3-x}$-based nanoionics devices, Appl Phys Lett 100 (2012). https://doi.org/10.1063/1.4726084.

Dissemination activities

Publications

M. Heggen, **J.E. Martinez Medina**, A.M. Philippe, E. Barborini, Experimental insights on the stability of core-shell structure in single Sn/SnOx spherical nanoparticles during room temperature oxidation, **Appl. Surf. Sci.** 684, 161984 (2025).

J.E. Martinez Medina, J. Polesel-Maris, A.M. Philippe, P. Grysan, N. Bousri, S. Girod and E. Barborini, The role of coalescence and ballistic growth on in-situ electrical conduction of cluster-assembled nanostructured Sn films, **Appl. Surf. Sci.**, 664, 160268 (2024).

J.E. Martinez Medina, A.M. Philippe, J. Guillot, C. Vergne, Y. Fleming and E. Barborini, Intermediate tin oxide in stable core-shell structures by room temperature oxidation of cluster-assembled nanostructured Sn films, **Appl. Surf. Sci.**, 658, 159846 (2024).

J.E. Martinez Medina, D. Arl, A.M. Philippe, P. Grysan, J. Guillot, C. Vergne and E. Barborini, Nanostructured nickel films by supersonic cluster beam deposition: Morphology, oxidation, and clues of hollow structures by Kirkendall effect at room temperature, **Vacuum**, 211, 111930 (2023).

Conferences

J.E. Martinez Medina, J. Polese, A.M. Philippe, P. Grysan and E. Barborini. Impact of nanoparticle size and coalescence on morphology and electrical properties of Sn and Pt cluster-assembled films. 32nd International Materials Research Congress (IMRC2024), Cancun, Mexico, **August 2024. Oral contribution.**

J. E. Martinez Medina, J. Polesel, D. Arl, A. M. Philippe, J. Guillot, C. Vergne and E. Barborini. Microstructure and electrical transport properties of cluster-assembled tin films. 23rd IEEE International Conference on Nanotechnology (IEEE-Nano 2023), Jeju, Korea, **July 2023. Oral contribution.**

J.E. Martinez Medina, D. Arl, J. Polesel, A.M. Philippe, P. Grysan1, J. Guillot1, C. Vergne and E. Barborini, Structural characterization of Sn atomic clusters synthesized by Cluster Beam Deposition, PACE Young Scientist Conference, Luxembourg, **October 2022. Oral contribution.**

J.E. Martinez Medina, D. Arl, J. Polesel, A.M. Philippe, P. Grysan, J. Guillot, C. Vergne and E. Barborini. Morphology and intraparticle structure of cluster beam synthesized Sn atomic clusters. 14th International Conference on Physics of Advanced (ICPAM-14) Materials, Dubrovnik, Croatia, **September 2022. Oral contribution.**

J.E. Martinez Medina, D. Arl, J. Polesel, A.M. Philippe, P. Grysan, J. Guillot, C. Vergne and E. Barborini, Cluster-assembled nanostructured films of Ni and Sn grown by cluster beam deposition technique. 5th Autumn School on Physics of Advanced Materials (PAMS-5), Dubrovnik, Croatia, **September 2022. Poster contribution. Best poster award.**

Outreach Activities

"No more battery, let's harvest energy!", FNR-Researchers' Day 2022, Esch-Sur-Alzette, Luxembourg, 2022.